High Precision Spectroscopy on Beams of Atoms and Dimers

Von der Fakultät für Mathematik und Physik der
Gottfried Wilhelm Leibniz Universität Hannover

zur Erlangung des Grades eines

Doktors der Naturwissenschaften
Dr. rer. nat.

genehmigte Dissertation

von

Dipl.-Phys. Dipl.-Math. Stephan Falke
geboren am 21.09.1977 in Bielefeld

2007

Referent: Prof. Dr. E. Tiemann

Koreferent: Dr. O. Dulieu, d.r.

Tag der Promotion: 30.01.2007

Abstract

This thesis is concerned with long range behavior of the interaction potential of two neutral atoms. Two aspects are of special interest: First, how the long range behavior changes if one of the atoms is replaced by another isotope. Second, how to model the influence of a laser field on long range interaction.

Several high precision spectroscopy experiments on particle beams are carried out. The transition frequencies of the D lines of ^{39,40,41}K are measured with frequency comb generated by a self-referenced femtosecond laser, which is locked to a Cs-clock. Discrepancies in the literature are removed and new values for the hyperfine structures of the $4p_{1/2}$ and $4p_{3/2}$ state and the isotope shift of both D lines are derive.

On a beam of potassium dimers the A $^1\Sigma_u^+$ state of K_2 is studied up to the dissociation limit complementing and extending photoassociation spectroscopy of ultracold ensembles. Local perturbation due to the spin-orbit coupling with the b $^3\Pi_u$ state are identified. Molecular hyperfine structure of levels close to the asymptote is observed and modeled by atomic parameter only. Improved values of the atomic radiative lifetime of the states $4p_{1/2}$ and $4p_{3/2}$ are derived from the long range parameter C_3 of the molecule. Also, an improved value for the dissociation energy of the X $^1\Sigma_g^+$ ground state is obtained and recipes for the investigation of cold collision via spectroscopy of the molecular structure at the ground state asymptotes are derived. For the first time asymptotic levels of two isotopomers of K_2 are studied and a comparison of asymptotic spectra of two isotopomers $^{39}K_2$ and $^{39}K\,^{41}K$ shows that corrections to the Born-Oppenheimer potential are needed.

Optical coupling between asymptotic ground state levels and long range levels of an excited state has been suggested as tool for influencing cold collisions. Here, we model lineshapes for an experiment which investigates such a coupling systematically in Na_2 by laser spectroscopy in a beam. A fit program for the lineshape is used to compare experimental and theoretical values and to check the validity of the applied model from multichannel quantum defect theory. The dependency on the detuning of the coupling laser is reproduced but other details failed.

To allow similar studies are reported for alkali metals on the simpler quantum system from alkali earth elements the development of an oven for a continuous beam of Ca_2 for Doppler-free spectroscopy is discussed including a major change of design and first experiences are reported. The heating of the oven is, unlike those for the beams applied above, outside the vacuum tank because of the high temperatures needed for the oven.

Keywords

Zusammenfassung

Diese Arbeit befaßt sich mit dem langreichweitigen Verhalten des Wechsewirkungspotentials zweier Neutralatome. Zwei Aspekte sind von besonderem Interesse. Erstens: Wie ändert sich das langreichweitige Verhalten wenn eines der Atome durch ein anderes Isotop ersetzt wird? Zweitens: Wie modelliert man den Einfluß eines Laserfeldes of die langreichweitge Wechselwirkung?

Mehrere hochauflösende Spektroskopieexperimente an Teilchenstrahlen werden durchgeführt. Die Übergangsfrequenzen der D-Linien von ^{39,40,41}K werden mittels Frequenzkamm gemessen, der von einem selbstreferenzierten Femtosekundenlaser erzeugt wird und an eine Cs-Uhr angeschlossen ist. Unstimmigkeiten von Literaturwerten werden geklärt und neue Werte für die Hyperfeinstrukturparameter des $4p_{1/2}$ und des $4p_{3/2}$ Zustandes sowie die Isotopieverschiebung beider D-Linien bestimmt.

An einem Strahl von Kaliumdimeren wird der A $^1\Sigma_u^+$ Zustand von K_2 bis zur Dissoziationsschwelle untersucht und damit komplementäre Messungen aus Photoassoziationspektroskopie ergänzt. Lokale Störungen durch die Spin-Bahn-Kopplung mit dem b $^3\Pi_u$ Zustand werden identifiziert. Molekulare Hyperfeinstruktur von Niveaus dicht unterhalb der Asymptote wird aufgelöst und allein durch atomare Parameter modelliert. Verbesserte Werte der atomaren Strahlungslebensdauer der Zustände $4p_{1/2}$ und $4p_{3/2}$ werden aus dem Parameter C_3 des langreichweitigen Molekülpotentials bestimmt. Zudem wird ein verbesserter Wert für die Dissoziationsenergie des Grundzustandes X $^1\Sigma_g^+$ bestimmt und Rezepte für die Untersuchung kalter Stöße mittels Molekülspektroskopie an der Grundzustandsasymptote abgeleitet. Erstmals werden asymptotische Niveaus zweier K_2 Isotopomere untersucht und ein Vergleich der asymptotischen Spektren der Isotopomere $^{39}K_2$ und $^{39}K\,^{41}K$ zeigt, dass Korrekturen des Born-Oppenheimer-Potentials nötig sind.

Optische Kopplung der Grundzustandsasymptote mit langreichweitigen Niveaus eines angeregten Zustands wurde als Möglichkeit zur Beeinflussung kalter Stöße vorgeschlagen. Hier modellieren wir Linienformprofile für ein Experiment, das eine solche Kopplung systematisch an Na_2 mittels Laserspektroskopie an einem Strahl untersucht. Eine Fitroutine für das Linienformprofil wird benutzt, um Therorie mit Experiment zu vergleichen und die Gültigkeit des angewandten Models der Multikanal-Quantendefekttheorie zu prüfen. Die Abhängigkeit der Laserverstimmung wird reproduziert, aber andere Details stimmen nicht überein.

Um ähnliche Untersuchungen wie die vorgestellten, die mit Alkalien durchgeführt werden, auch an den einfacheren Quantensystemen der Erdalkalien durchzuführen, wird ein Ofen für einen kontinuierlichen Strahl von Ca_2 zur dopplerfreien Spektroskopie inklusive einer bedeutenden Änderung der Bauart diskutiert, und zudem erste Erfahrungen vorgestellt. Die Heizung des Ofens erfolgt im Gegensatz zu den anderen oben vorgestellten Strahlen aufgrund der hohen benötigten Temperaturen von außerhalb des Vakuumtanks.

Schlagworte

Dopplerfreie Laserspektroskopie, Hyperfeinstruktur, Strahlungslebensdauer

Contents

7 Conclusion   **123**

Appendix

Chapter 1

Introduction

Spectroscopic experiments were essential in the development of models of the matter that we have reached until today. The interpretation of atomic spectra with the models by quantum mechanics has lead to a deep understanding of atoms. It is also confirmed by the periodic table of elements: the findings of quantum mechanical models for atoms are reflected by chemical properties of the elements. With higher resolution and precision, hyperfine structure was revealed and the inner structure of nuclei became subject of research.

Today, the highest precision of measured quanta is reached for frequency measurements. A significant contribution for the development of frequency measurements is the utilization of frequency comb generated by femtosecond lasers, for which the Nobel prize 2005 was awarded to Hänsch and Hall (along with Glauber).[1] Several high precision experiments aim on tests of the standard model.[2,3,4] Such experiments seek to measure or find upper limits of the variation of the fine structure constant α, which is constant within the standard model but not in extended theories.

This thesis, however, is not concerned with the limits of the standard model. Here, the well established quantum mechanics is used for the description of experiments done with the well established technique of laser spectroscopy on particle beams. We are interested in the description of binary cold and ultracold collisions of neutral atoms. These collisions are appearing in ensembles of dilute cold gases. Such gases are produced by laser cooling and trapping of atoms, a technique that opened doors to numerous experiments. The density of the cold atoms is so low that the atoms in the trapped ensemble could be considered free if the de Broglie wavelength of the particle would be small compared to average internuclear separation within the ensemble. But the dynamics of the ensemble is governed by the two particle interaction. For most experiments it is sufficient to approximate this interaction by a single value: the scattering length. The sign of this value explains whether the particle interaction is effectively attractive or repulsive and the absolute value of the scattering length indicates the interaction strength (or cross section). Rates for sympathetic cooling and rethermalization are described by the scattering length. Moreover, if the temperature of the trapped bosonic atoms is decreased until quantum degeneracy is reached, i.e., until a Bose-Einstein condensate is formed and the particles of the ensemble become coherent, the scattering length describes the mean field energy, i.e., the interaction of the ensemble with a single atom. But, after all, the

scattering length is a parameter that summarizes the interaction potential of two colliding atoms in a single value. It is a measure for the phase shift that a wavepacket describing one atom experiences while passing another atom. This measure can be calculated if the full interaction potential is known and characterizes the continuum levels populated in an ensemble of ultracold atoms.

The interaction potential can be studied by molecular spectroscopy. The potential energy curve that describes cold and ultracold collisions is the same that describes the structure of the dimer. For example the scattering length of sodium was measured by molecular spectroscopy.[5] Of high interest for a reliable prediction of cold collisions are the least bound levels of the interaction potential because the cold collisions are governed by the long range behavior. In fact, cold collisions can sometimes be described by knowing the asymptotic behavior of the interaction potential only.[6]

In recent years, experiments with ultracold atoms utilized more and more magnetic fields to tune the scattering length, i.e., the character of binary collisions changes under the influence of a magnetic field especially in the vicinity of a Feshbach resonance. A Feshbach resonance appears if a bound state of one potential energy surface that couple to continuum states of another interaction potential for example by hyperfine structure. The continuum states describe scattering states of two atoms and are populated in ensembles of ultracold atoms. An alternation of the coupling between bound levels and continuum states influences both, the bound state and the continuum states. Changing the magnetic field moves levels with different magnetic moments relative to another and alters, if these levels are coupled, both wavefunctions (see lower box in Figure 1.1). In case of continuum state, this change translates into a modification of the scattering length.

In many cases the scattering length can be tuned at will by magnetic fields. With this technique, the effective interaction could be switched from attractive to repulsive and *vice versa* for studies of the BEC-BCS[7,8] crossover in case of two Fermi particles. Ultracold ensembles of molecules were produced from ultracold atoms.[9] Feshbach resonances are described by the interplay of two molecular states. For this, knowledge about the long range interaction of two atoms is needed. For the description of the coupling strength atomic parameters such as the hyperfine structure parameters are needed.

In this thesis, two directions are followed to achieve a better understanding of long range interaction. First, the long range behavior of potassium is of interest because potassium has a very small hyperfine structure and offers several isotopes in natural abundance. Here we are mainly interested in comparing the two isotopomers $^{39}K_2$ and $^{39}K^{41}K$. These are the two most abundant combinations. We would like to understand better to which precision the knowledge of the interaction of one combination of isotopes may be transferred to another combination of isotopes. The main interaction of two atoms is clearly the interaction of the two electron clouds of the atoms. If one exchanges one of the two atoms with another isotope this interaction should remain the same. This is justified by the Born-Oppenheimer approximation. However, the level structure of the molecule changes according to the alternation of the reduced mass of the system. This scaling by mechanical principles from one isotopomer to another is called mass-scaling. For asymptotic levels of the potential the change of the hyperfine structure has to be taken into account, too. This is of great importance if one tries to mass-scale eigenenergies that are in the vicinity of the asymptote, e.g., Feshbach resonances. With incorporation

of changes for the hyperfine structure one can hope to mass-scale the scattering length of one isotope combination to another. But, since the scattering length is sensitive to tiny alternations of the potential, one relies on the Born-Oppenheimer approximation for the mass-scaling of ultracold collisions. Investigations of long range behavior of two isotopomers allows to study to which precision the Born-Oppenheimer approximation is valid.

Another interesting aspect about the comparison of $^{39}K_2$ and $^{39}K^{41}K$ is the difference of the 4s + 4p asymptote. The exchange symmetry is broken due to the isotope shift of the D lines (4s → 4p) and the different hyperfine structure. The degeneracy of this asymptote leads to a C_3/R^3 behavior for homonuclear molecules (resonant dipole-dipole interaction) whereas a C_6/R^6 behavior is obtained for molecules which have different transition frequencies of the D lines (detuned dipole-dipole interaction).

The second direction we are following in this thesis is the road towards alternatives for the manipulation of cold collisions. Laser fields have been suggested to be used for the manipulation of scattering states of the ground state asymptote, i.e., state populated in ultracold ensembles, by optical coupling to electronically excited molecular states.[10] The coupling is similar to photoassociation experiments but the laser should not be in resonance with a continuum-bound transition (see upper box in Figure 1.1). Instead it should induce a coupling between levels of an excited molecular state and scattering states of the ground state. The laser replaces the magnetic field that is used for the manipulation of cold collisions by Feshbach resonances. Such alternative method is interesting mainly because it can be applied to atoms without nuclear spin, for which Feshbach resonance cannot be utilized due to the lack of hyperfine structure. Laser fields can be switched faster than magnetic fields and might allow for the alternation of the scattering properties in a fraction of the cold ensemble. In the long run, the addressing of single sites of an optical lattice with a laser that is able to control the interaction of two atoms trapped in the addressed site, will be of great interest for quantum computing. However, here we are concerned with the fundamental understanding of this coupling between long range levels.

Laser cooling and trapping is mainly done for alkali metals and alkali earth metals. For this reason we are interested in understanding of the corresponding dimers. Conventional spectroscopy typically uses heat-pipes or heated cells to prepare the dimers. The population of levels results from the temperature of the reservoir and many levels are populated, mainly at the bottom of the potential, i.e., with short internuclear separation. By laser excitation, levels that are highly vibrationally excited can be investigated and by this the interval of investigations can be extended to higher energies and larger internuclear separations.

Dimers can also be produced from ultracold atoms, either by the utilization of Feshbach resonances with ramped magnetic fields or by photoassociation, in which a laser photon red detuned to an atomic resonance is absorbed by a pair of atoms. In this way, levels very close to the asymptote of molecular states can be investigated with high precision. But, the connection to energy intervals known from conventional spectroscopy is difficult (see the gap of observations on the energy axis in Figure 1.1).

The experiments described in this thesis are all experiments carried out with an experimental method that allows to bridge the gap. We are preparing the dimers in particle
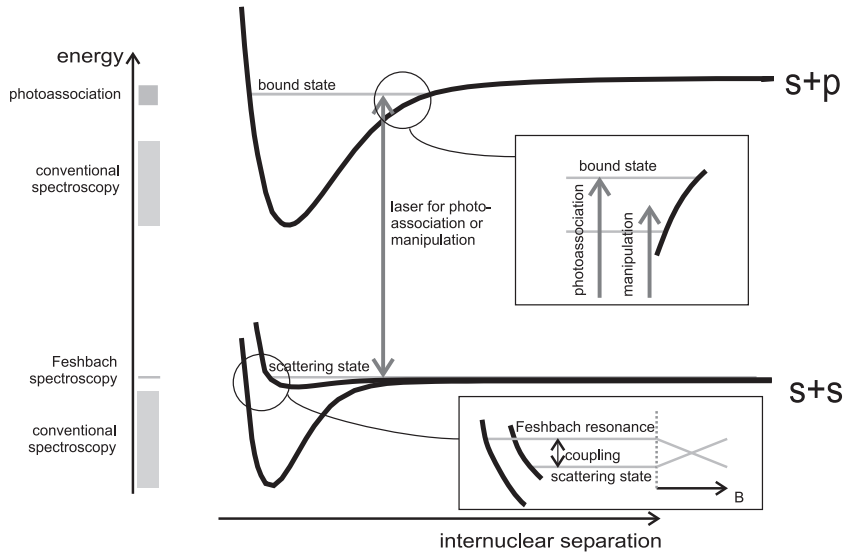
Figure 1.1: *Sketch of the lowest potential curves and illustration of experimental techniques. Dimer states populated in ultracold ensembles are levels just below the ground state asymptote (s+s). These dimers can be formed either with magnetic ramps with a Feshbach resonance (lower box) or with a photoassociation laser (upper box). Note the typical gap between the intervals of observations indicated at the energy axis for conventional spectroscopy and spectroscopy from ultracold atoms.*

beams. The dimers fall freely (at high horizontal speed) in vacuum and are well de-coupled from the environment. The shift of transition frequencies due to interactions with other particles from residual gases or other particles in the beam can be neglected for the precision of our experiments. Experiments for investigating these interactions show that such influences are less than 15 kHz on optical transition frequencies and particle densities in beams as applied in this thesis.[11] The dimers (and atoms) in the beam are therefore considered free. This is a big advantage over experiments in which the objects are prepared in a thermal reservoir, e.g., in a glass cell or in a heat pipe. Another advantage for molecules prepared in beams is that during the adiabatic expansion into the vacuum, the inner degrees of freedom, i.e., vibration and rotation, are cooled down. The population distribution over levels corresponds to temperatures of some tens Kelvin or only few Kelvin. The spectra of molecules in beams are therefore greatly simplified in comparison to cell experiments, in which these temperatures of the inner degrees of freedom are in equilibrium with the temperature of the reservoir, which is typically at several hundreds to thousand Kelvin.

The main advantage of beam experiments over cell experiments is the reduction of the Doppler width. By selecting those objects moving orthogonal to the probe laser beams, the Doppler width can be reduced to below the natural line width, which is typical of some MHz for optical, dipole allowed transitions. In cell experiments, the Doppler width is typically several hundreds of MHz. In beam experiments we do not need to perform saturation spectroscopy, which is often used in cell experiments to obtain linewidth below

preparation method:	cells	beams	trapped atoms
examples	Na$_2$, K$_2$, Rb$_2$, Ca$_2$, LiCs, NaK, NaRb, NaCs, KRb	Na$_2$, K$_2$, NaK	Li$_2$, Na$_2$, K$_2$, Rb$_2$, Ca$_2$, Sr$_2$, Yb$_2$, He$_2$, NaCs, KRb, RbCs
Doppler width[a]	400 MHz	5 MHz	10 kHz
time per scan	20 min	5 min	4 h
number of lines per scan	200	10	30
rotational level	15 to 60	0 to 25	0 to 4
complexity of spectra	high	low	medium
vacuum pressure required	10^{-3} mbar	10^{-6} mbar	10^{-9} mbar
complexity of setup	low	medium	high
energy interval (asymptote as reference)	bottom to -1 cm	bottom to asymptote	-15 cm^{-1} to close to asymp. [b]

Table 1.1: *Comparison of spectroscopic methods for diatomic molecules. Given are typical numbers. For actual experiments the numbers may vary significantly. The lists of investigated molecules are by no means complete.*

[a]The observed linewidth depends on the applied spectroscopic method. Techniques for Doppler-free spectroscopy are advantageous especially in cell experiments.

[b]Schemes with several laser fields allow for pumping of molecules down to the bottom of the ground state.[20]

the Doppler width.

Two more advantages of particle beams will be mentioned: First, good access to the particles is possible allowing to apply external magnetic, electric, or laser fields studying their influence on the atoms or molecules. Second, sequential multi-photon pumping schemes can be easily applied: The geometrical positioning of laser beams translated directly to a time sequence of laser pulses acting on the object, which flies through the laser beams.

Despite these advantages, particle beams do not resolve the problem of the limited time of the interaction between object and laser field: The objects have velocities of around 1 000 m/s in the laboratory frame. Thus, laser cooling and trapping allow for large observation time and thus for high precision experiments with atoms. Direct laser cooling of molecules is practically impossible. On the one hand, experiments try to decelerate molecules prepared in particle beams to a standstill.[12,13] On the other hand, molecules are prepared from trapped atoms either in photoassociation[14,15] or variation of the magnetic fields utilizing Feshbach resonances.[16,17] The translational temperature of the molecules is inherited from the ultracold atoms. In order to reduce line widths for high precision experiments, either the atoms can be cooled down, even to quantum degeneracy, or sub Doppler spectroscopy may be applied. Experiments with photoassociation below a narrow atomic transition were performed in strontium[18] and ytterbium.[19]

Experiments with molecules starting from cold atoms are not unique for performing

spectroscopy of lines, but they allow for studies of ensemble, e.g., phase transitions. This is possible because of the long time that the prepared molecules can interact with another.[21] Heteronuclear dimers can strongly interact via electric dipole moments. However, dimers close to the asymptote, i.e., dimers that are produced by photoassociation or Feshbach ramps from ultracold atoms, do not have a significant dipole moment. The dipole moments increase for bigger binding energies. Schemes for optical pumping of heteronuclear molecules to lower vibrational levels[22] offer a pathway to enter the strongly interacting regime and provide an alternative to the chromium BEC with the large magnetic dipole moment.[23]

In molecular beams we can investigate such population transfer processes in the inverse way: Dimers in the vibrational ground levels are successively excited and dissociated to pairs of atoms. Moreover, by applying optical pumping steps, gaps between knowledge of deeply bound levels obtained in conventional spectroscopy with cells and results from photoassociation are bridged. The three discussed classes of spectroscopic experiments — cell experiments, beam experiments, and experiments starting from ultracold atoms — supplement each other and benefit from the other classes. Properties of the three discussed experimental methods are summarized in Table 1.1. Spectroscopy with photoassociation from trapped atoms is mainly useful to gather data of low rotational levels of electronically and vibrationally excited states whereas cell experiments are typically used for the creation of datasets with a wide range in rotation for electronic states to which the molecules decay to, i.e., mostly to electronic ground states.

This thesis discusses a number of experiments on particles prepared in beams. The experimental equipment is introduced in Chapter 2. The subsequent chapters discuss the undertaken experiments individually. In Chapter 3 we investigate the potassium D lines and derive improved atomic parameters such as hyperfine structure constants and isotope shifts. These are important for the modelling of long range interaction. In Chapter 4 the long range behavior of two isotopomers of potassium is investigated. By comparing the results the Born-Oppenheimer approximation for long range levels is studied. In Chapter 5 we are interested in varying the long range behavior by laser fields. Models for experimental observations are tested and compared. The long range interaction of alkali earth metals allows for a simplification of the models due to the lack of hyperfine structure, which would greatly simplify the models for laser induced manipulation of long range behavior, too. In Chapter 6 progress towards a beam of alkali earth metal dimers and first achievements are reported. A summary of the obtained results is given in Chapter 7.

Chapter 2

Experimental Setups

As introduced above, several experiments are carried out within this thesis. All experiments are spectroscopic experiments using cw single-mode lasers. This chapter introduces important experimental tools, which are used in our investigations. Here, we focus on the general and common properties, whereas details and specialties are discussed in the corresponding subsequent chapters.

The objects we are interested in, namely atoms and dimers, are prepared in particle beams. With this method, these objects are well isolated from the environment and can be considered free. But, interaction of atoms may be investigated, too. The interaction potentials for two atoms is derived by spectroscopy of dimers that are made up from the two atoms whose interaction is of interest. For example, by studying K_2 one is able to investigate the interaction of two potassium atoms. Some general considerations were already discussed in the introduction. The beam apparatuses used in our experiments are described and compared in Section 2.1.

Spectroscopic experiments do not only require the preparation of the objects of interests, but also a probe-detection setup. Here, we use lasers to drive optical transitions. The laser induced fluorescence is our experimental signal. The used lasers are introduced in Section 2.2. Also, methods for the measurement of their frequency are discussed.

2.1 Beam Apparatuses

For the realization of a particle beam a vacuum setup is used. Atoms or molecules from alkali metal or alkali earth metal are produced in an oven located therein, in which the corresponding material is vaporized. Out of this reservoir the atoms and dimers travel through a nozzle into the vacuum chamber. The principal setup is shown in Figure 2.1. The particle with the desired direction, i.e., those moving horizontally and orthogonal to the applied laser beams, are selected by a spatial filter, a skimmer, that separates the vacuum tank into two chambers: an oven chamber and a beam chamber. Only a small percentage of the atoms and molecules enters the beam chamber. The selected particles make up the beam and are tested in the spectroscopic experiments by laser fields.

In the presented experiments, laser induced fluorescence is recorded. This is discussed in Section 2.1.1. Thereafter, three different beam apparatuses are introduced, in which the
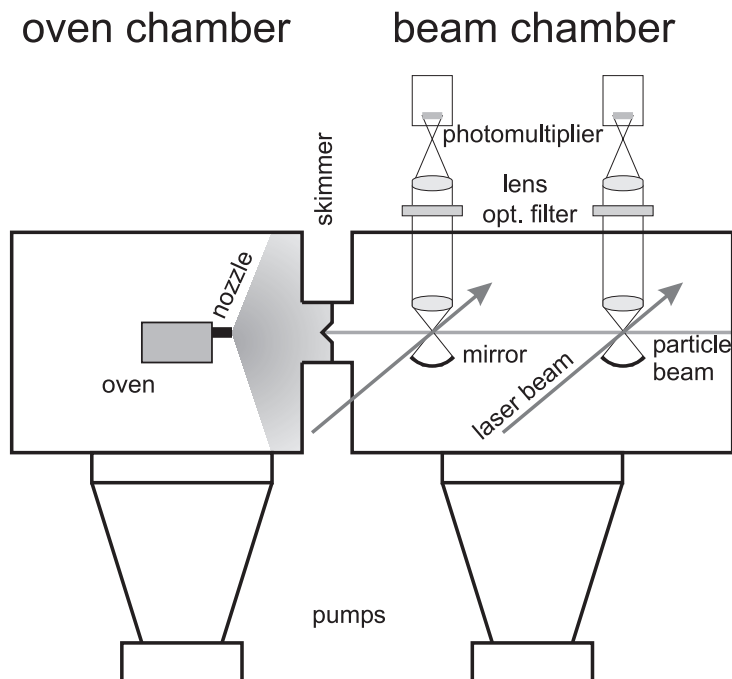
Figure 2.1: *Principal setup of a beam apparatus.*

experiments are performed. The properties of these machines are compared in Table 2.1.

2.1.1   Fluorescence Detection

The laser beams induce fluorescence if the field is in resonance with a transition starting from a populated level. For dimers, the decay channel of a molecular level is predominantly not the one that the laser drives. Thus, the molecule cannot be re-excited by the laser and each molecule contributes at most a single photon to the signal. The significant frequency shift of the fluorescence light allows to separate scattered stray light from the laser and the light from the laser induced fluorescence by optical filters. Most fluorescence photons have lower energy than the laser photons. Color glass filters are therefore appropriate for our applications. Interference filters, which act as band-passes, are often a good choice as an alternative or in addition to a color glass filter if the fluorescence is narrow banded.

The fluorescence from an interaction zone (the crossings between laser beams and particle beams) is detected by a photomutiplier located outside on top of the vacuum chamber. They are cooled down to around 270 K by Peltier elements to reduce the dark current. A lens system and a spheric mirror beneath the interaction zones are designed to image as much fluorescence as possible from the interaction zone onto the sensitive area of the photomultiplier.

	potassium	sodium	calcium
pump of oven chamber	diffusion	diffusion	diffusion
pump of beam chamber	turbomolecular	diffusion	diffusion
pressure, beam chamber	10^{-8} mbar	10^{-6} mbar	10^{-6} mbar
detection zones	1 near IR	2 visible	2 visible
oven temperature	650 K	750 K	1 300 K
heating of oven	inside vacuum	inside vacuum	outside vacuum
additional comments	μ-metal box, differential pump stage	suppression of stray laser light	cooling of oven chamber, suppression of stray laser light

Table 2.1: *Comparison of the beam apparatuses used.*

2.1.2   Potassium Beam

The main usage of the apparatus for a beam of potassium atoms and dimers is to run an interferometer on molecular lines. Here, tiny effects of dimer-atom collisions are of interest.[24,11] The pressure of the beam chamber is very low (below 10^{-8} mbar) to avoid decoherence effects due to collisions with residual gas. This is achieved by an additional separation of the beam chamber for which a differential pump stage is added. Details of beam apparatus[24] and recent modification[11] are discussed in the two corresponding PhD thesis.

The oven can be loaded with up to about 30 g of potassium. This material is used up within about twelve hours of operation. The oven is heated by a resistance heater inside the oven chamber. The nozzle is laser drilled with a diameter of 200 μm and its temperature kept about 100 K above the oven temperature by an additional heater.

The interaction zone is shielded by a μ-metal box. It suppresses the magnetic field in the laboratory, i.e., mainly the magnetic field of the earth, by a factor of twenty. Holes for the optical access limit the efficiency of the box.

The particles in the beam are mainly atoms. Some percent of the atoms emitted from the oven are bound in dimers, which are internally cooled in the adiabatic expansion into the vacuum in collisions with potassium atoms. Those can be considered as carrier gas for the dimers.

2.1.3   Sodium Beam

The oven chamber for the sodium beam is similar to the one in the potassium beam setup.[25] But, no additional intermediate chamber is used. Therefore, the residual gas pressure is higher but still in the order of 10^{-6} mbar.

No μ-metal box is installed around the interaction zone. This beam chamber has two subsequent interaction zones. The first zone is used to prepare molecules with a laser. The second zone is laid out to reduce scattered light from spectroscopic lasers scattered of the viewports as much as possible. This is done by mounting the viewports far away from

the interaction zone in Brewster angle and, additionally, a series of apertures between viewport and interaction zone.

2.1.4 Calcium Beam

Our experiments with calcium were done with the same apparatus the sodium beam was operated in. However, the oven concept was changed and thus only the beam chamber was used. The new oven chamber for an oven with higher temperatures will be introduced in detail in Chapter 6.

2.2 Lasers

The most important tool for any laser-spectroscopic experiment is of course the laser. Several continuous wave (cw) lasers are used for the experiments of this thesis. They are briefly introduced in the following. The laser light is distributed in our laboratories by optical fibers. This allows, e.g., to have the lasers in a room fairly quiet compared to that of the vacuum chambers with its rotary-vane pumps.

2.2.1 Dye Lasers

Several dye lasers are used. Linear laser (Coherent CR 599-21) and ring lasers (Coherent CR 699-21) are used in single mode operation pumped either by a high power frequency doubled Nd:YAG laser at 532 nm (Coherent Verdi 5 or Verdi 10) or an argon ion laser (Coherent Innova 400) with several Watt output power. The argon ion laser may pump several dye lasers, even on different lines if run in all-line operation. Blue and green pump light is then split by a dichroic beam splitter.[26]

The dye lasers are locked on a temperature stabilized external cavity for a reduction of the linewidth to about 1 MHz. The locked lasers have scanning ranges up to 20 GHz, achieved mainly by a galvo driven Brewster plate. Error signals may be added to the same electronics and by this the laser may be either frequency modulated or stabilized on another reference.

2.2.2 Ti:sapphire Lasers

In addition to the dye lasers, two Ti:sapphire lasers (Tekhnoscan TIS-SF-07) where used. With some modifications for frequency stabilization made within our group (by Horst Knöckel, Kirsten Jaspers, and Ivan Sherstov), the setup of these lasers corresponds basically to those of the ring dye laser. The scanning range is smaller (about 3 GHz) but the stabilization to an external cavity and possibility to use error signals are similar. Like dye lasers in the visible wavelength region, these lasers cover the near infrared region from 950 nm down to 700 nm with high power single-mode radiation.

2.2.3 Diode Laser

Additional to these high power lasers, a diode laser is used. A commercial laser diode is operated in a home-built extended cavity setup in Littrow configuration, which allows for a small linewidth. A piezoelectric actuator allows for scanning and the processing of error signals.

2.2.4 Offset Stabilization

At several points of the experiments, we made use of an offset stabilization setup. It allows to stabilize a cw laser to any frequency for several hours with very small drifts. A iodine stabilized HeNe laser (company: Präzisions-Mess-Technik) is used in this setup, which is stable to better than 5 kHz/h. Its frequency is shifted by an AOM in double pass and a temperature stabilized cavity with one mirror on a piezoelectric actuator is locked to the frequency shifted HeNe. The laser, which is supposed to be stabilized, is shined through this cavity with an orthogonal polarization axis. The cavity is transmitting for frequencies that are a multiple of the free spectral range of 150 MHz. This comb may be tuned via the AOM frequency of the HeNe. A modulation of the cavity allows to lock the laser to a specific transmission peak. In this way, the stability of the iodine is transferred via HeNe laser and cavity to the laser of interest. The residual frequency drift of the locked laser can be reduced to few 100 kHz/h.

The Allan standard deviation of a Ti:sapphire locked with offset stabilization was measured with a frequency comb (see below) to be 2.5×10^{-11} within one second. It decreased with a $1/\sqrt{t}$ dependence over to time t down to 5×10^{-12} after twenty seconds of averaging time.

2.2.5 Frequency Measurement

Several techniques for the measurement of the oscillation frequency of the laser are used in this thesis. A traveling Michelson interferometer with a HeNe laser as reference allows for quick measurements with a precision of better than 1 GHz.[27] In connection with pre-values from this wavelength meter, an iodine absorption setup allows for a precision of 150 MHz. The transition frequencies of the iodine lines are taken either from an atlas[28] or from profiles simulations with the program IodineSpec.[29] During the experiments of this thesis, a commercial wavelength meter was obtained (HighFinesse WS-7). It has a precision of 100 MHz with readout rates of twenty values per second with few μW laser light power. A link between a computer for the evaluation of the wavelength and the PC recording the experimental data allowed to include the measured wavelength into the files with tabulated experimental traces. At one occasion, a similar wavelength meter with even better precision of 60 MHz (HighFinesse WS-ultimate) was borrowed from another group of our institute, which is working with ultracold magnesium (Ertmer, Rasel).

Even higher precision of the measurement of transition frequencies was obtained by a frequency comb setup. For this technique, the Nobel prize was awarded to Hall and Hänsch (along with Glauber) in 2005. Gesine Grosche and Harald Schnatz from the PTB (Physikalisch-Technische Bundesanstalt, Braunschweig) measured the frequency of

a Ti:sapphire laser stabilized via the transfer cavity described in Section 2.2.4. A self-referenced frequency comb of a pulsed Ti:sapphire laser with repetition rate of 750 MHz was used. The uncertainty of the commercial wavelength meter is therefore seven times smaller than the repetition rate, which allows to derive the order of the comb peak uniquely.

For the relative frequency measurements, we record the transmission of a temperature stabilized Fabry-Perot interferometer with a free spectral range of 150 MHz. For the Ti:sapphire laser, the interpolation between the transmission peaks allows for a the measurement of relative frequencies with an uncertainty of 2 MHz.

Chapter 3

Transition Frequencies of the D lines of Potassium

The first spectroscopic experiment discussed in this thesis is not about dimers but its constituents: We re-measured the potassium D lines. Atomic resonance frequencies are usually well known since they are comparatively easy to measure and many experiments need this information, e.g., cooling lasers of trap experiments use these lines.

We discovered an astonishing difference between the resonance frequency measured by a newly obtained wavelength meter and recent publications[30,31] during the experiments, which will be described in Chapter 4. The transition frequency will be needed for the determination of the final results in our study. Both D lines for ^{39}K and ^{41}K showed discrepancies.

After verifying our result, we searched in the literature for other measurements. An additional publication[32] agreed with our results but not with the most recent publications. Thus, neither the new wavelength meter nor our frequency calibration were to be blamed. In contrast, it is our scientific duty to re-measure the transition frequencies as well as possible.

Our experimental apparatus, namely a highly collimated beam of potassium dimers and atoms, allows to detect the rare isotope ^{40}K, which has gained much interest in recent years among researchers of cold gases due to its fermionic character.[8]

The transitions of the atoms are a lot stronger than those of dimers. Experiments of the metrology of these transition frequencies aim for a precision that is better than the precision needed for the experiments that try to observe a big number of transitions frequencies to obtain potential energy curves describing a dimer state. Gesine Grosche and Harald Schnatz from the PTB joined our efforts. They provided and operated a frequency comb, with which the frequency of a laser was directly linked to the clock signal of a commercial Cs-clock, which was provided by the PTB as well.

Our findings and results were reported in an article. It is enclosed to this thesis in the following (Section 3.1). It is published originally in *Physical Review A*, Volume 74 under article number 032503 on 6th of September 2006. In Section 3.2 our considerations on the possible errors due to the ac-Stark effect are discussed in more detail.

3.1 Transition frequencies of the D lines of ^{39}K, ^{40}K, and ^{41}K measured with a femtosecond laser frequency comb

Stephan Falke, Eberhard Tiemann, and Christian Lisdat[a]

Institut für Quantenoptik, Universität Hannover, Welfengarten 1, 30167 Hannover, Germany

Harald Schnatz and Gesine Grosche

Physikalisch-Technische Bundesanstalt, Bundesallee 100, 38116 Braunschweig, Germany

Abstract: We report measurements of the transition frequencies $4s\ ^2S_{1/2} - 4p\ ^2P_{1/2}$ and $4s\ ^2S_{1/2} - 4p\ ^2P_{3/2}$ of the potassium isotopes 39, 40, and 41 through an atomic beam experiment with a fractional uncertainty of about 2×10^{-10}. For frequency calibration, a fs-laser comb referenced to a Cs atomic clock was used. Compared to previous results, hyperfine constants for the states $4p\ ^2P_{1/2}$ and $4p\ ^2P_{3/2}$ and isotope shifts are given with a considerably reduced uncertainty. This article also resolves the discrepancy of transition frequencies measured by A. Banerjee *et al.* [Phys. Rev. A **70**, 052505 (2004)] and W. Scherf *et al.* [Z. Phys. D **36**, 31 (1996)] and the hyperfine constant $A(^{39}\text{K},^2P_{1/2})$ reported by A. Banerjee *et al.* [Europhys. Lett. **65**, 172 (2004)] and N. Bendali *et al.* [J. Phys. B: At. Mol. Phys. **14**, 4231 (1981)].

[a]lisdat@iqo.uni-hannover.de

3.1.1 Introduction

The advent of femtosecond laser frequency combs has greatly simplified precision experiments in optical spectroscopy.[33] Of high importance are experiments which test fundamental concepts in physics e.g. the time independence of constants like the fine structure constant α. Here, the precise knowledge of optical transition frequencies of different atoms or molecules can be exploited to deduce variations of α.[3] Precise spectroscopic information also allows to test atomic structure calculations and can be used to determine properties of the nucleus like the nuclear moments or effective charge radius. Furthermore, well known transition frequencies can serve efficiently as frequency references for other experiments.

Very successful experiments have been performed with various atoms[34,35] and in particular with alkali metal atoms.[36,37,38,39] For potassium, Banerjee *et al.* recently investigated the most abundant isotope ^{39}K by saturation spectroscopy.[40,30,31] For these measurements, either a Michelson interferometer or a transfer-cavity with known free spectral range was used.[41] One determines the difference frequency between a known

laser (typically locked to the D_2 line of ^{85}Rb) and the laser used for spectroscopy on the system of interest. Banerjee *et al.* showed that their results agree with published ones from 1956,[42] but did not discuss more recently measured transition frequencies with improved uncertainty with respect to Ref.,[42] that deviate more than 400 MHz from their results.[32] A similar discrepancy exists for the magnetic dipole coupling constant $A(^{39}$K) of the $4p\ ^2P_{1/2}$ state reported in Ref.,[31] which agrees with the value from Ref.,[43] but is inconsistent with values in Refs.[44, 45] A more detailed discussion of these points will be given in Section 3.1.4.1 in combination with our own pre-investigations.

To resolve these discrepancies, we have now carried out precision measurements of the D lines of potassium with an improved experimental setup. For the frequency measurement, we use a fs-laser frequency comb referenced to a portable Cs atomic clock with an uncertainty below 10^{-11}. We have probed the potassium atoms in a highly collimated atomic beam. This method has the advantage over cell experiments that the Doppler width can be reduced well below the natural line width. The absence of a broad Doppler background allows the observation of the less abundant isotopes ^{40}K and ^{41}K.[44] Special care must be taken, as this experimental technique suffers from possible systematic shifts caused by a Doppler shift due to misalignment of laser probe beam and atomic beam. However, it has been shown that this draw-back can be overcome by thorough adjustment with the help of a retro-reflector[37] or by reciprocal fiber coupling.[46]

3.1.2 Experimental Setup

The atomic beam apparatus has been described previously in Ref.[47] The beam has supersonic character though no carrier gas is used. The mean particle velocity is about 1000 m/s with a velocity spread of ± 100 m/s. The beam has a collimation ratio of about 1000, which leads to a residual Doppler width of approximately 2 MHz in the spectral region considered here. The residual gas pressure in the interaction zone is below 10^{-8} mbar and the density of atoms in the beam is of the order of 10^9 cm^{-3}. The solid angle of detection is about 1.4 srad, the fluorescence is detected by a photomultiplier and current amplifier. The interaction volume of atomic and laser beam is shielded from magnetic fields by a μ-metal box, which reduces the residual magnetic field to below 20 mG.

Figure 3.1 shows schematically the optical setup. Light from an extended-cavity diode laser in Littrow configuration (called spectroscopy laser) is transferred with an optical fiber from a quiet lab to the atomic beam apparatus. The atoms are probed with a linearly polarized laser beam of 2 mm diameter. The polarization axis with respect to the residual magnetic field is unknown and possible errors are included in our analysis. The spectroscopy laser is locked to a cw titanium-sapphire transfer-laser by stabilizing the beat note of both with a phase-frequency comperator. Its reference frequency is provided by a frequency synthesizer, which is controlled by the data acquisition system.

The frequency of the transfer-laser is determined with a self-referenced Ti:Sa fs-laser frequency comb by counting the beat note between the transfer-laser and a comb tooth of the fs-comb. The repetition of the fs-comb (about 700 MHz) is stabilized using the clock signal of a commercial Cs-clock. The counted frequency value is used for the determination of the transfer-laser frequency. The carrier-envelope-offset frequency $\nu_{\rm ceo}$ of the frequency comb is not stabilized but counted. All counters have a gate time of 1 s.
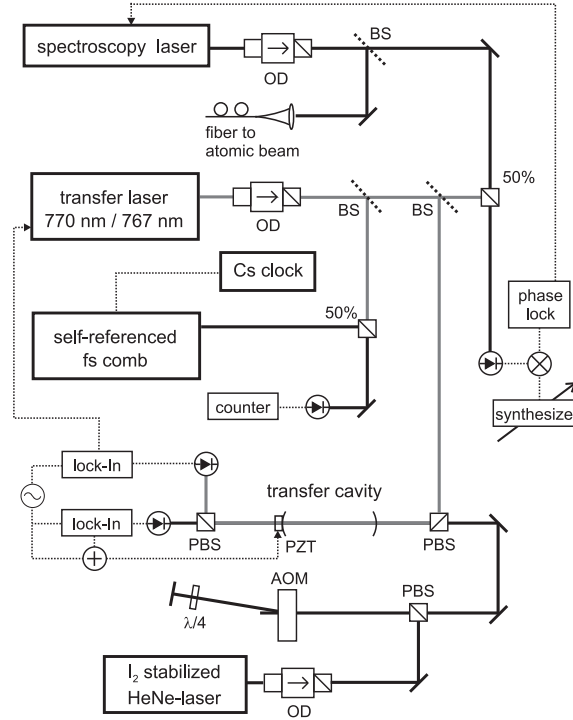
Figure 3.1: *Laser system used for the frequency measurement.* OD*: optical diode;* BS*: beam splitter;* 50%*: 50% beam splitter;* PBS*: polarizing beam splitter;* PZT*: piezo-electric actuator;* FPI*: Faby-Perot interferometer;* $\lambda/4$: $\lambda/4$ retarder.*

To improve the frequency stability of the transfer-laser, it is stabilized via a tunable transfer cavity to an I_2 stabilized He:Ne laser. Arbitrary difference frequencies are accessible by an acousto-optical modulator (AOM). In this way we observe a fractional frequency stability of the transfer laser of $3 \times 10^{-11} \tau^{-1/2}$, where τ is the averaging time in seconds. The frequency comb generator in connection with the Cs-clock allows to measure its frequency with a fractional accuracy of about 10^{-11} in 1 s.

To record the potassium spectra, the diode laser is tuned by the data acquisition system via the synthesizer as shown in Figure 3.1, while the frequency of the transfer laser is counted by the fs-comb. The synchronization between both recordings is done by additionally counting the synthesizer frequency. The typical step size of the spectroscopy laser was 200 kHz, the recording time per point 200 ms with 20 ms dead time to allow for delays in the frequency settling of the synthesizer. We recorded both directions of scan to detect and reduce shifts from electronic time constants.

3.1.3 Doppler Compensation

In precision experiments with particle beams, it is important to minimize the residual first order Doppler shift. It appears if the angle between probe laser beam and atomic beam deviates from 90°. For this purpose, we have recorded our spectra utilizing a cat's eye. It ideally retro-reflects the probe laser beam in itself without losses through the interaction region with the atomic beam. The retro-reflector consists out of an achromatic lens with

30 cm focal length and mirror in a gimbal mount. The distance between mirror and lens has to be exactly the focal length of the lens to achieve anti-parallelism of incoming and outgoing beam. It can be set by a micrometer screw adjustable translation stage, the alignment was done by means of an optical interferometer in which the cat's eye served as one end mirror.

According to Ref.,[48] the residual angle between both beams can be inferred from the uncertainty of the mirror's position, the residual angle between the axis of the cat's eye and the laser beam and the spatial displacement of the laser beam from the axis. Under our conditions we estimate a residual angle of less than 10 μrad between incoming and outgoing beam.

Assuming similar excitation and detection efficiency for both laser beam directions, the observed fluorescence signal will be symmetric around the unshifted frequency. Any deviation of the one-beam frequency from this Doppler-shift-free frequency can be due to either a residual Doppler shift or asymmetry. The residuals scatter after fitting a single beam profile with a symmetric model function justifies that for Doppler shift smaller than the residual Doppler width, the measured profile is sufficiently symmetric. Thus, the deviation has to be accounted to the residual Doppler shift in the single beam measurement and the resulting frequency of the two beam experiment can be considered Doppler-shift free.

If the signals from both beam directions have not the same strength, the observed line will not be centered at the Doppler free frequency. The imperfection of the Doppler compensation can be estimated from the intensity of one- and two-beam spectra. The deviation from the optimum factor of two between both spectra was less than 25%, from which a remaining error from the Doppler effect of less than 50 kHz can be inferred with the help of line profile simulations. Here, the imperfection of the cat's eye is already included.

We confirmed these considerations by a measurement with a completely independent technique. Two anti-parallel laser beams of the same intensity were generated by utilizing laser beams from two optical fibers and coupling the beam of one fiber into the other. With this technique a remaining angle between both beams of below 35 μrad can be achieved,[46] this limit corresponds to a shift of about 50 kHz. Spectra with both fibers were recorded independently, the averaged frequency is considered Doppler free. We have reproduced the measured frequency from one side within 10 kHz after recoupling that fiber, but will not claim to be in general better than the estimated 50 kHz. The average from both directions deviated for several lines by less than 30 kHz from transition frequencies measured with the cat's eye technique. Our final measurements were performed with the cat's eye technique because of a better long-term stability.

Moreover, from measurements with and without cat's eye one could derive the sign of the remaining Doppler shift with retro-reflector. In combination with the estimated Doppler suppression, a frequency correction can be calculated, which corresponded in sign and magnitude to the observed difference between measurements with two fibers and cat's eye. However, the correction of the remaining uncompensated Doppler shift is much smaller than its uncertainty. Therefore, no correction was applied.

3.1.4   Measurements and Analysis

3.1.4.1   Frequency pre-investigations

We have outlined in the introduction that inconsistent frequency values for the potassium D lines of ^{39}K appear in the literature. Banerjee *et al.*[30,31] reached an uncertainty of about 100 kHz for the D_2 line and better for the D_1 transitions. They compared their results with the value from Risberg.[42] Risberg's measurements had for the potassium D lines a rather large uncertainty of about 800 MHz plus uncertainties stemming from the dispersion correction formula[49] used to calculate vacuum wave numbers. The authors of Refs.[30,31] did not discuss the measurements of Scherf *et al.*[32] Here, an uncertainty of 20 MHz is stated.

    The discrepancy between Scherf and Banerjee is more than 400 MHz, which is not only many times the respective uncertainty but also comparatively easy to detect with classical spectroscopic means. Thus, we have performed several checks before the fs-comb supported frequency measurement.

    Potassium spectra were recorded together with I_2 Doppler broadened absorption spectra, that can be used as a frequency calibration with an uncertainty of about 100 MHz. The frequency of the nearest I_2 line was taken either from the iodine atlas[28] or from a simulation of the I_2 spectrum.[29] Both values are in perfect agreement. Furthermore, the frequency was measured with two commercial wavelength meters (HighFinesse WS-7, WS-8) with a reduced uncertainty of 100 MHz and 30 MHz, respectively. These methods have sufficient accuracy to distinguish between transition frequencies from both groups. All results were consistent with the transition frequencies given by Scherf.[32]

    Thus, we have to conclude that possibly the starting value of Banerjee *et al.* was not sufficiently precise to unambiguously determine the D lines' frequencies. This is also a possible explanation for the deviation between their hyperfine parameters and the values given in Refs.[44,45]

3.1.4.2 D_1 line

All lines belonging to the D_1 line at 12985 cm^{-1} of potassium are spectrally comparatively well isolated. They are grouped in pairs of two lines with common lower hyperfine level F and differing total angular momentum F' in the exited state. Thus two groups of two lines each were measured for the isotopes 39, 40, and 41. The spectra were recorded with retro-reflector to compensate for Doppler shifts. The typical peak intensity per laser beam was 13 μW/cm^2 of ^{39,41}K, while 280 μW/cm^2 had to be used to achieve a reasonable signal-to-noise ratio for ^{40}K. The residual Doppler shift was regularly checked by recording spectra without cat's eye to exclude unnoticed drifts in the setup.

    One record of the transition $F = 2 \rightarrow F' = 1, 2$ is shown in Figure 3.2. Each line was fitted with a modified Lorentzian function, where the parameters for amplitude, line width, and center frequency ν_0 were independent for both hyperfine transitions. Additionally, a constant background to account for stray laser light or photomultiplier dark current was adjusted. The Lorentzian profile was modified, since a small residual Doppler effect is expected. Due to the narrow velocity distribution of the atoms in the direction of flight and the high collimation ratio of the beam, we assumed constant amplitudes for
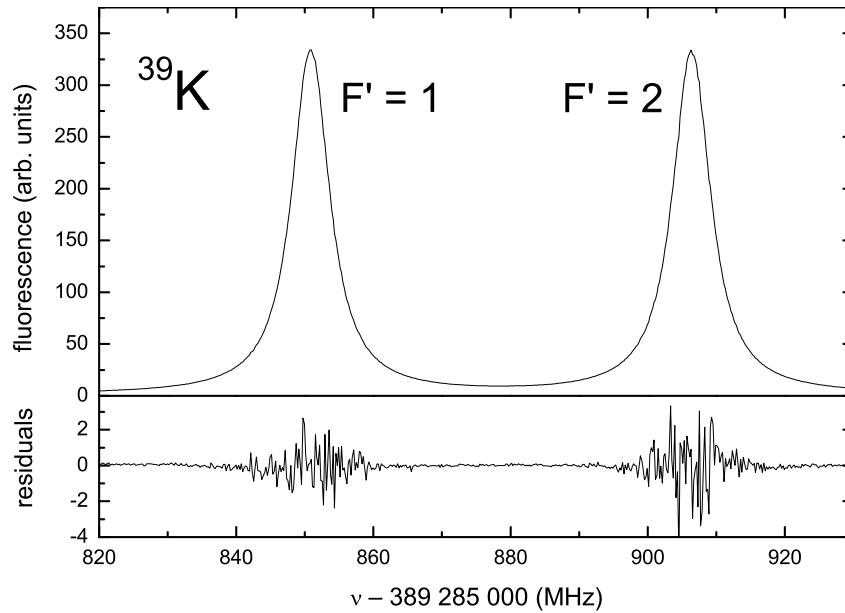
Figure 3.2: *Record of the D_1 transitions $F = 2 \rightarrow F' = 1, 2$ in ^{39}K. The lower trace shows the residuals of the fit, which was used to determine the line center. Note the zoom factor of about 50.*

the Doppler components in the frequency interval $\nu_0 \pm \nu_D$, and zero outside. The fitted values for ν_D were for all fits in good agreement with the expected value of about 1 MHz. The fitted homogeneous line width is about 6.5 MHz, which is very close to the value of 6.0 MHz expected from the life time of the excited state.[50] The residuals of the fit are depicted in the lower trace of Figure 3.2. A very good description of the observed line profiles is achieved.

When spectra of the less abundant isotopes ^{40}K and ^{41}K were fitted, additionally a frequency dependent background had to be taken into account. It originates from the Lorentzian wings of the transitions in the main isotope ^{39}K. For the background, the same function as described above was used; but only its amplitude was a fitting parameter. The width was fixed to a typical value, while the center frequency was taken from the nearest hyperfine transition of ^{39}K. An example for the transition $F = 9/2 \rightarrow F' = 9/2, 7/2$ in ^{40}K is shown in Figure 3.3. The residuals in the lower part of the figure are again very small and do not show any systematic deviations.

The statistical uncertainty of the fitted transition frequencies depend on the signal-to-noise ratio of the spectra. For the stronger spectra of ^{39,41}K, typically a value below 4 kHz was determined by the fit. For ^{40}K the statistical uncertainty is around 15 kHz.

A very significant consistency check of the data is to derive the ground state hyperfine splitting. We calculated it from the mean transition frequencies. Our values for the D_1 lines agree with the well known microwave spectroscopy data (Arimondo et al.:[51] ^{39}K: 461.720 MHz, ^{40}K: -1285.79 MHz, and ^{41}K: 254.014 MHz; values rounded to digits needed in the present case) to within 20 kHz. The hyperfine splittings of the excited state measured from ground states with different F are consistent within 10 kHz, which is another verification.
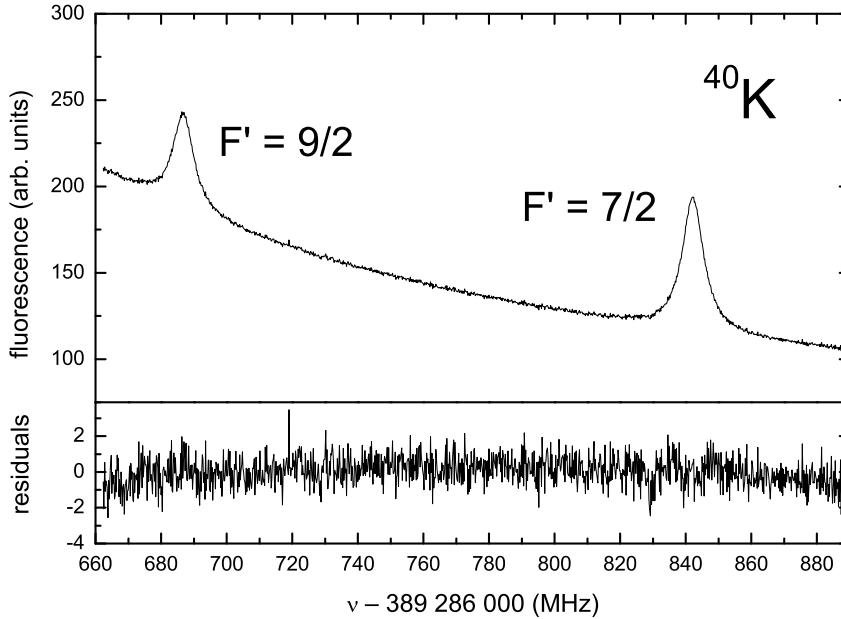
Figure 3.3: *The D_1 transitions $F = 9/2 \rightarrow F' = 9/2, 7/2$ in ^{40}K. The frequency dependent background stems from the wings of the transitions in ^{39}K. The lower trace shows the residuals of the fit magnified by a factor of about 40.*

Deviations of this magnitude are consistent with imperfections and changes in the Doppler compensation (Section 3.1.3) or other systematic line shifts (see Section 3.1.4.4), but can also be attributed to a larger error in the determination of the line center and underestimation of the corresponding uncertainty by the fit. An interpretation along this line is indicated by the increased deviation of the likewise determined ground state splitting in ^{40}K of 38 kHz for the common upper level $F' = 9/2$ and even 140 kHz for $F' = 7/2$, respectively. It has to be noticed that the transition $F = 7/2 \rightarrow F' = 7/2$ is very weak and sitting on a comparatively steep background. An exceptionally large variation in the residual Doppler effect due to rapid changes in the optical alignment can be excluded since the transition $F = 7/2 \rightarrow F' = 9/2$ was recorded in the same scan. The statistical uncertainty of the $F = 7/2 \rightarrow F' = 7/2$ line's frequency is with 35 kHz more than twice as big as for the other transitions of ^{40}K. We conclude therefore that the uncertainty in the determination of the line center is underestimated by the fit. Realistic uncertainty contributions for the determination of the line center are 20 kHz and 40 kHz for ^{39,41}K and ^{40}K, respectivly.

3.1.4.3 D_2 line

The D_2 lines of potassium at 13042 cm^{-1} were measured in a similar way to the D_1 lines. Differences in the analysis arise from the very small hyperfine splitting in the $^2P_{3/2}$ state of ^{39}K that leads to a triplet of transitions overlapping within the natural line width (see Figure 3.4). The situation is even worse for ^{41}K (see Figure 3.5), were the hyperfine splitting is about a factor of two smaller than in ^{39}K.[52]

Besides the nuclear magnetic dipole interaction parametrized by the A factor, for
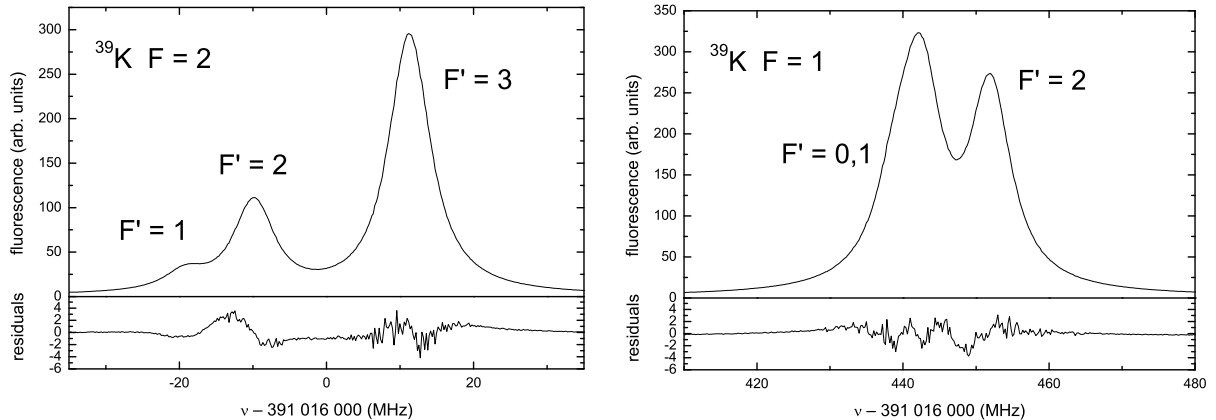
Figure 3.4: *Spectrum of the transitions belonging to the D_2 line of ^{39}K. On the left, the lower hyperfine state is $F = 2$, the right side depicts the spectrum from $F = 1$. The residuals are enlarged by a factor 30.*

the $^2P_{3/2}$ level the electric quadrupole interaction has to be taken into account, which is represented by the coupling constant B. For the individual analysis of each hyperfine group, this leads to the difficult situation that three free parameters determining the line positions have to be adjusted to an overlapping structure.

It was therefore preferred to perform joint fits of both groups' spectra $F = 1$ and $F = 2$ of each isotope with common hyperfine parameters. In this way, six transitions observed and recorded several times were described by only three parameters for the frequency, where we made use of the very precisely known ground state splitting $F = 1 \leftrightarrow F = 2$.[51] The other parameters discussed in Section 3.1.4.2 were individually adjusted for each recorded spectrum, but only two Lorentzian line widths were fitted to further reduce the number of free parameters: we found that the transitions with $\Delta F = \pm 1$ are satisfactorily described with a common Lorentzian line width. All lines are modeled with the same Doppler width. With these restrictions, the fitting is much more deterministic and produces reliable results. Such a lengthy fitting procedure was not necessary in the case of the D_1 lines, where the transitions are well separated and frequencies can be evaluated easily for each line.

The consistency of the measurements was checked by the isotope ^{40}K, which has a larger hyperfine splitting and shows less overlapping line profiles. The expected ground state splitting is reproduced with a deviation of less than 40 kHz by fitting the center frequency of each hyperfine multiplet individually with common parameters A and B.

The residuals depicted in Figure 3.4 for the ^{39}K D_2 line indicate some remaining mismatch of experimental observations and fit. This is also true but less severe in the case of ^{41}K (Figure 3.5), while for ^{40}K the quality of the fit is comparable to the one shown in Figure 3.3. In Figure 3.5, two traces of residuals are depicted for each group. They stem from fits with freely adjusted hyperfine parameters of the $^2P_{3/2}$ state and from a fit, where they were fixed to the values from Ref.[52] We will come to this again in Section 3.1.5.

We attribute the deviations to weak effects of optical pumping. Attempts to fit our spectra with a density matrix approach using our experimental parameters lead to no
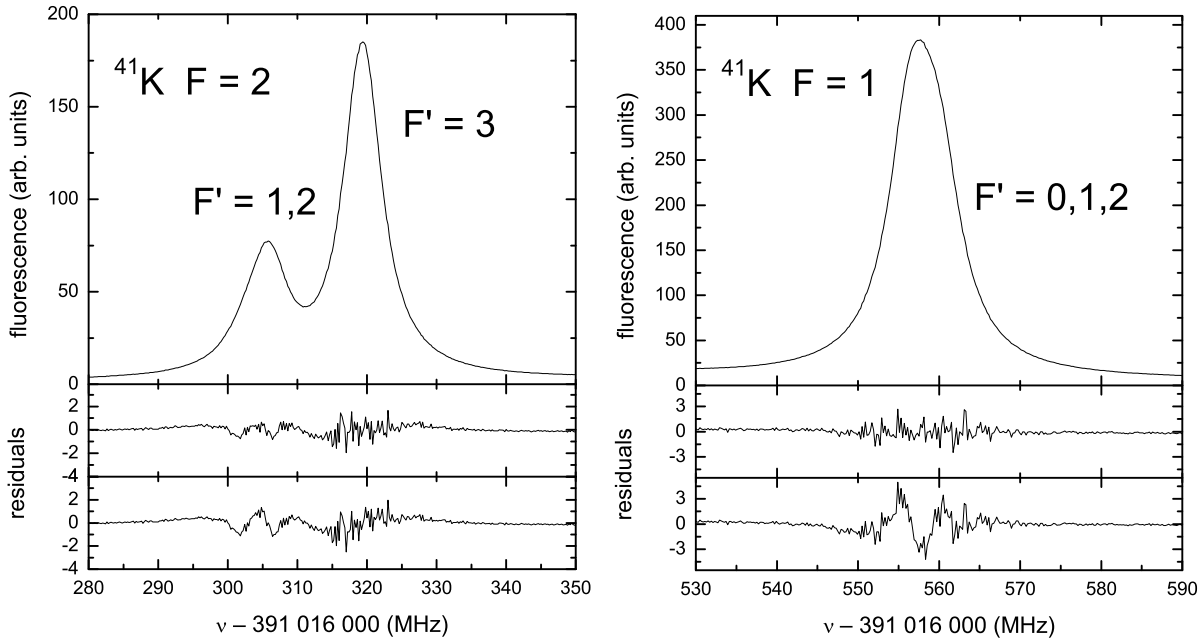
Figure 3.5: *The $F = 2 \rightarrow F' = 1, 2, 3$ component of the ^{41}K D_2 line (left), and the spectrum of $F = 1 \rightarrow F' = 0, 1, 2$ (right) is shown. In both parts, two curves with residuals are shown. The upper one is obtained when the hyperfine constants of the $^2P_{3/2}$ state are fitted. For the lower case, they were fixed to literature values[52] (see text).*

significant improvement. This may be due to the fact that the polarization of the spectroscopy laser beam with respect to the residual magnetic field is not known. We are therefore forced to increase for ^{39}K and ^{41}K the uncertainty, with which we can determine the line center. An uncertainty of 100 kHz is in our opinion well justified.

3.1.4.4   Uncertainty budget

The precision of the performed measurements is limited by several effects. The most crucial one is the residual first order Doppler effect, which was already discussed in Section 3.1.3. There, we showed that we can limit its influence to below 50 kHz for the absolute frequency. For relative frequency measurements, the contribution to the uncertainty budget from the Doppler shift will be smaller when the optical alignment is unchanged and not drifting. By repeated measurements with and without retro-reflected beam we monitored the change of the Doppler shift in time and estimated that the uncertainty contribution for difference frequency measurements is 20 kHz for data taken within a few hours.

The second order Doppler effect cannot be avoided by the use of a retro-reflector. For the most probable particle velocity of 1000 ± 100 m/s we have measured in our beam it amounts to -2.2(5) kHz. The velocity of the atoms was determined by means of a Doppler detector.[53] We have corrected the transition frequencies for the second order Doppler effect.

Magnetic fields are shielded from the interaction region by a μ-metal box. The re-

maining field of less than 20 mG can lead to a line shift of less than 30 kHz.

Two systematic shifts occur due to the photon recoil. To begin with, the peak of the absorption profile of an atom at rest is shifted from transition frequency ν_0 corresponding to the energy difference of the two involved levels by the recoil energy $h\nu_r = h^2\nu_0^2/2M_\text{K}c^2 \approx$ 8.7 kHz$\times h$ for the potassium D lines. Here, h is Planck's constant, c the speed of light, and M_K is the mass of the potassium atom.

The second contribution stems from the average velocity of $v_r = h(\nu_0 + \nu_r)/M_\text{K}c \approx$ 1.3×10^{-2} m/s gained by the atom after an absorption-emission cycle. Multiple cycles lead to a velocity redistribution and thus Doppler shift and line asymmetry. The maximum Doppler shift $2 \times \nu_r$ per cycle is about 17 kHz.

This influence can be kept small by low laser intensity and is further reduced by the two counter-propagating laser fields produced by the retro-reflector. We have calculated that under our experimental conditions for a laser beam in only one direction, on average less than 0.2 photons are scattered per atom for ^{39,41}K and 3 for ^{40}K. We think that shifts due to velocity redistribution are smaller than 1 kHz for ^{39}K and for ^{41}K. These considerations are very well confirmed by the observed intensity ratio of the lines that matches the relative line strengths for unsaturated excitation better than 3% for clearly separated lines, for which the intensities can be well determined.

For ^{40}K systematic frequency shifts could be present due to the higher number of scattered photons. Since the difference of intensity in the counter-propagating beams of the cat's eye is less than 25% the Doppler shift will mostly cancel. We attribute an uncertainty of 15 kHz to the possibly remaining asymmetry, which corresponds to difference of 1.5 in the number of scattered photons for both laser beam directions. A significant influence of optical pumping is observed for ^{40}K only on the cycling transition $F = 9/2 \leftrightarrow F' = 11/2$ of the D_2 line. For the other transitions, the expected and observed intensity ratios match within 7%. An energetic shift of the levels due to e.g. the Zeeman or ac-Stark effect and optical pumping could lead to additional line shifts. Since the uncertainties for Zeeman and Stark shifts discussed below account for the maximum expected effect, no additional uncertainty contribution appears here.

Coupling of the spectroscopy laser beam to near resonant transitions, in particular within the hyperfine multiplet, leads to an ac-Stark shift of the resonant transition. The shift can become important when the energetic spacing between transitions with common levels is small. This is the case for the small hyperfine splitting of potassium, especially in the $^2P_{3/2}$ state.

The maximum possible ac-Stark shift can be calculated with sufficient accuracy making use of the life time of the $4p\,^2P$ levels to determine the transition dipole moment. One of the most precise methods to determine the life time of the first exited P levels in alkali metals is to calculate it from the resonant dipole-dipole coupling coefficient C_3, which is determined from spectroscopy of long range molecular states.[50] Note, that this calculation involves the knowledge of the transition frequency of the D lines, but the change of this value for ^{39}K does not influence the results of Ref.[50] significantly.

The ac-Stark shift due to non-resonant coupling of the spectroscopy laser field is given for sufficiently large detunings Δ (here: Δ larger than the natural line width) by the eigen

energies of a two level system in the dressed state picture

$$\frac{1}{2}\left(\Delta \pm \sqrt{\Delta^2 + \Omega^2}\right) \tag{3.1}$$

where $2\pi\Omega$ is the Rabi frequency. For determining an upper limit of the ac-Stark effect we calculate with twice the peak intensity of a single beam to account for the retro-reflected beam. The detuning Δ has to be set to the hyperfine splitting of the excited state. The hyperfine splitting of the ground state is large enough, such that coupling to the other ground state hyperfine state can be neglected. For the D_1 line, ac-Stark shifts are below 6 kHz for all isotopes. The larger hyperfine splitting of ^{40}K compensates for the higher intensity that was necessary to observe this isotope.

The hyperfine splittings of the $^2P_{3/2}$ state are smaller than for $^2P_{1/2}$. Due to the overlap of lines, a simple calculation according to equation (3.1) strongly over-estimates the possible Stark shifts of the D_2 lines. In order to derive a more realistic limit, we undertook density matrix simulations modeling the experimental conditions. From these calculations, we derive an upper limit of 6 kHz for ^{39}K and ^{41}K and 50 kHz for ^{40}K.

The last contribution to the uncertainty budget stems from the frequency measurement itself. It amounts to less than 1 kHz for the synchronisation of the frequency trace and spectrum and the uncertainty of the Cs clock.

In Table 3.1, we have summarized the contributions to the uncertainty budget of the transition frequency.

3.1.5   Results

From the description of the measurements and analysis in Section 3.1.4 follows that we have determined the transition frequency of each hyperfine transition of the D_1 lines individually. The average values are given in Table 3.2 with the uncertainties and corrections according to Table 3.1.

Using the transition frequencies in Table 3.2, we have determined the hyperfine parameter A for all observed isotopes. Since the A factor depends on difference frequencies only, the reduced uncertainty stated in Table 3.1 can be applied. As uncertainty of the energy splitting of the excited levels we took twice this uncertainty. The A factor is connected to the level splitting by $\Delta\nu = A \cdot (F' + 1)$ where F' is the smaller one of both quantum numbers involved in the excited state. Thus the uncertainty of the A factor is given by the uncertainty of the level splitting divided by $F' + 1$.

The values of the hyperfine parameters A are given in Table 3.3 and compared with literature values. All parameters are visualized in Figure 3.6. It can be seen that the agreement of our A factor for the $^2P_{1/2}$ level and the results from Refs.[44,45] is very good while the values from Refs.[43,31] deviate from our results. In the case of Ref.,[31] the deviation has possibly the same reasons as for the disagreement of the transition frequencies discussed in Section 3.1.4.1. The transition frequencies and hyperfine parameters of both states can be combined to calculate hyperfine-free transition frequencies of each isotope's D_1 line. The values are given in Table 3.4. The results of the frequency comb measurements agree with our pre-investigations (see Section 3.1.3) and Scherf's finding.[32]

Table 3.1: *Summary of the different contributions to the error budget. The values in parenthesis for the sum in quadrature refer to relative measurements with a reduced Doppler uncertainty.*

source	correction	uncertainty
1st order Doppler effect	0 kHz	50 kHz
(for relative meas.)	(0 kHz)	(20 kHz)
2nd order Doppler effect	2.2 kHz	0.5 kHz
Zeeman effect	0 kHz	30 kHz
Recoil shift	−8.7 kHz	0.1 kHz
Velocity redistribution		
^{39,41}K	0 kHz	1 kHz
^{40}K	0 kHz	15 kHz
ac-Stark effect		
D_2 line ^{40}K	0 kHz	50 kHz
all other lines	0 kHz	6 kHz
Line center/profile		
^{39,41}K D_1		20 kHz
^{39,41}K D_2		100 kHz
^{40}K		40 kHz
Frequency measurement	0 kHz	1 kHz

	sum	sum in quadrature
D_1 ^{39,41}K	−6.5 kHz	62(42) kHz
^{40}K	−6.5 kHz	73(56) kHz
D_2 ^{39,41}K	−6.5 kHz	116(117) kHz
^{40}K	−6.5 kHz	88(75) kHz

Table 3.2: *Transition frequencies ν of the D_1 lines. For convenience, an offset of 389285 GHz is subtracted.*

isotope	F	F'	ν in MHz
^{39}K	1	1	1312.574(62)
	1	2	1368.124(62)
	2	1	850.838(62)
	2	2	906.386(62)
^{40}K	9/2	9/2	1686.785(73)
	9/2	7/2	1842.157(73)
	7/2	9/2	400.957(73)
	7/2	7/2	556.224(200)[a]
^{41}K	1	1	1433.888(62)
	1	2	1464.386(62)
	2	1	1179.890(62)
	2	2	1210.380(62)

[a]The larger uncertainty is due to the difficulties determining the line center discussed in Section 3.1.4.2.

Table 3.3: *Derived hyperfine parameters A and B and constants from literature. All values are in* MHz.

isotope	source	$A\ ^2P_{1/2}$	$A\ ^2P_{3/2}$	$B\ ^2P_{3/2}$
^{39}K	this work	27.775(42)	6.093(25)	2.786(71)
	Ref.[44]	27.80(15)		
	Ref.[45]	27.5(4)		
	Ref.[31]	28.859(15)		
	Ref.[43]	28.85(30)		
	Ref.[54]		6.00(10)	2.9(2)
	Ref.[55]		6.13(5)	2.72(12)
	Ref.[51]		6.06(8)	2.83(13)
^{40}K	this work	-34.523(25)	-7.585(10)	-3.445(90)
	Ref.[44]	-34.49(11)	-7.48(6)	-3.23(50)
	Ref.[56]		-7.59(6)	-3.5(5)
^{41}K	this work	15.245(42)	3.363(25)	3.351(71)
	Ref.[44]	15.19(21)		
	Ref.[45]	15.1(8)		
	Ref.[55]		3.40(8)	3.34(24)
	Ref.[52]		3.325(15)	3.320(23)

The analysis of the D_2 line data was done in a different way than in the case of the D_1 transition (see Section 3.1.4). The results of the fitting procedure are directly hyperfine-free transition frequencies and the hyperfine parameters of the $^2P_{3/2}$ level. Their uncertainties were determined from a fitting procedure, in which an artificial dataset with the reduced uncertainties given in Table 3.1 was used. The hyperfine-free transition frequencies are listed in Table 3.4, the hyperfine parameters are given in Table 3.3 and are depicted in Figure 3.6. In Table 3.5, we have given frequencies of comparatively weakly overlapping transitions of the D_2 line. They were calculated from the fitting procedure introduced in Section 3.1.4.3.

The values of the hyperfine parameters are generally in agreement with previous measurements with the exception of $A(^{39}\text{K},^2P_{1/2})$, where we find the already discussed discrepancies. In the case of ^{41}K, where high precision measurements on the D_2 line were presented in Ref.,[52] our results have a larger uncertainty than earlier measurements. We have shown in Figure 3.5 that an acceptable fit of our spectra can be achieved with the parameters of Ref.,[52] but the fit improves significantly by small variations of the hyperfine parameters. Thus, we give our fit results including the A and B parameters, also because of the completely different nature of both experiments.

From the hyperfine-free transition frequencies, the fine structure splitting and isotope shifts can be calculated. As reference isotope, we chose ^{39}K. We regard the measurements on different isotopes and D lines as sufficiently independent to add their uncertainties in quadrature. The results are given together with data from literature in Table 3.6. Our
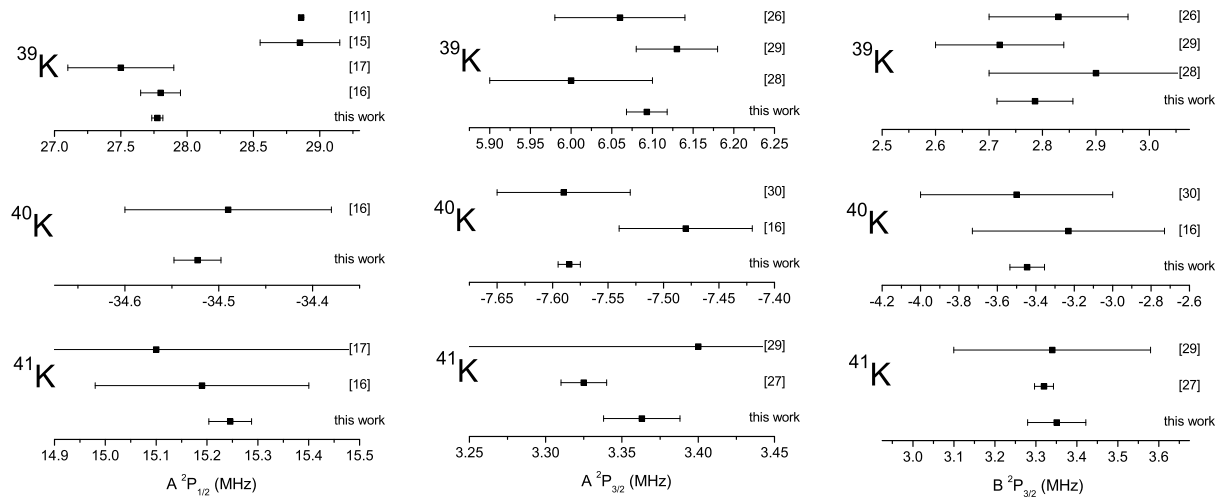
Figure 3.6: *Hyperfine constants determined from our work and by other authors. left: A $^2P_{1/2}$; center: A $^2P_{3/2}$; right: B $^2P_{3/2}$.*

Table 3.4: *Hyperfine-free transition frequencies ν of the D_1 and D_2 lines.*

isotope	source	$\nu(D_1)$ in MHz	$\nu(D_2)$ in MHz
^{39}K	fs comb	389 286 058.716(62)	391 016 170.03(12)
	wavelength meter	389 286 068(30)	391 016 190(30)
	I$_2$	389 285 980(100)	
	Ref.[32]	389 286 078(20)	391 016 188(20)
	Ref.[30,31]	389 285 580.908(50)	391 015 578.04(11)
^{40}K	this work	389 286 184.353(73)	391 016 296.050(88)
^{41}K	this work	389 286 294.205(62)	391 016 406.21(12)

Table 3.5: *Frequencies ν of weakly overlapping transitions of the D_2 lines. For convenience, an offset of* 391 015 GHz *is subtracted.*

isotope	F	F'	ν in MHz
^{39}K	2	3	1011.286(116)
^{40}K	9/2	11/2	1821.134(88)
	9/2	9/2	1865.221(88)
	9/2	7/2	1898.523(88)
	7/2	9/2	579.431(88)
	7/2	7/2	612.733(88)
	7/2	5/2	636.912(88)
^{41}K	2	3	1319.356(116)

Table 3.6: *Isotope shifts (*IS*) and fine structure (*FS*) splittings for the observed isotopes. All units are* MHz.

isotope	source	FS splitting	IS(D_1)	IS(D_2)
^{39}K	this work	1 730 111.31(13)	–	–
	Ref.[32]	1 730 110(30)	–	–
	Ref.[30]	1 729 997.132(120)	–	–
^{40}K	this work	1 730 111.70(12)	125.64(10)	126.03(15)
	Ref.[44]		125.58(26)	126.43(30)
^{41}K	this work	1 730 112.01(13)	235.49(9)	236.18(17)
	Ref.[44]		235.27(33)	236.15(37)
	Ref.[45]		235.25(75)	

results are again consistent with the values from other sources with the exception of the value for the fine structure splitting given by Banerjee *et al.*[30]

3.1.6   Conclusion

We have measured all optical transitions of both D lines in the isotopes 39, 40, and 41 of potassium by laser induced fluorescence spectroscopy on a highly collimated atomic beam with a fractional uncertainty of about 2×10^{-10}. The absolute frequencies were measured with a self-referenced femtosecond laser frequency comb generator that supplied the link from the spectroscopy laser to a Cs atomic clock.

With our measurements, we confirm the transition frequencies for ^{39}K measured by Scherf *et al.*[32] or determined by conventional spectroscopic means like the I$_2$ atlas or commercial wavelength meters. We were not able to reproduce the results of Refs.[40,30,31]

From our measurements, the fine structure interval and hyperfine parameters A and B for the excited states $4p^2P_{1/2}$ and $4p^2P_{3/2}$ were derived. They have a significantly reduced uncertainty compared to data from literature and are consistent with those. The isotope shifts of D_1 and D_2 line of ^{40}K and ^{41}K were determined from the hyperfine-free transition frequencies with reduced uncertainty.

Acknowledgments

3.2   ac-Stark Effect

In our determination of uncertainty contributions density matrix simulations were performed to obtain a reasonable upper limit for ac-Stark effects. Such effects on transition lines are due to off-resonant coupling to states, which are not involved in the transition itself. Dipole traps utilize this effect: a laser red detuned from all relevant transitions shift the ground state downwards according to the local power density. Thus, the atoms minimize their energy if they are in the maximum field intensity of the trap lasers. More sophisticated examples are crossed dipole traps with two laser fields or optical lattices with standing waves in one, two, or three directions.

The lasers inducing the ac-Stark effect are usually far detuned to reduce the probability of photon absorption. However, high power is needed for the formation of a potential minimum in the center if the beam. Such traps utilize the dependence of the ac-Stark shift described by equation (3.1) on the field strength, i.e., the variation of Ω. In our spectroscopic experiment, we have to consider ac-Stark effects not because of high laser powers (high Ω) but because of small detunings Δ. Several hyperfine levels of the 4p state are energetically close and if driving a transition to one hyperfine state, the coupling of another hyperfine state lets the spectroscopy laser induce an ac-Stark effect on the ground state, i.e., the starting state of the considered transition.

3.2.1   Three-State Model

In a first step of understanding we take a look at a model with three states: A single ground state is coupled via a laser to two excited states, which are energetically separated by Δ. If the laser is in resonance with one of the excited state the ground state is shifted due to the ac-Stark effect induced by coupling to the second excited state following equation (3.1)

$$\delta_\pm = \frac{1}{2}\left(\Delta \pm \sqrt{\Delta^2 + \Omega^2}\right) \xrightarrow{\Delta \to 0} \pm\frac{1}{2}\Omega \;. \tag{3.2}$$

The picture described above breaks down if the energy difference of the two excited states becomes small, i.e., smaller than the inverse lifetime γ (linewidth). Graph (c) in Figure 3.7 illustrates this situation, in which the additional state is partly above and partly below the state of interest. One part shifts the state of interest up, the other part shifts down

We performed density matrix simulations including spontaneous decay from the two excited states. The time sequence of the interaction reproduces our experimental conditions: The three-state atoms travels through a laser fields with the peak Rabi frequency of Ω. We integrate the spontaneous decay from each excited state separately. By doing this time integration for several detunings of the coupling laser Δ, we obtain two data traces, which simulate spectra. By fitting a Lorentzian line shape to each spectrum, we derive an ac-Stark effect. These ac-Stark shifts of the two state are shown in Figure 3.8, where in Graph (a) Rabi frequencies are used that correspond to the experimentally applied ones for ^{39}K and ^{41}K and in Graph (b) the simulated Rabi frequency corresponds to the ^{40}K measurements. The shifts are derived in the simulation for several energy separations between the two excited states. As expected, the two observed shifts are similar but opposite in sign. The solid lines indicate the estimation of the ac-Stark shifts by the
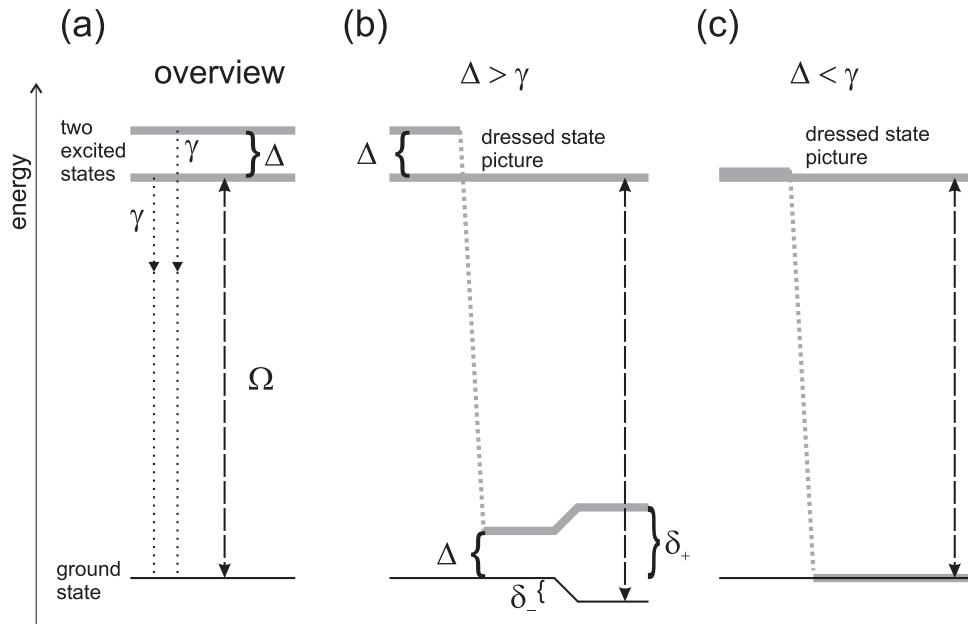
Figure 3.7: *Illustration of the ac-Stark effect.* Graph (a) *depicts the model. For large detunings, the effect can be estimated by equation (3.1) as illustrated in* Graph (b). *For small detunings shown in* Graph (c), *the shift of the ground state and thus of the transition frequency becomes smaller. The ac-Stark shift in the excited states of the tested transition is not shown.*
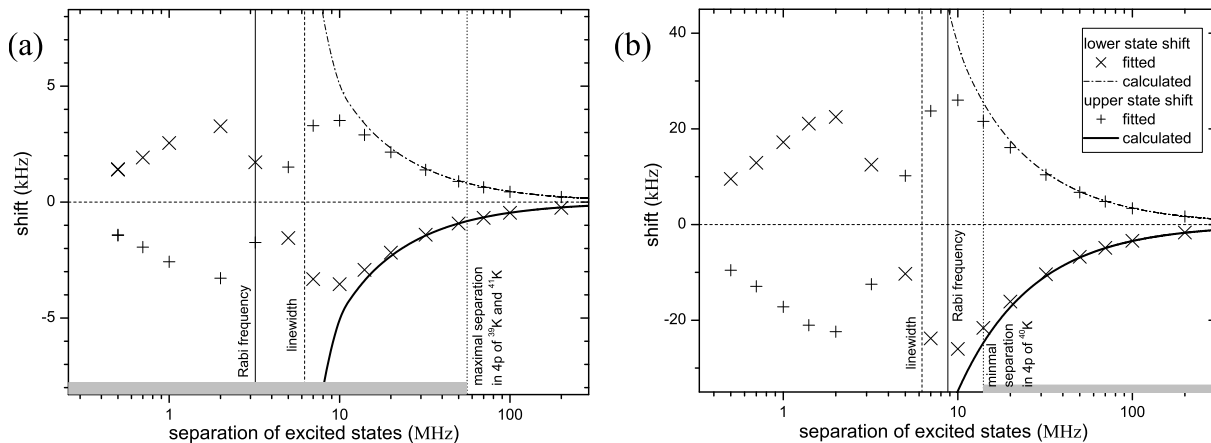

Figure 3.8: *ac Stark-effect calculated in a three state model. Density matrix simulations are compared to calculations following equation (3.1).* Graph (a) *shows the results for parameters corresponding to the spectroscopy of* ^{39}K *and* ^{41}K. *The experimental parameters for the experiments on* ^{40}K *were used in* Graph (b).
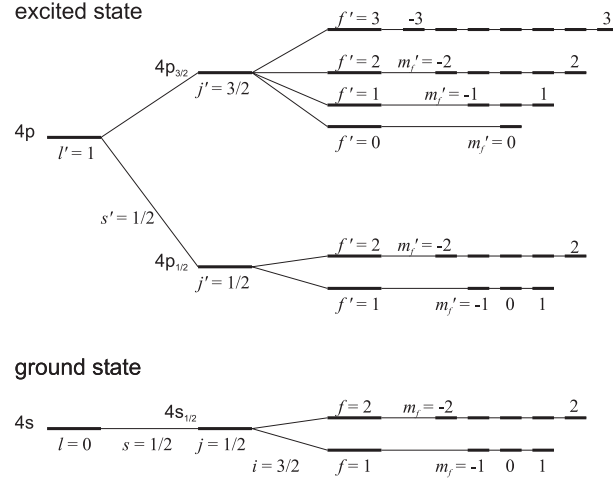
Figure 3.9: *Level scheme of the 4s and the 4p states of potassium. Here, the situation for the nuclear spin $i = 3/2$ is illustrated, which corresponds to ^{39}K and ^{41}K. From left to right are the splitting due to fine structure (coupling of $\vec{l}$ and $\vec{s}$ to $\vec{j}$), the splitting due to hyperfine structure (coupling of $\vec{j}$ and $\vec{i}$ to $\vec{f}$), and the degeneracy due to the different projections f labeled by m_f illustrated. For ^{40}K, i and in consequence the values of f are bigger and more projections m_f are possible. The laser field of polarization q couples two levels if $f' = f-1, f, f+1$ and $m'_f = m_f + q$, with the exception that for $q = 0$ and $m_f = m'_f = 0$ no coupling between two states of the same total angular momentum f is possible.*

simple formula equation (3.1). For large detuning they agree perfectly, but for smaller detunings this formula strongly overestimates the effect.

In our effort to reproduce the experimental conditions, we simulated a Gaussian beam profile in the density matrix simulations. The solid lines in Figure 3.8 are calculated with Rabi frequencies corresponding to $\sqrt{2}$ times the peak Rabi frequency of the Gaussian profile. The correction factor was obtained by a comparison of density matrix simulations for constant coupling strength with simulations with a Gaussian profile.

We can conclude: the simple formula over-estimates the error on the transition frequency due to the ac-Stark effect of the spectroscopy laser significantly if the spacing of two levels is smaller than the natural linewidth.

3.2.2   Detailed Density Matrix Simulations

By extending the density matrix simulations with more states, a better reproduction of the experimental condition is possible. However, only one of the hyperfine states of the ground state could be considered because of numerical problems occurring at high separation of the involved states. But, the expected shift due to ac-Stark effects originating from the second ground state are significantly lower than the effects of the various excited states and negligible in the error budget.

The coupling strength of the levels depends on the magnetic quantum number m_f, the projection of f on the magnetic field axis, and on the polarization q of the laser beam.

The transition dipole moment, with usual notation for quantum numbers, is

$$
\langle \alpha' \left[(l',s)\, j', i \right] f', m'_f | \, \mu_q \, | \alpha \left[(l,s)\, j, i \right] f, m_f \rangle . \tag{3.3}
$$
$$
= \; (-1)^{1+l'-s+j+j'+i+m'_f} \times \sqrt{2j+1} \; \sqrt{2j'+1} \; \sqrt{2f+1} \; \sqrt{2f'+1} \, \langle \alpha', l' | \, |\mu| \, | \alpha, l \rangle
$$
$$
\times \left\{ \begin{array}{ccc} l' & j' & s \\ j & l & 1 \end{array} \right\} \left\{ \begin{array}{ccc} j' & f' & i \\ f & j & 1 \end{array} \right\} \left(\begin{array}{ccc} f & 1 & f' \\ m_f & q & -m'_f \end{array} \right) .
$$

If one wants to relate the reduced dipole moment to a decay rate A one has to consider the degeneracies:

$$
\langle \alpha', l' | \, |\mu| \, | \alpha, l \rangle \sim \sqrt{\frac{2l'+1}{2l+1}} \; A\,(\alpha' \to \alpha) \; , \tag{3.4}
$$

where α and α' represent all quantum numbers for the identification of the state. In our example we have to multiply the angular part from equation (3.3) by $\sqrt{3}$ and the inverse atomic lifetime to obtain coupling strengths. The polarization was not defined in our experiment. Therefore, simulations with all three possible polarizations were performed.

With our simulations we want to derive upper limits for effects that may shift the transition frequency in our experiments. First, the spectroscopy laser may shift level positions due to the ac-Stark effect. Second, the overlap of lines may lead to asymmetric lineshapes because the atoms are optically pump on via one transition, which leads to a variation of population in the ground state over the interval of another transition. In other words, the two lines compete for ground state atoms and by removing more atoms on the neighboring side than on the opposite side, the lineprofiles have an additional underlying slope. This slope differs from the slope, which is simulated by adding several Lorentzian line profiles.

We undertook two simulations. First, spontaneous decays were simulated such that the atoms always decay back to the ground state from which they were excited, i.e., all atoms decay with a photons of a specific polarization. Here, effects of optical pumping as discussed in the preceding paragraph are not occurring. Second, we simulated the spontaneous decays with branching ratios for the decay channels. Also, the decay from all involved levels were integrated separately. In this way, the line positions could easily be derived individually by profile fits to the simulated spectra. Moreover, the effect of optical pumping and ac-Stark effects could be distinguished. The ac-Stark effects are in general bigger. The errors given in Section 3.1.4.4 are from the simulations with the realistic branching ratios.

Chapter 4

The A $^1\Sigma_u^+$ State of K$_2$

The particle beam of potassium used for the study of the D lines discussed in the preceding chapter does have a significant contribution of K$_2$. Originally, the beam apparatus was designed for — and is mainly used for — studies of K$_2$. Matterwave interferometer are run with these dimers.[57]

In this chapter, we study the first electronically excited singlet state A $^1\Sigma_u^+$ of K$_2$ in high resolution. A preparation step with a laser for optical pumping allowed for the study of long-range levels of the A $^1\Sigma_u^+$ state up to the dissociation limit. We reached levels with classical turning points of up to about 300 Å. These are two-atom molecules with the size comparative to quantum dots made up from several 10 000 atoms. We report this study in an article, which is enclose to this thesis in Section 4.1. It was published originally in *The Journal of Chemical Physics*, Volume 125 under article number 224303 on 12th of December 2006. The hyperfine structure calculations mentioned therein are discussed in greater detail in Section 4.2.

The two non-decaying isotopes of potassium ^{39}K and ^{41}K have significant natural abundance. We investigate not only the most abundant isotopomer ^{39}K$_2$ but also the heteronuclear dimer ^{39}K ^{41}K. Both isotopomers have in the Born-Oppenheimer approximation the same potential energy curves. Deviations from this approximation will accumulate for asymptotic levels. By comparing the levels of the two dimers, the Born-Oppenheimer approximation is studied (Section 4.3).

Properties of cold collisions of two atoms are of high importance for experiments with ultracold atoms. A very important research subject is to predict these properties for specific combinations of isotopes from the measured properties of other isotopes, especially in the rich field of two-species traps. However, this so-called mass-scaling relies on the Born-Oppenheimer approximation for the interaction between the two atoms in the ground state, i.e., of the singlet and triplet ground state of the corresponding dimer. The investigation of the A state of potassium opens a road for the experimental study of the precision of the Born-Oppenheimer approximation for cold collisions. Therefore, we conclude this chapter by an outlook on experiments at the ground state asymptotes in Section 4.4.

All gathered spectroscopic data of the A–X system is given in Appendix B.

4.1 The A $^1\Sigma_u^+$ state of K$_2$ up to the dissociation limit

St. Falke[a], I. Sherstov, E. Tiemann, and Ch. Lisdat[b]

Institut für Quantenoptik, Universität Hannover, Welfengarten 1, 30167 Hannover, Germany

Submitted 11 September 2006; accepted 04 October 2006; published online 12 December 2006

Abstract: We report an experimental study of the K$_2$ A $^1\Sigma_u^+$ state. Long-range levels up to the dissociation limit were observed in a two laser spectroscopic experiment using a highly collimated molecular beam. We derive an analytical potential energy curve for the complete A state including long-range dispersion terms. From these, we obtain radiative atomic lifetimes of 26.74(3) ns for the 4p$_{1/2}$ state and 26.39(3) ns for the 4p$_{3/2}$ state of ^{39}K. The dissociation energy of the X $^1\Sigma_g^+$ ground state with respect to $v = 0, J = 0$ is found to be $D_0 = 4404.808(4)$ cm^{-1}.

4.1.1 Introduction

Laser cooling has opened a pathway to experiments testing fundamental physical concepts using the cold and ultracold temperature regimes. In these experiments it is essential to have a good understanding of the collisions of cold atoms, i.e., collisions with almost zero kinetic energy. Studies of the crossover between the BCS regime (Bardeen, Cooper, Schrieffer) and the regime, in which Bose-Einstein condenstates (BEC)are formed, need a tunable interaction.[7,8] The dynamics of BEC strongly depends on the two particle interaction and is fundamentally different for positive or negative values of scattering length, which describes the effective interaction in the ultracold regime.[58] The generation of quantum degenerate Fermi gases[59] is greatly simplified by sympathetic cooling via a Bose-Einstein condensed second species, a method relying on appropriate two particle interaction between the species.[60] Phase diagrams of ultracold atoms in periodic potentials, usually mediated by optical lattices, are very rich. For their modeling, the two particle interaction is taken into account.[61] Also, the formation of ultracold molecules via three particle collisions[62] or adiabatic ramps of the interaction strength, which is tuned by an external magnetic field,[63] are experiments that utilize cold collisions.

These cold collisions of atoms are best described by precise molecular interaction potential curves. Properties such as the scattering length can be derived from such potentials. It is essential to gather information about weakly bound molecular levels in order to derive potentials at large internuclear distance. Experiments with ultracold atoms achieve this by monitoring the behavior of cold collisions in magnetic fields and the interpretation of Feshbach resonances.[64,65,66]

Among the alkali metal elements, only two naturally occurring fermionic isotopes are available: ^{6}Li and ^{40}K. This fact, and convenient transition frequencies, have caused big interest in ultracold potassium. Currently all three stable isotopes (39 – 41) have been trapped, some in two-isotope traps. The ground state potential of K_2 is known from Fourier-transform spectroscopy of an internuclear distance of up to 15 Å.[67] The observed least bound level in that study lies 1.8 cm^{-1} below the atomic asymptote, i.e., below the region of observations with ultracold atoms. This gap of observations may be closed by spectroscopy via electronically excited states. The A $^1\Sigma_u^+$ state is a very good candidate for providing access: in sodium similar studies were successful with the corresponding A state serving as a transfer state.[5]

Another interest in the A state is to derive the radiative lifetime of p states of potassium. Precise measurements of the atomic lifetime were performed: direct measurements by laser spectroscopy in an atomic beam[68] agree with lifetimes derived from long-range parameters investigated in photoassociation experiments.[50] With our spectroscopic technique of Franck-Condon pumping, levels all the way up to the atomic asymptote will be investigated, i.e., levels that are even less bound than those observed in photoassociation. In the case of sodium, an experiment similar to ours allowed for the determination of a precise value of the radiative lifetimes[69] from the dipole-dipole interaction constant C_3.

Since the A state is correlated to the 4s+4p$_{1/2}$ asymptote, an improved value for the ground state dissociation energy (4s+4s asymptote) will be derived using the atomic transition frequency of the D_1 line.

Finally, an interesting feature of the A $^1\Sigma_u^+$ state is its coupling to the triplet manifold: It leads to perturbed levels which show strong singlet-triplet mixing. Such levels may be used for transforming molecules from triplet to singlet or vice versa. In our study, the perturbed vibrational levels and their energy position with respect to the dissociation threshold of the A state, i.e., the detuning of the photoassociation lasers from the atomic line, were identified.

This article is organized as follows. Our experimental setup is described in Section 4.1.2. The underlying theoretical model for our analysis is discussed in Section 4.1.3. In Section 4.1.4, we present and discuss our obtained results. We conclude and give an outlook on future work in Section 4.1.5.

4.1.2 Experiment

We study K_2 molecules in a molecular beam. The beam apparatus was described previously.[47] In short, a cold molecular beam is produced by adiabatic expansion from a heated potassium reservoir through a nozzle of 200 μm diameter into vacuum. After the expansion, the dimers are mainly in the lowest vibrational level of the electronic ground state X $^1\Sigma_g^+$. The rotational level with maximal population probability is around $J_X = 10$. The geometrical arrangement of the two skimmers between the pumping stages leads to a collimation ratio of 1000. The residual gas pressure is below 10^{-8} mbar in the last stage while the beam is running. The molecules fly at 950$\pm$70 m/s and are interrogated by laser fields. The laser beams cross the molecular beam perpendicularly. The residual Doppler width of about 2 MHz is below the natural linewidths for transitions to the A state.

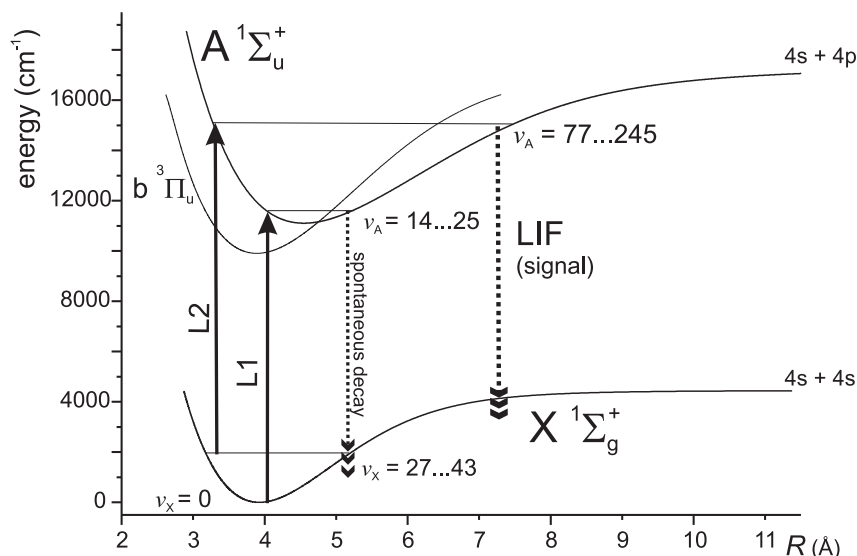We apply two laser fields, which are spatially separated by several centimeters and

Figure 4.1: *Simplified potential scheme of K_2. Initially, the molecules are in the vibrational ground state of the $X\,^1\Sigma_g^+$ state. The first laser (L1) drives Franck-Condon pumping. The spectroscopy is done with a second laser (L2).*

interact with the molecules successively. With the first laser (L1) we drive a transition to a low vibrational level of the $A\,^1\Sigma_u^+$ state ($14 \leq v_A \leq 25$; see Figure 4.1). The dimers decay and populate various vibrational levels of the X state according to the corresponding Franck-Condon factors. By selecting an appropriate vibrational state of state A, we are able to choose which levels of state X are predominantly populated in this preparation step. The laser intensity of about 2 W/cm^{-2} is high enough to saturate the transition of this Franck-Condon pumping step. We use a cw Ti:sapphire laser with about 50 mW power after an optical fiber link to the vaccum apparatus. This laser is tuned to resonance and then stabilized via an offset cavity to an iodine stabilized HeNe laser to ensure a continuous flux of vibrationally excited K_2 molecules downstream.

The actual spectroscopy is done with a second laser (L2). It is applied downstream from the first laser. Scattered light from L1 is strongly suppressed by the spatial separation. The vibrational relaxation of the molecule between the two laser fields is negligible. We record the laser induced fluorescence from L2 by an infrared sensitive photomultiplier (Hamamatsu R943-02) and current amplifier. Optical filters are used to suppress scattered light, originating from L2. Power and diameter (2 mm) of this laser beam are similar to L1. The frequency calibration of L2 was done either by a wavelength meter (HighFinesse WS-7 or WS-8) or by recording I_2 absorption spectra simultaneously. These reference spectra are simulated based on earlier studies.[29] The reached absolute uncertainty was 100 or 40 MHz for the two wavelength meters and 150 MHz for iodine. For the iodine recordings, the transmission of a 150 MHz marker cavity was used to interpolate between iodine lines. Due to the large potential energy interval covered in this experiment, two different lasers were applied for the spectroscopy. A cw linear dye laser running with DCM was used for the lower vibrational levels and a second cw Ti:sapphire laser was

introduced to extend the data field up to the dissociation limit.

We started our study at the upper energy limit of the previously investigated levels[70] of the A state by detecting $v_A = 84$. The intermediate levels prepared by L1 were mainly $v_X = 27$ and 28. The window for the detection of fluorescence induced by L2 is narrow because the scattered light from L2 at 740 nm had to be suppressed by an optical filter and the detection is sensitive only up to a wavelength of 930 nm. For the lowest observed vibrational levels, we periodically chopped L1 while L2 was scanning slowly. Using a lock-in amplifier triggered by the switch, the fluorescence signals induced by L2 were revealed despite a high background signal due to residual scattered light from L2. Going to higher vibrational levels led to bigger and bigger signals due the higher quantum efficiency of photomultiplier for higher energy photons. This made the lock-in detection redundant. After the observation of several vibrational levels, the Franck-Condon factors for the detected transitions died out. By selecting a higher v_A for L1, we were able to start from higher v_X in the spectroscopy and thus with sufficient Franck-Condon factors again.

Due to the Franck-Condon pumping step, the number of observed rotational levels is reduced. If L1 excites a rotational level J_A^{FCP} then the two rotational levels $J_X = J_A^{\mathrm{FCP}} \pm 1$ are populated in each vibrational level of the ground state. Therefore, three rotational levels of the A state are accessible by L2 without change of the preparation step: $J_A = J_A^{\mathrm{FCP}} - 2, J_A^{\mathrm{FCP}}, J_A^{\mathrm{FCP}} + 2$. For each v_A, we investigated these three rotational levels starting from two different vibrational levels of the ground state. From the observed lines, ground state splittings were calculated. These ground state splittings can also be interfered from studies of the ground state,[67] where a rms of the deviations between observed and calculated levels of 0.0017 cm^{-1} was achieved. The results from measurements match the calculated ground state splittings better than 0.003 cm^{-1} confirming the rotational assignment.

The vibrational spacing gets narrower as we approach the dissociation limit. Close to the asymptote, we scanned the laser and recorded several vibrational levels of the A state in a single scan of the laser. Figure 4.2 shows a typical recording. For each vibrational level of the A state, P and R lines are resolved. All lines in the spectrum start from a common level of the X state. Transitions starting from another ground state level are not in this scan because we selected the lowest rovibrational level of the ground state that was populated in the Franck-Condon pumping step: L2 cannot drive transitions from another ground state levels to bound region below the asymptote. The scan in Figure 4.2 shows that the vibrational spacing and Franck-Condon factors tail off as the asymptote gets closer. For the very weakly bound levels, hyperfine structure appears. Above the threshold the dissociation continuum is visible by increased fluorescence. For such asymptotic scans, we use a bandpass filter around the D_1 line of potassium to filter the fluorescence since weakly bound molecules of the A state decay mainly to continuum levels just above the 4s+4s asymptote. In our experiment the laser is far detuned from this atomic resonance due to the binding energy of the level we start from. In photoassociation experiments levels very close to the asymptote are difficult to resolve due to the overlap of rovibrational series of several electronic states.

A summary of the observed levels is shown in Figure 4.3. Our data with 160 new vibrational levels extend all the way to the asymptote. Moreover, an absolute vibrational assignment of the levels recorded in photoassociation[71] is now possible. In the follow-
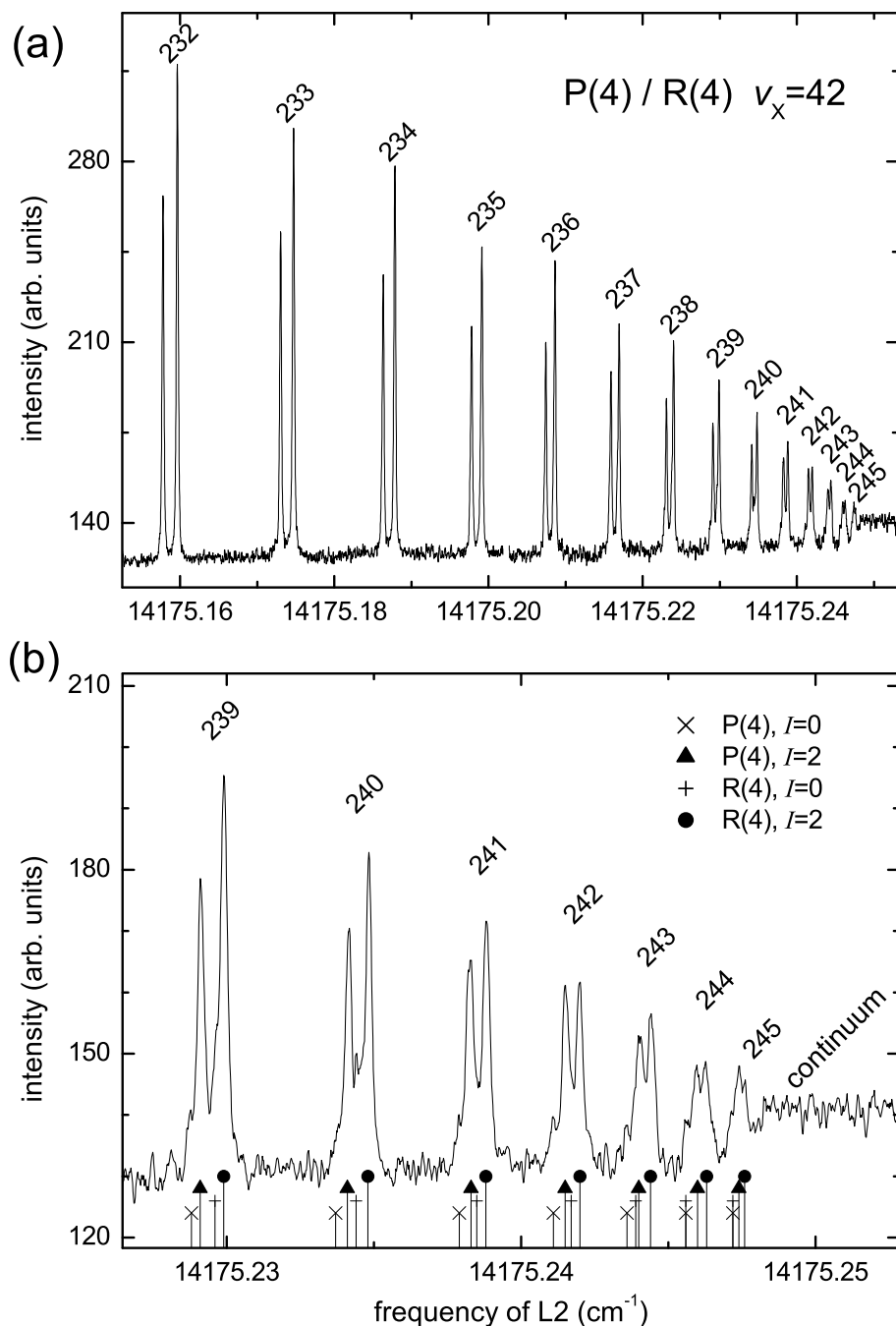
Figure 4.2: *Scan below the* $4s_{1/2}$ ($f = 1$)+$4p_{1/2}$ ($f = 1$) *asymptote: Laser-induced fluorescence over the frequency of L2. Vibrational quantum numbers* $v_A = 232$ *to* 245 *of the transitions are assigned to each pair of rotational lines. The lower graph shows the spectrum of the least bound levels in more detail. Here, the positions of the two hyperfine structure components for each rotational line are also indicated.*

ing section we will describe how a potential energy curve is derived from this combined spectroscopic data set.

4.1.3 Theoretical Model

The A $^1\Sigma_u^+$ state is coupled to the b $^3\Pi_u$ state by spin-orbit coupling. This coupling was analyzed by Manaa *et al.*[74] over a wide energy interval. To our knowledge the best previously derived A state potential was obtained by this deperturbation analysis. With the widely extended data field (see Figure 4.3) the A state potential can now be continued to its asymptote. In this study, we focus on the singlet state and derive a single potential curve describing an effective A state. Note that the coupled channel analysis used the Fourier-grid method and would need to cover not only a large energy but also a wide internuclear separation interval giving huge matrices, which need long computing time. Using a single potential analysis keeps the complexity of the problem manageable and allows for direct comparison of the assigned and calculated vibrational quantum number. The road of the deperturbation analysis started by Ross *et al.*,[72] persued by Jong *et al.*,[73] Lisdat *et al.*,[47] and by Manaa *et al.*[74] may be picked up with the here derived curve for the A state in the future, but would benefit greatly from an enlarged data set for the $^3\Pi_u$ potentials. Knowledge about these potentials may also be obtained by further investigations of the perturbed regions of the A state, i.e., by enlarging the interval of observed rotational levels J_A.

4.1.3.1 Representation of Potential Energy Curve

It is crucial to use an appropriate representation of the potential energy curve. As in other studies,[75,76] we split the internuclear distance axis (R axis) into several intervals. A representation of the potential well is connected to a repulsive wall part at small R and to a long-range part for large R, in which well known dispersion formulas are used. Additionally, we introduce a fourth interval for even bigger R in order to model the observed hyperfine structure of asymptotic levels.

For the potential well, a power series in a scaled internuclear separation is used to describe the potential by

$$V = \sum_i b_i \left(\frac{R - R_m}{R + a R_m} \right)^i,$$ (4.1)

where R_m is close to the equilibrium separation. The parameter a allows one to adjust the scaling according to the asymmetry of the potential well. The coefficients b_i of this power series are used to adjust the potential, i.e., in a fit procedure they are free parameters.

At short internuclear distances ($R \leq R_1$), a repulsive wall is modeled by the form

$$V = A_1 + A_2 R^{-C},$$ (4.2)

and we use A_1 and A_2 to ensure a continuously differentiable connection to the potential well. The repulsive wall can be adjusted using the parameter C. The connection point R_1 to the potential well is chosen such that only the energy positions of weakly bound levels are influenced if C is altered.
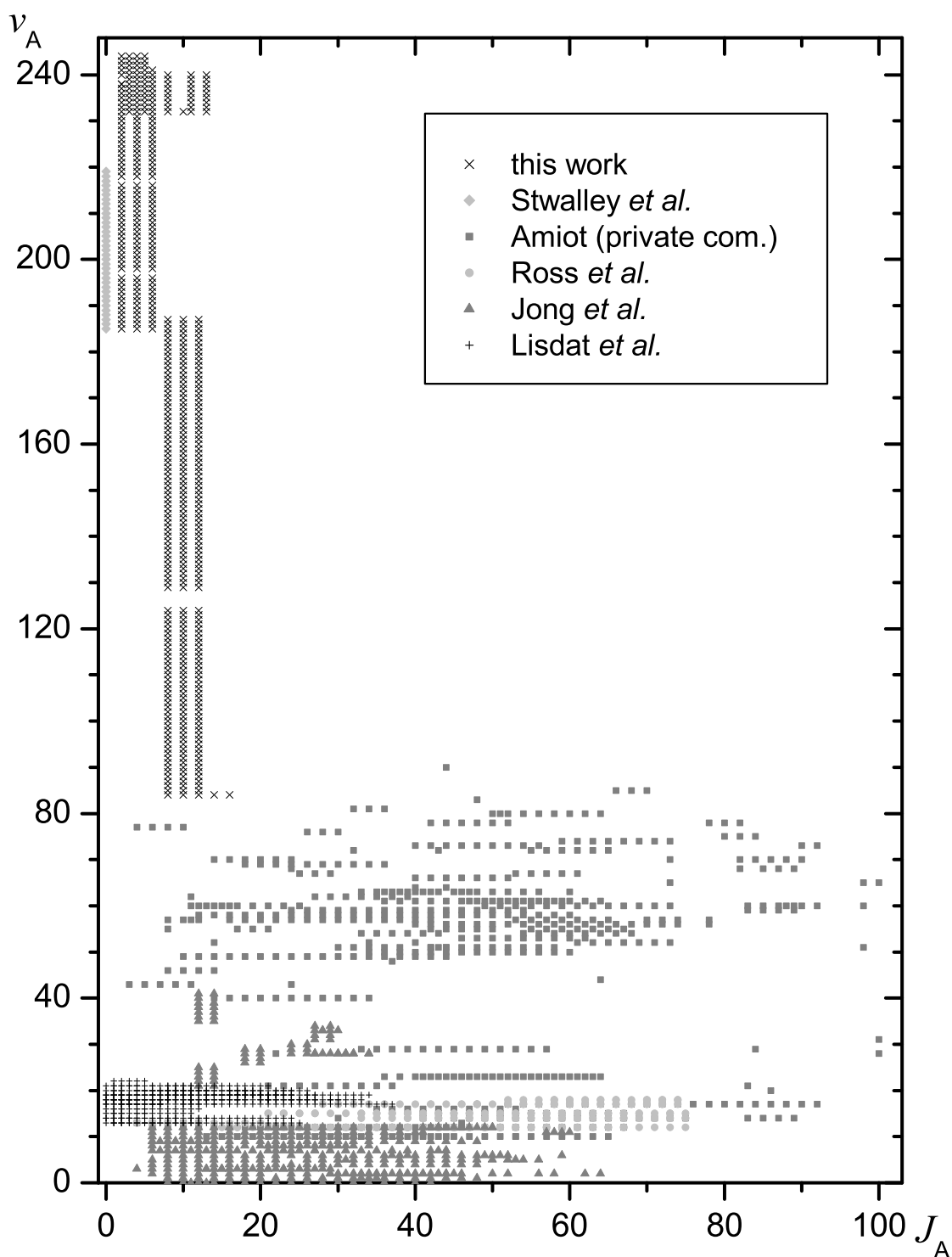
Figure 4.3: *Observed levels of the A $^1\Sigma_u^+$ state. Indicated are data obtained in this study and from earlier experiments by Stwalley et al.,[71] Amiot et al.,[70] Ross et al.,[72] Jong et al.,[73] and Lisdat et al.[47] The term energies of the levels observed in this study are listed in Appendix B.1*

For larger internuclear distances the potentials are usually described in Hund's case (c). The A state becomes the 0_u^+ state that is correlated to the $4s_{1/2}+4p_{1/2}$ asymptote. One spin-orbit component of the b state changes over to a second 0_u^+ state, which ends at the $4s_{1/2}+4p_{3/2}$ asymptote. These two adiabatic potential curves are obtained by solving an eigenvalue problem of a 2×2 matrix[50] because there are no other 0_u^+ components at the $4s + 4p$ asymptote. The two involved diabatic potential curves V_Π and V_Σ are described by truncated expansions in inverse power of R:

$$V_{\Pi/\Sigma} = D - f^{\Pi/\Sigma}\frac{C_3^{\Pi/\Sigma}}{R^3} - \frac{C_6^{\Pi/\Sigma}}{R^6} - \frac{C_8^{\Pi/\Sigma}}{R^8}, \tag{4.3}$$

where the two resonant dipole-dipole interaction constants C_3 obey the relation $C_3^\Sigma = 2C_3^\Pi$. They are modified by retardation effects via $f^{\Pi/\Sigma}$ (see below). $C_6^{\Pi/\Sigma}$ and $C_8^{\Pi/\Sigma}$ are higher order dispersion constants. The asymptotic energy D is the center of gravity of fine and hyperfine structures at the $4s+4p$ asymptote. From these Born-Oppenheimer potentials and the atomic spin-orbit splitting Δ the two adiabatic curves are obtained by solving the eigenvalue problem. They are described by

$$V_{\text{adiab}}^\pm = -\frac{1}{2}\left(\frac{\Delta}{3} - V_\Pi - V_\Sigma\right)$$
$$\pm \frac{1}{2}\sqrt{8\left(\frac{\Delta}{3}\right)^2 + \left(V_\Pi - V_\Sigma - \frac{\Delta}{3}\right)^2}. \tag{4.4}$$

Since we are interested in the curve connected to the A state, the solution with the minus sign is the relevant one. We recently remeasured the D_1 and D_2 lines of potassium and take the spin-orbit splitting as well as the transition wavelength $\lambda_{4s-4p} = c/\nu_{4s-4p}$ from that measurement[77] (c being the speed of light). The transition frequency enters our potential calculation via retardation effects, which become important for $2\pi R \gtrsim \lambda_{4s-4p}$. Retardation effects are introduced by the correction factors $f^{\Pi/\Sigma}$ in equation (4.3). They are given by[78]

$$f^\Sigma = \cos\left(\frac{R}{\lambdabar}\right) + \left(\frac{R}{\lambdabar}\right)\sin\left(\frac{R}{\lambdabar}\right) \quad \text{and} \tag{4.5}$$
$$f^\Pi = \cos\left(\frac{R}{\lambdabar}\right) + \left(\frac{R}{\lambdabar}\right)\sin\left(\frac{R}{\lambdabar}\right) - \left(\frac{R}{\lambdabar}\right)^2\cos\left(\frac{R}{\lambdabar}\right)$$

with $2\pi\lambdabar = \lambda_{4s-4p}$. Additionally, we introduce the exchange energy by adding

$$V_{\text{ex}} = B_1 R^{B_2} e^{-B_3 R} \tag{4.6}$$

to the selected adiabatic long range curves. The parameters B_i are calculated from *ab-initio* methods by Marinescu and Dalgarno.[79] A continuously differentiable connection of the long-range curves to the potential well at R_2 is ensured by adding additionally higher order dispersion terms to the adiabatic curves. By choosing the powers 10 and 12 we reflect possible multipole terms. In summary, the potential curve of the A state at long-range is represented by

$$V = V_{\text{adiab}}^- - V_{\text{ex}} - \frac{C_{10}}{R^{10}} - \frac{C_{12}}{R^{12}}. \tag{4.7}$$

The connection point to the potential well R_2 is chosen a little outside the modified LeRoy-radius of 16.24 Å,[50] which ensures that the dispersion coefficients C_i in equation (4.3) represent the multipole interaction of two atoms and are only weakly influenced by the overlap of the wavefunctions of electrons.

For even bigger internuclear separations, the hyperfine structure becomes important. In principle, each rovibrational level has a number of hyperfine subeigenstates. These are effectively degenerate if the hyperfine structure is small compared to other interactions and a single potential curve may be used. For levels close to the dissociation threshold, the degeneracy is removed by the hyperfine interaction. Consequently, for each hyperfine state an individual potential energy curve should be derived that represents the corresponding levels. Figuratively speaking, the A state curves fan out into several hyperfine curves. We neglect any dynamical coupling due to rotation or hyperfine structure. The curves are calculated using atomic parameters only: fine and hyperfine structure constants, the 4s-4p transition wavelength, and — via the C_3 coefficient — the lifetime of the p-state. A diagonalization procedure is executed at several R. Due to symmetry arguments, levels with odd rotation quantum number J are allowed with even total nuclear spin I only and vice versa. Going to very large R, the two groups of hyperfine curves are formed for both the even-I and the odd-I subsets. For even I, a single curve is below a group of five curves; for odd I a group of three curves lies below a group of seven curves (see Figure 4.4). By going to small internuclear separations, where I and its projection on the nuclear axis Ω_I are good quantum numbers for a non-rotating molecule, we can assign the lower groups to $I = 0$ and $I = 1$, whereas the higher groups are $I = 2$ and $I = 3$. The different curves of each group have different $\Omega_I = -I, -I + 1, \ldots, I$. This explains the observed splitting of the lines for levels very close to the dissociation limit as shown in Figure 4.2. Since only two hyperfine components can be identified for each rotational level, it is sufficient to select a single potential curve per group (here $\Omega_I = 0$). We ensure continuous connections of the four selected curves at R_3 to the branch from equation (4.7) by adding A_3/R^8 terms to them. The four A_3 coefficients must be adjusted if any other potential parameter is changed. The power -8 ensures that this artificial correction falls off quickly for larger R and the dipole interaction term $-C_3/R^3$ is not influenced.

4.1.3.2   Fitting Procedure

The set of observed data covers the full energy interval of the A state. Almost all vibrational levels have now been observed. As indicated in Figure 4.3, several rotational levels have been investigated for each vibrational level. The assignment is unambiguous because of the experimental resolution, the well known ground state, and the gap-free observations. Our spectra are rather simple due to the Franck-Condon pumping step. In our aim to derive an effective potential energy curve for A state, we created a set of artificial energy levels from the deperturbation analysis of the A state and the b state.[74] This analysis took all measurements into account, which were available before we started this study. We calculated the eigenenergies of the deperturbed A state up to the vibrational level $v_A = 80$ for even J_A between 0 and 20. The single channel eigenenergies where calculated using the Numerov method. With these artificial term energies, the bottom of the potential curve is fixed to the result from the deperturbation analysis. The measurements
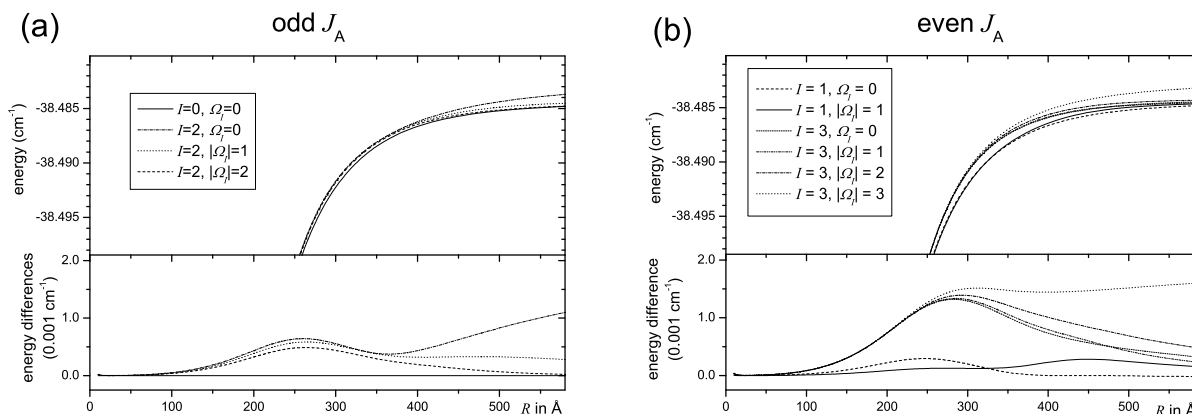
Figure 4.4: *Hyperfine potential curves. As discussed in the text, they can be grouped into those which combine with odd J_A (left-hand side) and those combining with even J_A (right-hand side). In the top graphs the calculated potential energy curves are shown. The energy reference is the center of gravity of the $4s + 4p$ asymptote. Below, the differences with respect to the curve $I = 0, \Omega_I = 0$ are depicted. The differences between 100 and 300 Å explain the hyperfine splitting of rotational lines into two components, as shown in Figure 4.2.*

of this study constitute a second set of term energies. The two sets used for the fit are summarized in Table 4.1.

We used a least squares fit routine to derive a potential energy curve for the A state. Free parameters in the fit are the various potential parameters introduced in Section 4.1.3.1: b_i, C, C_3^{Σ}, C_6^{Σ}, C_6^{Π}, and D. The minimized function is the sum of all squared differences between the eigenvalue calculated from the parametrized potential and the corresponding observed or constructed eigenenergy normalized to the squared experimental uncertainty. If several transitions to the same excited level were observed, an averaged term energy was used for this level.

The eigenvalues of the potential were calculated by the Numerov method. The vibrational assignment is checked against the number of nodes of the found eigenvalues.

We fitted the potential along with our observations. Every few (say about ten) newly observed vibrational levels we extended the data field for the fit by these new values. The influence of local perturbations due to the coupling of the A state to the b state is assumed to average out. However, because we might have hit the perturbation resonances in the observed small J interval, strongly perturbed levels were removed from the data field. The interval of internuclear separation on which the potential was simulated was chosen such that the classically allowed region of R was clearly inside. This interval $(R_0 \leq R \leq R_4)$ was increased along with the data set and R_4 was held significantly larger than any classical turning point because the wave functions of weakly bound levels extend far into the classically forbidden region at large internuclear separations.

We started the fit with *ab inito* values for C_6 and C_8 dispersion coefficients.[80] The coefficient C_6^{Σ} was turned into free parameters of the fit after a good result was already achieved.

We include the dissociation asymptote of the A state D as a free fit parameter. All term energies and D are given with respect to the zero point energy of the Dunham series

Table 4.1: *Summary of term energies used in the fit for the determination of the A $^1\Sigma_u^+$ state potential curve. Constructed levels were created from the deperturbation analysis published by Manaa et al.[74] (see details in text). Their uncertainties are set to a low value in order to keep the bottom of the potential fixed.*

	constructed levels	this work
method	deperturbation	double resonance
	analysis	beam spectroscopy
term energies	11 142 to	15 704 to
	15 674 cm^{-1}	17 436 cm^{-1}
vibrational levels	0 to 80	84 to 245
rotational levels	0 to 20	2 to 13
uncertainty	(0.001 cm^{-1})	0.001 to 0.005 cm^{-1}
number of levels	891	534

for the X $^1\Sigma_g^+$ state published by Amiot *et al.*[67] excluding $Y_{00}^{\mathrm{X}} = -0.022$ cm^{-1}.

4.1.4   Results

The potential energy curve of the A $^1\Sigma_u^+$ state is derived in a least squares fit with 30 free parameters. More than 1400 energy levels are used, 534 are from the experiments described in this paper (see Table 4.1). The resulting parameters are given in Table 4.2 for the potential well, Table 4.3 for the repulsive branch, Table 4.4 for the long-range dispersion part, and Table 4.5 for the hyperfine asymptotes. A diamond ($\diamond$) indicates that this parameter ensures proper connections between the intervals and an asterisk (*) indicates that this parameter is not fitted, e.g., connection points. We give the potential parameters with many digits to ensure numerical reproducibility, i.e., not all digits are physically significant.

The resolved hyperfine structure is understood and modeled quantitatively. Perturbations due to the coupling to the b state increase the error sum. However, the unperturbed levels are reproduced by our potential within the corresponding experimental uncertainties as shown in Figure 4.5. It is easy to identify the vibrational levels with a strong perturbation in this plot. Table 4.6 lists the identified perturbations in the asymptotic region. These are levels with strong ad-mixture of the second 0_u^+ state, which correlates to the higher fine-structure asymptote $4s + 4p_{3/2}$. The vibrational wave function has contributions from the two coupled states, mainly at the classical turning points of the corresponding potential curve. Spectroscopy of these perturbed levels allows for studies of the two states and their coupling.[47]

The radiative atomic lifetime τ can be calculated from the C_3^Σ coefficient, which was derived from the fit. The equation connecting the two properties is[81]

$$\tau = \frac{3\hbar}{2} \left(\frac{\lambda_{4s-4p}}{2\pi} \right)^3 \frac{1}{C_3^\Sigma}. \tag{4.8}$$
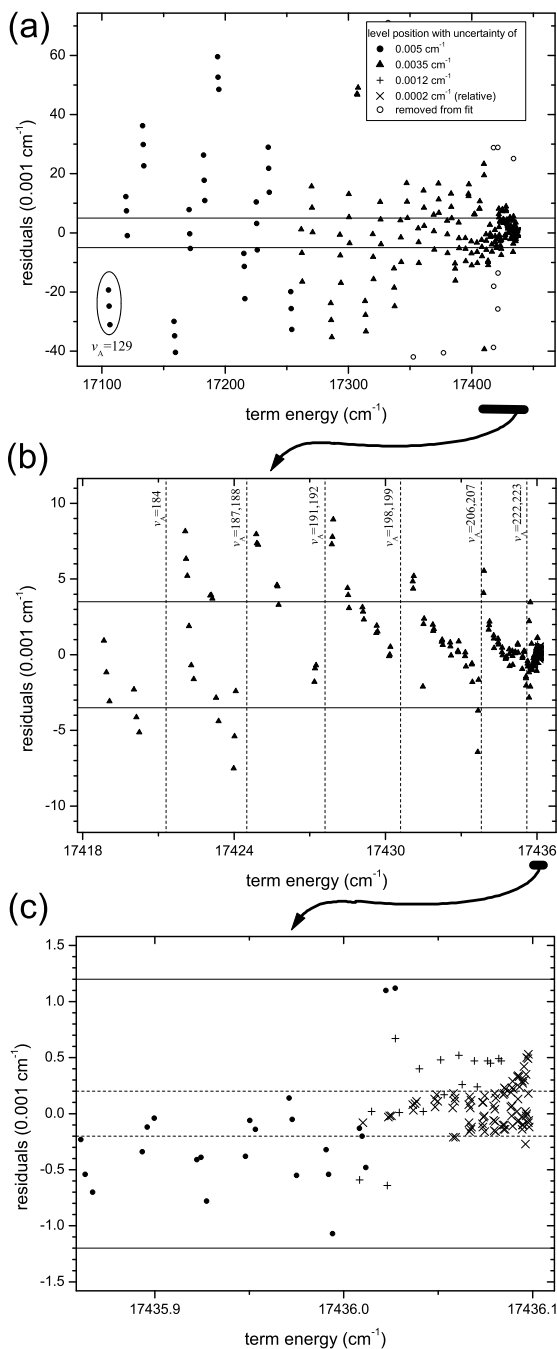
Figure 4.5: *Residuals for the eigenvalues of the potential and experimentally determined term energies. Graph (a) depicts an overview of the residuals of the levels investigated in this study. Perturbations due to coupling to the b state are clearly visible. They are getting smaller but extend to the asymptote. Graph (b) is a zoom onto the asymptotic region. Here, the perturbations are smaller but can be easily identified. The energy positions of the perturbing levels can be derived from these plots. They are indicated by the vertical lines. Graph (c) shows the residuals of the weakest bound levels, including the discussed hyperfine levels. The experimental error of each point is indicated by symbols. Horizontal lines indicate experimental error limits in the observation window.*

Table 4.2: *Potential parameters for the potential well.*

$R_1^* = 3.025$ Å$\leq R \leq R_2^* = 18.5$ Å			
b_0	$=$	$1.110701931 \qquad\qquad \times 10^4$	cm^{-1}
b_1	$=$	$-4.36925369044300638 \times 10^1$	cm^{-1}
b_2	$=$	$4.76297891975524326 \times 10^4$	cm^{-1}
b_3	$=$	$-2.09601115045173974 \times 10^4$	cm^{-1}
b_4	$=$	$-7.01984407530179014 \times 10^4$	cm^{-1}
b_5	$=$	$-3.01001775238950504 \times 10^4$	cm^{-1}
b_6	$=$	$1.55968559608675539 \times 10^6$	cm^{-1}
b_7	$=$	$-5.00914579944727710 \times 10^5$	cm^{-1}
b_8	$=$	$-5.73511453432456404 \times 10^7$	cm^{-1}
b_9	$=$	$1.15249130719885722 \times 10^8$	cm^{-1}
b_{10}	$=$	$1.04092244644117713 \times 10^9$	cm^{-1}
b_{11}	$=$	$-3.80659260027934456 \times 10^9$	cm^{-1}
b_{12}	$=$	$-7.09216903641955090 \times 10^9$	cm^{-1}
b_{13}	$=$	$5.45659790420072861 \times 10^{10}$	cm^{-1}
b_{14}	$=$	$-5.92912726136713181 \times 10^{10}$	cm^{-1}
b_{15}	$=$	$-2.36187587414028015 \times 10^{11}$	cm^{-1}
b_{16}	$=$	$1.17116364854221021 \times 10^{12}$	cm^{-1}
b_{17}	$=$	$-2.50404040001589111 \times 10^{12}$	cm^{-1}
b_{18}	$=$	$-1.89576460672672681 \times 10^{12}$	cm^{-1}
b_{19}	$=$	$2.86804447527311953 \times 10^{13}$	cm^{-1}
b_{20}	$=$	$-6.17994630589855469 \times 10^{13}$	cm^{-1}
b_{21}	$=$	$-3.03985720429939258 \times 10^{13}$	cm^{-1}
b_{22}	$=$	$3.59974601606658937 \times 10^{14}$	cm^{-1}
b_{23}	$=$	$-5.75771007718742750 \times 10^{14}$	cm^{-1}
b_{24}	$=$	$-5.16723472499104531 \times 10^{13}$	cm^{-1}
b_{25}	$=$	$1.47635288904728050 \times 10^{15}$	cm^{-1}
b_{26}	$=$	$-2.40901143313356450 \times 10^{15}$	cm^{-1}
b_{27}	$=$	$1.95020021872318475 \times 10^{15}$	cm^{-1}
b_{28}	$=$	$-8.34049836318447375 \times 10^{14}$	cm^{-1}
b_{29}	$=$	$1.50984509388737000 \times 10^{14}$	cm^{-1}
R_m^*	$=$	4.551 Å	
a^*	$=$	0.26	

Table 4.3: *Potential parameters for the repulsive branch.*

$R_0^* = 2.55$ Å$\leq R \leq R_1^*$	
C	$=$ 1.4954055
$A_1^\diamond$	$= 6.15621691 \times 10^3$ cm^{-1}
$A_2^\diamond$	$= 5.7847022 \ \times 10^4$ cm^{-1}Å^C

Table 4.4: *Potential parameters for the long-range part and atomic parameters for constructing the adiabatic branches of $A\,0_u^+$ and $b\,0_u^+$.*

$R_2^* \le R \le R_3^* = 100$ Å				
C_3^{Σ}	$=$	5.483104	$\times 10^5$ cm^{-1}Å^3	
C_6^{Σ}	$=$	5.122770	$\times 10^7$ cm^{-1}Å^6	
$C_8^{\Sigma *}$	$=$	2.6654	$\times 10^9$ cm^{-1}Å^8	[80]
C_6^{Π}	$=$	3.0319	$\times 10^7$ cm^{-1}Å^6	[80]
$C_8^{\Pi *}$	$=$	1.02877	$\times 10^9$ cm^{-1}Å^8	[80]
D	$=$	17474.5848 cm^{-1}		
ν_{4s-4p}^*/c	$=$	13023.6587 cm^{-1}		[77]
Δ^*	$=$	57.7103 cm^{-1}		[77]
B_1^*	$=$	6.282509	$\times 10^3$ cm^{-1} Å$^{-B_2}$	[79]
B_2^*	$=$	6.0213760140		[79]
B_3^*	$=$	1.9132288453$\times 10^0$ Å^{-1}		[79]
$C_{10}^{\diamond}$	$=$	4.379437	$\times 10^{12}$ cm^{-1}Å^{10}	
$C_{12}^{\diamond}$	$=$	-1.314013	$\times 10^{15}$ cm^{-1}Å^{12}	

Table 4.5: *Parameters for the hyperfine asymptotes. The A parameters describe the magnetic hyperfine structure. In case of the $4p_{3/2}$ state, an effective A value is used, because the quadrupole hyperfine structure is not explicitly taken into account. It is fitted to the level structure resulting from the hyperfine structure described by the A and B values published by Falke et al.[77] Additionally, Δ, C_3^{Σ} and ν_{4s-4p} (see Table 4.4) are used in the calculation. In the bottom of this table, a value A_3 is listed for each of the four hyperfine curves according to the nuclear spin I. These values ensure continuous connection at R_3.*

$R_3^* \le R \le R_4^* = 450$ Å			
$A_{s1/2}^*$	230.8598534	MHz	[51]
$A_{p1/2}^*$	27.775	MHz	[77]
$A_{p3/2}^*$	5.714	MHz	[77]
$A_3^{\diamond}\,(I=0)$	6.89436 $\times 10^{12}$	Å^8 cm^{-1}	
$A_3^{\diamond}\,(I=1)$	6.63504 $\times 10^{12}$	Å^8 cm^{-1}	
$A_3^{\diamond}\,(I=2)$	6.39555 $\times 10^{12}$	Å^8 cm^{-1}	
$A_3^{\diamond}\,(I=3)$	6.06493 $\times 10^{12}$	Å^8 cm^{-1}	

Table 4.6: *Perturbations in the asymptotic region of the A state. Listed are perturbed vibrational levels. We give the term energy of $J_A = 0$ calculated from the effective potential. The real levels are expected to be shifted in the order of 0.01 cm^{-1}. Also listed are the corresponding binding energies with respect to the $4s\,(f=1) + 4p_{1/2}\,(f=1)$ asymptote. In a photoassociation experiment, this is the detuning of the association laser from the atomic resonance. In addition, for each level the classical outer turning point of the effective potential is given.*

v_A	term energy in cm^{-1}	detuning in cm^{-1}	turning point in Å
179	17 414.572	−21.527	26.2
182	17 418.648	−17.451	27.9
184	17 420.981	−15.118	29.3
187	17 423.979	−12.120	31.4
188	17 424.858	−11.241	32.2
191	17 427.176	−8.923	34.7
192	17 427.852	−8.247	35.6
198	17 431.064	−5.035	41.9
199	17 431.479	−4.620	43.1
206	17 433.656	−2.443	53.1
207	17 433.881	−2.218	54.2
222	17 435.684	−0.414	94.8
223	17 435.736	−0.363	98.7

Table 4.7: *Measured and calculated lifetimes of the $4p_{1/2}$ and $4p_{3/2}$ states of potassium in ns.*

method	$4p_{1/2}$	$4p_{3/2}$	year
molecular spectrosc.; C_3 analysis of 0_u^+	26.74(3)	26.39(3)	present work
photoassociation; improved C_3 analysis	26.72(5)	26.37(5)	1997[50]
photoassociation; C_3 analysis of 0_g^-	26.69(5)	26.34(5)	1997[82]
laser spectroscopy in atomic beam	26.79(7)	26.45(7)	1996[68]

Here, C_3^Σ is defined in a Born-Oppenheimer potential correlated to the center of gravity of the 4p state, which we applied in equations (4.3) and (4.4). However, two different lifetimes are derived for the $4p_{1/2}$ and $4p_{3/2}$ due to the different transition wavelengths of the D_1 and D_2 lines, respectively (λ_{4s-4p}). Determinations of the atomic lifetimes of potassium via analysis of the C_3 coefficient are done with photoassociation data to the 0_g^- state by Wang *et al.*[82] and in greater detail in a subsequent publication.[50] The best direct measurement of these lifetimes was derived in a beam-gas-laser spectroscopy setup by Volz and Schmoranzer.[68,83] A compilation of the measured values of the atomic lifetimes of potassium is given in Table 4.7. Our values agree well with the two most recent measurements discussed above. We estimated an uncertainty of 0.03 ns (corresponding to 0.1%) for the lifetimes by altering the C_3 value and fitting other parameters to reach the best possible representation of the data with the altered C_3. Changing the C_3 by 0.1% already resulted in shifts at the tolarable limit in the residual plot after refitting all other parameters. In another verification, we altered the internuclear separation at which the long-range potential starts, namely R_3, by ± 1 Å. After fitting all parameters, the C_3 coefficient was modified by less than 0.05%.

We were provided with detailed photoassociation data from Stwalley, *et al.*[71] With our new observations it was possible to bridge the gap to conventional spectroscopy data and assign the vibrational quantum numbers to their observations. Rotational lines were not resolved in their experiment. The best agreement is obtained by assigning the lines to $J_A = 1$ and using the new value of the D_1 line[77] for the absolute frequency calibration of the scan. However, we did not include these data into our fit since their absolute frequency calibration could not be completely traced back and due to the larger experimental uncertainty from the residual temperature of the trapped atoms and the not very good signal-to-noise ratio.

A value for the of the X $^1\Sigma_g^+$ ground state can be derived using the asymptotic value D of the center of gravity of the 4s + 4p asymptote, the transition frequency of the 4s to 4p transition of potassium ν_{4s-4p},[77] and the Dunham correction Y_{00}^X.[67] Our value of

the dissociation energy (center of gravity of hyperfine structure) $D_e = D - \nu_{4s-4p}/c + Y_{00}^X = 4450.904(4)$ cm^{-1} is within the limits of the previous value of 4450.78(15) cm^{-1} derived from spectroscopy of the ground state by Amiot et al.[67] but with significantly reduced uncertainty (discussed below). A more detailed analysis of the same spectroscopic results of the ground state led to a dissociation energy with reduced uncertainty.[84] The final value of 4450.674(72) cm^{-1} is inconsistent with our derived value. However, our method does not need extrapolation to higher energies as by Amiot et al.[67] and Zhao et al.[84] Our method is thus more direct. The biggest contribution in the error of our value stems from possible errors in the term energies of the ground state levels that are populated by the Franck-Condon pumping (0.003 cm^{-1}) and our frequency calibration (0.0012 cm^{-1}). Both the uncertainty of the atomic transition frequency and that of the derived dissociation energy of the A state are unimportant in this error budget. The dissociation energy given above depends on the reprensentation of the ground state potential. In our opinion it is better to give the dissociation energy with respect to a directly observable level, namely, the absolute ground state of K_2, i.e., $v_X = 0$, $J_X = 0$. The dissociation energy with this energy reference (center of gravity of the ground state asymptote) $D_0 = 4404.808(4)$ cm^{-1} is independent from a ground state model and any Dunham correction Y_{00}^X. For the uncertainty considerations the same arguments as above hold.

4.1.5 Conclusion and Outlook

The A $^1\Sigma_u^+$ state of K_2 was studied in a molecular beam experiment by Doppler free laser spectroscopy. The high lying vibrational levels were reached by successive excitation with two laser fields. More than 500 new levels were added to the data field with their vibrational and rotational assignment. A piecewise analytic potential energy curve was derived in a least squares fit leading to improved long-range parameter C_3, with which values for the atomic lifetimes were derived being consistent with earlier determinations, but with reduced uncertainty. Additionally, an improved value for the ground state dissociation energy of K_2 is given.

In the future, we will study the heteronuclear dimer $^{39}K^{41}K$ in our molecular beam. The observed signal-to-noise ratio for $^{39}K_2$ allows for the detection of the heteronuclear molecule, which is about eight times less abundant in our beam than the homonuclear dimer. The R^{-3} behavior of the A state is expected to be modified due to the isotope effect of the 4s-4p transition of potassium. The resonant dipole-dipole interaction of the homonuclear dimer will go over to a detuned dipole-dipole interaction for binding energies in the order of the isotope effect of the heteronuclear dimer.

The new results will be applied to study ultracold collisions of two ground state potassium atoms in the beam. A detailed spectroscopic study of the molecular ground states X $^1\Sigma_g^+$ and a $^3\Sigma_u^+$ at their asymptotic asymptotes can lead to precise descriptions of such collision as demonstrated in the case of sodium.[5] Scattering lengths and their behavior in magnetic fields or Feshbach resonances can be calculated from precise molecular potentials. Of high importance is the spectroscopic knowledge about levels at the 4s+4s asymptote. Such levels can be addressed in our molecular beam: Franck-Condon pumping step followed by spectroscopy in a lambda scheme that couples the pumped level of

the X state to asymptotic levels of the X state via a level of the A state. The spectroscopy of this work is essential for such high-resolution spectroscopic studies of asymptotic levels allowing reliable predictions of the best transitions of the lambda scheme. Moreover, we think that it is possible to undertake such studies not only for $^{39}K_2$ but also for $^{39}K^{41}K$. Ultimately, we hope to verify to which precision mass-scaling of cold collision parameters from one isotopomer to the other is sufficiently correct, i.e., to check the Born-Oppenheimer approximation with respect to cold collissions.

Acknowledgments

4.2   Hyperfine Structure

The observed hyperfine structure of asymptotic levels of the A $^1\Sigma_u^+$ state of K_2 deserves a closer look. Long-range dispersion expression for the interaction potential may be used for internuclear distances, where the multi-pole interaction energies of the electrons are larger than contributions due to the overlap of their wavefunctions. The LeRoy radius[85,86] indicates this interval, in which long-range interaction dominates chemical bindings. For even larger internuclear separations, these interaction energies are getting smaller than the atomic hyperfine structure. Here the coupling of the electrons to the nuclei influences long-range interaction.

The hyperfine structure of the singlet state is only observed for levels bound less than the atomic hyperfine structure, i.e., only for levels very close to the asymptote, where the levels are no longer pure singlet levels. Hyperfine interaction is one of the rare possibilities for a coupling between *gerade* and *ungerade* states. Such couplings became very prominent in the community of ultracold alkali metal atoms: Feshbach resonances are – from a molecular point of view — molecular levels in the vicinity the ground states asymptotes. Two molecular states are correlated to these asymptotes: the X $^1\Sigma^+$ state and the a $^3\Sigma^+$ state. In case of homonuclear dimers, i.e., for a single species trap, these two states have contrary *gerade-ungerade* symmetry. The hyperfine interaction allows for coupling between levels of these two states. This leads to a mixing of significant singlet and triplet character for asymptotic levels. The rich field of levels gets even more interesting if external magnetic fields are considered. With their different magnetic moments, the levels can be brought to degeneracy and avoided crossings appear. These avoided crossings are utilized if magnetic fields are used to manipulate the scattering length around a Feshbach-resonance[9] or to transfer effectively ultracold atoms into a weakly bound dimer level by a Feshbach-ramp[87] or an association by a radio frequency pulse.[88]

The hyperfine structure of levels below an electronically excited asymptote are of less interest for trap experiments because the atoms are usually not in the corresponding
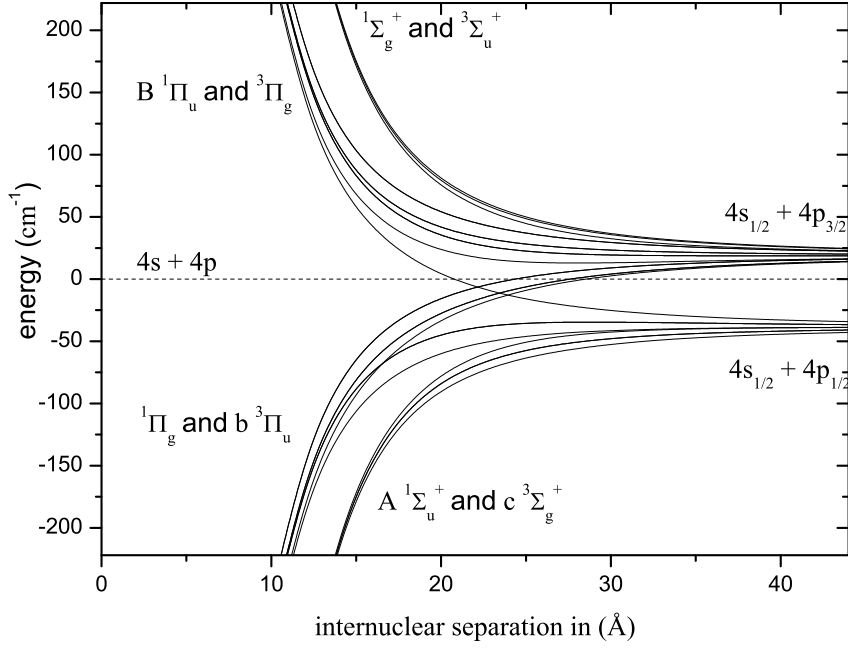
Figure 4.6: *Adiabatic curves for* K$_2$ *calculated from atomic parameters only. All potential energy curves that relate to the* 4s + 4p *asymptote are depicted. The dashed line indicates the center of gravity of the* 4s + 4p *asymptote.*

electronic states. The same models and tools that describe the hyperfine structure may be applied in both cases. The modelling of the observed hyperfine structure as described above is therefore an additional confirmation of the models applied for the description of cold collisions. Moreover, photoassociation accesses similar levels as our experiment. In our study of the A state the modeling of hyperfine structures was motivated by the quest of obtaining a correct long-range parameter C_3. In equation (4.8) this parameter is considered for an artificial fine and hyperfine free asymptote, which is used for the determination of the atomic lifetime.

In the following, we will discuss, firstly, how the potential curves are derived (Section 4.2.1) and, secondly, the calculation of term energies (Section 4.2.2).

4.2.1   Adiabatic Hyperfine Potential Curves

The magnitude of the dipole-dipole interaction of a s-electron and a p-electron is different for the four orientations of the orbitals. Using molecular quantum numbers, these four orientations of the dipoles are labeled by Σ and Π and are either attractive or repulsive. In our example, namely the 4s + 4p asymptote, the spin has to be considered and in total eight electronic states develop for not too large internuclear distances: $^1\Sigma_u^+$ (A state), $^3\Sigma_g^+$, $^1\Pi_g$, and $^3\Pi_u$ (b state for $\Omega = 0$) are attractive whereas $^1\Sigma_g^+$, $^3\Sigma_u^+$, $^1\Pi_u$ (B state), and $^3\Pi_g$ are repulsive (see Figure 4.6).

The 4s + 4p asymptote splits at long range into several hyperfine branches. The largest interaction is the spin-orbit interaction of the 4p state (about 170 GHz). The hyperfine

structure of the 4s atom is larger than the one of the 4p atom. Both lead to splittings in the order of 100 MHz. In total,

$$\underbrace{2}_{\substack{\text{degeneracy} \\ \text{of } 4s_{1/2}}} \times \left(\underbrace{2}_{\substack{\text{degeneracy} \\ \text{of } 4p_{1/2}}} + \underbrace{4}_{\substack{\text{degeneracy} \\ \text{of } 4p_{3/2}}} \right) = 12 \tag{4.9}$$

asymptotic energies are possible.

Adiabatic hyperfine and spin-orbit potential curves connect the eight potentials at short internuclear separations, which are split by hyperfine interaction to the twelve asymptotes. The interactions remove the degeneracy and lead to avoided crossings. A rich field of adiabatic potential curves, often referred to as hyperfine spaghetti, is obtained. We choose a hybrid basis for the calculation of the potential curves: the two nuclear spins are combined but the total momenta of the two valence electrons are treated separately. The basis wavefunctions are therefore a product of a wavefunction for the nuclear spin labeled by the total nuclear spin I and its projection on the molecular axis Ω_I and a wavefunction for the electrons. This is a product of a s-electron and a p-electron. The electronic wavefunction has therefore four labels, two for each atom: j is the total electronic angular momentum and its projection on the molecular axis Ω_j. The number of basis functions (with a maximal possible I of three for the atomic nuclear spin 3/2 of ^{39}K) is

$$\underbrace{\sum_{i=0}^{3} (2i+1)}_{\text{nuclear wavefunction}} \times \underbrace{\underbrace{2}_{\text{permutation}} \times \underbrace{2}_{4s} \times \underbrace{6}_{4p}}_{\text{electronic wavefunction}} = 16 \times 24 = 384. \tag{4.10}$$

The resulting potential matrix of the 384×384 representing the adiabatization process is block diagonal because states with different total projection on the molecular axis $\Omega_F = \Omega_I + \Omega_{j1} + \Omega_{j2}$ are not coupled. Also, the blocks with positive and negative Ω_F are the same. Thus, in total $76 + 68 + 48 + 26 + 10 + 2 = 230$ different adiabatic eigenenergies are obtained. The potential energy curves are created by calculating the potential energies at several internuclear separations R and connecting these points by comparing the eigenvectors of the coupling matrix. The step of R has to be small enough such that change of the eigenvectors can be followed and the connection of the potential energy points is correct. In this way, 230 different adiabatic hyperfine potential energy curves are created (see Figure 4.6 and Figure 4.7).

How the diabatic states are coupled was described in detail in preceding studies at the corresponding state of Na_2[69,89] and is not repeated here, instead the most important issues are discussed. The calculation does consider a single long-range interaction coefficient C_3 as defined in Section 4.1.3.1. Retardation effects for this coefficient are included in the calculation. Higher order dispersion terms are not included because their influence is small at the considered internuclear separations. For the $4p_{3/2}$ state, the quadrupole hyperfine structure is not taken explicitly into account. Instead, the magnetic hyperfine structure is adjusted such that the energy positions of the four hyperfine states are best reproduced with a single parameter for the hyperfine structure, namely an effective A-parameter. All hyperfine curves are calculated purely from atomic parameters, i.e., without knowledge of the inner potential well.
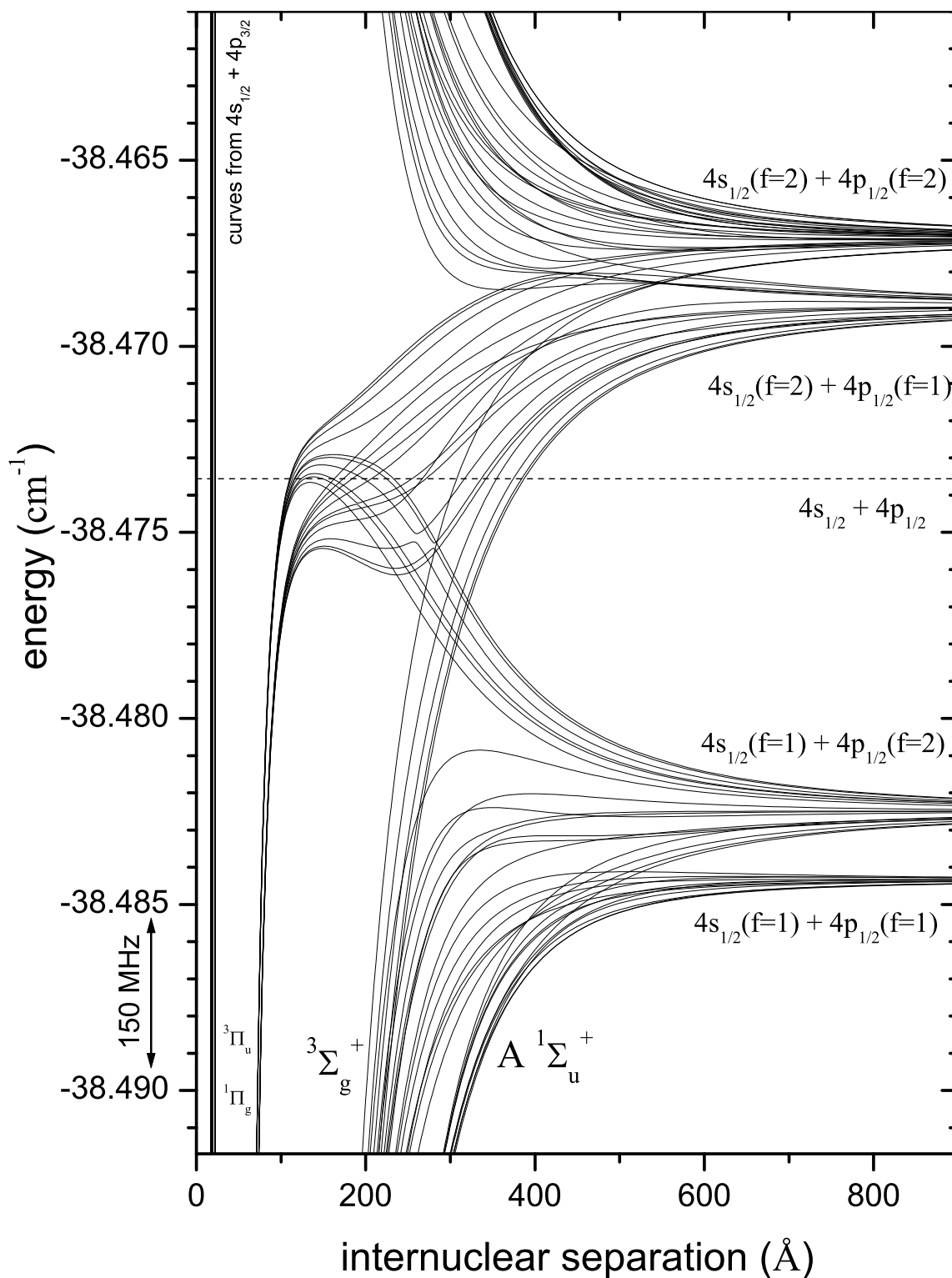
Figure 4.7: *Adiabatic hyperfine potential curves in the* $4s_{1/2} + 4p_{1/2}$ *region. The dashed line indicates the center of gravity of the lower fine structure asymptote of the* $4s + 4p$ *asymptote. The ten curves correlated to the A state are shown in more detail in Figure 4.4.*

4.2.2   Term Energies of Hyperfine Levels

In order to connect the obtained adiabatic potential curves to the experiment, the eigen-
values of the relevant potential have to be calculated. Without knowledge of the inner
potential well, this is possible by applying the accumulated phase method. Instead of
looking for bound states of a closed potential, we are looking for wavefunction that have
a certain phase at a selected internuclear separation R_{AP} and decay exponentially for
large R. The inner nodes of asymptotic wavefunctions of a closed potential well are al-
most at the same R. By approximating the inner structure up to R_{AP} with an appropriate
accumulated phase, a good description for the ladder of eigenstates can be obtained.[90]
This method can be used to derive to the scattering length of the potential. Here, we
calculate this ladder using atomic parameters only and neglect fine adjustments of the
accumulated phase for the moment.

We have to select the hyperfine curves, which have the right symmetry to be seen
in our experiment, i.e., those correlated to the A $^1\Sigma_u^+$ state. This filter is applied at
short internuclear distances and delivers ten curves, one for each nuclear wavefunction
$|I, \Omega_I \geq 0\rangle$. For symmetry reasons, eigenstates only exist for an even I combined with
an odd J and *vice versa*. In Figure 4.8 the resulting asymptotic energies are shown for
these two cases. This plot confirms the observed hyperfine structure below the asymptote.
Only two components for each rotational line are visible. Their relative weights are 1:5
and 3:7 according to the total nuclear spins I of (0,2) for odd J and (1,3) for even J
respectively. The hyperfine spacing increases with higher v_{A}. This increase is stopped
before the asymptote is reached.

4.2.3   Description of Molecular Hyperfine Structure by Poten-
tials

One of the objectives of the study of the A state of K_2 was the measurement of an improved
value of the atomic radiative lifetimes, i.e., the determination of a C_3 coefficient. Three
approaches ensure that the derived C_3 coefficient is not just a potential parameter ensuring
proper representation of energy levels but reproduces the expectation value of the dipole
moment

$$C_3^\Sigma \sim |\langle 4\mathrm{s}| \, ez \, |4\mathrm{p}\rangle|^2 \tag{4.11}$$

and thus radiative lifetimes can correctly be derived (see equation (4.8)). First, one
can use molecular states (or regions of molecular states), which are little perturbed and
coupled. This was done in the analysis of photoassociation spectra. This clever approach
leads to the simplest determination of the long-range parameter, e.g., by the LeRoy-
Bernstein formalism.[91] Well isolated states are difficult to reach but it is possible, e.g., in
photoassociation experiments. The levels, which carry most of the information about the
long-range interaction, i.e., the weakest bound ones, are excluded because they are not
only difficult to observe but also not usable due to the perturbing hyperfine structure.

The second method is to calculating from the observed hyperfine levels an effective
potential and model the hyperfine structure by a parameterized, phenomenological correc-
tion as in the analysis for sodium.[69] The third method, followed by us, is the calculation
of hyperfine curves, which are included to the potential for modelling of the state. This
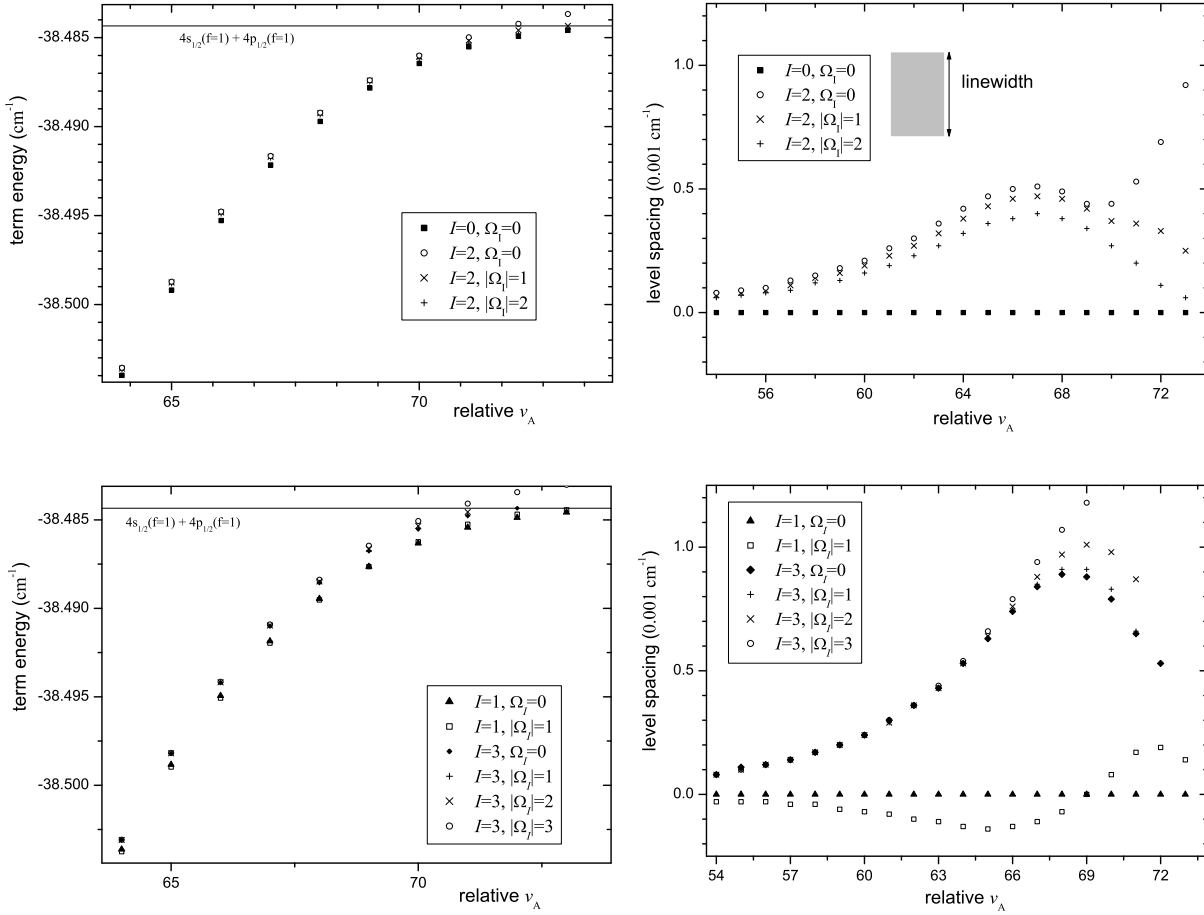
Figure 4.8: *The left hand side shows term energies of hyperfine levels in the asymptotic region of the A state with respect to the center of gravity of the* 4s + 4p *asymptote for even and odd J separately. The energies are calculated with an approximated phase method using the adiabatic potential energy curves shown in Figure 4.6. The energies are plotted as a function of the number of nodes in the vibrational wavefunction counting outward from the starting point of the integration, and it corresponds to a local counting of the vibrational levels. On the right hand side, the energy difference to the levels of $I = 0$, $\Omega_I = 0$ and $I = 1$, $\Omega_I = 0$ respectively are depicted in top and bottom graph respectively. Here, the hyperfine structure observed in the rotational lines is better visible.*
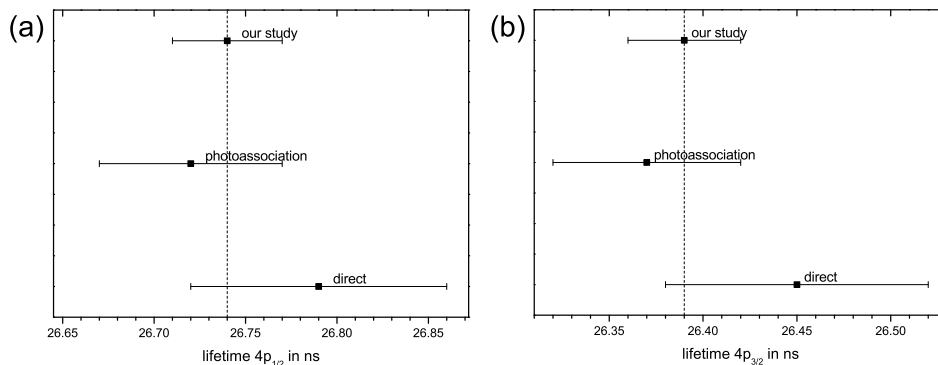
Figure 4.9: *Comparison of recently determined lifetimes of* $4p_{1/2}$ *in Graph (a) and* $4p_{3/2}$ *in Graph (b). All studies are consistent.*[50, 68]

method needs a significant computational effort because the hyperfine curves have to be re-calculated in a fitting routine every time the C_3 coefficient is altered. Ten years ago, at the time of the sodium measurements, this methods could not reasonably be used due to the high complexity. We believe that this method leads to a good physical model and thus precise atomic lifetimes. The model does not account for dynamical coupling but for the observed low rotational level and the small hyperfine structure of potassium, the perturbations are small.

The resulting lifetimes of our study are in between values from photoassociation spectra (first method) and direct measurements with overlapping error bars as depicted in Figure 4.9. Thus, both studies are confirmed and the uncertainty is decreased to half of the previous uncertainties.

4.3   Study of the Born-Oppenheimer Approximation

In general, the Born-Oppenheimer approximation allows to separate the electronic, vibrational, and rotational degrees of freedom. But, couplings between different electronic states lead to perturbations. They cannot be modeled by a single potential energy curve but by two or more curves and — in general R-dependent — couplings between the electronic states. A coupled channels analysis uses therefore Born-Oppenheimer potential curves and coupling curves. Also, if the perturbations shift some levels upwards and others downwards without systematic trend a potential curve may be derived by averaging across these perturbations. This was done in the Section 4.1.

Born-Oppenheimer potential energy curves may be used for mass-scaling between isotopomers. It is assumed that the potential energy curves are not depending on the isotopes: vibration and rotation is not influencing the eigenspectrum of the electrons. Only the change in the reduced mass has to be considered for comparing two isotopomers. This technique allows for the verification of an absolute assignment of vibrational quantum numbers. For levels accessible by conventional spectroscopy the findings are in agreement within typical experimental uncertainty of about 10^{-5} and often a single potential

curve is obtained from transition frequencies from several isotopomers.[92] However, high precision experiments on iodine were able to derive corrections to the Born-Oppenheimer potentials.[93]

The same method may be applied to properties of cold collisions. From spectroscopy of a specific isotope combination with reduced mass μ a potential is derived. From this, an effective number of vibrational levels v_D may be interfered. This number may be mass-scaled to another isotope combination with the reduced mass μ' by

$$v_D' = \sqrt{\frac{\mu'}{\mu}} v_D \qquad (4.12)$$

and a corresponding scattering length may be derived[94] from the non-integer modulo of the scaled effective number of vibrational levels $\lfloor v_D' \rfloor$. It is also possible to derive a value for $\lfloor v_D \rfloor$ by asymptotic methods as a starting point for the mass scaling in experiments with ultracold atoms. But, a good estimate for the integer part of v_D needs to be found before performing the mass scaling according to equation (4.12).

However, due to the strongly non-linear dependency of the scattering length on the effective number of vibrational levels, small uncertainties may translate to very big errors in the derived scattering length. Also, positions of Feshbach resonances relate to term energies and thus may be mass-scaled from one isotope combination to another. Here, experiments with trapped atoms allow for a very high resolution. The Born-Oppenheimer approximation serves as a basis for the connection between different isotope combinations. However, it has not been studied to which precision it is valid for the prediction of scattering lengths and Feshbach resonances by mass-scaling.

Here, the precision of the Born-Oppenheimer approximation is demonstrated for the A $^1\Sigma_u^+$ state of K$_2$. We compare asymptotic levels of the two most abundant isotopes, namely the homonuclear ^{39}K$_2$ and the heteronuclear ^{39}K^{41}K. Thus, the isotope shift (measured in Section 3.1) of the D lines adds another aspect. Two asymptotes separated by the isotope shift are existing.

4.3.1 Theory

The first electronically excited asymptote of alkali metal dimers has substantial differences if homonuclear dimers are compared to heteronuclear dimers. The long-range behavior of the electronic states of alkali metal dimers at the $n_1\,s + n_2\,p$ asymptote is such that they are shorter range in the heteronuclear case than in the homonuclear case (see Figure 4.10). Therefore, photoassociation experiments at this asymptote in two species traps have another characteristics than photoassociation of homonuclear dimers from single species traps.[95]

Photoassociation of heteronuclear dimers from alkali metals is a promising way to produce ultracold gases of particles that carry a permanent dipole moment. Ground state heteronuclear dimers will allow for tests of theoretical models for the strong interaction regime. The interaction is the stronger, the more polar the combination is and the deeper the molecules in the ground state are bound. Efficient ways to produce the ultracold polar molecules are therefore subject of research. Significant progress was achieved in
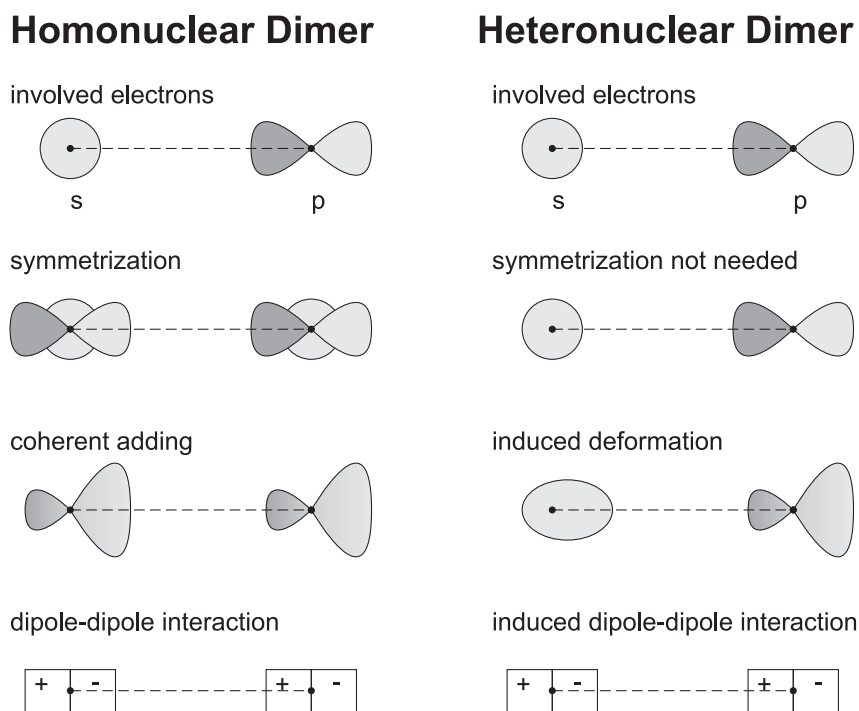
Figure 4.10: *Fundamental difference of long-range behavior of heteronuclear dimers in comparison with homonuclear dimers. In the homonuclear case both nuclei are indistinguishable. The symmetrization of the electronic wavefunction leads to a shift of the center of the electron wavefunction due to the opposite phase in the two cones of the p orbital. This results in permanent dipole moments, the nuclei are kept at the same place. The two atoms are thus interacting via a dipole-dipole interaction, i.e., the interaction is proportional to R^{-3}. The symmetrization is done in fact automatically if the $s - p$ transitions of the atoms are of the same frequency and the two asymptotes are degenerate. The case of the heteronuclear dimer is the more general one. The leading multipole interaction is the induced dipole-dipole interaction, resulting from the deformation of the two electronic wavefunctions due to the other electron. This interaction is proportional to R^{-6}, which leads to shorter range potentials than in the homonuclear case.*

recent years. As examples, three combinations are mentioned here: First, the production and detection — an often neglected part of such experiments — of ground state RbCs dimers were achieved.[20] In this experiment in DeMille's group at Yale, work towards a better efficiency is done now. Second, KRb is a combination that benefits from easily available trapping laser frequencies. Many experiments concentrate on the atoms, e.g., investigations on the quantum degenerate Fermi gas of ^{40}K. However, photoassociation was done with these elements[96] in Stwalley's group at the University of Connecticut for ^{39}K^{85}Rb. Third, LiCs provides the most polar combination. The experiment of Weidemüller's group in Freiburg is equipped with mass selective detection and optical traps.[97]

On the other end of the polarity scale are heteronuclear dimers from a single species, e.g., ^{39}K^{41}K. The only difference between the two bound atoms is the number of neutrons in the two nuclei. In our experiment, we studied to which extend the heteronuclear potassium dimer is actually heteronuclear, i.e., what is the difference to ^{39}K$_2$. As illustrated in Figure 4.10, the leading long-range interaction is different between a homonuclear and a heteronuclear dimer. However, our test candidate ^{39}K^{41}K may be considered heteronuclear only for binding energies in the order of the isotope shift of the D lines. In Figure 4.11, adiabatic potential curves are shown for the asymptotic region. In Graph (a), the fine and hyperfine structure at the 4s+4p asymptote of K_2 is artificially removed. The difference between the homonuclear and the heteronuclear dimer is well pronounced. In Graph (b), the spin-orbit interaction is included. Only the curves correlated to the lower fine structure asymptote $4s_{1/2}+4p_{1/2}$ are shown. A substantial difference between the two considered cases is still well visible. How the situation looks like if hyperfine structure is taken into account will be discussed later on.

4.3.2 Experiment

A comparison of the potentials of the A $^1\Sigma_u^+$ states of two isotopomers needs spectroscopy of both isotopomers. We are interested mainly in the weakest bound levels of the less abundant isotopomer. In comparison with the already investigated molecule, the heteronuclear combination is by a factor of seven less abundant. For the spectroscopy, this results directly in a loss of signal strength, assuming that in the preparation step the Franck-Condon pumping transition is saturated. The transitions driven in the spectroscopy are due to the small Franck-Condon factors not saturated and similarly weak.

The increased reduced mass results in smaller vibrational spacing. The vibrational level of the A state used for the preparation step for ^{39}K$_2$ ($v_A = 25$) is strongly perturbed for ^{39}K^{41}K and the assignment was not easily possible. In order to avoid further problems, the experiments are performed with Franck-Condon pumping using $v_A = 26$ for ^{39}K^{41}K. Due to the higher mass, this level is energetically already close to $v_A = 25$ of ^{39}K$_2$. However, saturation was not achieved with the available laser power. Therefore, the laser beam for the Franck-Condon pumping was back-reflected across the molecular beam several times leading to an optical pumping of more than half of the molecules originally in the starting level.

We are mainly interested in energy spacing for two reasons. First, an absolute frequency measurement with high precision needs big experimental efforts. Second, the rela-
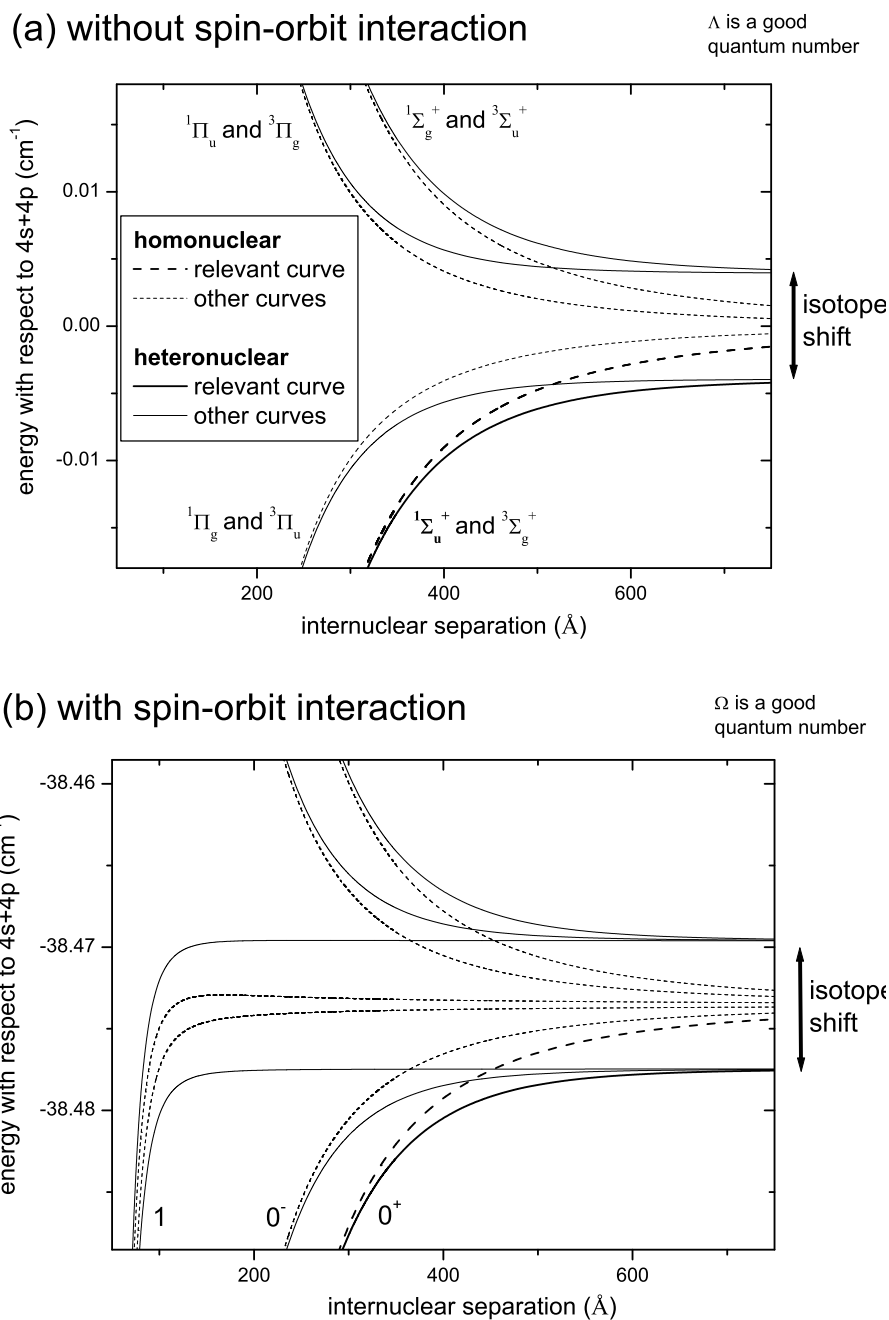
Figure 4.11: *Adiabatic potentials of $^{39}K_2$ and $^{39}K^{41}K$ without hyperfine structure for a resonant dipole-dipole interaction (homonuclear case) and a detuned dipole-dipole interaction (heteronuclear case).* Graph (a) *shows the long-range behavior without spin-orbit interaction. This interaction is taken into account in* Graph (b). *Only the asymptote* $4s_{1/2} + 4p_{1/2}$ *is shown.*

tive energy position of levels of the ground state are not known better than 50 MHz.[67] We use a temperature stabilized Fabry-Perot interferometer (FPI) for the relative frequency calibration and record the transmission from the spectroscopy laser simultaneously with the laser-induced fluorescence at the molecular beam. Typically, this laser scans an interval of 3 GHz. The positions of the FPI peaks are determined by a local fit. Then, a polynomial of fourth order is fitted to the list of positions of FPI peaks. From this a polynomial frequency axis for the scan is obtained. Up to twelve scans were recorded and linearized per scan interval of the laser. These are then averaged and the resulting curve smoothed by adjacent filtering with fifteen data points, corresponding to about 5 MHz.

We concentrated on spectra starting from $J_X = 9$. This allows for good signal since the population in the ground state level is high. Also, the spacing between the P and R lines is big enough to avoid overlapping lines in the region where the molecular hyperfine structure becomes significant. In Figure 4.12 scans for both isotopomers are shown.

4.3.3 Analysis

Starting from the adiabatic potential curves of the A state as derived in Section 4.1 for $^{39}K_2$, some changes need to be considered for calculations of the term energies of $^{39}K\,^{41}K$. First, the heavier reduced mass of the heteronuclear molecule has to be used. This leads to smaller energy spacing. The potential supports about three additional vibrational levels. The atomic masses are well known and this change can be applied easily. Second, one of the two atoms contributes a smaller hyperfine structure. This removes the degeneracy of asymptotic energies. This change is applied by keeping the center of gravity for both atoms at the same point in the energy scale. The fine structure of both isotopes remains almost unchanged and the isotope shift of it does therefore play no important role in our modeling. Third, the D lines have an isotope shift of about 235 MHz (see Table 3.6). However, it is not known how the 4s and the 4p level are shifted individually on the absolute scale. The asymptotic energies for different steps of the considerations are depicted in Figure 4.13. A forth change needs to be pointed out. No g/u symmetry can be defined. Consequently, every rotational state J may be combined with any total nuclear spin I.

In the following we will discuss how we used the obtained experimental findings. As an overview, the steps taken are summarized here:

1. fine adjustment of the potential of the A state for the asymptotic region of the homonuclear molecule,

2. comparison of the heteronuclear with the homonuclear dimer, and

3. correction to the Born-Oppenheimer potential of the heteronuclear dimer.

4.3.3.1 Homonuclear Dimer

For a direct comparison between the two isotopomers, we recorded spectra of the homonuclear molecule starting from the same rotational state, i.e., $J_X = 9$ (see Figure 4.12, Graph (a)). The hyperfine structure of the least bound levels is nicely resolved and can easily be seen, e.g., for $v = 239$. We assigned the observed lines and determined energy
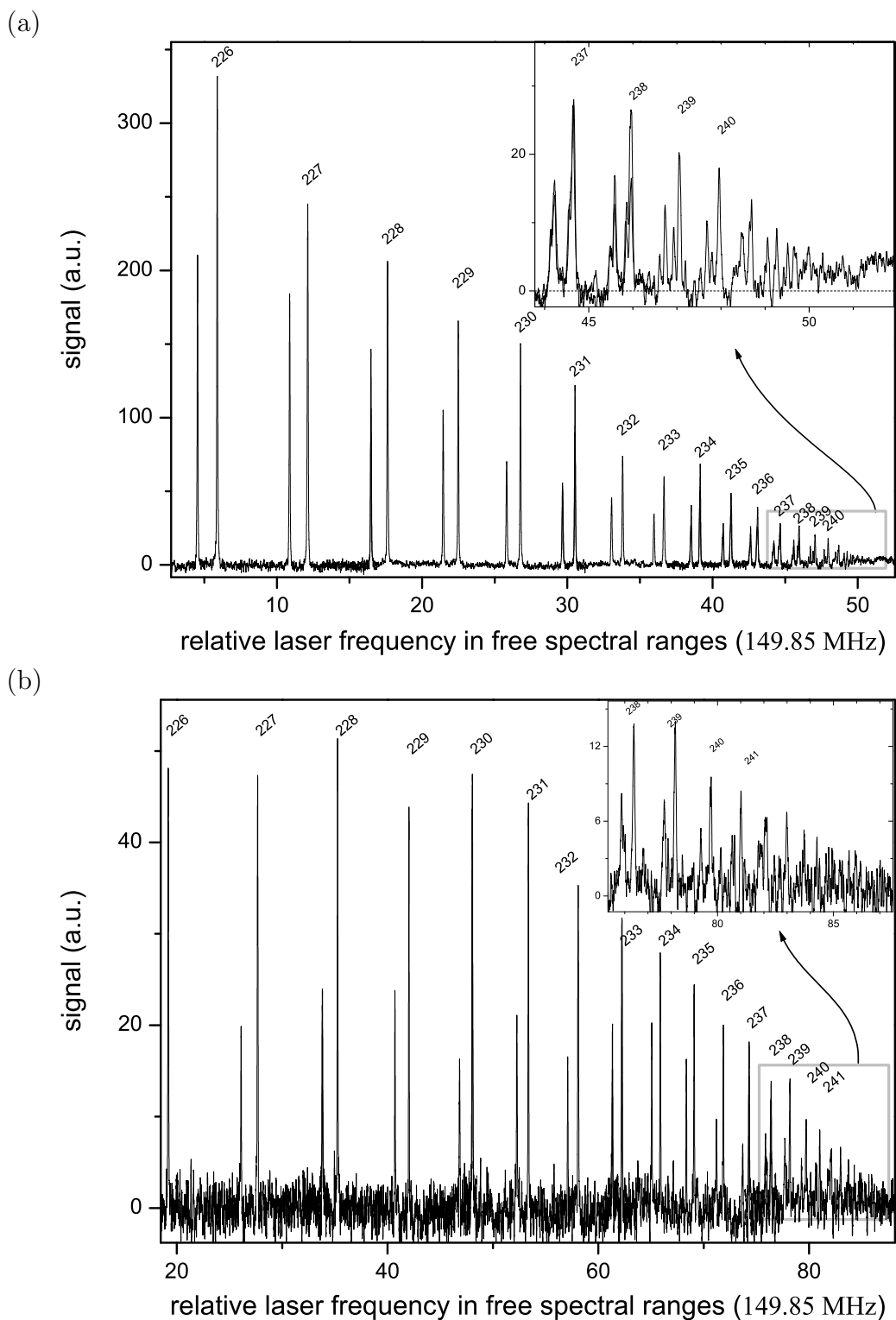
Figure 4.12: *Scan across the asymptotic region of the* A *state of the homonuclear dimer* $^{39}K_2$ *in* Graph (a) *and of the heteronuclear dimer* $^{39}K\,^{41}K$ *in* Graph (b). *For both isotopomers P(9) and R(9) lines are observed. The labels indicate the vibrational quantum number of the A state level.*
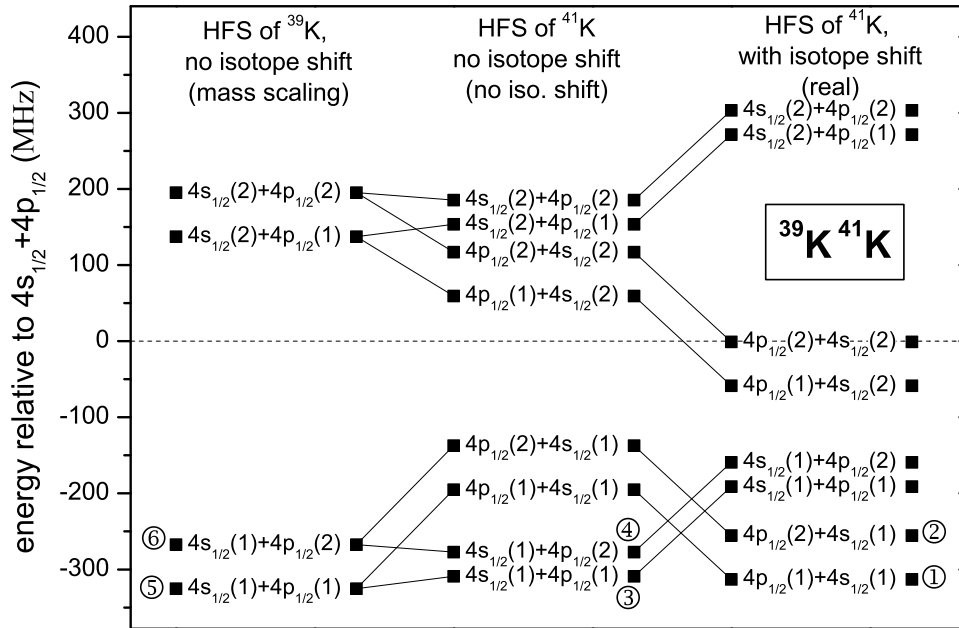
Figure 4.13: *Deriving asymptotic energies of* $^{39}K^{41}K$ *at the* $4s_{1/2} + 4p_{1/2}$ *asymptote, which is also the reference energy. The total angular momentum of the atomic states is given in brackets. On the left hand side, the asymptotic energies of* $^{39}K_2$ *are shown. In the middle ladder, the hyperfine structure of* ^{41}K *is considered, which removes the exchange degeneracy. First, the state of the* ^{39}K *atom is given and, second, the state of the* ^{41}K *atom. Finally, the isotope shift is taken into account, as illustrated on the right hand side. Here the effect is distributed to equal parts on the* 4s *and the* 4p *electron for reasons discussed in Section 4.3.3.2. The circled numbers indicate energies to which potential curves are correlated that are related to the* A *state (see Figure 4.17). For these lowest asymptotes, the hyperfine structure and isotope shift compensate each other to some degree.*
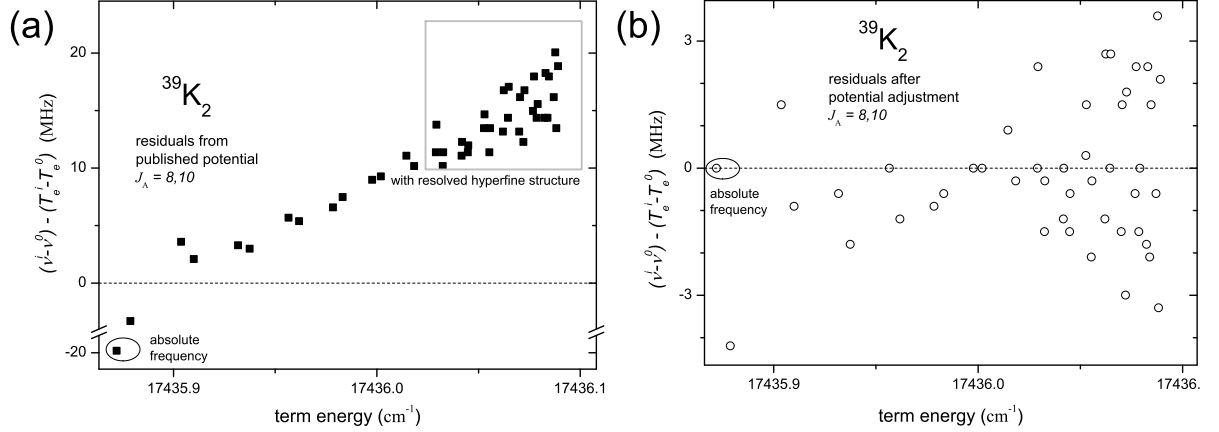
Figure 4.14: *Analysis of the spectra of homonuclear dimer.* Graph (a) *shows the residuals of the energy spacing resulting from the potential derived in Section 4.1. After adjusting the inner branch of the potential by a fit, the residuals are reduced as shown in* Graph (b), *note the scale change of factor of about three compared to* Graph (a)

.

spacings with the FPI marker trace. The absolute frequency was set by transition energy of the lowest line ν^0 (P(9) line to $vA = 226$). The free spectral range of the FPI was measured to be 149.85 MHz.[24]

We compared the experimental observations to calculations from the potential derived in Section 4.1. To do so, a list of measured transition energies ν^i and a list of calculated term energies T_e^i ($i = 0, \ldots N$) are derived. The residuals in plot in Graph (a) of Figure 4.14 are the differences

$$
\begin{array}{ll}
(\nu^0 + T_{\mathrm{X}}) - T_e^0 & \text{for the absolute position and} \\
(\nu^i - \nu^0) - (T_e^i - T_e^0) & \text{for } i = 1, \ldots, N.
\end{array}
\tag{4.13}
$$

The term energy of the ground state level from which we are starting is indicated by T_{X}, where we keep the energy reference at the zero point of the Dunham series describing the ground state without any Y_{00} correction. Although the residuals are small, a trend is clearly visible. Due to the wide range of term energies for the fit resulting in the derived potential, this is not surprising. A similar trend in the residuals remained for the published potential, see Graph (c) in Figure 4.5. However, for the comparison with the heteronuclear dimer, a better reproduction of the energy spacing is desirable.

In order to achieve this, a fit was started. We consider the full potential but we allow adjustments of the inner-branch. This leads to a little altered phase of the wavefunction in the long range region and hence to a modified ladder of levels. The single parameter of the potential curve was freed for a least squares fit of the differences given in equation (4.13). By varying C (see equation (4.2)) (and the connection ensuring parameter A_1 and A_2) the residuals are reduced as shown in Graph (b) of Figure 4.14. We have to mention that in addition to C a second free parameter was included to the fit. This parameter shifts all measured absolute frequencies ν^i simultaneously. This pushes the residuum for $i = 0$ automatically to zero. Consequently, the absolute frequency measurement does not

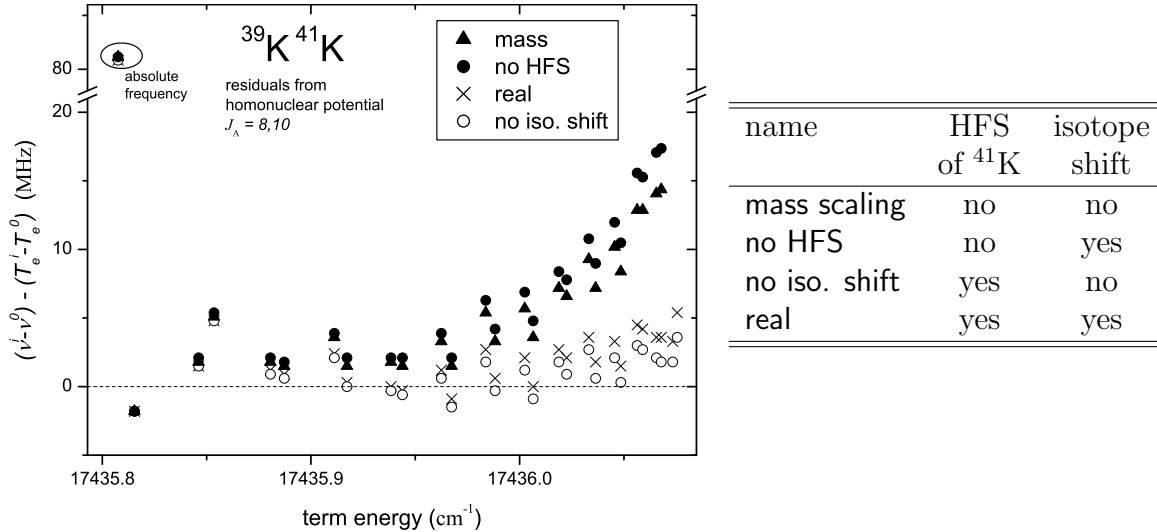| name	HFS of ^{41}K	isotope shift
mass scaling	no	no
no HFS	no	yes
no iso. shift	yes	no
real	yes	yes

Figure 4.15: *The four symbols show the differences between the observed and modeled energy spacing in the asymptotic region for different models. The initial potential curve is taken from the analysis of ^{39}K$_2$. To this, four different asymptotic behaviors are connected.*

influence the result of the fit any more (except for the newly introduced parameter, which remains well inside the interval of precision of the absolute frequency measurement).

Although C changes its sign during the fit (it is -13.939 instead of 1.495), the potential does not bend over within the needed interval of internuclear separations. No trend in the residuals is visible any more and the spread is within about ± 2 MHz, a reasonable number, considering the linearity of the laser scan and the reached signal-to-noise ratio in relation with the linewidth.

4.3.3.2   Scaling to the Heteronuclear Dimer

The adjusted potential energy curve is now used to calculate term energies ν^i of the heteronuclear dimer. As listed in Figure 4.15, four models are used to derive hyperfine potential energy curves:

- **mass scaling**: In this model the potential curves are the same as in the homonuclear case. The only difference is the reduced mass with which the term energies are calculated.

- **no HFS**: In the second model it is taken care of the isotope shift. The degeneracy of the asymptotic energies is removed, since asymptotes with the ^{41}K in the 4p state are shifted upwards and asymptotes with the ^{39}K in the 4p state are shifted downwards. The center of gravity of the isotopomer with the ^{41}K in the excited state is above the center of gravity with the ^{39}K in the excited state. This difference is the isotope shift of the D lines.

- **no iso. shift**: Here, it is taken care of the fact that the hyperfine structure of ^{41}K is smaller than for ^{39}K. However, the center of gravity of the combinations remains

the same as for ^{39}K$_2$.

- **real**: This model considers, both, isotope shift and different hyperfine structure at the same time. This represents the model we expect to give a correct description.

By keeping the center of gravity of the hyperfine structure it is ensured that the curves are the same at the inner region of the potential. The effect on the term energy of an altered potential energy curves integrates towards higher energies. The differences of the various models are bigger the higher the term energy is. The isotope shift of the D lines is distributed to equal parts to the 4s and 4p atom. Again, the center of gravity is kept for an alternation of the asymptotic energies. For smaller internuclear spacing, the curves overlap with those calculated in models neglecting the isotope shift. Therefore, the energy scales of the two isotopomers are adjusted relative to another such that the bottom of the A state is at the same energy. Furthermore, that means that the ground state asymptote (center of gravity of the hyperfine structure) of ^{39}K^{41}K is shifted to lower energy by half of the isotope shift of the D lines.

The different potential branches for ^{39}K^{41}K were constructed as for ^{39}K$_2$ as described in Section 4.1. Again, the residuals from equation (4.13) are plotted as a function of term energy. No parameter of the potential was adjusted except for the parameters that ensure proper connections. The energy spacing for the lower term energies, i.e., the low energy spacings are fairly well described with all four models. However, the models with the hyperfine structure of ^{39}K for both atoms (mass scaling and no HFS) are obviously not describing the observation to the asymptotes well. Moreover, the highest vibrational level in the fit was not supported by the potential curve. The two models with the correct hyperfine splitting (no iso. shift and real) are describing the data better, but a residual trend away from zero is remaining. The spread of the residuals is comparable to the one for the homonuclear dimer. The signal-to-noise ratio of the two compared spectra is similar. Both models describe the observed energy spacing already within few MHz.

Another observation may be done in Figure 4.15. The residuum for the reference energy $(\nu^0 + T_{\mathrm{X}}) - T_e^0$ is similar for all four models. They are within one MHz. In fact, we started the experimental observation in the region bound so deeply that the four models are not differing yet. Second, the observed term energy is above the calculated one. The observed term energy is the sum of the transition energy and the calculated term energy of the starting level T_{X}. In the calculation of T_{X} it is assumed that the two ground state curves of the two isotopomers are coinciding. As discussed above, we should correct the term energies by half of the isotope effect of the D lines to lower energies. This would reduce the four residuals. But, this may be taken only as an indication and not a confirmation of our reasoning due to the uncertainty of the laser frequency (100 MHz) and the quality of the ground state levels calculated from the Dunham series (50 MHz standard deviation).

4.3.3.3   Corrections to the Born-Oppenheimer Potential

The observed trend in the residuals of the energy spacing for the least bound levels is a signature for the fact that the potential of the heteronuclear dimer cannot be derived
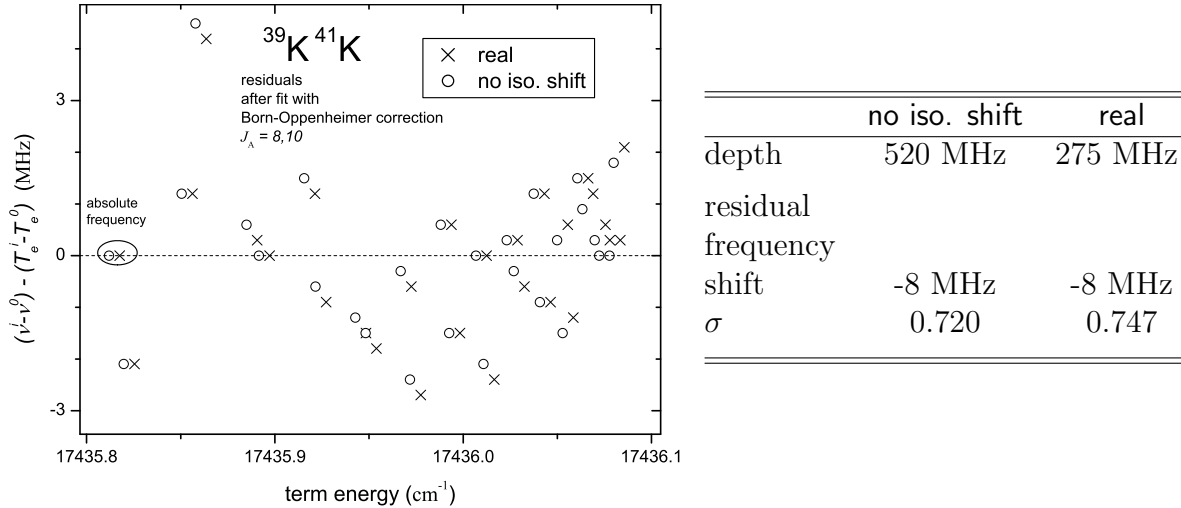
	no iso. shift	real
depth	520 MHz	275 MHz
residual frequency shift	-8 MHz	-8 MHz
σ	0.720	0.747

Figure 4.16: *Residuals of a fit with Born-Oppenheimer corrections to the potential for ^{39}K^{41}K. Two models were applied: with and without isotope shift (real and no iso. shift, see Figure 4.15). The listed values are the shift of the dissociation energy D, the difference of the shift of D and the absolute frequency calibration, and the σ values from the fit for an assumed uncertainty of 2 MHz for all relative line positions.*

completely from the potential of the homonuclear dimer. We need to correct the Born-Oppenheimer potentials. But we have observed that for scaling from one isotopomer to another the Born-Oppenheimer potentials reproduce energy spacing of asymptotic levels, which are in the order of 2 GHz, to within 4 MHz.

In a further step, we analyze how the correction may be applied. We have concentrated on asymptotic levels. In asymptotic methods, a simple approximation of the inner potential is usually done by starting the integration of the Schrödinger equation for the vibration outwards from a certain internuclear distance with a defined phase as a starting condition. Simple functional relations are used in fits to adjust the starting condition such that the inner part of the potential is well described. But in our analysis a full potential was used. We now perform another least-squares fit for the energy spacing of the heteronuclear molecule. In order to have a similar effect as in asymptotic methods, we allow to adjust the depth of the molecular potential. In principle, one would like to keep the asymptote and stretch the bottom of the potential. However, it is more simple to use the parameter for the dissociation energy D (see equation (4.3)) while keeping the bottom of the potential fixed. As in the fit for the homonuclear molecule, a further free parameter for the absolute frequency scale is used. Both parameters should be adjusted more or less similarly if we want to simulate an up- or downshift of the potential minimum while keeping the asymptotic energy fixed and hence the difference of the shift should be small.

Such a fit was undertaken with the two models for the hyperfine structure asymptotes that include the hyperfine structure of ^{41}K (no iso. shift and real). The residuals are shown in Figure 4.16. Both fits result in residuals spread around zero by about ± 2 MHz. No trends are visible in both cases. The applied change of the depth of the potential

are comparative. In conclusion, we cannot derive which of the two models describes the observations better. Therefore, we could not find a clear signature of the change-over from a resonant to detuned dipole-dipole character. In terms of asymptotic behavior at the first excited electronic asymptote, the heteronuclear character of ^{39}K^{41}K is hidden by the hyperfine structure.

4.3.3.4   Further Observations

Judging by the hyperfine free potential curves shown in Figure 4.11, it is disappointing that the change-over of the long range behavior from a homonuclear character $\sim R^{-3}$ to a heteronuclear dependence $\sim R^{-6}$ could not be observed. However, if we compare the adiabatic potential curves including hyperfine structure shown in Figure 4.17, the differences between the two compared models are only tiny. The two lowest asymptotes differ for these two models, i.e., the adiabatic potential curves are correlated to different combinations (see Figure 4.13) but the behavior in the relevant energy interval is almost unchanged. Simulations show that the difference of the two models no iso. shift and real results in level differences of at most 2 MHz (between $v = 226$ and 238), which is in the order of the scatter of our residuals. An experiment that distinguishes between dissociation channels in which ^{39}K is in the ground state from dissociation channels in which ^{41}K is in the ground state would allow to study the asymptotic structure under this aspect even more.

Some crossings of the relevant curves occur above the energy interval of investigated levels. However, this region just below and in between the asymptotes cannot be investigated thoroughly because the vibrational spacing allows only for one vibrational spacing in this region, as shown in Figure 4.18. The hyperfine structure leads to four groups of levels for $v_{\mathrm{A}} = 246$ and $v_{\mathrm{A}} = 247$, each corresponding to a specific I. The change-over of the potential energy curves is visible in $v_{\mathrm{A}} = 248$ and those components of $v_{\mathrm{A}} = 249$ that support an additional level. Overall, these are too few levels for a systematic study of this region.

Another observation is that the linewidth for all the asymptotic levels are about 8 MHz, i.e., for both heteronuclear ($J_{\mathrm{A}} = 2, 3, 4, 5, 8, 10$) and homonuclear ($J_{\mathrm{A}} = 8, 10$) down to binding energies of more than 1 GHz. This is evidence for a strong spin-orbit mixing between singlet and triplet since levels of a pure singlet asymptote have an expected lifetime of half the atomic lifetime, which would lead to linewidth of about 12 MHz. Other couplings might also increase the lifetime (hyperfine structure and retardation) but would show systematic trends over the covered energy interval because we see the variation of the hyperfine structure.

For the scans starting from $J_{\mathrm{X}} = 9$, the rotational doublets of both dimers (homonuclear and heteronuclear) does not show the relative intensity ratio one expects from the Hönl-London factors, namely 9:10. Instead, they are in the order of 2:3. This may be accounted to the fact that the Hönl-London factors are defined for Hund's case (a) and we are clearly not in this case any more, for the same reasons as the reduced linewidth discussed above.
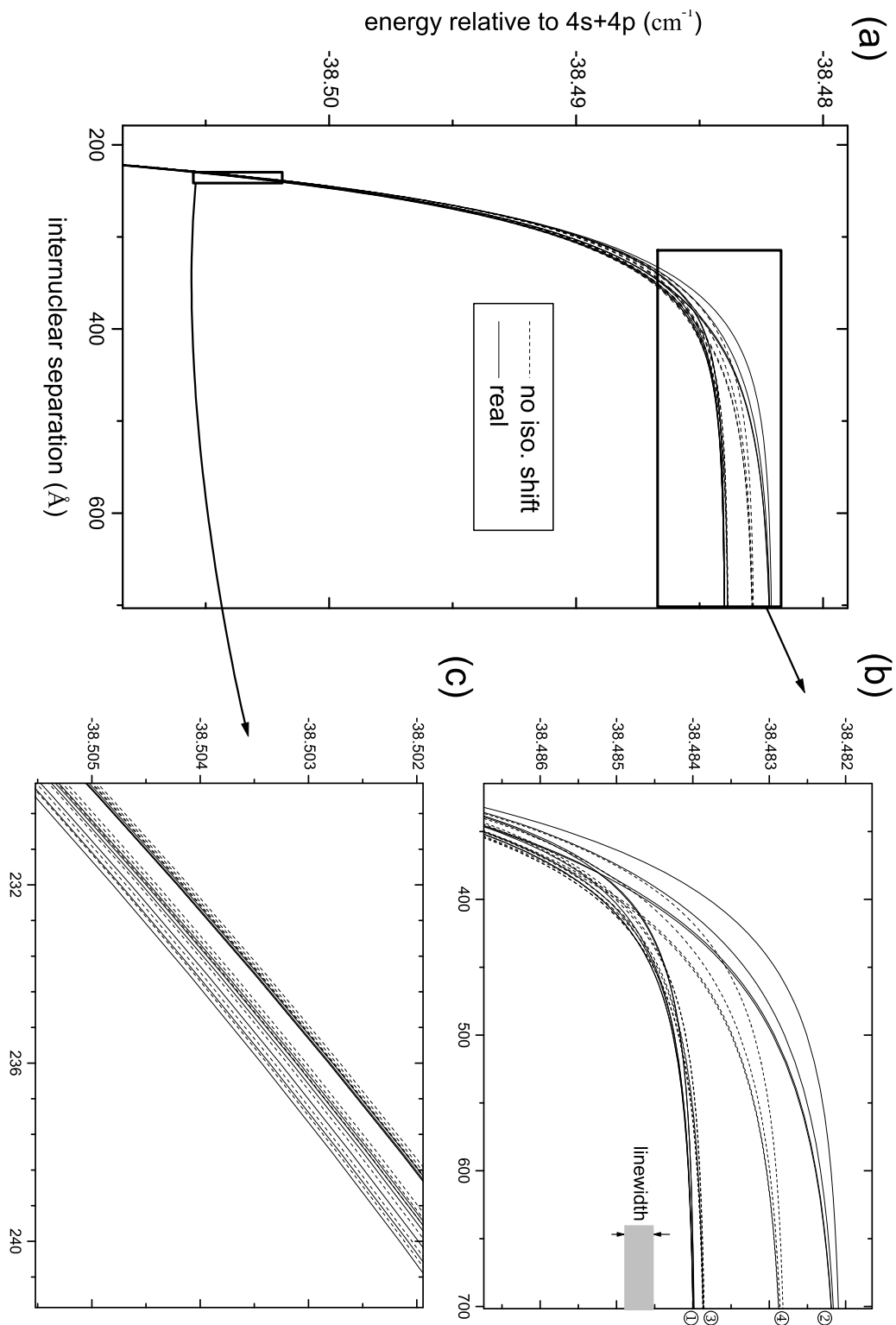
Figure 4.17: *Adiabatic hyperfine potential energy curves correlated to the A state. Two sets of ten curves are shown for the heteronuclear ^{39}K^{41}K. First, neglecting the isotope shift (*no iso. shift*), and, second, ^{39}K^{41}K considering the isotope shift of the D lines (*real*). The circled numbers in Graph (b) relate the asymptotes to the overview graph given in Figure 4.13.*
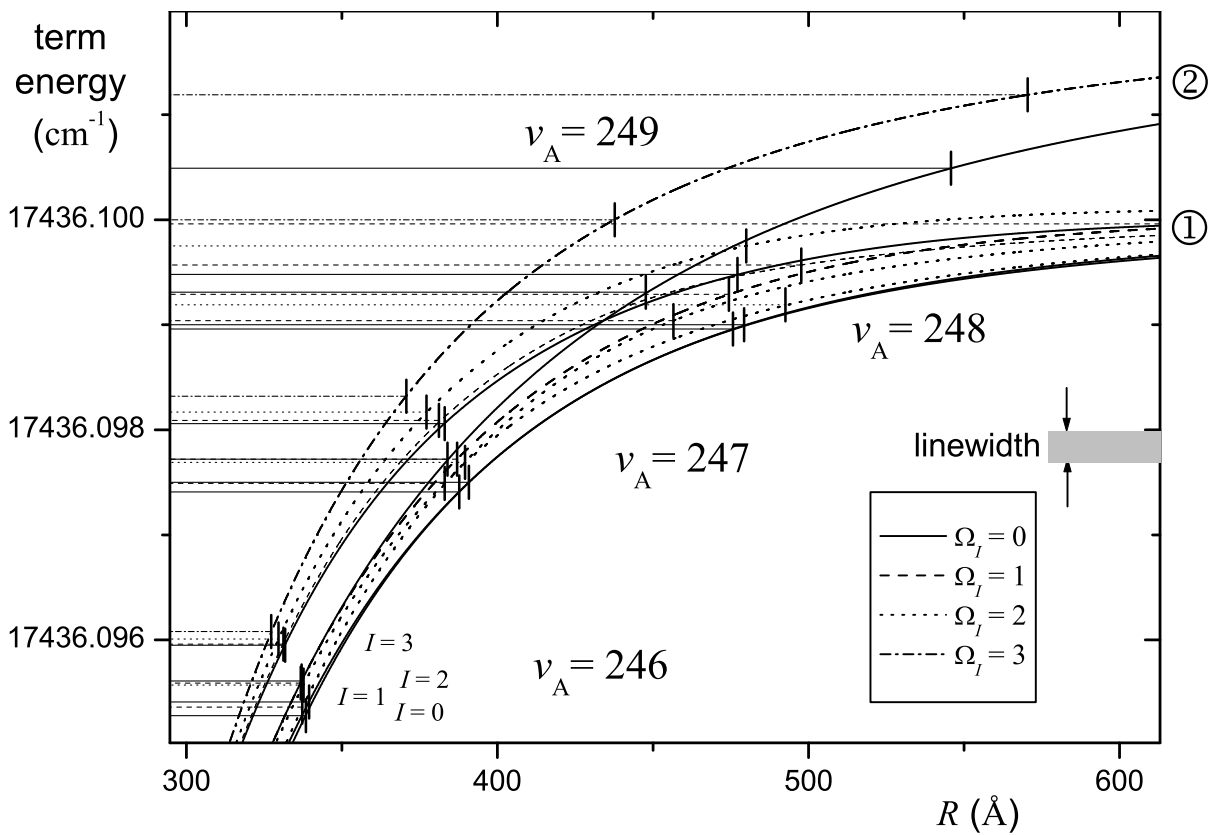
Figure 4.18: *The least bound levels of the heteronuclear dimer* ^{39}K^{41}K *calculated for* $J_A = 0$. *The energy curves go asymptotically either to* $4p_{1/2} (f = 1) + 4s_{1_2} (f = 1)$ *indicated by* ① *or* $4p_{1/2} (f = 2) + 4s_{1/2} (f = 1)$ *indicated by* ②.

4.3.4   Conclusion

We compared the A states of two potassium isotopomers close to the dissociation energy. We have studied the Born-Oppenheimer approximation. The need of considering the correct hyperfine structure became evident. However, the adiabatic potential curves cannot fully describe the observations. Corrections to the Born-Oppenheimer potentials were applied and the observations are modeled. The direction and amount of the correction is similar as for the atomic D lines: The depth of the potential is increased by about the isotope shift between ^{39}K and ^{41}K of the D lines.

It was not possible to observe the change-over from a resonant to a detuned dipole-dipole interaction due to the hyperfine structure hiding this effect. An experimental attempt to reveal this needs to measure energy spacing better than the expected differences between the models, i.e., better than 2 MHz. This is possible with better scanning properties of the laser, absolute frequency measurements with a frequency comb, or an additional stabilized laser with which beat signals may be recorded.

4.4   Towards Investigations of the 4s+4s Asymptote

The spectroscopy of the A $^1\Sigma_u^+$ reported above opens the door for spectroscopic studies of the ground state asymptote. In case of sodium corresponding studies allow for precise description of cold collisions by scattering lengths and Feshbach resonances.[5] Beam experiments are well adjusted for easy application of multi-laser pump schemes and good resolution. In comparison with trap experiments, the energy interval that can be covered is bigger. Lasers allow for easy tuning. In traps, one is limited by the low rotational quantum number and the need for strong magnetic fields, which are used for tuning scattering states with respect to Feshbach resonance states. Those lead to trap loss which is the experimental signal. The calibration of the magnetic field strength can be done with the ultracold atoms and thus the position of Feshbach resonances can be measured very precisely. An alternative method for trap experiments is the application of photoassociation. Here, not only the excited state may be tested, but also the wavefunction of scattering states in the trap can be tested and properties of cold collisions interfered.[98,6] Measurements in traps of the scattering length by thermalization rates or Bragg spectroscopy[99] typically have big error bars.

The unique opportunity of spectroscopy on molecular beams is the possibility to connect conventional spectroscopy to measurements from cold atoms. The knowledge of full potential is essential if cold atoms should be transferred to deeply bound dimers, a goal followed with big interest, especially in case of heteronuclear dimers. The ground state of potassium is already well described up to close to the dissociation limit. The remaining gap may be closed in a three-laser experiment, to which the study of the A state has been essential.

The experiment is corresponding to that, which was performed with sodium and led to precise models of cold collision.[5] In principle, an additional laser has to be included that drives transitions that the molecules from laser prepared levels of the A state are decaying over (see Figure 4.1.) In more detail: the Franck-Condon pumping step must be kept. The laser for the spectroscopy of the A state should now be stabilized such

that it drives a transition to the A state. An offset stabilization like that used for the first laser is appropriate (see also Section 2.2.4). Now, a third laser must be overlapped with the second laser and scan and drive transitions from the prepared A state level down to asymptotic levels at the ground state asymptotes. The experimental signature is a decrease of the fluorescence, which is induced by the second laser, if the third laser is in resonance with a transition from the excited level and an asymptotic level of the ground state. It thus reduces the spontaneous decay from this level, i.e., the laser induced fluorescence is smaller if the third laser hits a resonance. An experimental issue of this experiment is the suppression of the scattered light of the two laser of this lambda-like pumping scheme. The additional laser is red detuned to the D_1 line of potassium, therefore another Ti:sapphire laser is a good choice. The Franck-Condon pump laser, which was a Ti:sapphire laser in the experiments described above, may be replaced by a diode laser. The Franck-Condon factors allow to saturate this transition even with lower powers, which are typically available from diode lasers. The A state is wider than the ground states and the intermediate level of the lambda scheme is far below the asymptotic levels the preceding section was discussing, which allows for a lower v_A in the preparation step and thus a bigger Franck-Condon factor.

The strength of the observed fluorescence should allow to study the two most abundant isotopomers. This should allow for an even more interesting study of the Born-Oppenheimer approximation and mass-scaling of properties of cold collisions. By measuring the asymptotic structure for the two isotope combinations of ^{39}K with ^{39}K and ^{41}K independently, a direct comparison of them is possible and the precision of the mass-scaling for cold collisions can be determined. Both scattering lengths can be measured and their values could be compared to those obtained from mass-scaling.

The potentials are of shorter range than the one of the A state due to the van der Waals interaction dominating at long range. In order to select a good level of the A state, which serves as a transfer state to the ground state asymptote, one has to select a level that has a good Franck-Condon overlap with the ground state levels, i.e., a level with a similar classical outer turning point should be selected. In Table 4.8, we suggest vibrational bands for the Franck-Condon pumping and the second laser for ^{39}K$_2$. The Franck-Condon pumped level $v_A = 22$ decays to 20% to $v_X = 39$ and 40 respectively.

turning point (Å)	V_X (cm^{-1})	T_A (cm^{-1})	second laser		first laser	
			P(9)	(cm^{-1})	R(9)	(cm^{-1})
14	-2.85	12 810.91	143←39	14176.802	22←0	12 440.521
15	-1.84	12 842.23	147←40	14147.452	22←0	12 440.521
16	-1.22	12 874.85	152←40	14180.069	22←0	12 440.521
18	-0.58	12 910.13	159←40	14215.353	22←0	12 440.521
20	-0.30	12 938.51	167←40	14243.729	22←0	12 440.521
22	-0.17	12 948.89	171←40	14254.112	22←0	12 440.521
24	-0.10	12 957.24	175←40	14262.463	22←0	12 440.521

Table 4.8: *Optical pumping schemes to reach the ground state asymptote of ^{39}K$_2$. For each classical outer turning point, the potential energy of the ground state is given, calculated from the long-range parameters published by Amiot et al.[67] The term energy of an unperturbed vibrational level of the A state with similar turning point is given (for $J_A = 8$). The reference energy for these two energies is the center of gravity of the ground state asymptote. Moreover, the vibrational bands for the two preparation lasers are given. The listed transition frequencies were measured in our study of the A state. They are pumping the R(9) line for the first laser, which drives the Franck-Condon pumping, and P(9) for the second laser. The third laser should scan around $T_A + V_X$.*

Chapter 5

Manipulation of Cold Collisions with Laser Light

In the preceding chapter experiments were suggested for the investigation of cold collisions of potassium atoms. Similar experiments on binary sodium collisions already investigated the energy regime of cold collisions. The scattering length and the positions and widths of Feshbach resonances can be calculated from the two diabatic ground state potential curves for the X $^1\Sigma_g^+$ and the a $^3\Sigma_u^+$ state and the atomic hyperfine structure and magnetic moments.[5] Hence, it is known how the scattering properties behave in magnetic fields.[100] An alternative methods is to manipulate cold collisions with laser light. Models have been developed for this technique, in which long range levels of electronically excited states are coupled to scattering states at the ground state asymptote. The level of the excited state acts like a Feshbach resonance state and is therefore often referred to as optical Feshbach resonance.

An optical coupling between asymptotic levels of the A $^1\Sigma_u^+$ state below the 3s + 3p asymptote and scattering states at the 3s + 3d asymptote was investigated in a preceding study.[101] The results were quantitatively modeled in a coupled-channel analysis using a method for the determination of eigenenergies of the optically coupled system. Light shift of asymptotic levels of the A $^1\Sigma_u^+$ state was induced by coupling to the continuum above the 3s + 3d asymptote via a laser. The effective asymptote of the A state was altered so much that vibrational levels were removed. In the picture of scattering atoms, this corresponds to an alteration of the scattering length across a pole. The simulation of the observed light shift agreed qualitatively and quantitatively with the experiments.

It is, however, more interesting to investigate possibilities of light induced manipulation at the ground state asymptote, i.e., the manipulation of cold collisions of two ground state atoms because this is the scattering appearing in trap experiments. Prior to the work of this thesis, experiments were performed for a systematic study of the relevant coupling.[102, 101] The influence of laser induced coupling to levels at the ground state asymptote 3s + 3s on long range molecular level of the A state was investigated in a Doppler-free spectroscopic experiment of the coupled A state levels. Like in the preceding study, a molecular beam apparatus was used to record line profiles under several settings of the laser light inducing the coupling.

We introduce the experiment, the adapted model, and the comparison of simulation

and experimental recordings in a form of an article in the following (Section 5.1). Thereafter, additional comments and considerations are given.

5.1 Laser-induced Manipulation of Atom Pair Interaction of Two Ground State Sodium Atoms

St. Falke[a], Chr. Samuelis, H. Knöckel, and E. Tiemann[b]

Institut für Quantenoptik, Universität Hannover, Welfengarten 1, 30167 Hannover, Germany

Abstract: We investigate the influence of a laser field, which is red-detuned to the atomic sodium $3^2S_{1/2} \rightarrow 3^2P_{1/2}$ transition, on levels of the $A^1\Sigma_u^+$ state of Na_2. These levels are coupled by the laser field to the last bound levels and resonance states of the electronic ground states of Na_2. Laser-induced line shifts and line broadening are observed on Doppler-free transitions in a molecular beam experiment. Our experiment is an inverted two-laser photoassociation experiment. We model lines shapes using a theory based on multichannel quantum defect theory and describe to which extend this model can be applied quantitatively.

PACS numbers	34.50.Rk	Laser-modified scattering and reactions
	33.80.-b	Photon interactions with molecules
	42.62.Fi	Laser spectroscopy

[a]falke@iqo.uni-hannover.de
[b]tiemann@iqo.uni-hannover.de

5.1.1 Introduction

The application of manipulating cold collisions by magnetic fields has enhanced the fast progress in cooling and trapping of atoms and transfer into molecules.[103,104,105,106,107,108,109] Often, the description of ultracold collisions is given by a single parameter, the s-wave scattering length a_s, which is derived from the scattering wave function at vanishing collisional energy. It has been shown[110,111,5] that this important physical quantity can be derived from spectroscopy of the vibrational levels and resonance structures around the atomic asymptotes. The scattering length can even be determined by asymptotic methods if the complete interaction potential is not known.[90] Such methods are also sufficient for the description of the variation of scattering length with an external magnetic field.[112,113]

The quest for quantitative recipes for the manipulation of cold collisions by external light fields arises for several reasons. First, magnetic fields cannot be used for some atoms due to unlucky positions of Feshbach resonances or due to the absence of hyperfine structure and thus the lack of Feshbach resonances. Examples are optical clock candidates like calcium[114] or strontium[115] and metastable helium.[116] Second, laser fields could be applied locally, e.g., on a few grid points of an optical lattice[117] without effecting other atoms of the cold ensemble. In contrast, magnetic fields and optical lattices, which can be applied to alter the effective mass of the atoms,[118] effect the entire ensemble simultaneously and equally. Third, the interaction can be tuned in very short times. Moreover, with the

laser frequency and intensity two parameters are available for the external control of the interaction of the binary collision. Also, the induced effect of the laser field depends on its polarization.

The proposal of applying near-resonant laser fields to control the interaction strength of two atoms has been discussed already in several studies.[10, 119, 120] First experiments with ultra-cold ensembles have been performed.[121] In this photoassociation experiment a vibrational level of an electronically exited molecular state is coupled to the ground state asymptote. This level can then be considered as an optically induced Feshbach resonance. Another experiment focuses on the direct measurement of such a laser-induced change of the scattering length by Bragg spectroscopy.[99, 122] It was, to our knowledge, the first time the laser-induced change of the scattering length was observed in a cold ensemble directly. A theoretical approach was used to obtain a parameterized analytical formula for the observation. The coupling strengths are represented by parameters but the observed magnitude of the effect is not compared to values one could derive from known coupling strength and applied field intensities.

In this work, we start from bound molecules instead of starting from an ultra-cold ensemble or a Bose-Einstein condensate. Thus, we approach the coupling of interest, i.e., the ground state continuum to a bound level of an electronically excited molecular state, from the opposite side. Two atoms of the collision of interest are deeply bound. We are investigating exemplarily the atom-pair influence of sodium.

This article is organized as follows. First, an outline of our experimental setup and the excitation scheme is given (Section 5.1.2). In the following Section 5.1.3 we introduce our line-profile simulation and its utilization in fits to recordings from our experiment. We conclude by relating our results to the range of light manipulated ultracold collisions in Section 5.1.6. Additional, we present in the appendix how molecular dipole coupling strength can be computed.

5.1.2 Experiment

The bound atom pairs, i.e., Na_2 dimers, are produced and investigated using a molecular beam apparatus. It has been described in preceding articles.[69, 101] Only the two lowest vibrational levels of the X $^1\Sigma_g^+$ state are thermally populated. The rotational levels with the highest population are $J_X \approx 10$. For our experiment the second molecular state of interest is the electronically exited A $^1\Sigma_u^+$ state. The rotation, denoted by J respectively l, changes by one for each dipole transition between these states, regardless whether laser-driven or spontaneous because of selection rules for Σ–Σ transitions.

We start with molecules in the lowest vibrational level of the X $^1\Sigma_g^+$ state with an even $J_X = 0,2,4$ because from these levels one can access $l = 0$ levels, i.e., scattering states of s-wave collisions. The transfer between the start and the asymptotic ground state levels was a double lambda scheme (see Figure 5.1). The first lambda scheme increases the vibrational quantum number of the ground state. This preparation step is referred to as Franck-Condon pumping. The molecules are excited by a laser excited molecules populated few vibrational ground state levels according to Franck-Condon factors. Starting from one of the prepared level, a lambda scheme towards the ground state asymptotes is possible with two additional lasers.[5] A direct transfer without a preparation step is
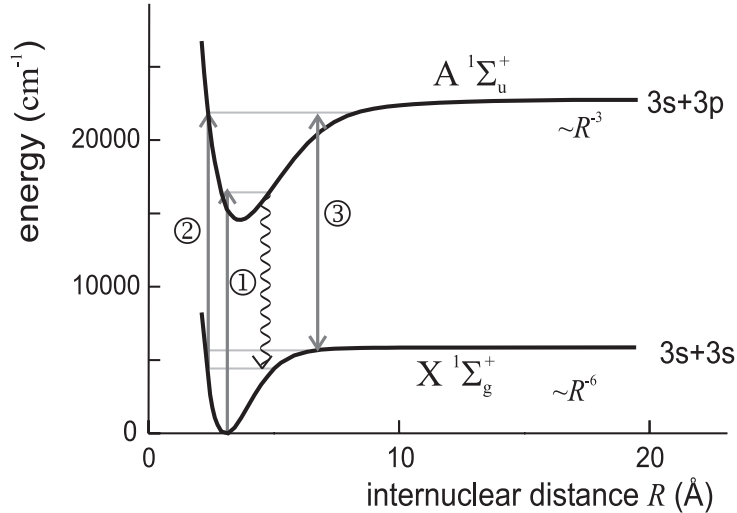
Figure 5.1: *Simplified potential scheme of* Na$_2$. *The three lasers are indicated by* ① *for the preparation laser,* ② *for the scanning laser, and* ③ *for the coupling laser.*

impossible due to the lack of levels of excited states that have a good Franck-Condon factor with, both, the start levels and ground state asymptote levels.

The preparation of the molecules is done with a first laser (laser ① in Figure 5.1), a dye laser (sulforhodamine b) operating at about 615 nm, which pumps molecules to the A state level $v_A = 15$, $J_A = 1$ or 3. An overview of the optical setup of all applied lasers is given in Figure 5.2. Guided by Franck-Condon factors, some vibrational levels of X state with $J_X = 0,2$ or 2,4 are populated predominantly. In the ground state, only molecules with an even total nuclear spin I are allowed for even quantum of rotation J. Therefore we have to consider molecules with $I = 0,2$ only. The laser for the preparation step is stabilized on the maximal laser induced fluorescence. Its light is not polarized. Due to this and the traveling time of about 350 μ s to the second interaction zone, we can assume that we have an un-polarized ensemble of molecules in the $v_X = 29$, $J_X = 0,2$ level with an equal ratio in each nuclear state $|I,M_I\rangle$, with M_I being the projection of I into the lab frame. Six nuclear wavefunctions are involved: $|0,0\rangle$, $|2,-2\rangle$, $|2,-1\rangle$,... $|2,2\rangle$.

This ensemble is entering a second interaction zone, which is spatially separated by 0.35 m from the first zone. Here, two laser fields are applied. Again, the two involved molecular states are the X state and the A state (see Figure 5.1). The test laser (see ② in Figures 5.1 and 5.2), a dye laser at 535 nm operating with coumarin 6, induces transitions from one of the ground state levels, $v_X = 29$, $J_X = 0, 2$ to $v_A = 120,139$, $J_A = 1$. The molecular fluorescence originating from the crossing point of the laser beam with the molecular beam is imaged via a lens system onto a photomultiplier. Color glass filters are used to suppress stray laser light to avoid a background signal. While scanning the laser in frequency, we record the transmission of a temperature stabilized Fabry-Perot interferometer to obtain a marker trace for the determination of a frequency axis.

Typically, the lines observed by scanning the laser across the resonance show an almost perfect Lorentzian profile. The Doppler broadening due to the residual divergence of the
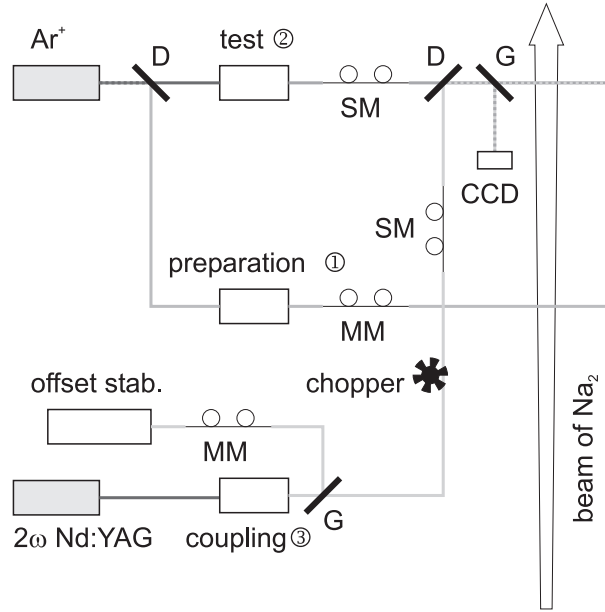
Figure 5.2: *Optical experimental setup.* G*: glass plate,* D*: dichroic beam splitter,* MM*: multi mode fiber,* SM*: single mode fiber.*

molecular beam is with 8 MHz below the natural linewidth of about 20 MHz. The lines are slightly power broadened. No hyperfine structure could be resolved for these levels. However, these levels have a significant triplet contribution and the symmetry of the molecular state usually is described in Hund's case (c) by 0_u^+ instead of using the case (a) notation $^1\Sigma_u^+$.

The third involved laser is responsible for the optical coupling we are interested in (coupling laser, see ③ in Figures 5.1 and 5.2). It is a dye laser operated with rodamin 6G around 592 nm. We use an offset stabilization with a transfer cavity (free spectral range 150 MHz) to achieve long term frequency stability. In this setup an iodine stabilized HeNe laser beam is modulated with an AOM in double pass enabling us to stabilize a laser on an arbitrary frequency.

The third laser beam is applied in the second interaction zone, too. It is overlapped with the beam of the test laser by a dichroic beam splitter. Both beams are focused onto the molecular beam to obtain high field intensities. The waists are about 100 μm and measured by a CCD camera, to which a small fraction of the power is sent with a glass plate. The camera with a pixel size of 23 μm $\times$ 27 μm is located at the same distance from this glass plate as the molecular beam. The measurement of the beam sizes and the laser power (measured by Coherent Fieldmaster) is needed for the determination of the field strengths. Typically, the relative intensities of related measurements is known better because the waist of the laser beams remain unchanged.

The coupling laser is chopped mechanically. The chopper triggers a lock-in switch that divides the photomultiplier signal into two traces: By adjusting the phase correctly these two traces correspond to (a) the situation without the coupling laser field and (b) to the coupling laser field switched on. These two spectra are recorded simultaneously.

level	position line width in cm^{-1}	in MHz
$v_X = 64$, $\ell = 0$, $I \approx 0$	$-0.3744(9)$	—
$v_X = 64$, $\ell = 0$, $I \approx 2$	$-0.3696(9)$	—
$v_X = 64$, $\ell = 2$, $I \approx 0$	$-0.3227(9)$	—
$v_X = 64$, $\ell = 2$, $I \approx 2$	$-0.3177(9)$	—
$v_X = 65$, $\ell = 0$, $I \approx 0$	$-0.0131(7)$	—
$v_X = 65$, $\ell = 0$, $I \approx 2$	$-0.0106(7)$	—
$f_A = 1$, $f_B = 1$ asymptote	0.0 (reference)	
shape res. $\ell = 2$, $I \approx 0, 2$	$+0.0024(9)$	80
Feshbach res. $\ell = 0$, $I \approx 0, 2$	$+0.0416(9)$	185
$f_A = 1$, $f_B = 2$ asymptote	$+0.0591$	
Feshbach res. $\ell = 0$, $I \approx 0, 2$	$+0.0584(9)$	96
$f_A = 2$, $f_B = 2$ asymptote	$+0.1182$	

Table 5.1: *Levels and resonance at the ground state asymptote.*[25]

For the experiments, first the laser for the Franck-Condon pumping is locked to a selected transition. Second, the test laser is tuned to the maximal fluorescence. Third, the coupling laser is tuned such that the fluorescence induced by the test laser is reduced as much as possible. This is assumed to be the resonance condition for the coupling transition. At this frequency it is locked to the HeNe stabilized transfer cavity. Fourth, the test laser is scanned across the line to obtain the line profiles we are interested in. The parameter of the coupling laser is altered between scans. Either by attenuating the power or detune it from resonance by altering the frequency of the AOM that shifts the frequency of the HeNe laser for the offset stabilization. Typically, we record for each setting of conditions of the coupling laser several scans that are overlapped by the marker cavity peaks and then averaged.

We investigate the coupling of four asymptotic ground state levels to A state levels. The $v_X = 64$, $\ell = 0$ level is optically coupled to the $v_A = 120$, $J_A = 1$ level. The last bound level, i.e., $v_X = 65$, $\ell = 0$ is coupled to $v_A = 139$, $J_A = 1$. Also, we couple the lowest shape resonance with $\ell = 0$ and a Feshbach resonance with $\ell = 0$ to that particular A state level. For details of levels at the ground state asymptotes see Table 5.1.

The simplest model for an optical coupling like we are investigating involves three states. First, a start state, in which the objects are initially in. A second state that is tested and coupled by a laser field to a third state. If the coupling laser is in resonance with the transition between the second and the third state, one expects the line in the spectra to split into two lines symmetrically around the position of the line in the un-coupled situation. The distance of the splitting corresponds to the coupling strength induced by the coupling laser. If the coupling laser is detuned, the splitting gets asymmetric for, both, position and intensity of the two lines. However, detuning the coupling laser
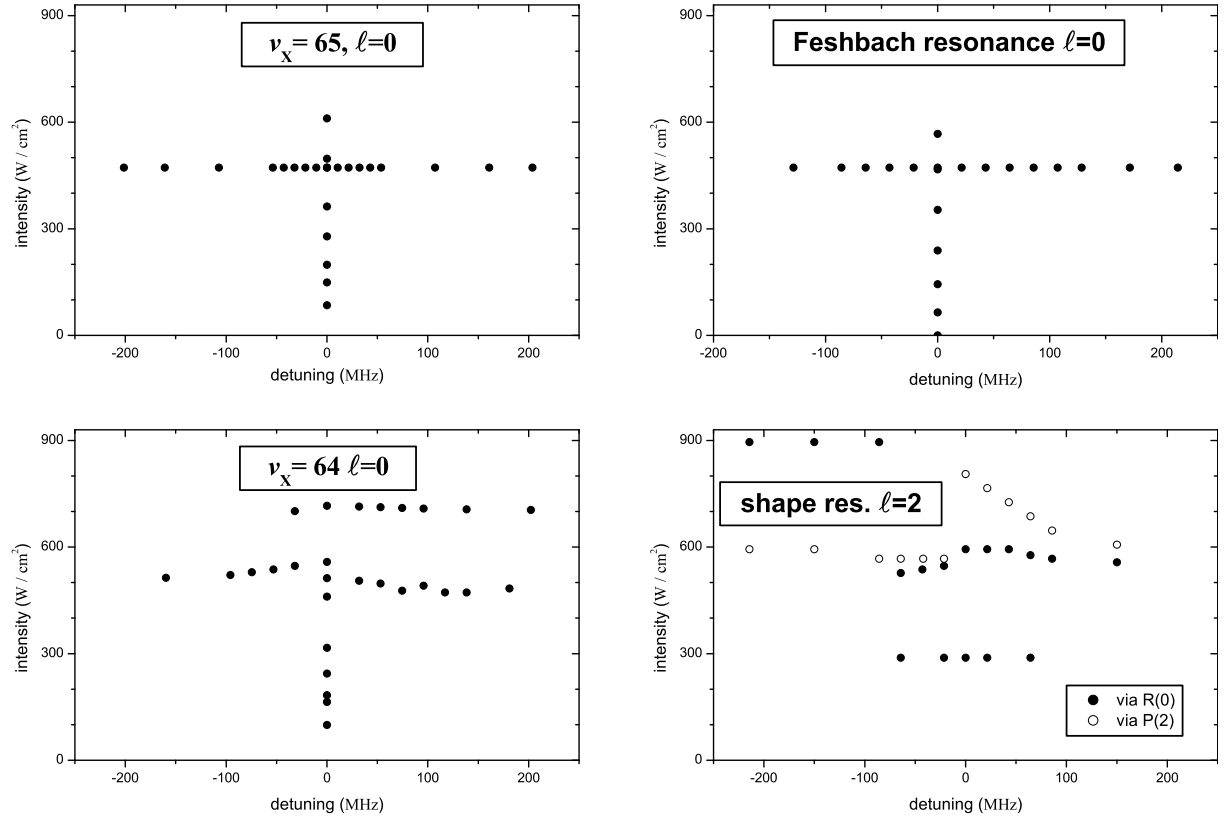
Figure 5.3: *Field of observations. For each of the four asymptotic levels or resonances of the ground state we show the applied parameters of the coupling laser. Each point indicates an experimentally recorded and analyzed spectrum. The axes give the parameters of the coupling laser.*
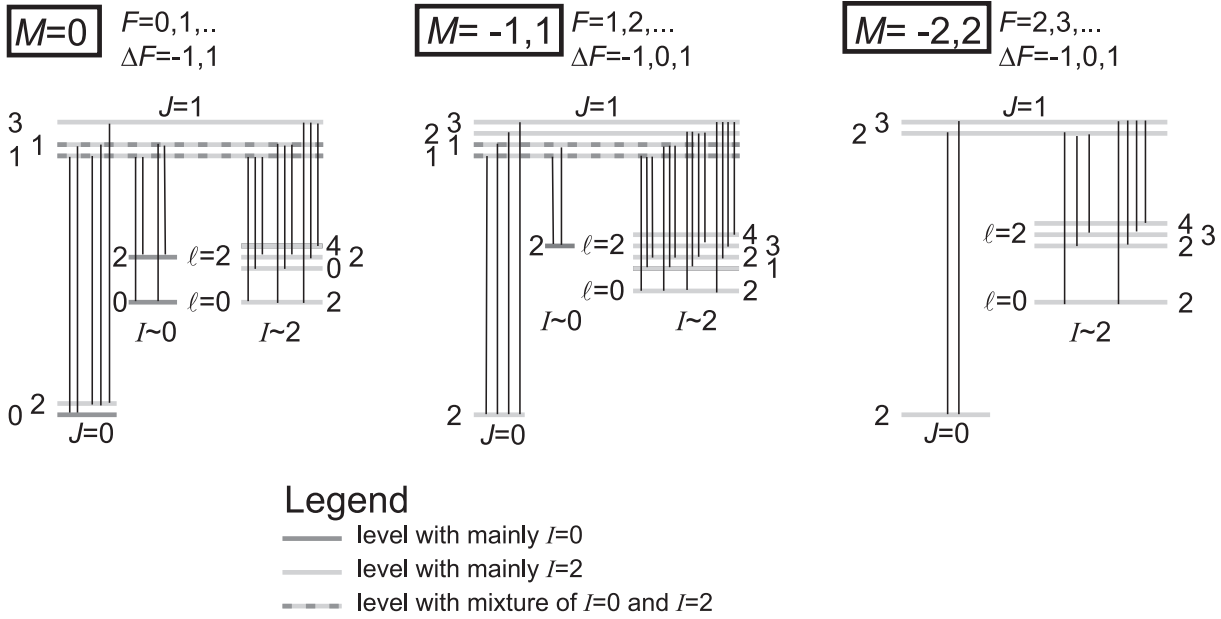
Figure 5.4: *Coupling Schemes. For the simulation we consider five separate coupling systems. Systems with positive and negative M are distinguished only by a sign change of coupling strength for couplings between levels with the same F. The un-labeled numbers indicate F for each level. Energies are not to scale.*

in opposite direction will lead to the same line profile but mirrored at the position of the unperturbed line. This is called Autler-Townes splitting. In this experiment, the line profiles show much more structure, but qualitatively the same behavior as the two Autler-Townes components in the simple three-state model.

An overview of the couplings we were applying and recording in the spectroscopic experiment is given in Figure 5.3. For each of the four couplings a plot is given where each recording is represented by a point with detuning and intensity of the coupling laser as coordinates.

5.1.3 Lineshape Simulation

In order to investigate the coupling, we need to model the observed lineshapes. Before doing so, we start with some general considerations. The power broadening of the observed lines is only a factor of about five smaller than the observed line splitting induced by the coupling laser. Therefore, one has to include the test laser in the modeling of line profiles.

A second important point is the polarization of the laser fields. We assume that an unpolarized ensemble of molecules enters the second interaction zone and can hence neglect from now on the laser for the preparation via Franck-Condon pumping. This laser field is un-polarized at the molecular beam after a fiber connection. The two laser fields we need to consider are linearly polarized with a parallel polarization axis. This axis defines our lab frame. Any molecule with a projection of the total angular momentum F on the lab frame axis M will therefore keep this projection during the complete interaction with

the two laser fields, at least until it decays spontaneously. Consequently, the involved molecular levels may be grouped by M. Since spontaneous decay removes the molecule from the levels coupled by the lasers it is a good approximation to model the different M-systems individually. The different coupling schemes are depicted in Figure 5.4. The only good quantum numbers for all molecular levels involved are F, its projection M, and the inversion symmetry denoted by $\pm$. However, we take rotational wavefunction from Hund's coupling case (a) as a basis to describe the molecular level as a linear combination. With such wavefunctions, the coupling strength may be computed as elaborated in Appendix A. We start from levels with $J = 0$, thus F is equal to I. For asymptotic levels, the hyperfine structure admixes to a level with I contributions with $I+1$ and $I-1$ but the two manifolds $I \sim 0$ and $I \sim 2$ remain separate. For $\ell = 0$, the equality $F = I$ is again valid but for $\ell = 2$ and $I = 2$ these two momenta can be coupled to any F between 0 and 4. The coupling schemes depicted in Figure 5.4 reflect that $|M|$ has got to be smaller than F and the selection rules $\Delta F = -1, 1$ for $M = 0$ and $\Delta F = -1, 0, 1$ for other values of M.

The lambda scheme that we apply with the two lasers corresponds to an inverted two-color photoassociation[121] operating in the singlet manifold. A method describing spectra in photoassociation processes is the multichannel quantum defect theory (MCQD).[123, 119] Moreover, it is developed how to take parameters for lasers (power and detuning) and the trap (temperature) as main input to simulate experimental recordings such as trap loss or ionization spectra.[124]

Three major differences to the intended utilization of this approach need to be pointed out: First, we start from a deeply bound molecular level and not from continuum states. We do not need to consider a thermal distribution over continuum states. But we artificially adapt the model suited for collisions to simulate the breaking of a compound, namely the dimer breaking into two atoms sometimes called half collision. Second, in MCQD theory molecular levels are considered. The reflection approximation introduces the interaction potentials for the determination of the coupling strengths between the involved levels, i.e., for the determination of Condon points. In our case, we know the wavefunctions of the involved levels from coupled channel calculations based on experimentally obtained interaction potentials.[125] Along with R-dependent dipole transition moments,[126, 127] this knowledge allows us to compute coupling strengths (see Appendix A). We do not use the reflection approximation. Third, the original intention was to determine analytical lineshape formulas. Due to high dimension of our coupling schemes (see Figure 5.4), we determine the fluorescence based on the parameters, detuning and power of both lasers (test and coupling), numerically.

As discussed earlier, we consider five coupling schemes, one for each possible M. For $M = 0$ we have to consider two start levels for $v_X = 29$, $J_X = 0$, i.e., $F = 0$ and 2. These are almost degenerate are due to the tiny hyperfine interaction for singlet states. We denote the number of start levels by q_M with $q_0 = 2$ and $q_{\pm 1} = q_{\pm 2} = 1$. Due to the degeneracy and the un-polarized beam source, we consider the six start levels equally populated: $\rho(M, i) = 1/6$.

For each coupling scheme, the scattering matrix S is set up. Its elements $S_{i,j}$ represents the inelastic scattering of a molecule in the selected start level i (called incoming channel in scattering theory) to a channel that represents an atom pair (bound or free) that was created via spontaneous decay of the A state level labeled by j. Every molecule in

these open outgoing channels corresponds to one spontaneously emitted photon, which is detected as signal. The scattering matrix S is computed from the reaction matrix K. In the case of a single start level ($q_M = 1$) it looks like as follows (the lines are only to guide the eye, empty elements are zero):

$$
K = \left(\begin{array}{c|c} K^{\mathrm{oo}} & K^{\mathrm{oc}} \\ \hline K^{\mathrm{co}} & K^{\mathrm{cc}} \end{array} \right) =
\left(\begin{array}{ccc|cc}
\multicolumn{3}{c|}{\begin{array}{ccc} v_{\mathrm{X}}=29 \ \ \mathbf{LIF} & & \begin{array}{c}\text{free}\\ \text{atom pairs}\end{array} \end{array}} & \multicolumn{2}{c}{\begin{array}{cc} v_{\mathrm{A}}=120,139 & v_{\mathrm{X}}=64,65 \end{array}} \\
\hline
 & & & \Gamma_{11} \cdots \Gamma_{1n} & \\
 & & & \gamma \ \ \ddots & \\
 & & & \ \ \ \ \ \gamma & \\
 & & & & \alpha \ \ \ \ddots \\
 & & & & \ \ \ \ \ \alpha \\
\hline
\Gamma_{11} \ \gamma & & & \Omega_{11} \cdots \Omega_{m1} & \\
\vdots \ \ \ \ddots & & & \vdots \ \ \ \ \vdots & \\
\Gamma_{1n} \ \ \ \ \gamma & & & \Omega_{1n} \cdots \Omega_{mn} & \\
 & \alpha & & \Omega_{11} \cdots \Omega_{1n} & \\
 & \ddots & & \vdots \ \ \ \ \vdots & \\
 & & \alpha & \Omega_{m1} \cdots \Omega_{mn} &
\end{array} \right)
\tag{5.1}
$$

The number of levels in the coupling scheme for the A state and the asymptotic region are n and m. This matrix corresponds to the matrix in equation (2.19) of the underlying theoretical paper.[124] The natural linewidth for the vibrational A state level v_{A} is $2\bar{v}_{v_{\mathrm{A}}}^{A}\gamma^2$. This definition of γ ensures the correct linewidth in simulation of spectra. If the coupling laser couples to a resonance state, the dissociation lifetime of that resonance can be taken into account by α, which is set to zero for bound states (see Table 5.1).

The reduced K-matrix is defined as

$$
K^{\mathrm{red}} = K^{\mathrm{oo}} - K^{\mathrm{oc}} \times \mathrm{inv}\left(\tan\nu + K^{\mathrm{cc}}\right) \times K^{\mathrm{co}}
\tag{5.2}
$$

with the diagonal quantum defect matrix

$$
\tan\nu = \left(\begin{array}{cc}
\multicolumn{2}{c}{\begin{array}{cc} v_{\mathrm{A}}=120,139 & v_{\mathrm{X}}=64,65 \end{array}} \\
\hline
\dfrac{\delta_1}{\bar{v}_{v_{\mathrm{A}}}^{\mathrm{A}}} & \\
\ \ \ \ \ddots & \\
\ \ \ \ \ \ \dfrac{\delta_n}{\bar{v}_{v_{\mathrm{A}}}^{\mathrm{A}}} & \\
\ \ \ \ \ \ \ \ \ \ \dfrac{\Delta_1}{\bar{v}_{v_{\mathrm{X}}}^{\mathrm{X}}} \\
\ \ \ \ \ \ \ \ \ \ \ \ \ \ddots \\
\ \ \ \ \ \ \ \ \ \ \ \ \ \ \ \ \dfrac{\Delta_m}{\bar{v}_{v_{\mathrm{X}}}^{\mathrm{X}}}
\end{array} \right)
\tag{5.3}
$$

Equation (5.2) corresponds to equation (2.20) in the paper by Bohn and Julienne[124] but in a different notation. The matrix K^{oo} is set to zero because we do not consider elastic

processes. We construct the scattering matrix S by

$$S = \left(\mathbb{1} + iK^{\mathrm{red}}\right) \times \mathrm{inv}\left(\mathbb{1} - iK^{\mathrm{red}}\right) \tag{5.4}$$

where we neglected the elastic phase shift. $\mathbb{1}$ denotes the identity matrix.

The local vibrational spacing $\frac{\partial E}{\partial v}$ at the vibrational level v_{P} is denoted by $\bar{v}^{\mathrm{P}}_{v_{\mathrm{P}}}$ (P=X, A indicating the state). Before defining quantum defects with δ and Δ, we need to introduce some notations.

The energy $E^{\mathrm{g}}_{M,q}$ is the eigenenergy of level l of system M. We distinguish start (g=s, $v_{\mathrm{X}} = 29$), intermediate (g = m, $v_{\mathrm{A}} = 120, 139$), and asymptotic (g = a, $v_{\mathrm{X}} = 64, 65$) levels. Our model assumes that the start levels of each system M are energetically degenerate: $E^{\mathrm{s}}_{M,1} = \ldots = E^{\mathrm{s}}_{M,q_M} =: E^{\mathrm{s}}_{M,\bullet}$.

We denote the frequency of the test laser by $\nu\mathrm{T}$ and of the frequency of the coupling laser by $\nu\mathrm{C}$. The detuning of the two lasers is defined with respect to the levels $l=1$ of the system $M=0$ of the two manifolds that the laser couples:

$$
\begin{aligned}
\text{test laser}: \quad d_{\mathrm{T}} &= h\nu_{\mathrm{T}} - \left(E^{\mathrm{m}}_{0,1} - E^{\mathrm{s}}_{0,\bullet}\right) \text{ and} \\
\text{coupling laser}: \quad d_{\mathrm{C}} &= h\nu_{\mathrm{C}} - \left(E^{\mathrm{m}}_{0,1} - E^{\mathrm{a}}_{0,1}\right)
\end{aligned}
\tag{5.5}
$$

The quantum defects of equation (5.3). Here, δ_i and Δ_i reflect the dressed state picture. With the introduced notation, they are defined as follows:

$$
\begin{aligned}
\delta_{M,j} &= \left(E^{\mathrm{m}}_{M,j} - E^{\mathrm{m}}_{0,1}\right) - \left(E^{\mathrm{s}}_{M,\bullet} - E^{\mathrm{s}}_{0,\bullet}\right) - d_{\mathrm{T}} \text{ and} \\
\Delta_{M,k} &= \left(E^{\mathrm{a}}_{M,k} - E^{\mathrm{a}}_{0,1}\right) - \left(E^{\mathrm{s}}_{M,\bullet} - E^{\mathrm{s}}_{0,\bullet}\right) - d_{\mathrm{T}} + d_{\mathrm{C}}
\end{aligned}
\tag{5.6}
$$

The label M is suppressed in the matrix equation above. The matrices for different M are set up separately but related via equation (5.6).

The coupling strength between molecular levels is represented by Γ and Ω. They are computed from the laser intensity, the dipole operator $\vec{d}$, and the local vibrational spacings of the two coupled states by

$$
\begin{aligned}
\Gamma_{ij} &= \frac{-\hbar \vec{E}^{p}_{\mathrm{T}} \cdot \vec{d}_{ij}}{2\sqrt{\bar{v}^{\mathrm{A}}_{120}\,\bar{v}^{\mathrm{X}}_{29}}} \quad \text{and} \tag{5.7} \\
\Omega_{jk} &= \frac{-\hbar \vec{E}^{p}_{\mathrm{C}} \cdot \vec{d}_{jk}}{2\sqrt{\bar{v}^{\mathrm{X}}_{64}\,\bar{v}^{\mathrm{A}}_{120}}}
\end{aligned}
$$

with indices for the levels we start from $i=1,\ldots,q$, for the levels of the A state $j=1,\ldots,n$, and for asymptotic levels $k=1,\ldots,m$. The electric field strength depends on the distance of the molecule to the axis of propagation of the two laser beams. Both laser beams are focused. Various coupling laser intensities, i.e., coupling strengths, are detected by the test laser. Moreover, the excitation probability, and thus detection likelihood, depends on the test laser local intensities. We approximate the laser beam profiles by a number of hollow-cylinders of finite wall width, in which we assume that the intensity is constant. These cylinders are aligned in direction of the laser propagation axis. This method was

applied in a similar, preceding experiment.[101] The average electric field strength in hollow cylinder number p results for a Gaussian beam profile to

$$E^p = E_0 \frac{2p_0}{2p-1} \left[(p_0 + p - 1)e^{-(p-1)/p_0} - (p_0 + p)e^{-p/p_0} \right] \qquad (5.8)$$

where the inner cylinder is $p = 1$. The number of hollow cylinders within the beam waist is p_0. The electric field strength at the center of a Gaussian beam is

$$E_0 = \frac{2}{w_0} \sqrt{\frac{I}{\pi c \epsilon_0}} \qquad (5.9)$$

with I being the laser powers and w_0 the beam waist of test or coupling laser, what ever coupling Γ or Ω has to be calculated. For the detailed evaluation of the vector product $\vec{E}^p \cdot \vec{d}$ we refer to Appendix A. We will use $p_{\max}$ cylinders to approximate the Gaussian beam profile, where $p_{\max}/p_0$ is the width that is considered measured in beam waists.

With this, we simulate line profiles by adding the contribution of all hollow-cylinders taking the size of the hollow-cylinder into account:

$$\textbf{Signal}\,(v_{\mathrm{X}} = 29, J_{\mathrm{X}} = 0 \rightarrow \mathrm{LIF}) \sim \underbrace{\sum_{p=1}^{p_{\max}} \frac{2p-1}{p_{\max}{}^2}}_{\substack{\text{beam} \\ \text{profile}}} \underbrace{\sum_{M=-2}^{2}}_{\substack{\text{coupling} \\ \text{systems}}} \underbrace{\sum_{i=1}^{q_M}}_{\substack{\text{start} \\ \text{levels}}} \underbrace{\sum_{j=q_M+1}^{q_M+n_M}}_{\substack{\text{A state} \\ \text{levels}}} \underbrace{\rho\,(M, i)}_{\text{here: } \equiv 1/6} \, |S_{i,j}|^2$$

$$(5.10)$$

This summation can be done for both situations: with and without the coupling laser. In this way, the experimental curves can be modeled.

5.1.4   Profile Fit

We integrated the lineshape simulations into a fit program applying the MINUIT package.[128] The free parameters of the fit include the four parameters for the laser fields used in the calculation of the scattering matrix, i.e., detuning and intensity of, both, test and coupling laser. The parameter for the detuning of the test laser corresponds to a parameter for the position of the line. For each of the two corresponding experimental traces with and without coupling, two additional parameters are introduced: a background level and a parameter to scale the amplitude. In Table 5.2, all free parameters are listed.

The two traces are fitted subsequently. In a first step, the experimental trace 1 of the uncoupled situation is fitted. Only four parameters are free during the fit: two related to curve and two to the parameters of the test laser. In a second step, the trace 2 of the situation with the coupling laser is fitted with four parameters: two parameters for the trace and two for the parameters of the coupling laser. The two parameter for the test laser do have an influence on the simulated curve but kept at their values obtained in the previous fit. In Figure 5.5 typical fit results is shown. The overall appearance of the observed line profiles are described. However, some features are not reproduced well. The wings are steeper in the experiment than in the simulation, especially for the components that are shifted away most from the original position of the line. The fit is able to produce

	uncoupled	coupled
scaling parameters:		
offset trace 1	$\times$	
offset trace 2		$\times$
amplitude trace 1	$\times$	
amplitude trace 2		$\times$
laser parameters:		
power test laser	$\times$	$\cdot$
power of coupling laser		$\times$
line position	$\times$	$\cdot$
detuning of coupling laser		$\times$

Table 5.2: *Parameters of the simulation of trace 1 and trace 2. A $\times$ indicates a free parameter, a $\cdot$ indicates a fixed parameter with influence on the simulated trace.*

line profiles for the laser manipulated system that are very close to the experimentally observed traces by basically using only two free parameters, namely the detuning and the intensity of the coupling laser. The background and the amplitude parameter do not change the structure of the simulation.

The parameters obtained from the fit can be compared to properties measured in the experiment. Three comparisons between experimental values and values obtained with the fit procedure are reasonable. The detuning of the coupling laser and the two intensities. A comparison for the detuning of the coupling laser is presented in Figure 5.6. The values from the fit follow the experimental detunings quite nicely. The offset from the expected linear dependence around the line position comes probably from the fact that the fit tries to adjust via the detuning parameter differences in the lineshapes between experiment and simulation.

Disappointing is that the resulting laser intensities from the fit with the lineshape simulations do not agree with the experimentally applied ones. For the test laser, we obtain about 100 times bigger field intensities from the fit than we measured. The fit derives this value from the line broadening. For the coupling laser, the fit obtains field intensities that are a factor of about ten smaller than experimentally applied ones.

5.1.5   Discussion

The experiment was laid out to produce simple lineshapes with the smallest number of components. By starting from $J_X = 0$, the total angular momentum of the dimer is simply the total nuclear spin. Moreover, only $I = 0, 2$ is allowed to combine with even J for *gerade* states. A purification of the prepared levels to a single nuclear spin state would only be possible by choosing levels in a preparation step, for which hyperfine splitting is large enough, e.g., levels of the b $^3\Pi_u$ state. Spin-orbit coupling to levels of the A state allows for their excitation[24] but the efficiency of the Franck-Condon pumping is greatly reduced.
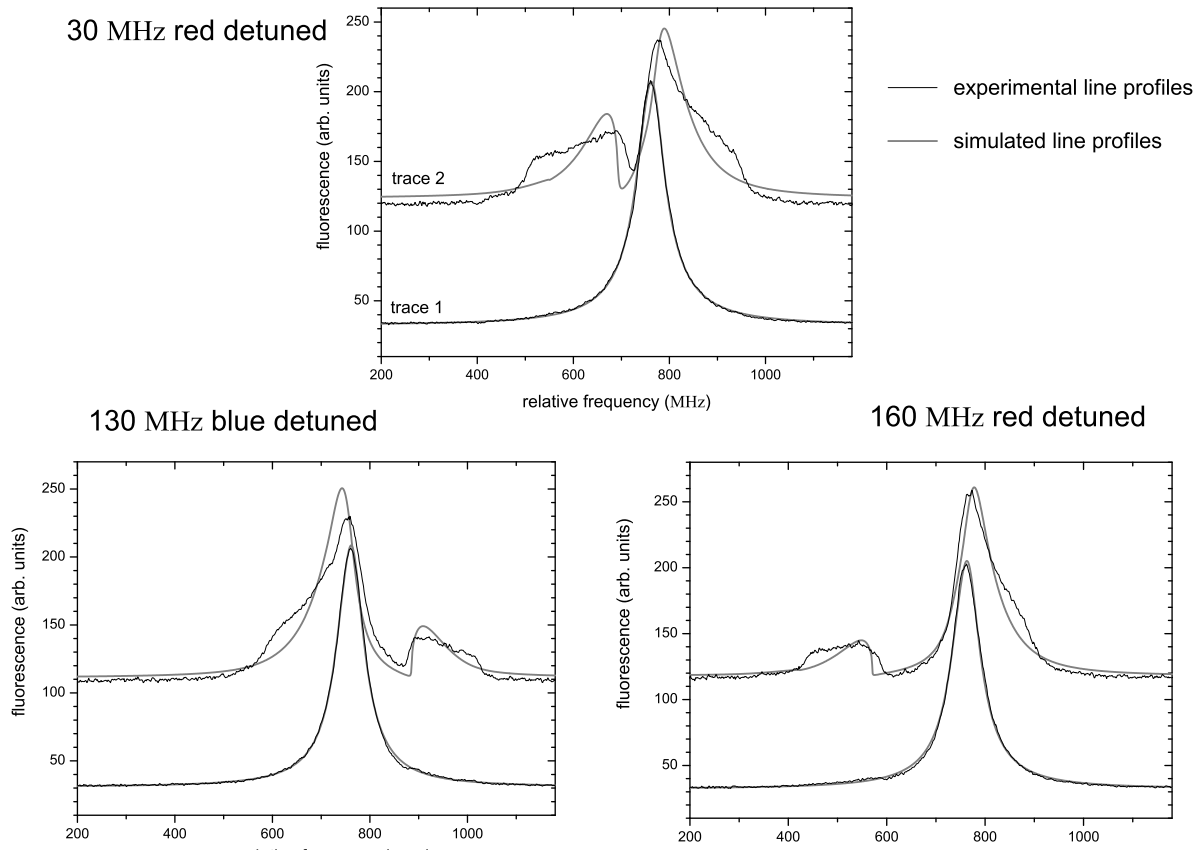
Figure 5.5: *Resulting line profile curves obtained with the fit. For three different detunings of the coupling laser the two traces are shown for both recordings and simulations. The test laser is tuned across the R(0) line of the 120 ← 29 band. The coupling lasers is near the transition $v_A = 120$, $J_A = 1 \leftarrow v_X = 64$, $\ell = 0$ transition. The offset of the trace 2 and its additional noise are due to additional scattered light originating from the coupling laser. In trace 1 the simulation is almost perfect, thus lines are hardly separated from each other.*
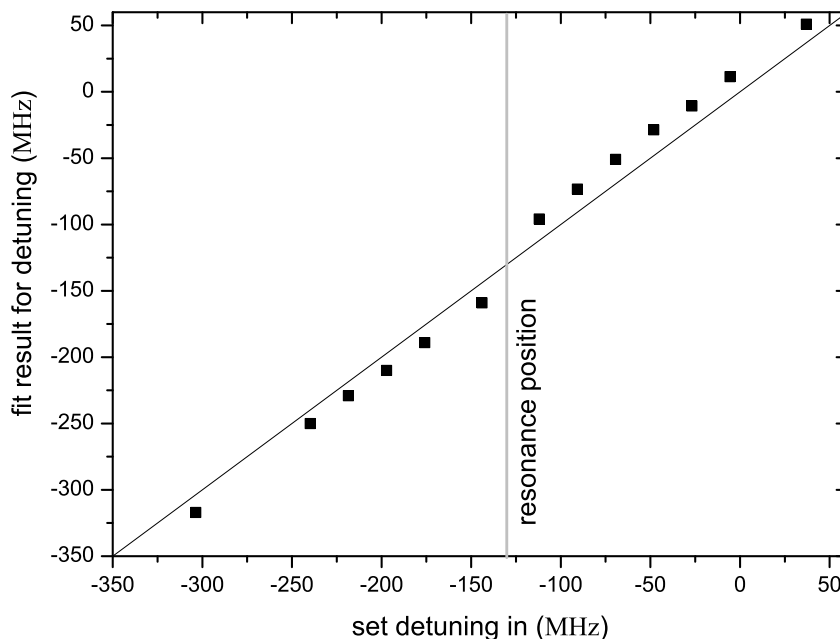
Figure 5.6: *Comparison of the detunings of the coupling laser. The detuning set in the experiment and the detunings obtained in a simulation fit are compared. The diagonal line indicates the expected behavior.*

The linear polarization of the two laser fields and the parallelism of the two polarization axes allows to separate different coupling schemes. However, many couplings contribute in the experiment, as shown in Figure 5.4. But, these are known and therefore it was possible to fit the lineshapes with few free parameter only. The detuning of the coupling laser is well reproduced (see Figure 5.6).

For the comparison of experimental and simulated laser intensities, many steps need to be taken. The measured values are the power and the waist of the laser beam. For the calculation of the coupling strength, the wavefunctions are calculated in multi channel calculations. For the transition dipole moments as function of internuclear separation R, we take splines through *ab-initio* values.[126, 127] The calculation of coupling strength of the angular momentum wavefunction is discussed in Appendix A. All this effort is however not rewarded. We have stretched the MCQD model too much, e.g., the start levels are artificially open channels. The corresponding analytical formula for a simple two-level system does not describe the power broadening as expected. The broadening would depend not only on the Rabi frequency but also on vibrational spacings. Thus, we cannot expect to reproduce the experimental laser intensities with the lineshape fit.

In photoassociation experiments, the hyperfine state of the two atoms is well defined. Therefore, the number of couplings that need to be considered is smaller, at least for single laser photoassociation. If one applies a second laser, e.g., in order to drive the molecules to bound levels of the ground state, similar complications will appear, i.e., several hyperfine levels need to be considered.

5.1.6   Conclusion

This work is aimed on a better understanding of laser induced manipulation of cold collisions. In a systematic study, we measured the influence of a laser coupling of asymptotic ground state levels to levels close to the first electronic excited state. In a quantitative model, we are able to reproduce the dependence of the peculiar lineshapes on the detuning of the coupling laser. But this model, based on MCQD theory developed for photoassociation experiments, does not lead to the correct amplitude of the influence of the coupling laser. Due to hyperfine structure the coupling schemes are, in this experiment as well as in experiments with ultracold atoms, much more complicated than a two state model. For systematic studies of laser control of cold collisions, experiments with atoms without nuclear spin are much more appropriate due to the simplicity of the system. Here, the interest for such a tool, often referred to as optical Feshbach resonances, is higher because no Feshbach resonances are available that can be utilized by magnetic fields.

Acknowledgments

5.2   Transition Dipole Moments

The calculation of the transition dipole moments and the coupling schemes deserve an extended discussion. The computation of the transition dipole moments takes several steps of consideration for the angular momenta. We use Hund's case (a) wavefunctions as a basis for description of the wavefuntions. A complete set of quantum numbers for the description of the angular wavefunction is: the projection of the orbital angular momentum on the molecular axis Λ, the total spin S, its projection Σ, the total nuclear spin I, and its projection Ω_I.

For the start levels, which are prepared by Franck-Condon pumping, no angular momenta of the electrons have to be considered. Moreover, the two electron spins are paired and the molecule is not rotating. The total angular momentum of the dimer is simply the total nuclear spin, which has to be even for a $J_X = 0$ molecule, thus $F = I = 0, 2$. In total, six degenerate hyperfine levels exist if the projection of I onto the molecular axis $\Omega_I = -I, \ldots, I$ is taken into account.

For the excited state levels, an angular momentum of one is absorbed an the rotation of the dimer changes to $J_A = 1$. For levels of the A $^1\Sigma_u^+$ state the projection onto the molecular axis is zero. Every level has a specific total angular momentum F and is a linear combination of several wavefunctions with even I (and $\Lambda = \Sigma = 0$). Spin-orbit interaction with the b $^3\Pi_u$ state leads to an admixture of levels with $\Lambda = 1 = -\Sigma$, again only even I wavefunctions are contributing. These admixtures are not contributing to the coupling strength from the ground state because the ground state wavefunctions are with $S = 0$ different than for the triplet admixtures with $S = 1$.

	$M=0$		$M=1$	$M=2$
	$F{=}I{=}0$	$F{=}I{=}2$	$F{=}I{=}2$	$F{=}I{=}2$
$F{=}1,\ I{=}\{0,2\}$	-0.131	-0.635	-0.550	—
$F{=}1,\ I{=}\{0,2\}$	-0.131	0.635	0.550	—
$F{=}2,\ I{=}2$	—	—	-0.667	-0.133
$F{=}3,\ I{=}2$	—	0.147	0.138	0.109

Table 5.3: *Transition dipole momement of spectroscopy transition in Debye for linear polarized light. The values are for the transition $v_X = 29$, $J_X = 0$ to $v_A = 120$, $J_A = 1$ of the A–X system. By multiplying with $\hbar \vec{E}_T^p$ one obtains the coupling strengths for this transition, see also the definition of Γ_{ij} in equation (5.7). For each hyperfine level of the X state a column is given and each row corresponds to an hyperfine level of the excited state.*
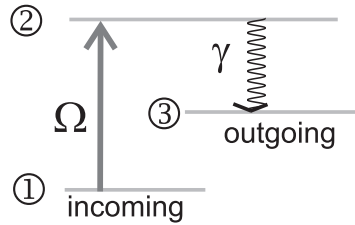
Figure 5.7: *Sketch of a three level system considered for checking the obtained analytical formula obtained with the simplified MCQD theory.*

For the asymptotic ground state a hyperfine state I gets admixtures from levels with $I - 1$ and $I + 1$ via hyperfine interaction. This is a seldom mixing between *gerade* and *ungerade* states. Again, these admixtures cannot contribute to the coupling strength because electronic dipole transitions do not change the nuclear wavefunction. Therefore, the admixtures reduce the coupling strength.

The multichannel wavefunctions were calculated in coupled channel systems with a mapped grid of internuclear distances. For the excited state levels, the two electronic states A $^1\Sigma_u^+$ and b $^3\Pi_u$ are taken into account.[125] For the ground state, the X $^1\Sigma_g^+$ and the a $^3\Sigma_u^+$ states are considered.[125] Additionally, R dependent transition dipole moments from *ab-initio* calculations were used.[126, 127] All this information contributed to the calculated electronic transition dipole moments listed in Table 5.3 and Table 5.4. In recent experiments on a sodium heat-pipe, calculated and directly measured coupling strengths for deeply bound states were compared and found to be in good agreement.[129]

5.3   Multichannel Quantum Defect Theory

The method for the simulation of line profiles is taken from multichannel quantum defect (MCQD) theory. As mentioned above, an unexpected dependence of the power broadening on vibrational spacing is found in the derived analytical formulas for systems with a small

	M = 0			M = 1				M = 2	
	$F=1$	$F=1$	$F=3$	$F=1$	$F=1$	$F=2$	$F=3$	$F=2$	$F=3$
$I \approx 0$									
$F=0, \ell=0$	-0.944	-0.944	—	—	—	—	—	—	—
$F=2, \ell=2$	0.827	0.827	—	0.716	0.716	—	—	—	—
$I \approx 2$									
$F=2, \ell=0$	0.463	-0.463	-1.069	0.401	-0.401	0.487	-1.008	0.973	-0.797
$F=0, \ell=2$	-0.211	0.211	—	—	—	—	—	—	—
$F=1, \ell=2$	—	—	—	0.407	-0.210	0.144	—	—	—
$F=2, \ell=2$	0.407	-0.407	-0.336	0.353	-0.353	-0.427	-0.317	-0.855	-0.251
$F=3, \ell=2$	—	—	—	—	—	-0.532	0.150	-0.421	0.300
$F=4, \ell=2$	—	—	-0.865	—	—	—	-0.838	—	-0.749

Table 5.4: *Transition dipole momement for linear polarization of coupling transition in Debye. The values are for coupling between $v_A = 120$, $J_A = 1$ of the A state (columns) and asymptotic $v_X = 64$, $\ell_A = 0, 2$ singlet ground state (rows). By multiplying with $\hbar \vec{E}_C^p$ one obtains the coupling strengths, similar to Ω_{ij} as introduced in equation (5.7).*

number of coupled levels. For a simple two state model (see Figure 5.7) of an excited state with lifetime $1/\gamma$ and a Rabi frequency for the coupling of Γ the analytical formula derived via the K-matrix the fluorescence is proportional to

$$|S_{1,3}| \sim \frac{1}{d_\mathrm{T}{}^2 + \gamma^2 \left(1 + \frac{\Gamma^2}{\gamma \overline{v}^\mathrm{X}}\right)^2} \; . \tag{5.11}$$

The expected dependence on the detuning of the coupling laser d_T for this simple two level system is[130]

$$|S_{1,3}| \sim \frac{1}{d_\mathrm{T}{}^2 + \gamma^2 + \Gamma^2} \; , \tag{5.12}$$

i.e., no dependence on the vibrational spacing $\overline{v}^\mathrm{X}$ should appear. In an effort to understand this better, we changed the entries in the K-matrix in order to remove the dependence on the vibrational spacing. However, this does not allow to reproduce the spectra with the experimental laser powers either and the functional dependence of the elements in the K-matrix on the laser power is not as expected.

5.4   Density Matrix Simulations

An alternative to the discussed method is to simulate the spectra by looking at the evolution over the time of the dimers described by a wavefunction. This is done by the von Neumann equation using a density matrix. Such a simulation takes into account the time dependent field strength that the molecules are experiencing during the flight through the laser fields. We used experimental parameters for power and waist of the

(a)

(b)
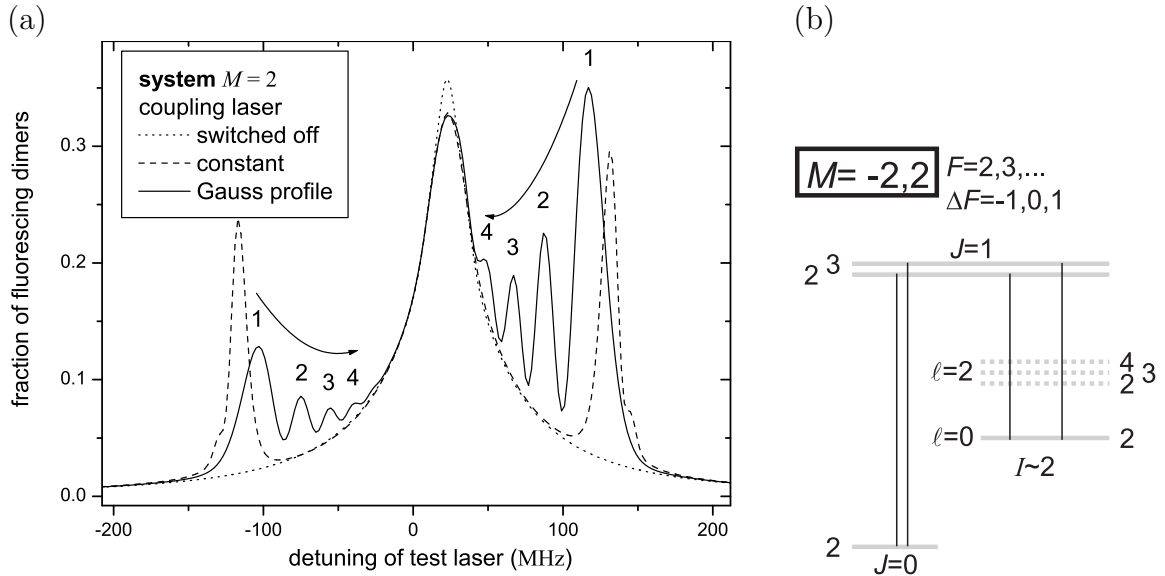
Figure 5.8: Graph (a) *shows lineshapes simulated by integration of the von Neumann equations. Three situations of the coupling lasers are simulated for the reduced $M=2$ system depicted in* Graph (b). *For the Gaussian beam the Autler-Townes components are split into several peaks. Each peak corresponds to a field strength of a position where many excitations are taking place. The peaks indicated by* 1 *correspond to the excitation position with the highest field.*

laser beams (25 mW and 100 μm) as well as the velocity of the molecules (1000 m/s) to simulation a molecule passing the laser beam perpendicular though the beam axis. The derived Rabi frequencies of spectroscopy laser explains the line broadening observed in the experiment but allows for ten Rabi oscillations during the interaction at most. This is too little for a treatment with rate equations and too much to consider the spectroscopy laser as a small perturbation.

The difficulty in integrating the von Neumann equation is the needed calculation power. Not only many levels are coupled, which leads to matrices of the order thirteen. But also, large detunings and strong couplings need to be simulated, which limits time per step in the integration of the von Neumann equation. The later problem can be reduced, if levels, which are almost not contributing to the coupling due to large detunings, are excluded from the simulation.

Spectra are simulated by computing the time evolution of the density matrix, which describes the dimer, for different detuning of the spectroscopy laser. We are using an artificial level representing molecules that decay from the A state level. The population in this level after the complete interaction, i.e., after the time integration, corresponds to the observed fluorescence. Here, we do the calculation with a single molecule that passes the center of the laser beam and as a certain velocity. In a first check, the line broadening in the situation, in which the coupling laser is switched off, is reproduced. This is the dotted trace in Figure 5.8.

The second step of our simulations includes a laser field representing the coupling laser. For simplification, we assume a constant field strength during the complete interaction for

the moment. In comparison to the experiments, we do simulations for fields corresponding to $1/\sqrt{10}$ of experimentally applied field strength in the center of the coupling laser. This is done only to sace computing time because we can reduce the interval of the simulated spectrum due to the smaller shifts. We obtain the dashed trace in Figure 5.8. Three components are visible: one is at the position of the unperturbed line and two additional components are shifted symmetrically around this position. These are three Autler-Townes components that are expected from the coupling scheme for $M = 2$, where all levels of the asymptote of the $\ell = 2$ manifold are neglected since the coupling laser is almost resonant with the transition to $\ell = 0$ (see Figure 5.8, Graph (b)). In a third simulation, we now assume a Gaussian beam profile for the coupling laser instead of the constant field strength. As in the experiment, both waist of the two lasers are the same with a common beam axis. Here, the shifted components are split into several components (labeled by 1, 2, 3, and 4; solid line in Figure 5.8) that are getting smaller towards the position of the unperturbed line (with higher label). In additional simulations, the periodicity of these structures gets smaller with higher test laser intensities. We explain this behavior by the fact that the molecules is driven by the test laser to undergo Rabi oscillations between the start state and levels of the A state. Due to this, several times (or locations) are marked out, in which the excitation takes place. Each of the peaks of one Autler-Townes components corresponds to one of these positions. The peak shifted the most (labeled by 1) corresponds to the position with the strongest laser fields. By going closer to the unperturbed line position one passes the peaks of lower field strength. This structure was not observed in the experiment. Two things have to be taken into account that have not been considered yet. First, the molecules travel through the laser fields with various separations of the trajectory to the axis of the laser. The further they are away, the lower is the peak electric field intensity. Second, the molecules are traveling with different speeds, which would translate to different interaction times with the two laser fields. However, the change of the laser fields in laser beam direction is small due to the long Rayleigh range if compared to the size of the particle beam. Final results would need averaging over beam divergence and speed.

We undertook simulations with the density matrix approach for all M and simulated thereby the experimental trace. As in the MQDC approach, no differences between M and $-M$ are found. In Figure 5.9 a series for several detunings of the coupling laser is shown. Here, the discussed oscillations are again occurring. However, one can find the changeover of the Autler-Townes components from one side of the position of the unperturbed line to the other for an inversion of the detuning of the coupling laser. In the experiment, the components are shifted more. This can be accounted to the fact that the intensity of the coupling laser was reduced by $\sqrt{10}$ to simplify the simulations and, moreover, because the simulations due not average for different minimal distances of the molecules to the laser beam axis. But, we can conclude that the order of magnitude of the laser induced shift is observed in the experiment. Therefore, extensive density matrix simulations will be able to predict the magnitude of effects of coupling lasers on asymptotic levels.
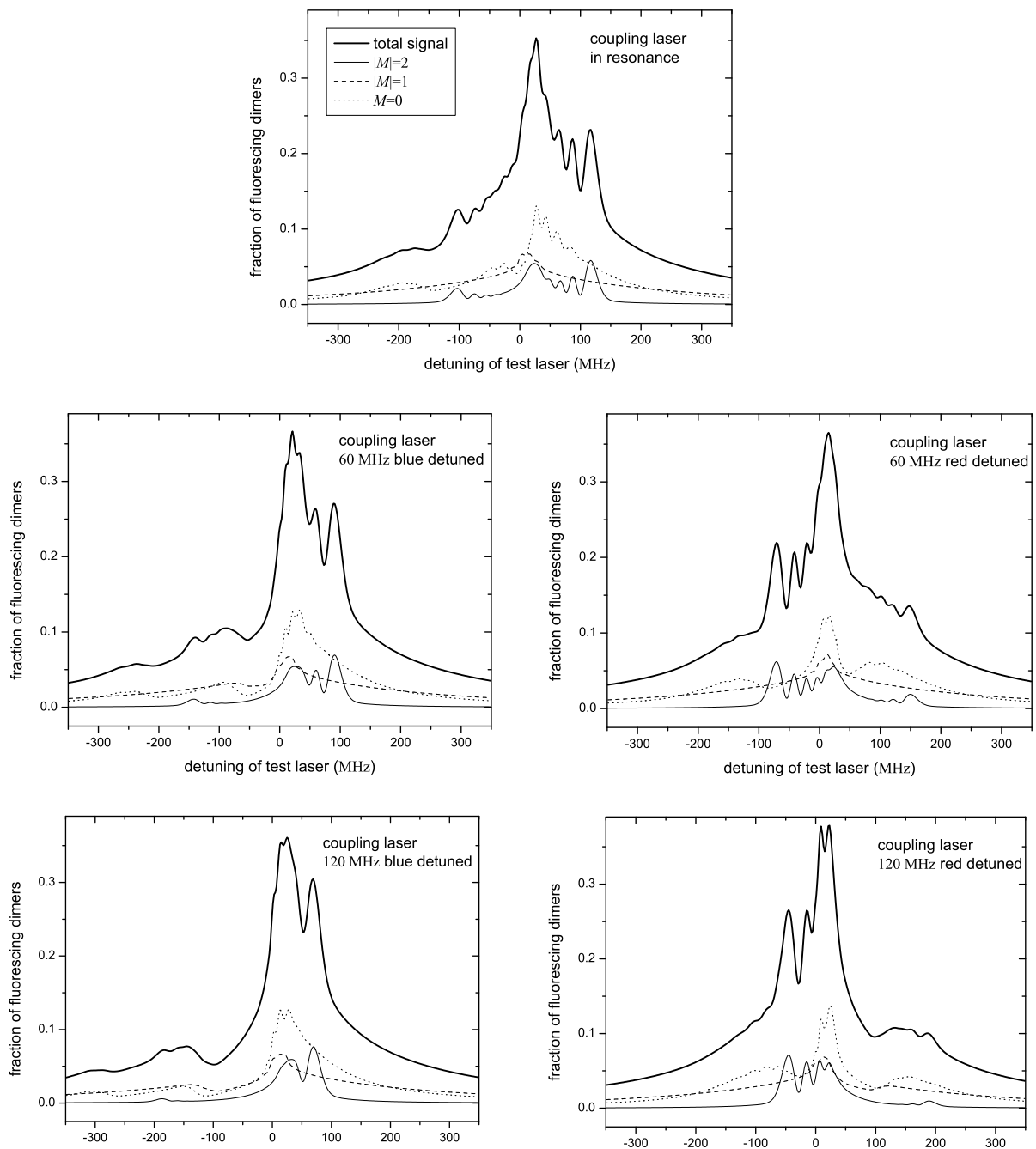
Figure 5.9: *This series shows the spectra obtained from density matrix simulations. Several detunings of the coupling laser are simulated. The individual M-systems are shown as well as the overall spectrum.*

	coupled system	MCQD	density matrix
using relative coupling strength	yes	yes	yes
consideration of coherences	no	yes	yes
consideration of time dependence of laser fields	no	no	yes
included to a fit procedure	yes	yes	no
computational effort	low	medium	very high

Table 5.5: *Comparison of three approaches for line profiles simulations as discussed in the text.*

5.5   Concluding Remarks

Preceeding to this work, another approach was followed.[102, 25] It is simpler and was the first try of understanding of the spectra. Assuming that the spectroscopy leads to small perturbations only allows to model a system of A state levels and asymptotic ground state levels which are coupled by the laser field of the coupling laser. Eigenvalues and eigenvectors of this coupled systems are calculated. It is simulated that the spectroscopy laser probes these eigenstates of the coupled system. However, this model does not take into account coherences between the involved levels. Consequently, dark states cannot be modeled. Such states lead to electrically induced transparency (EIT) and in the discussed experiment to steep wings of the line profiles.

In total, three approaches were tried for the simulation of the observed line profiles. Of these, two were introduce in this work (MCQD theory and density matrix simulations). The three approaches are compared in Table 5.5. Although none of these implementations allows for a direct comparison between experimentally applied and simulated optical manipulation of long range levels of the ground state, significant steps in the understanding of optically induced manipulation of long range interaction were taken. The models do need to include hyperfine structure in order to precisely describe the coupling. The amplitude of the coupling strength is not modeled correctly by the simplified models of MCQD theory. However, density matrix simulations show that the compute coupling strengths are in the right order of magnitude. This allows to predict what field strength is needed in order to obtain a certain influence of an optical induced Feshbach resonance.

An even better quantitative understanding of optical Feshbach resonances is needed in order whether or not an optical Feshbach resonance is applicable under certain circumstances. Not only that one needs to predict the needed laser power, but also what are side effects of the manipulation laser, e.g., photoassociation at large detuning or multiphoton processes. Systems without hyperfine structure are much better for systematic studies since the coupling schemes are simpler. Spectroscopy of alkali earth metal dimers can supplement experiments on ensemble of cold atoms. Investigations of the behavior of asymptotic molecular levels can be much more detailed if a beam of these dimers is used, mainly because this allows for observation of spectra without Doppler broadening.

Chapter 6

Doppler Free Spectroscopy of Alkali Earth Metal Dimers

Alkali metal atoms are widely used in experiments with ultracold gases. This is due to their simple electronic structure and the good possibilities for laser cooling. In recent years, the interaction of the particle of these dilute gases became more and more important. These interactions allow for experiments on quantum degeneracy, phase transitions, and many more topics of fundamental physics. Precise, quantitative models of the interaction are essential for the understanding of the observations.

A second branch of the dilute gases community is however interested in ultracold gases without interactions of the atoms: frequency standards in the optical frequency region are proposed. The quality factor of intercombination lines in the visible frequency regions as for alkali earth metals are orders of magnitude better than for the microwave transition of cesium that defines the second. A time definition via a clock transition is defined via the transition frequency of a single, unperturbed atom. Thus, the experiments seek to produce ensembles of non-interacting atoms at rest with long interrogation times. For two main reasons it is of interest to understand the interaction of these atoms: First, interactions of clock atoms can lead to pressure shifts of the transition frequency of the standard. Second, in the preparation of ultracold ensembles scattering processes are essential. Investigation of cold collisions of alkali earth metal atoms is therefore interesting in the development of optical frequency standards.

A second motivation to investigate long range interaction of alkali earth metal atoms is the simplicity of the atoms. The isotopes with high natural abundance do not have a nuclear spin. Thus, only a single electronic ground state of the dimers exists and the structure of the asymptote of electronically excited pair becomes simpler, too. The changeover from alkali metals to alkali earth metals is therefore a step that simplifies the investigated system. Hence, a better test of models for the description of the long range interaction can be reached. Potential descriptions as well as atomic structure calculations leading to long range parameters will benefit.

This chapter discusses our efforts towards high precision spectroscopy of long range levels of alkali earth metal dimers. Spectroscopic experiments on a heat-pipe for calcium that spectrally resolve laser-induced fluorescence are a solid base for Doppler-free spectroscopy on a Ca_2 beam.[75, 131, 132] These experiments were undertaken with calcium as an

exampel. Calcium is cheap, easy to handle as bulk material and has easily reachable transition frequencies. Also, ^{40}Ca is much more abundant than other isotopes, which simplifies the assignment of spectra. An additional argument for choosing calcium is that complementary experiments on ultracold calcium exist, e.g., at the Physikalisch-Technischen Bundesanstalt (PTB), where photoassociation experiments were undertaken.[98] All these arguments lead to the decision to choose calcium as an example for the beam experiment, too.

The preceding experiments in our group[75] show by Monte-Carlo simulations that only higher precision on the transition frequencies (and not more term values) will improve the precision of scattering parameters, namely the scattering length and the long range parameter. Therefore, an experimental method is needed to replace the setup of heat-pipe in combination with the Fourier-transform spectrometer or monochromator. Like in the case of alkali metal atoms, we change towards a beam apparatus. However, only pulsed beams were experimentally realized for dimers of alkali earth metals until now.[133] In the experiments we aim for, we need to use continuous lasers for the desired resolution. In principle, it is possible to combine a pulsed particle beam with continuous lasers by gating the detection, but the experimental time will be much longer than in case of a continuous beam for the same effective observation time. The same argument why a pulsed beam is less complicated to be built explains why high resolution experiments are more complicated: less material is used for a certain time of operation.

The current experimental knowledge is described in the PhD Thesis of Olivier Allard.[131] Our development of a beam apparatus for Ca$_2$ is motivated by four possible experiments: First, a detailed spectroscopy of the ground state X $^1\Sigma_g^+$, which will allow for an improved determination of the scattering length obtained from the potential derived from the molecular spectroscopy.[75] An analysis of the line shapes obtained in a photoassociation experiment lead to an alternative interval of the scattering length.[98] Second, systematic studies of states correlated to the $4^1S_0 + 4^3P$ asymptote can be detailed.[132] The coupled channel analysis is of importance for scattering processes of atoms in the two clock states. Moreover, the levels of the coupled manifold may serve as a transfer state for the formation of ground state molecule via photoassociation. The efficiency of this process depends strongly on details of the potential curves. Third, predissociation of the B $^1\Sigma_u^+$ state can be systematically studied in a beam because the lines are not broadened by the Doppler effect and the predissociation rates can therefore be derived similar to a study in sodium.[134] Fourth, the study of manipulation of cold collisions by laser fields should be continued on calcium. The lack of hyperfine structure simplifies the modeling. Also, magnetically tuned Feshbach resonances are not available for such atoms, which increases the interests in alternative methods for influencing cold collisions, e.g., by optically induced Feshbach resonances.

6.1 Experimental Requirements

Beams of alkaline metal dimers are successfully applied for Doppler-free spectroscopy. Examples discussed in this thesis are K$_2$ and Na$_2$. However, some fundamental differences of alkaline earth metals to alkaline metals have to be considered for the concept of the

experiment. The consequences on the experiment are discussed in this section, which should answer the readers questions 'Why is it not sufficient to fill the sodium oven with calcium?'

An obvious difference between dimers of alkaline metal and alkaline earth metal is the different electronic structure. In case of alkalines, a single valence electron in a $^2S_{1/2}$ state has to be considered for each atom. This leads to two electronic ground states: The singlet ground state, labeled by X $^1\Sigma_g^+$ is about $4\,500$ cm^{-1} deep. The triplet state, a $^3\Sigma_u^+$ is with about 200 cm^{-1} shallower. At the asymptote, they are coupled via the hyperfine structure of the atoms, leading to a rich field of Feshbach resonances, that are often utilized via magnetic fields for spectroscopy, for the manipulation of the two particle interaction, or for the production of ultracold molecules from laser cooled atoms. All these phenomena and techniques are not available if atoms have no hyperfine structure, e.g., due to the lack of a nuclear moment.

This is the case for most isotopes of alkaline earth metals. The even (*gerade*) number of protons is grouped by an even (*gerade*) number of neutrons for the most abundant isotopes, which allows to pair the nuclear spins, leading to $i = 0$. In case of alkalines, the odd (*ungerade*) number of protons prefer to combine with a even (*gerade*) number of neutrons, the nuclear spins cannot be paired.

For each atom of an alkaline earth metal, two valence electrons need to be considered. They combine to a $^1S_0$ state. This is basically a spherically symmetric state, in which the spins are compensates: No inner structure is visible. If two such particles interact, only a single interaction channel is possible. It is described by the molecular interaction potential X $^1\Sigma_g^+$. This potential is shallower than in case of dimers of alkali metals. Also the minimum is shifted to larger internuclear distances. The potential curves are such that one lambda scheme with two laser fields allows already to perform spectroscopic experiments of the least bound levels of the ground state starting with levels, which are expected to be populated in a molecular beam: The low rotational levels of the vibrational ground state of the electronic ground state. Such experiments can only be done in alkali metal dimers after the molecules are optically pumped to vibrationally excited states, i.e., by applying a Franck-Condon pump step. However, a drawback is that depth of the shallow potential corresponds to the window of detection: The fluorescence, which is the experimental signal, is between the two laser frequencies. Typically, scattered laser light is filtered by color-glass or interference filters in the detection of alkali metal dimers. An experimental challenge is therefore to reduce the scattered light and to find an appropriate combination of excitation scheme and available filters.

However, the main difference between sodium and potassium on one hand side, which are successfully investigated in beams, and alkali earth metals on the other hand side is shown in Figure 6.1: the vapor pressure is lower for alkali earth metals. This is of high importance because the vapor pressure determines the density of particles in the oven and thus the flux of the beam. Moreover, the dimers of interest are created in collisions in the oven and inside the nozzle. Their production rate depends strongly on the density of atoms. Therefore, an oven for Ca$_2$ needs to be run with a temperature higher than the operation temperature of an oven for K$_2$ or Na$_2$.

The requirements for a source of a continuous beam of Ca$_2$ are summarized in the following:
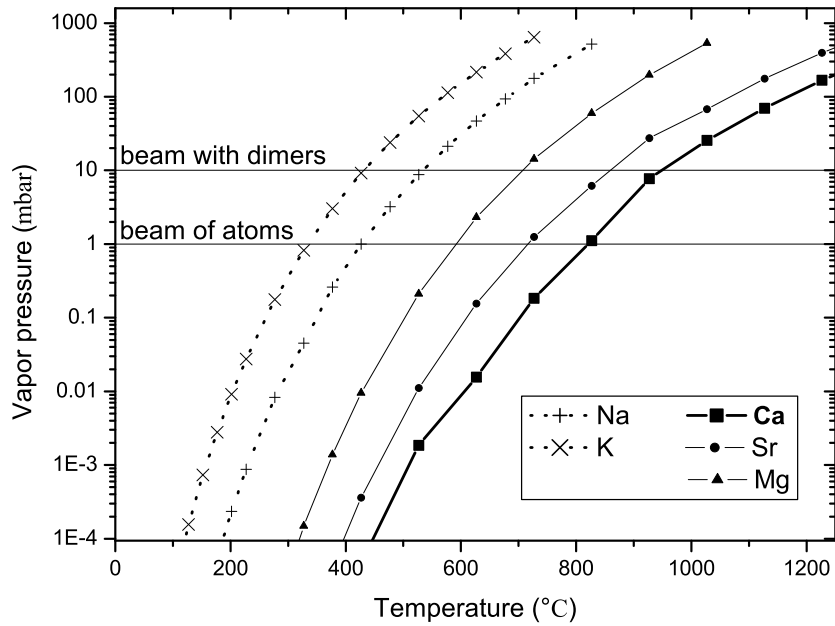
	K	Na	Mg	Sr	Ca
atomic beam	335	425	590	715	820
melting point	63	98	650	777	842
molecular beam	430	530	710	860	950
boiling point	759	883	1090	1382	1484

Figure 6.1:   *Vapor pressure curves of alkali metals and alkali earth metals.[135] The coldest part of the oven needs to be heated to a temperature that implies a pressure of about* 1 mbar *to obtain an atomic particle beam and* 10 mbar *for a beam with dimers. Beneath the graph is a list of relevant temperatures in degrees Celsius; melting and boiling points are given for one atmosphere. The beam temperatures are the temperatures that lead to a vapor pressure of* 1 mbar *and* 10 mbar *respectively.*

- The reservoir must be able to hold about one mol of calcium as bulk material and if liquid without clocking the nozzle.

- The reservoir must be constructed such that cleaning and re-use is possible without help of any craftsmen not involved in the research project itself directly.

- The reservoir must be tight up to the operating temperature.

- No materials may be used that have a significant vapor pressure at the operating temperatures.

- The nozzle should be about 100 K hotter than the coldest point of the reservoir, which determines the vapor pressure. At higher nozzle temperature, molecules might be destroyed, whereas lower temperatures might cause the nozzle to clock. The nozzle is cooled down by the particle flow and the gas might condense here.

- From the vapor pressure curves shown in Figure 6.1, the operating temperature of the reservoir is expected to be 1000°C. Here we added 50 K because the signals of the preceding calcium heat-pipe experiments[131] were weaker than in alkali metal experiments.

- The heating must be reliable: High voltages cannot be applied for resistance heaters in the vacuum because of danger of discharges, which typically break a supply wire and end the experimental run.

- The alignment of the source must be reproducible and small changes of the source position must be allowed. At the high temperatures, displacements of the source due thermal expansions are expected. The alkali metal sources need to be aligned very precisely because the nozzle of the source has to be on the line defined by the positions of skimmer and optical interaction zone.

- The pressure in the beam path has to be low enough to allow for a free expanding beam. The pump speed has to be sufficient, especially in the region around the nozzle in order to allow for cooling of the inner degrees of freedom of the dimer by collisions with Ca atoms in the particle beam.

Calcium is available in granules. For an estimate of the needed size of the reservoir, the lowest density of the calcium during a run has to be considered. This is the effective density of the granules of 0.6 g/cm^3. The minimal surface of a reservoir for one mol — a sphere of 5 cm diameter — emits 1 200 W at 1 000°C. This is about ten times more than in case of potassium or sodium.

The straightforward solution is to increase the size of the vacuum tank, install additional heat shields, improve the cooling of the tank, and increase the voltage for the resistance heaters are supplied with. But, this will decrease the pump speed at the nozzle and increase the risk of discharges. Also, tantalum wires, typically installed for high temperature applications, break easily after a first operation. This is problematic for re-filling the reservoir. In summary, scaling up the alkali metal beams is not as simple as it seems on the first glance. In the following sections, an alternative system is introduced.

material	heat conduction $(K/(m \cdot W))$	at temperature (°C)	melting point (°C)
glass wool	0.08	300	
teflon	2.5	230	
magnesia (MgO)	5.8	1200	
alumina (Al_2O_3)	6	1300	
stainless steel A2	15	25	1425
stainless steel A2	27	1000	1425
copper	350	700	1085
nickel			1455
tantalum			3017
tungsten			3422

Table 6.1: *Melting temperatures and thermal conductivities of selected materials including the temperature it was measured at.[136, 137] Although steel is a metal, it may be considered a heat insulator since the heat conductivity is similar to ceramics like magnesia and alumina.*

6.2   Oven Construction

The principle idea of an alternative system is to move the heaters outside the chamber. Fewer parts have to be inside the vacuum and consequently the oven construction is less complicated. In this section, we describe the first realization of an oven heated from outside the vacuum chamber. After gaining experience with this setup, an improved version of this indirect heating system was developed, which is discussed in Section 6.4.

We started from the beam apparatus used for the experiments on sodium, which were discussed in Chapter 5. The oven chamber is replaced by a CF-100 stainless steel double cross. To this, a diffusion pump is mounted. On the end opposite to the beam chamber an tube connected, the oven tube. We started with the oven tube depicted in Figure 6.2, Graph (a).

The principle of the indirect heating system is as follows. Into the oven tube, a cylindrical symmetric oven is put, which has a nozzle on the symmetry axis. As long as the tube is aligned, the oven is aligned, too. The tube is heated from outside the vacuum. Here, commercial tube heaters may be used. Both, oven and oven tube are fabricated from stainless steel, which has a melting temperature that is with 1425°C significantly above the needed temperature of the oven of 1000°C. Although considering steel a heat insulator, the heat conduction towards the vacuum system will be significant due to the high temperature gradient. Therefore, both ends of the tube are cooled by water, which flows though an hollow ring that was welded to the oven tube. The back end of the oven tube is closed with a CF-100 blind flange. Through this, the oven may be taken out for refilling.

The oven is closed from both sides with CF-40 flanges. The nozzle is in the middle of the front flange. Gaskets made of nickel are used to allow for higher temperatures than copper gaskets do (see Table 6.1). This gasket material is often used for lithium beams.[138]

The nozzle was placed in beam direction to the middle of the oven tube. This place to

be the hottest, which will avoid clogging. The nozzle itself has a diameter of 200 μm and a length of about 1 mm and was drilled by a laser. With alkali metal beams the nozzles usually widen during operation and have to be exchanged after about fifty runs. In this setup, the nozzle piece is a tube that is mounted into the front flange of the oven by a press connection in order to allow for exchange.

For the installation of the heater, experiences from the preceding heat-pipe experiment can be used: The heated tube has to be supported because otherwise it bends under its own weight. However, this support is mobile since the heat extension of the oven tube is a few millimeter. The heaters are two half-cylinder that provide 875 W each and are designed for temperatures up to 1150°C.

Several problems occurred while the oven was put into operation. They are discussed in the following. We sorted out them out bit by bit which led to the modified illustrated in Figure 6.2, Graph (b).

6.2.1 Temperature Measurements

For temperature measurements thermocouples were installed. We used K-type thermocouples, which cover a dynamic range from -200 to 1250°C and are widely used in many applications. Another method to measure the temperature is to use the black body radiation emitted from the oven. The beam chamber is equipped with a viewport at the position were particle beam ends. The temperature derived from the color of the glowing oven[139] agree with the readings from the thermocouples. More precise measurements would be possible with the help of well calibrated pyrometer.

6.2.2 Gasket Dissolved

In the first run with an oven filled with calcium the oven leaked substantially. The nickel gasket reacted with liquid calcium. The gasket at the back end was completely washed away. This end is the coldest part of the reservoir and therefore most of the vaporized calcium will condense at this side. We dissolved nickel-calcium alloy with nitric acid and several hours of reaction time.

No better gasket material was found mainly due to the high temperature requirements. Also, it should be softer than steel, should have a low vapor pressure, and needs to be affordable. We tried to use steel gaskets that we soft annealed before installation. However, the knife edge of the flange and the oven were significantly damaged and the steel gasket needed to be removed with big efforts. However, only small leaks were observed during operation.

A second, more successful approach to seal the oven was to minimize the contact of liquid calcium with the gasket. A second improved oven was designed that is loaded from the front and does not have direct contact between the liquid reservoir of calcium and the gasket. Also, the path for calcium vapor to the gasket increased. The oven will be described in detail in Section 6.4. Although the gasket is still attacked, no leaks were found during operation. It is not clear wether the remaining reactions take place during the run of the beam or in the cool-down process at the end of the experiment.

(a) short tube
(first approach)

- calcium
- stainless steel
- water
- water cooling
- air cooling
- fibrothal
- sheet of steel
- glass wool

CF40

CF 100

double cross:
connection to
beam chamber

(b) short tube
(second approach)

(c) long tube (final)

CF40
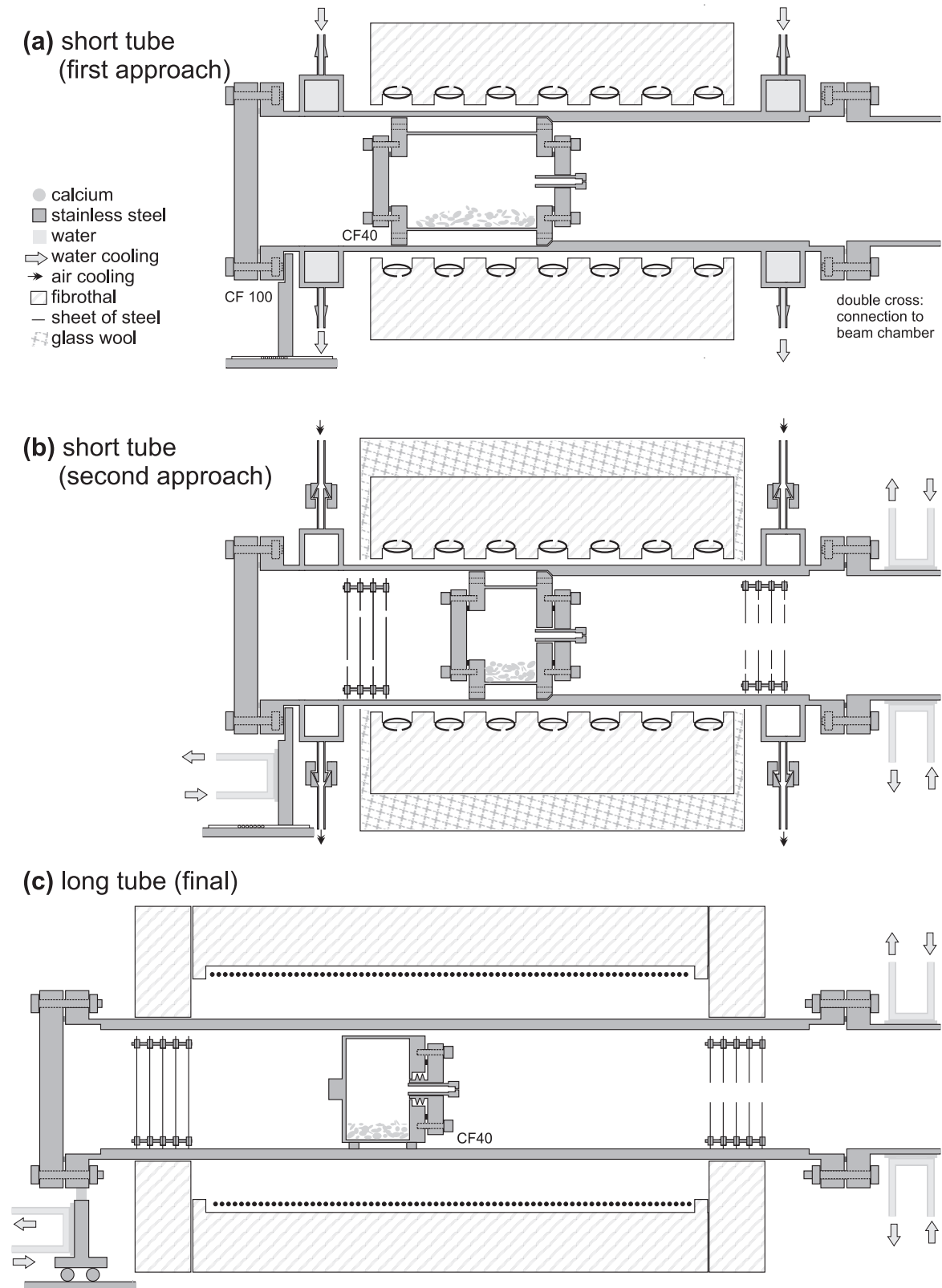
Figure 6.2: *The development of the oven. The cross sections are almost to scale but simplified to show the discussed details.*
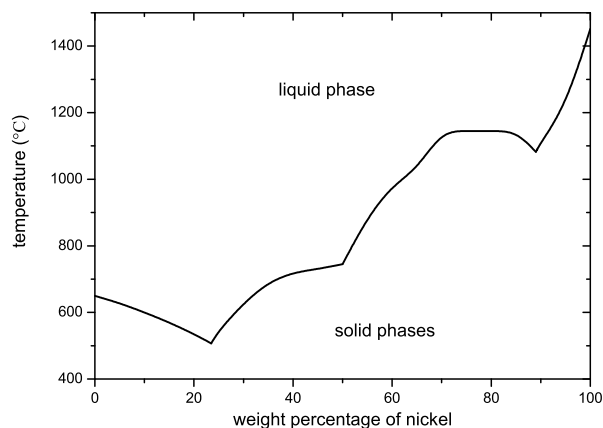
Figure 6.3: *Phase diagram of magnesium and nickel.[140] The steepness on the right hand side indicates that a small amount of magnesium on a nickel part reduces the melting temperature of that part, in our case the gasket.*

To our best knowledge was the alloy of nickel and calcium not investigated. Interestingly, phase diagrams of magnesium and nickel are available. The melting temperature of nickel with a small fraction of magnesium is significantly below the melting temperature of pure nickel (see Figure 6.3 at the right end side). This situation occurs if a nickel gasket is covered by a thin layer of liquid magnesium.

6.2.3   Re-opening the Oven

The oven is sealed by CF flanges and thighten with machine screws. Under the high temperatures the screws tend to seizure. Using screws from steel for high temperature applications and a high temperature anti-seize lubrication compound (Never-Seez) enabled the opening of the screws. Moreover, tapped holes in the flange were added to the flange outside the edge knife such that the oven can be opened by pushing the flange away from the oven with screws.

6.2.4   Undesired Heating

The vacuum chamber was getting very warm despite the water cooling acting at both ends of the oven tube. The temperatures reached 200°C already when the oven was at 800°C. The chamber is heated by radiation. Heat shields and additional cooling plates were installed. Moreover, the connectors for the water cooling at the end of the oven tube were extended by steel tubes to reduce the risk of melting water hoses. Also, this allows to cool with a flux of air, which allows for higher temperature of the ends of the tube.

6.2.5   Lack of Power

After sorting out the teething troubles discussed, a major problem remained: The oven did not reach the desired temperature while running the oven at full voltage. Five actions
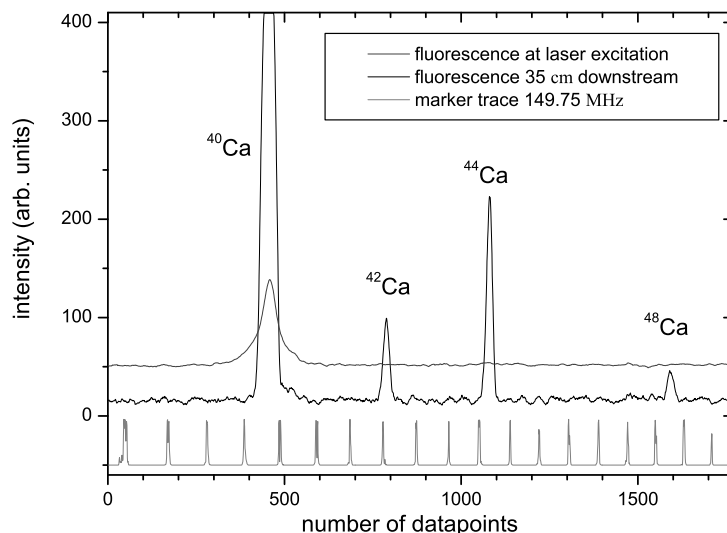
Figure 6.4: *Spectroscopy of the intercombination lines of several calcium isotopes. The laser excites atoms at the first interaction zone. The photomultiplier signal of this zone shows the stray laser light as a background. The Doppler width of the fluorescence recorded from the second interaction zone (which is used here as a detection zone only) is smaller because a spatial filter is between the zones. The free traveling of the atoms between the two interaction zones in the metastable state $4s\,4p\,{}^3P$ is an indicator for good beam conditions.*

were successively taken to trim the oven to higher temperature:

1. Heat shields were installed because an analysis revealed that the main loss channel of power is black body radiation inside the vacuum chamber. The analysis is discussed in Section 6.3.

2. The oven was shortened by reducing the length of the reservoir. The temperature of the oven tube is strongly depending on the position in beam direction. It is hottest in the middle but decreases almost linearly in both directions.

3. The water cooling was replaced by air cooling. Compressed air flows through the coolers. This increased the temperature at the coolers and thus also at the back end of the oven, which is the reference point for the oven temperature.

4. The heat losses from the heater to the laboratory directly were reduced by adding glass-wool and a metal box around the heater.

5. Finally, the voltage applied to the two resistance heaters was increased above the specifications.

A couple of runs were possible with about 140 V. This corresponds to sixty percent more power than specified with 110 V. The analysis of the heat losses allowed us to predict very precisely which temperature we could expect with which voltage. Unfortunately, the wire of one of the heaters burned out after some test runs.
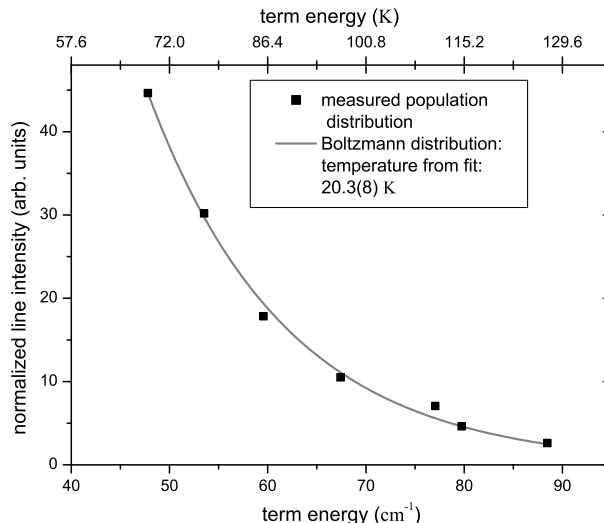
Figure 6.5: *Rotational temperature of K_2 measured on the 18–0 band of the A–X system. The line intensities are normalized by division by the degeneracy and the Hönl-London factor. The measured oven temperature during the measurement was 730 K. The derived rotational temperature of 20 K indicates that the cooling of the internal degrees of freedom of the dimer during the adiabatic expansion into the vacuum is as efficient as in a beam setup with a smaller distance between the first spatial selector and the nozzle.*

6.2.6   Summary

With the gathered experience we started the design of a second, improved system. The reasons to keep the concept of an external heating are manifold:

- We detected a beam of calcium atoms by laser spectroscopy on the intercombination line (see Figure 6.4).

- Running the oven filled with potassium allowed us to detect a beam of K_2 in Doppler-free laser spectroscopy of transitions of the A $^1\Sigma_u^+ \leftarrow$ X $^1\Sigma_g^+$ band. The rotational temperature is low (see Figure 6.5). This indicates that the cooling of the inner degrees of freedom during the expansion into vacuum does work even without a skimmer close to the nozzle.

- The nozzle of the oven was never clocked.

- Alignment of the oven is not a problem.

Before describing the improved system, our analysis of the loss processes is discussed in the following Section 6.3. It did help the understanding of the system and led to the design of the new system.
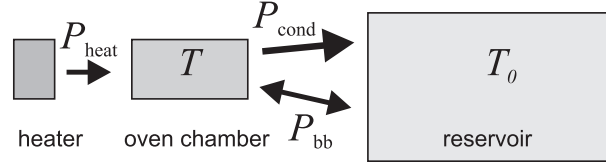
Figure 6.6: *Model for the thermodynamics of the oven system.*

6.3 Heat losses

In experimental setups, heat losses are not necessarily unwanted. They can also be used to set a temperature difference between two points of a heated material. Two types of losses are distinguished: losses due to heat conduction P_{cond} and losses due to black body radiation P_{bb}. They have a substantial different behavior as a function of the temperature T of the material. In this section, we want to utilize this phenomenon in order to understand our oven setup better. Heat convection is neglected since the air flow with contact to the hot surfaces is quite small.

A strongly simplified model of the oven is shown in Figure 6.6. The oven at temperature T is in contact with the lab at temperature $T_0 \approx 300$ K, which is treated as infinitely big reservoir. The air conditioning of the laboratory justifies this approximation by ensuring temperatures within ± 2 K. Two mechanisms couple oven and reservoir: First, heat conduction is proportional to the difference of temperature and a conductivity parameter C:

$$P_{\text{cond}} = C\left(T - T_0\right). \tag{6.1}$$

Second, for the black body radiation we assume that oven and reservoir act as a black body. It is proportional to the fourth power of the temperature of the emitter and to the surface area A. The total loss of energy per time unit due to black body radiation is thus

$$P_{\text{bb}} = B\left(T^4 - T_0^4\right) \text{ with} \tag{6.2}$$
$$B = A\sigma.$$

This is simply the Stefan-Bolzmann law with the corresponding constant σ, the Stefan-Bolzmann constant.

If oven is heated with a constant power P_{heat}, an temperature of the oven T will eventually reach an equilibrium T_{op} such that the losses compensate the heating power:

$$P_{\text{heat}} = P_{\text{cond}}\left(T_{\text{op}}\right) + P_{\text{bb}}\left(T_{\text{op}}\right). \tag{6.3}$$

If the heating is abruptly stopped, i.e., P_{heat} is set to zero, the oven will cool down until it reaches the temperature T_0. By analyzing the cool down curve $T(t)$, we can determine what the dominant loss process is. If the whole oven arrangement has a heat capacity of O, then the arrangement will change its temperature by $\mathrm{d}T$ for an energy flow of $P(t)$ in time $\mathrm{d}t$:

$$\mathrm{d}T = \frac{P(T)\cdot \mathrm{d}t}{O} \,. \tag{6.4}$$

| | C | B |
	(W/K)	(10^{-9}W/K^4)
(a) short oven (first approach)	0.23	1.31
(b) short oven (second approach)	0.87	0.47
(c) long oven tube (final)	1.07	0.54

Table 6.2: *Coefficients for loss channels of different oven setups. They are determined from the cool down curve and the applied heating power as described in the text and shown in Figure 6.7.*

Thus:

$$\frac{\mathrm{d}T}{\mathrm{d}t} = \frac{1}{O}\ P\left(t\right) = \frac{1}{O}\ \left[-P_{\mathrm{bb}}\left(T\right) - P_{\mathrm{cond}}\left(T\right)\right] \sim \frac{\mathrm{d}T}{\mathrm{d}t}\left(T\right) \tag{6.5}$$

Including equation (6.1) and equation (6.2) provides us with a model for the oven. The parameters B and C are derived in a fit to the measured curve. Since we do know P_{heat} from the operating voltage of the oven and the corresponding temperature T_{op}, it is easy to derive the parameter C and B, which characterize the oven arrangement.

Three different oven arrangements have been analyzed and characterized by this methods. The obtained parameters are summarized in Table 6.3. By analyzing the cool down curves like shown in Figure 6.7, the parameters describing loss channels 'conduction' and 'radiation' are derived. They are shown in Table 6.2. In our starting setup (a) the losses due to radiation are dominant. In setup (b), the changes described in Section 6.2 were applied. Most importantly, heat shields are now installed. The losses due to black body radiation are reduced by 60 percent but are still bigger than conduction losses above 500°C. The setup (c) will be introduced in the following. A bigger thickness of the oven tube increases the conduction losses and the heat capacity O.

6.4   Improved Oven Construction

The breakdown of the heater used in the first setup and with the new oven concept, gave us the opportunity to optimize our oven system. It is not enough to simply replace the two half-cylinder heater with more powerful heaters that resist higher temperatures: The temperature needed in the nozzle region is in this geometry about 200 K higher than the needed temperature. This might not only cause molecules to break up due to a too high nozzle temperature but also drives the steel of the oven tube very close to the melting point. The corrosion on the oven tube caused significant material loss already. In consequence, a longer oven tube was manufactured in the workshop of the institute.

The thickness of the walls for the oven tube is increased to tolerate the corrosion at high temperatures for longer times. No water coolers were installed: The cooling is done on the vacuum chamber in the beam forward direction and on the support of the oven tube at the back end.

The oven is again sealed by a nickel gasket but can only be opened at the front end. The pipe with nozzle is pressed into CF 40 flange, which was extended such that the path for vapor from the reservoir to the gasket is increased and the gasket less attacked. The
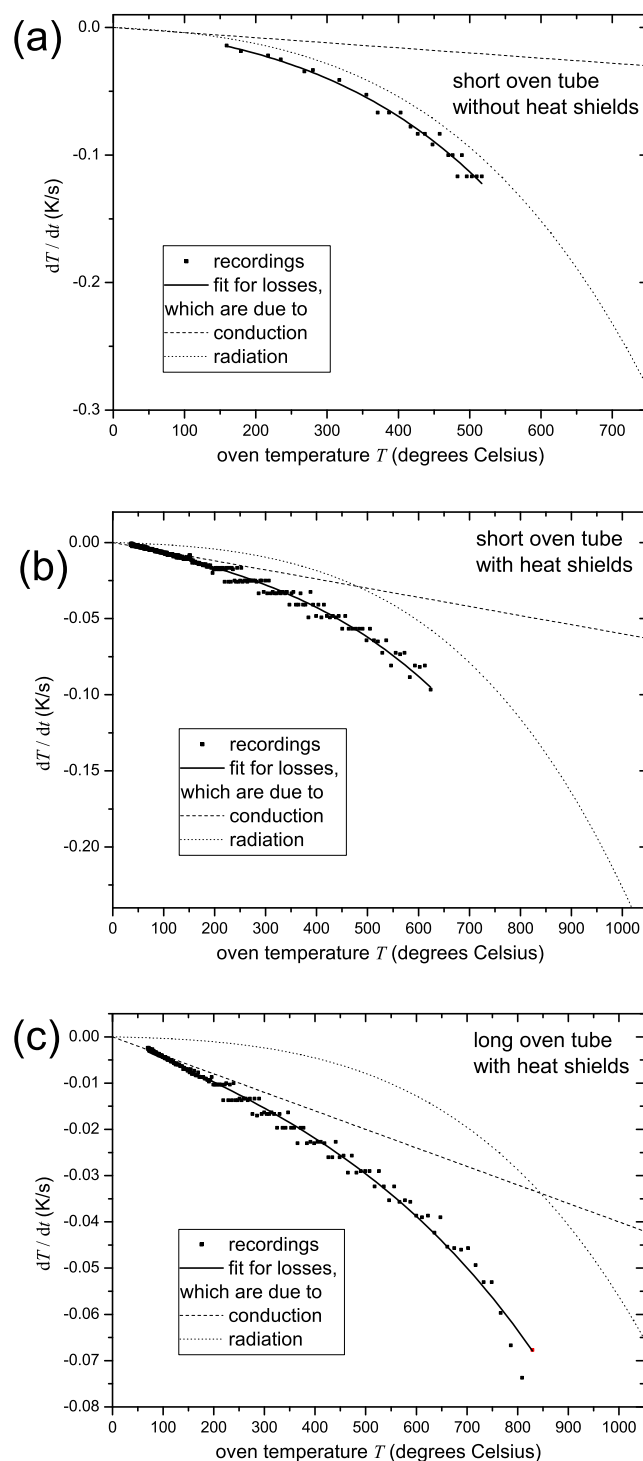
Figure 6.7: *Analysis of the loss channels of three different oven setups. The difference of* (b) *to* (a) *are additional heat shields that reduce the losses due to radiation. The setup* (c) *is with a longer oven tube (see Section 6.4), which also includes heat shields. The curves are obtained with a thermometer, that gives values in steps of* 1 K *above* 200°C, *which led to the grouping of the* dT/dt *values.*

	(a) short tube (first approach)	(b) short tube (second approach)	(c) long tube (final)
tube			
length	434 mm	434 mm	718 mm
outer diamter	100 mm	100 mm	108 mm
inner diamter	88 & 94 mm	88 & 94 mm	92 mm
heat shields	–	4 plates	5 plates
coolers	water	air	–
addit. cooling	–	chamber	chamber & oven support
heater			
types	2 half-cylinders	2 half-cylinders	1 tube
length of heater	300 mm	300 mm	500 mm
inner diameter	100 mm	100 mm	150 mm
max. temperature of heating element	$1\,150$°C	$1\,150$°C	$1\,300$°C
max. power specified	$1\,750$ W	$1\,750$ W	$7\,500$ W
max. power used	$1\,750$ W	$2\,650$ W	$2\,600$ W
additional insulation	wool	wool & metal box	end plates
oven			
length of oven	159 mm	112 mm	98 mm
reservoir length	90 mm	43 mm	58 mm
reservoir diameter	64 mm	64 mm	74 mm
reservoir volume	116 cm^3	55 cm^3	103 cm^3
refilling	back end	back end	front end
sealing	nickel	steel	nickel
steel of screws	A4	high temp.	high temp.
leakage	big	small	none
specialities	–	holes for thermocouples	holes for thermocouples & thread for removal
temperatures at maximal operation			
oven	(550°C)[a]	$1\,050$°C	$1\,020$°C
nozzle	(650°C)[a]	$1\,230$°C	$1\,100$°C
tube outside	850°C	$1\,270$°C	$1\,140$°C

Table 6.3: *Comparison of oven setups as illustrated in Figure 6.2.*

[a]The heater was switched off before an equilibrium was reached

back end of the oven was extended by a M16 thread for the removal of the oven with a stick with a corresponding thread. The oven tends to stick on the oven tube and some force needs to be applied.

The heating is now done with a single element. We use a tube with an inner diameter not only bigger than the oven tube but also bigger than the end flanges of the oven tube. Both ends are equipped with two half plates that close the gap between oven tube and heater. The wire of the heater is thicker and is specified for higher temperatures.

From first tests with the new oven setup it became evident that the heater is powerful enough to melt the oven tube, i.e., the vacuum chamber, before the wires of the heater burn out. Also the chamber might get warm very soon if the water cooling of the chamber breaks. In order to minimize the probability and the damage originating from not proper working parts or wrong usage of the equipment, an automatic interlock for the power supply of the heater was built. It monitors several temperatures and the water flow in the cooling circuit in order to give an alarm and interlock the heater in case of critical situations.

6.5   Outlook

With the reached oven setup, the list of requirements discussed in Section 6.1 is fulfilled with the apparatus. Comparing between the oven setup used for the experiments on potassium described in Chapter 3 and Chapter 4 and the oven discussed in this chapter leads to the following conclusions. The cooling of the inner degrees of freedom of the dimers is similar although no skimmer for a spatial selection of the particles is close to the nozzle. Collisions with residual gas in the oven chamber have no significant effect. With the new configuration, the alignment of the oven is less critical. A second observation is, that the temperature readings of the ovens are different. We expect that this is due to the way the thermocouple tips are placed in the chamber. We expect that the oven has to be run at higher temperature readings than originally intended. The current oven constructions is capable of oven temperatures, i.e., the coldest part of the reservoir, of up to 1150°C. The residual gas pressure is low enough since beam conditions are reached. All in all, the newly constructed and developed oven is able to compensate for the change of vapor pressure between alkali metals and alkali earth metals,

A second change appearing if one takes the step from the first to the second column in the periodic table of elements is the depth of the ground state of the dimers. Due to this, laser induced fluorescence is not so widely distributed among the spectra and the suppression of stray laser light is more difficult. If suppression by viewports in Brewster angle or with anti-reflection coating, irises for spatial filtering, or color glass and interference filter fail to help enough, an additional option is to collect the fluorescence with a bundle of optical fibers and shine the light though a monochromator. It would act as a tunable narrow band pass. A similar idea enabled the observation of asymptotic levels of Ca_2 in the heat-pipe experiment.[75] However, the spectral distribution of fluorescence is comparable to the spectroscopy starting from vibrational levels in alkali metal dimers that are populated by Franck-Condon pumping.

Chapter 7

Conclusion

Several experiments were carried out throughout the work presented in this thesis. All experiments are laser-spectroscopic experiments on particles prepared in beams. The precision was improved for several measured properties. The most important results are summarized in the following.

Potassium D lines

The D_1 and D_2 lines of the three stable isotopes of potassium ^{39}K, ^{40}K, and ^{41}K where re-measured with a precision of 40 kHz, i.e., with a fractional uncertainty of 2×10^{-10}. This was possible by using a self-referenced frequency comb generated from a pulsed femtosecond laser in combination with a Cs-clock. Improved parameter for the hyperfine structure of the $4p_{1/2}$ and $4p_{1/2}$ where derived as well as the isotope shift of the two lines. Inconsistencies of earlier literature values are resolved.

Lifetime of the 4p Levels of Potassium

In a spectroscopic experiment with K_2, the lifetimes of the $4p_{1/2}$ and $4p_{3/2}$ of ^{39}K were measured to $26.74\,(3)$ ns and $26.39\,(3)$ ns respectively. For this, the A $^1\Sigma_u^+$ state of ^{39}K$_2$ was investigated gap-free from the region known from conventional spectroscopy up to the dissociation limit. This allow for the interpretation of photoassociation data. Our model includes adiabatic curves in the long range region that are derived purely from atomic parameter. We include fine and hyperfine structure, retardational effects, and the dipole coupling between the 4s and the 4p state. The obtained data field is a good starting point for an extension of the analysis of the system A $^1\Sigma_u^+$–b $^3\Pi_u$, which is coupled by the spin-orbit interaction, up to the dissociation asymptote.

Dissociation Energy of the X $^1\Sigma_g^+$ state of K_2

As a further result of the A $^1\Sigma_u^+$ state, the dissociation energy of the X $^1\Sigma_g^+$ state could be derive because the atomic transition frequencies are known. It is found to be $D_0 = 4404.808(4)$ cm^{-1} with respect to $v = 0, J = 0$. This agrees with extrapolations from spectroscopic experiments of the ground state. However, we were able to reduce the uncertainty substantially.

Observation of Breakdown of the Born-Oppenheimer Approximation

By comparing asymptotic levels of the A $^1\Sigma_u^+$ state of two isotopomers of the potassium dimer, namely $^{39}K_2$ and $^{39}K\,^{41}K$, we were able to obtain information about the precision of the Born-Oppenheimer approximation for long range levels, i.e., for the energy regime relevant for photoassociation of ultracold atoms at the asymptote $4s + 4p$. The mass scaling of the potential curves accompanied by an adjustment of the atomic hyperfine structure parameter according to the isotope exchange describes the energy spacing to a precision of 2 MHz. However, deviation between observation and simulations with this description remain. Corrections to the interaction potential, i.e., to the Born-Oppenheimer approximation, allow for a satisfying description. It was not possible to observe a clear signature for the changeover of the resonant dipole-dipole interaction to a detuned dipole-dipole interaction, which is expected due to the isotope shift of the potassium D lines. This effect related to the heteronuclear character of $^{39}K\,^{41}K$ is washed out by the hyperfine structure, which so different between ^{39}K and ^{41}K.

Models for Laser-induced Change of Cold Collisions

We adapted a model, which is qualitatively often applied to simulate photoassociation spectra and the influence of near resonant light on atomic collisions, to describe laser induced changes of lineshapes of transitions between corresponding molecular levels for the example Na_2. Although the overall appearance of the experimental traces were reproduced, a big drawback was identified: the effect of the coupling laser field could not be quantitatively simulated with the adapted model. With additional density matrix simulation we verified that the observed lightshift corresponds to the calculated coupling strength.

Development of a Beam Source for Alkali Earth Metals

The progress development of a beam source for alkali earth dimers operating at 1000° C is reported. Many technical difficulties were overcome. Hope for a reliable, continuous, bright, yet cold beam of alkali earth metal dimers is well justified.

Outlook

Some of the studies should be continued. The study of the A $^1\Sigma_u^+$ state of K_2 can be continued in two ways: First, a coupled channel analysis for the entire internuclear distance can be undertaken. The data field on the A state obtained in this work is very rich and precise. Moreover, since experimental data for the b $^3\Pi_u$ state up to large internuclear separations is available, too, a good basis for a challenging analysis is set. Second, the study of the ground state asymptotes for two isotopomers can be now undertaken. This should then allow for the study of mass scaling for cold collisions, i.e., of the Born-Oppenheimer approximation.

The realization of a beam of calcium dimers will allow for experiments with unpreceding precision for long range states of calcium. Models and methods for dimers,

which were mainly developed and used for alkali metal dimers, can be tested and adjusted. Only with thorough experimental verification, these models will allow for precise descriptions of binary collisions of alkali earth metal atoms. These collisions are important for metrology of the intercombination line of alkali earth metal atoms. These lines are discussed candidates for a new frequency standard, and the systematic analysis of the scattering properties of the atoms will be important at the level of precision the proposals are aiming for. Collisional effects are less important if the atoms are kept isolated by optical lattices. However, an analysis of the coupling between light and atoms might need to take levels of dimers into account. Here, and for experiments aiming on the laser induced manipulation of cold collisions, a molecular beam can be useful for systematic studies of the coupling between a laser field and colliding atoms.

Appendix A

Molecular Dipole Coupling Strengths

This appendix is dedicated to the computation of laser-induced dipole coupling strengths between two molecular levels. We need to consider various angular momenta, both, describing the inner degrees of freedom of the molecules and the photons of a laser field. For diatomic molecules, the Hund's coupling cases (a) and (e) provide basis sets of angular wavefunctions. Typically, Hund's coupling case (e) is well suited for descriptions of cold collisions and Hund's case a) for deeply bound molecular levels. Regardless of the approximation, any molecular state can be associated with a total angular momentum F and its inversion symmetry $\pm$. The eigenstate can be described as a linear combination of angular momentum basis states with the same F and parity. We chose as a basis set of Hund's case (a) like wavefunctions, which are labeled by

$$|F,S,I,\Lambda,\Sigma,\Omega_I\rangle , \tag{A.1}$$

with the total spin S and the total nuclear angular momentum I. Their projections onto the molecular axis are Σ and Ω_I. The total angular momentum F includes the rotation of the molecule ell and has the projection onto the molecular frame $\Lambda+\Sigma+\Omega_I$. The linear combination of the angular wavefunctions varies with the internuclear distance R, thus:

$$|F,\pm\rangle = \sum_m a_m(R) \frac{1}{\sqrt{2}} \left[|F,S_m,I_m,\Lambda_m,\Sigma_m,\Omega_{Im}\rangle \pm (-1)^{F-S_m-I_m} |F,S_m,I_m,-\Lambda_m-\Sigma_m,-\Omega_{Im}\rangle \right] \tag{A.2}$$

Normalization is ensured by

$$\int \sum_m |a_m|^2 \, dR = 1 . \tag{A.3}$$

In the squared bracket the wavefunction is symmetrized with respect to an inversion of the orientation of the projection axis. For the special case $\Lambda_m = \Sigma_m = \Omega_{Im} = 0$ the two wavefunctions in the squared brackets are the same. For each combination of F, S_m, and I_m, only one parity exist. By replacing $1/\sqrt{2}$ by $1/2$ in equation (A.2) for this special case the correct normalization is ensured.

In order to describe the coupling of two molecular states induced by an external laser field with defined polarization in the lab frame we label the projection of F on the lab frame axis with M. The coupling strength of two states $|F, M, \pm\rangle$ and $|F', M', \pm'\rangle$ due to

an electric field $\vec{E}$ is in dipole approximation described by the Rabi frequency

$$^{\pm\pm'}\Omega_{FF'}^{MM'} = \frac{-1}{\hbar} \int_0^\infty \langle F,M,\pm|_R \ \vec{d}(R) \cdot \vec{E} \ |F',M',\pm'\rangle_R \ \mathrm{d}R \ , \qquad (A.4)$$

with the dipole transition operator $\vec{d}$ given in the lab frame. The three components of this vector are denoted by d_i ($i = -1, 0, 1$; spherical coordinates). They vary with the internuclear separation R. The R dependence of the wavefunctions is indicated by the index. In the case of linear polarized light ($\vec{E} = \overrightarrow{\epsilon_0} E_0$, with $\overrightarrow{\epsilon_0}$ being the unit vector for linear polarization) equation (A.4) is simplified by the following identity, which uses the definition of reduced matrix elements by Edmonds' equation (5.4.1):[141]

$$
\begin{aligned}
\langle F, M, \pm| \, \vec{d} \cdot \vec{E} \, |F', M', \pm'\rangle &= E_0 \, \langle F, M, \pm| \, \vec{d} \cdot \overrightarrow{\epsilon_0} \, |F', M', \pm'\rangle \qquad (A.5) \\
&= E_0 \, \langle F, M, \pm| \, d_0 \overrightarrow{\epsilon_0} \, |F', M', \pm'\rangle \\
&= E_0 \, (-1)^{F-M} \begin{pmatrix} F & 1 & F' \\ -M & 0 & M' \end{pmatrix} \langle F, \pm| \, d_0^\bullet \, |F', \pm'\rangle
\end{aligned}
$$

The equality $M = M'$ follows from choosing the lab frame axis to be parallel to the polarization vector ϵ_0 and can be seen in the 3J symbol. The dot of the $d_0^\bullet$ indicates that the information about the orientation in the lab frame of d_0 is already separated.

Because $d_0^\bullet$ is independent on I we introduce the total angular momentum without nuclear spin J (see for example Hund's case (a) without hyperfine effects) with Edmonds' definition of the 3J-symbol in equation (3.7.3):[141]

$$
\begin{aligned}
&|F,S,I,\Lambda,\Sigma,\Omega_I\rangle \qquad\qquad\qquad\qquad\qquad\qquad\qquad\qquad\qquad\qquad (A.6) \\
&= \underbrace{\sum_{J=|F-I|}^{F+I} |F,J,S,I,\Lambda,\Sigma\rangle \, \langle F, J, S, I, \Lambda, \Sigma| \ |F, S, I, \Lambda, \Sigma, \Omega_I\rangle}_{=1} \\
&= \sum_{J=|F-I|}^{F+I} (-1)^{J-I-\Lambda-\Sigma-\Omega_I} \, \sqrt{2F+1} \begin{pmatrix} J & I & F \\ \Lambda+\Sigma & \Omega_I & -\Lambda-\Sigma-\Omega_I \end{pmatrix} |F,J,S,I,\Lambda,\Sigma\rangle
\end{aligned}
$$

And we can de-couple the angular momentum I by introducing a 6J-symbol as defined by Edmonds[141] in equation (7.1.8). This gives coupling of reduced matrix elements of the form

$$
\begin{aligned}
&\langle F, J, S, I, \Lambda, \Sigma| \, d_0^\bullet \, |F', J', S', I', \Lambda', \Sigma'\rangle \qquad\qquad\qquad\qquad\qquad\qquad (A.7) \\
&= (-1)^{I+J+F} \, \sqrt{2F+1}\sqrt{2F'+1} \begin{Bmatrix} J & F & I \\ F' & J' & 1 \end{Bmatrix} \delta_{I,I'} \ \langle J, S, \Lambda, \Sigma| \, d_0^\bullet \, |J', S', \Lambda', \Sigma'\rangle \, .
\end{aligned}
$$

This reduction has to be undertaken a second time, this time for the spin S. Firstly, its projection is separated by introducing the total angular momentum without spin N:

$$
\begin{aligned}
|J,S,\Lambda,\Sigma\rangle &= \underbrace{\sum_{N=|J-S|}^{J+S} |J,N,S,\Lambda\rangle \, \langle J, N, S, \Lambda| \ |J, S, \Lambda, \Sigma\rangle}_{=1} \qquad\qquad\qquad (A.8) \\
&= \sum_{N=|J-S|}^{J+S} (-1)^{N-S-\Lambda-\Sigma} \, \sqrt{2J+1} \begin{pmatrix} N & S & J \\ \Lambda & \Sigma & -\Lambda-\Sigma \end{pmatrix} |J,N,S,\Lambda\rangle
\end{aligned}
$$

Secondly, the spin is decoupled by

$$\langle J, N, S, \Lambda | d_0^\bullet | J', N', S', \Lambda' \rangle \qquad (A.9)$$
$$= (-1)^{S+N+J} \sqrt{2J+1}\sqrt{2J'+1} \begin{Bmatrix} N & J & S \\ J' & N' & 1 \end{Bmatrix} \delta_{S,S'} \ \langle N, \Lambda | d_0^\bullet | N', \Lambda' \rangle .$$

Last, we need to consider that the wavefunctions are given in molecular frame whereas the dipole transition moment d_0 is given in the lab frame. In order to transform it to the molecular frame and to obtain b_q as dipole component in the molecular frame, one introduces a first rank spherical operator, namely the rotation operator $\mathrm{D}^1_{qq'}$:

$$d_q(R) = \sum_{q'=-1}^{1} \mathrm{D}^1_{qq'} b_{q'}(R) \qquad (q = -1, 0, 1) \qquad (A.10)$$

We end with the coupling strength for a dipole transition (see equations (4.6.1), (4.6.2), and (4.2.7) by Edmonds[141]):

$$\langle N, \Lambda | d_0^\bullet | N'\Lambda' \rangle = \langle N, \Lambda | \sum_{q'=-1}^{1} D^1_{\bullet q'} b_{q'} | N', \Lambda' \rangle \qquad (A.11)$$
$$= \sum_{q'=-1}^{1} (-1)^{N-\Lambda} \sqrt{2N'+1} \sqrt{2N+1} \begin{pmatrix} N & 1 & N' \\ \Lambda & q' & -\Lambda' \end{pmatrix} \langle \Lambda | b_{q'} | \Lambda' \rangle$$
$$= (-1)^{N-\Lambda} \sqrt{2N'+1} \sqrt{2N+1} \begin{pmatrix} N & 1 & N' \\ \Lambda & \Lambda'-\Lambda & -\Lambda' \end{pmatrix} \underbrace{\langle \Lambda | b_{\Lambda'-\Lambda} | \Lambda' \rangle}_{R \text{ dependend}} .$$

Back insertion of the equations leads to the calculation of transition dipole moments for molecular levels and along with equation (5.9) to Rabi frequencies for laser driven molecular transitions.

Appendix B

Spectroscopic Data of the A $^1\Sigma_u^+$ State of K$_2$

In this appendix, the spectrocopic data of the A $^1\Sigma_u^+$ state of K$_2$ is given. In Section B.1, the derived term energies of the levels are given. They are derived from the transition frequencies measured in our study. Those are given in Section B.2.

B.1   Term Energies

In Table B.1 we give a list of term energies as in a EPAPS file attached to our maniscript, which was given in Section 4.1. The listed properties are:

v_A	vibrational quantum number
J_A	roational quantum number
T_E	term energie in cm^{-1}
uncert.	uncertainty in 0.001 cm^{-1}, 9 cm^{-1} added if this term energy is removed from fit
obs-calc	difference of obsered and calculated term energy in 0.001 cm^{-1}
I	total nuclear moment of hyperfine structure component (only if hyperfine structure splitting is resolved)

v_A	J_A	T_e	uncert.	obs-calc	I	v_A	J_A	T_e	uncert.	obs-calc	I
84	8	15870.19565	9010	-70.48							
84	10	15871.278	9010	-57.68		84	12	15872.603	9010	-27.08	
84	14	15874.18255	9010	33.38		84	16	15876.1221	9010	229.35	
85	8	15909.94065	10	-180.21		85	10	15911.006	10	-175.55	
85	12	15912.295	10	-170.23		86	8	15949.32565	10	-160.53	
86	10	15950.381	10	-156.87		86	12	15951.655	10	-155.67	
87	8	15988.216	10	-139.91		87	10	15989.25928	10	-139.21	
87	12	15990.525	10	-135.24		88	8	16026.626	10	-97.83	
88	10	16027.663	10	-94.15		88	12	16028.9154	10	-92.3	

Table B.1: *Term energies of the A state of* ^{39}K$_2$.(continued)

v_A	J_A	T_e	uncert.	obs-calc I	v_A	J_A	T_e	uncert.	obs-calc I
89	8	16064.361	9010	-222.61	89	10	16065.396	9010	-211.55
89	12	16066.6454	9010	-201.33	90	8	16101.7823	10	-146.58
90	10	16102.799	10	-144.29	90	12	16104.0255	10	-145.44
91	8	16138.6323	10	-120.92	91	10	16139.6439	10	-114.06
91	12	16140.863	10	-110.89	92	8	16174.97	10	-80.14
92	10	16175.9683	10	-76.77	92	12	16177.17635	10	-72.78
93	8	16211.1017	9003.5	288.52	93	10	16212.184	9003.5	385.85
93	12	16213.543	9003.5	552.85	94	8	16245.8982	3.5	-137.63
94	10	16246.878	3.5	-132.7	94	12	16248.063	3.5	-127.47
95	8	16280.622	3.5	-89.62	95	10	16281.58948	3.5	-86.76
95	12	16282.76	3.5	-83.6	96	8	16314.785	3.5	-49.11
96	10	16315.741	3.5	-47.34	96	12	16316.8983	3.5	-44.79
97	8	16348.438	9003.5	41.07	97	10	16349.388	9003.5	47.4
97	12	16350.539	9003.5	56.43	98	8	16381.235	9003.5	-158.75
98	10	16382.17933	9003.5	-147.39	98	12	16383.3199	9003.5	-135.83
99	8	16413.7581	3.5	-60.31	99	10	16414.6825	3.5	-58.02
99	12	16415.801	3.5	-55.37	100	8	16445.64645	3.5	-18.39
100	10	16446.559	3.5	-16.93	100	12	16447.664	3.5	-14.45
101	8	16476.964	3.5	36.83	101	10	16477.86615	3.5	39.05
101	12	16478.958	3.5	41.91	102	8	16507.06875	9003.5	-530.99
102	10	16508.05675	9003.5	-431.59	102	12	16509.22215	9003.5	-341.47
103	8	16537.6287	3.5	-48.41	103	10	16538.50915	3.5	-45.08
103	12	16539.574	3.5	-41.62	104	8	16567.156	3.5	1.86
104	10	16568.022	3.5	2.36	104	12	16569.0706	3.5	3.66
105	8	16596.07	3.5	43.96	105	10	16596.9234	3.5	43.64
105	12	16597.9572	3.5	44.4	106	8	16624.476	9003.5	187.63
106	10	16625.332	9003.5	201.83	106	12	16626.37405	9003.5	225.29
107	8	16651.8687	3.5	-68.42	107	10	16652.704	3.5	-62.85
107	12	16653.7135	3.5	-57.33	108	8	16678.972	3.5	3.24
108	10	16679.79	3.5	3.71	108	12	16680.78	3.5	4.52
109	8	16705.4185	3.5	38.22	109	10	16706.2234	3.5	37.94
109	12	16707.1964	3.5	36.69	110	8	16731.2694	3.5	100.15
110	10	16732.064	3.5	102.03	110	12	16733.026	3.5	104.89
111	8	16756.15455	9003.5	-179.32	111	10	16756.9562	9003.5	-157.8
111	12	16757.921	9003.5	-136.9	112	8	16780.85955	3.5	-13.48
112	10	16781.626	3.5	-14.46	112	12	16782.5543	3.5	-14.67
113	8	16804.808	3.5	21.67	113	10	16805.56025	3.5	19.29
113	12	16806.471	3.5	17.04	114	8	16828.133	3.5	58.82
114	10	16828.87338	3.5	57.47	114	12	16829.769	3.5	55.7
115	8	16851.177	9003.5	439.21	115	10	16851.997	9003.5	530.46
115	12	16853.02575	9003.5	677.54	116	8	16872.737	3.5	-42.24
116	10	16873.452	3.5	-42.94	116	12	16874.317	3.5	-43.82
117	8	16894.201	3.5	-0.49	117	10	16894.90075	3.5	-3.35
117	12	16895.7463	3.5	-7.8	118	8	16915.0378	3.5	29.37
118	10	16915.72375	3.5	25.85	118	12	16916.554	3.5	22.01

Table B.1: *Term energies of the A state of ^{39}K$_2$.*(continued)

v_A	J_A	T_e	uncert.	obs-calc	I	v_A	J_A	T_e	uncert.	obs-calc	I
119	8	16935.3333	9003.5	128.43		119	10	16936.0169	9003.5	135.73	
119	12	16936.847	9003.5	147.68		120	8	16954.7173	3.5	-79.25	
120	10	16955.382	3.5	-77.67		120	12	16956.1848	3.5	-77.07	
121	8	16973.77548	5	-14.64		121	10	16974.421	5	-19.07	
121	12	16975.20268	5	-23.64		122	8	16992.208	5	14.86	
122	10	16992.84	5	10.05		122	12	16993.604	5	3.72	
123	8	17010.08019	5	66.14		123	10	17010.7	5	62.24	
123	12	17011.45307	5	60.86		124	8	17027.11981	9005	-142.27	
124	10	17027.7416	9005	-131.14		124	12	17028.492	9005	-119.4	
129	8	17105.2627	5	-19.32		129	10	17105.80404	5	-24.75	
129	12	17106.459	5	-31.09		130	8	17119.3366	5	12.3	
130	10	17119.8661	5	7.45		130	12	17120.504	5	-0.91	
131	8	17132.9115	5	36.23		131	10	17133.4272	5	29.86	
131	12	17134.05144	5	22.69		132	8	17146.0703	9005	122.41	
132	10	17146.5862	9005	128.35		132	12	17147.223	9005	148.42	
133	8	17158.52525	5	-29.95		133	10	17159.01836	5	-34.82	
133	12	17159.615	5	-40.43		134	8	17170.718	5	7.84	
134	10	17171.196	5	-0.34		134	12	17171.779	5	-5.3	
135	8	17182.452	5	26.33		135	10	17182.918	5	17.79	
135	12	17183.485	5	10.92		136	8	17193.774	5	59.56	
136	10	17194.23015	5	52.64		136	12	17194.786	5	48.52	
137	8	17204.511	9005	-78.		137	10	17204.96664	9005	-74.11	
137	12	17205.51521	9005	-71.83		138	8	17215.0547	5	-6.93	
138	10	17215.4909	5	-11.34		138	12	17216.0128	5	-22.24	
139	8	17225.15483	5	10.46		139	10	17225.57721	5	3.2	
139	12	17226.08772	5	-5.79		140	8	17234.878	5	28.98	
140	10	17235.28966	5	21.82		140	12	17235.788	5	13.74	
141	8	17243.89144	9005	-295.66		141	10	17244.37246	9005	-222.81	
141	12	17244.91886	9005	-169.96		142	8	17253.15	5	-19.89	
142	10	17253.542	5	-25.59		142	12	17254.0158	5	-32.65	
143	8	17261.80955	3.5	1.12		143	10	17262.189	3.5	-6.82	
143	12	17262.6477	3.5	-16.51		144	8	17270.1292	3.5	15.72	
144	10	17270.4992	3.5	8.47		144	12	17270.947	3.5	0.16	
145	8	17278.17105	9003.5	75.52		145	10	17278.5449	9003.5	82.1	
145	12	17279.006	9003.5	99.16		146	8	17285.741	3.5	-23.78	
146	10	17286.0927	3.5	-29.53		146	12	17286.5191	3.5	-35.3	
147	8	17293.1304	3.5	-0.67		147	10	17293.4712	3.5	-7.67	
147	12	17293.8824	3.5	-16.94		148	8	17300.217	3.5	13.12	
148	10	17300.54745	3.5	5.27		148	12	17300.9476	3.5	-3.56	
149	8	17307.03935	3.5	47.03		149	10	17307.368	3.5	46.74	
149	12	17307.768	3.5	49.07		150	8	17313.482	3.5	-23.07	
150	10	17313.797	3.5	-27.81		150	12	17314.178	3.5	-33.34	
151	8	17319.75	3.5	-0.48		151	10	17320.053	3.5	-8.16	
151	12	17320.42105	3.5	-15.66		152	8	17325.747	3.5	10.43	
152	10	17326.0428	3.5	4.48		152	12	17326.3992	3.5	-3.87	

Table B.1: *Term energies of the A state of* ^{39}K$_2$.(continued)

v_A	J_A	T_e	uncert.	obs-calc	I	v_A	J_A	T_e	uncert.	obs-calc	I
153	8	17331.523	9003.5	51.86		153	10	17331.8204	9003.5	56.3	
153	12	17332.1893	9003.5	71.09		154	8	17336.94985	3.5	-12.02	
154	10	17337.2276	3.5	-18.57		154	12	17337.565	3.5	-24.81	
155	8	17342.2206	3.5	4.26		155	10	17342.49055	3.5	-1.58	
155	12	17342.81555	3.5	-9.92		156	8	17347.2589	3.5	16.83	
156	10	17347.52	3.5	10.51		156	12	17347.8377	3.5	4.99	
157	8	17351.998	9003.5	-48.36		157	10	17352.2593	9003.5	-46.25	
157	12	17352.57685	9003.5	-41.96		158	8	17356.6376	3.5	1.49	
158	10	17356.884	3.5	-3.2		158	12	17357.18045	3.5	-10.21	
159	8	17361.032	3.5	14.27		159	10	17361.2693	3.5	8.47	
159	12	17361.557	3.5	2.37		160	8	17364.98905	9003.5	-208.46	
160	10	17365.2993	9003.5	-133.47		160	12	17365.6373	9003.5	-79.78	
161	8	17369.189	3.5	6.14		161	10	17369.411	3.5	0.54	
161	12	17369.6798	3.5	-5.71		162	8	17372.9994	3.5	16.7	
162	10	17373.2142	3.5	11.32		162	12	17373.4757	3.5	6.74	
163	8	17376.513	9003.5	-91.57		163	10	17376.75975	9003.5	-57.7	
163	12	17377.0341	9003.5	-40.56		164	8	17380.056	3.5	4.07	
164	10	17380.257	3.5	-0.51		164	12	17380.499	3.5	-6.91	
165	8	17383.343	3.5	13.25		165	10	17383.537	3.5	8.77	
165	12	17383.773	3.5	4.95		166	8	17386.43515	3.5	-10.41	
166	10	17386.625	3.5	-12.09		166	12	17386.8523	3.5	-16.18	
167	8	17389.4078	3.5	3.43		167	10	17389.5872	3.5	-1.88	
167	12	17389.807	3.5	-5.23		168	8	17392.264	9003.5	51.09	
168	10	17392.307	9003.5	-83.97		168	12	17392.49755	9003.5	-108.52	
169	8	17394.87485	3.5	-1.78		169	10	17395.04275	3.5	-5.44	
169	12	17395.2458	3.5	-9.62		170	8	17397.415	3.5	13.18	
170	10	17397.57945	3.5	12.43		170	12	17397.783	3.5	16.42	
171	8	17399.791	3.5	-2.91		171	10	17399.94595	3.5	-6.98	
171	12	17400.134	3.5	-11.01		172	8	17402.065	3.5	6.28	
172	10	17402.218	3.5	6.29		172	12	17402.4028	3.5	6.31	
173	8	17404.19845	3.5	-3.29		173	10	17404.3424	3.5	-6.46	
173	12	17404.5163	3.5	-10.24		174	8	17406.2364	3.5	8.16	
174	10	17406.3778	3.5	8.15		174	12	17406.5511	3.5	10.67	
175	8	17408.1411	3.5	-2.43		175	10	17408.2746	3.5	-4.78	
175	12	17408.4355	3.5	-7.93		176	8	17409.976	3.5	23.34	
176	10	17410.1026	3.5	19.49		176	12	17410.20125	3.5	-39.38	
177	8	17411.66	3.5	-0.49		177	10	17411.783	3.5	-2.7	
177	12	17411.93115	3.5	-5.73		178	8	17413.26235	3.5	-9.44	
178	10	17413.382	3.5	-9.9		178	12	17413.526	3.5	-10.93	
179	8	17414.79385	3.5	2.69		179	10	17414.906	3.5	-0.34	
179	12	17415.044	3.5	-1.39		180	8	17416.2218	3.5	-1.23	
180	10	17416.3295	3.5	-3.92		180	12	17416.4603	3.5	-6.38	
181	8	17417.60045	9003.5	28.82		181	10	17417.6386	9003.5	-38.78	
181	12	17417.787	9003.5	-18.03		182	8	17418.842	3.5	0.93	
182	10	17418.94115	3.5	-1.17		182	12	17419.06145	3.5	-3.08	

Table B.1: *Term energies of the A state of ^{39}K$_2$.*(continued)

v_A	J_A	T_e	uncert.	obs-calc	I	v_A	J_A	T_e	uncert.	obs-calc	I
183	8	17420.033	3.5	-2.3		183	10	17420.12805	3.5	-4.14	
183	12	17420.244	3.5	-5.13		184	8	17421.187	9003.5	28.9	
184	10	17421.225	9003.5	-25.77		184	12	17421.349	9003.5	-13.62	
185	2	17422.0668	3.5	8.16		185	4	17422.0978	3.5	6.33	
185	6	17422.1482	3.5	5.21		185	8	17422.215	3.5	1.89	
185	10	17422.301	3.5	-0.7		185	12	17422.407	3.5	-1.62	
186	2	17423.0601	3.5	3.91		186	4	17423.0915	3.5	3.94	
186	6	17423.1405	3.5	3.71		186	8	17423.286	9003.5	82.2	
186	10	17423.2856	3.5	-2.85		186	12	17423.3862	3.5	-4.39	
187	2	17423.985	3.5	-7.52		187	4	17424.0171	3.5	-5.39	
187	6	17424.0671	3.5	-2.41		188	2	17424.8788	3.5	7.96	
188	4	17424.9068	3.5	7.36		188	6	17424.9516	3.5	7.27	
189	2	17425.6988	3.5	4.6		189	4	17425.726	3.5	4.51	
189	6	17425.7676	3.5	3.29		191	2	17427.1858	3.5	-1.8	
191	4	17427.2115	3.5	-0.9		191	6	17427.2506	3.5	-0.7	
192	2	17427.8704	3.5	7.29		192	4	17427.8945	3.5	7.78	
192	6	17427.9327	3.5	8.93		193	2	17428.499	3.5	4.41	
193	4	17428.521	3.5	3.94		193	6	17428.5554	3.5	3.08	
194	2	17429.0876	3.5	3.13		194	4	17429.1087	3.5	2.85	
194	6	17429.1417	3.5	2.32		195	2	17429.6365	3.5	1.43	
195	4	17429.6573	3.5	1.91		195	6	17429.6888	3.5	1.53	
196	2	17430.1485	3.5	-0.1		196	4	17430.1679	3.5	0.	
196	6	17430.1987	3.5	0.52		198	2	17431.0776	3.5	4.84	
198	4	17431.0945	3.5	4.36		198	6	17431.1226	3.5	5.2	
199	2	17431.4852	3.5	-2.11		199	4	17431.5058	3.5	2.02	
199	6	17431.532	3.5	2.38		200	2	17431.8746	3.5	1.98	
200	4	17431.8898	3.5	1.57		200	6	17431.9144	3.5	1.7	
201	2	17432.2313	3.5	0.86		201	4	17432.2462	3.5	0.99	
201	6	17432.269	3.5	0.64		202	2	17432.5632	3.5	0.81	
202	4	17432.5769	3.5	0.54		202	6	17432.5982	3.5	-0.05	
203	2	17432.8703	3.5	0.25		203	4	17432.8834	3.5	0.16	
203	6	17432.9048	3.5	0.87		204	2	17433.1548	3.5	-0.1	
204	4	17433.1675	3.5	0.15		204	6	17433.1861	3.5	-0.78	
205	2	17433.4177	3.5	-0.64		205	4	17433.4295	3.5	-0.59	
205	6	17433.4467	3.5	-1.81		206	2	17433.6553	3.5	-6.43	
206	4	17433.6691	3.5	-3.7		206	6	17433.6885	3.5	-1.66	
207	2	17433.8904	3.5	4.07		207	4	17433.9023	3.5	5.54	
207	6	17433.9382	9003.5	25.11		208	2	17434.095	3.5	1.65	
208	4	17434.1051	3.5	1.95		208	6	17434.1207	3.5	2.19	
209	2	17434.2852	3.5	1.27		209	4	17434.2942	3.5	1.06	
209	6	17434.308	3.5	0.43		210	2	17434.4602	3.5	1.05	
210	4	17434.4686	3.5	0.81		210	6	17434.482	3.5	0.67	
211	2	17434.6202	3.5	0.16		211	4	17434.6286	3.5	0.46	
211	6	17434.6408	3.5	-0.04		212	2	17434.7673	3.5	-0.27	
212	4	17434.77496	3.5	-0.2		212	6	17434.7869	3.5	-0.14	

Table B.1: *Term energies of the A state of* ^{39}K$_2$.(continued)

v_A	J_A	T_e	uncert.	obs-calc	I	v_A	J_A	T_e	uncert.	obs-calc	I
213	2	17434.903	3.5	0.35		213	4	17434.9098	3.5	0.05	
213	6	17434.9201	3.5	-0.76		214	2	17435.0264	3.5	0.24	
214	4	17435.0327	3.5	-0.09		214	6	17435.0425	3.5	-0.67	
215	2	17435.1391	3.5	0.19		215	4	17435.1452	3.5	0.1	
215	6	17435.1549	3.5	0.12		216	2	17435.2424	3.5	0.72	
216	4	17435.2481	3.5	0.66		216	6	17435.2566	3.5	0.14	
218	2	17435.4192	3.5	-0.94		218	4	17435.4249	3.5	-0.22	
218	6	17435.4328	3.5	-0.11		219	2	17435.4974	3.5	0.24	
219	4	17435.502	3.5	0.22		219	6	17435.5092	3.5	0.19	
220	2	17435.5653	3.5	-1.56		220	4	17435.5697	3.5	-1.45	
220	6	17435.5758	3.5	-2.04		221	2	17435.6294	3.5	-0.43	
221	4	17435.6332	3.5	-0.59		221	6	17435.6392	3.5	-0.78	
222	2	17435.6888	3.5	2.21		222	4	17435.6874	3.5	-2.84	
222	6	17435.6948	3.5	-1.16		223	2	17435.7411	3.5	3.46	
223	4	17435.7389	3.5	-2.11		223	6	17435.7454	3.5	-0.87	
224	2	17435.7825	3.5	-0.94		224	4	17435.7858	3.5	-0.74	
224	6	17435.7921	3.5	0.72		225	2	17435.8238	3.5	-0.63	
225	4	17435.8266	3.5	-0.67		225	6	17435.8307	3.5	-1.01	
226	2	17435.8608	3.5	-0.23		226	4	17435.8631	3.5	-0.54	
226	6	17435.867	3.5	-0.7		227	2	17435.8933	3.5	-0.34	
227	4	17435.8959	3.5	-0.12		227	6	17435.8997	3.5	-0.04	
228	2	17435.9222	3.5	-0.41		228	4	17435.9244	3.5	-0.39	
228	6	17435.9274	3.5	-0.78		229	2	17435.9479	3.5	-0.38	
229	4	17435.9502	3.5	-0.06		229	6	17435.9532	3.5	-0.14	
230	2	17435.9711	3.5	0.14		230	4	17435.9727	3.5	-0.05	
230	6	17435.975	3.5	-0.55		231	2	17435.9906	3.5	-0.32	
231	4	17435.992	3.5	-0.54		231	6	17435.994	3.5	-1.07	
232	2	17436.0083	3.5	-0.13		232	3	17436.0084	1	-0.59	
232	4	17436.0097	3.5	-0.2		232	5	17436.0102	0.2	-0.08	
232	6	17436.0117	3.5	-0.48		232	8	17436.0148	1.2	0.02	
232	11	17436.0223	3.5	1.1		232	13	17436.0272	3.5	1.12	
233	2	17436.0231	1	-0.64		233	3	17436.0236	0.2	-0.03	
233	4	17436.0244	0.2	-0.02		233	5	17436.0253	0.2	-0.02	
233	6	17436.0273	1.2	0.67		233	8	17436.0294	1.2	0.01	
234	2	17436.0365	0.2	0.08		234	3	17436.0369	0.2	0.03	
234	4	17436.0377	0.2	0.09		234	5	17436.0385	0.2	0.11	
234	6	17436.04	1.2	0.4		234	8	17436.0421	1.2	0.02	
235	2	17436.0481	0.2	0.13		235	3	17436.0484	0.2	0.06	
235	4	17436.0492	0.2	0.17		235	5	17436.0498	0.2	0.11	
235	6	17436.0513	1.2	0.48		235	8	17436.0532	1.2	0.17	
236	2	17436.0581	0.2	0.18	3	236	3	17436.058	0.2	-0.21	2
236	4	17436.059	0.2	0.14	3	236	5	17436.0592	0.2	-0.21	2
236	6	17436.061	1.2	0.52		236	8	17436.0627	1.2	0.26	
236	2	17436.0577	0.2	0.05	1	236	4	17436.0587	0.2	0.11	1
237	2	17436.0666	0.2	0.15	3	237	3	17436.0665	0.2	-0.16	2

Table B.1: *Term energies of the A state of ^{39}K$_2$.*(continued)

v_A	J_A	T_e	uncert.	obs-calc	I	v_A	J_A	T_e	uncert.	obs-calc	I
237	4	17436.0674	0.2	0.12	3	237	5	17436.0676	0.2	-0.12	2
237	6	17436.0692	1.2	0.47		237	8	17436.0707	1.2	0.24	
237	2	17436.0662	0.2	0.08	1	237	3	17436.0663	0.2	-0.08	2
237	4	17436.067	0.2	0.05	1	237	5	17436.0673	0.2	-0.14	2
238	2	17436.0738	0.2	0.1	3	238	3	17436.0737	0.2	-0.12	2
238	4	17436.0746	0.2	0.16	3	238	5	17436.0746	0.2	-0.16	2
238	6	17436.0762	1.2	0.47		238	8	17436.0777	1.2	0.45	
238	2	17436.0734	0.2	0.1	1	238	3	17436.0734	0.2	-0.09	0
238	4	17436.074	0.2	-0.03	1	238	5	17436.0744	0.2	-0.02	0
239	2	17436.08	0.2	0.18	3	239	3	17436.0797	0.2	-0.15	2
239	4	17436.0806	0.2	0.14	3	239	5	17436.0805	0.2	-0.16	2
239	6	17436.0821	1.2	0.49		239	8	17436.0834	1.2	0.47	
239	2	17436.0794	0.2	0.07	1	239	3	17436.0794	0.2	-0.06	0
239	4	17436.08	0.2	0.04	1	239	5	17436.0802	0.2	-0.07	0
240	2	17436.0851	0.2	0.18	3	240	3	17436.0847	0.2	-0.14	2
240	4	17436.0857	0.2	0.22	3	240	5	17436.0854	0.2	-0.14	2
240	2	17436.0845	0.2	0.17	1	240	3	17436.0843	0.2	-0.1	0
240	4	17436.0851	0.2	0.23	1	240	5	17436.085	0.2	-0.1	0
241	2	17436.0894	0.2	0.29	3	241	3	17436.0889	0.2	-0.02	2
241	4	17436.0898	0.2	0.22	3	241	5	17436.0894	0.2	-0.11	2
241	2	17436.0886	0.2	0.19	1	241	3	17436.0885	0.2	0.06	0
241	4	17436.0891	0.2	0.23	1	241	5	17436.0891	0.2	0.07	0
242	2	17436.0928	0.2	0.33	3	242	3	17436.0921	0.2	-0.07	2
242	4	17436.0931	0.2	0.24	3	242	5	17436.0926	0.2	-0.06	2
242	2	17436.092	0.2	0.33	1	242	3	17436.0917	0.2	0.02	0
242	4	17436.0924	0.2	0.34	1	242	5	17436.0923	0.2	0.13	0
243	2	17436.0955	0.2	0.42	3	243	3	17436.0946	0.2	-0.1	2
243	4	17436.0957	0.2	0.3	3	243	5	17436.095	0.2	-0.1	2
243	2	17436.0945	0.2	0.29	1	243	3	17436.0942	0.2	-0.03	0
243	4	17436.0948	0.2	0.27	1	243	5	17436.0945	0.2	-0.14	0
244	2	17436.0975	0.2	0.49	3	244	3	17436.0966	0.2	-0.02	2
244	4	17436.0978	0.2	0.53	3	244	5	17436.0969	0.2	0.2	
244	2	17436.0965	0.2	0.35	1	244	3	17436.0962	0.2	0.02	0
244	4	17436.0969	0.2	0.5	1	244	5	17436.0962	0.2	-0.27	0
245	3	17436.098	0.2	-0.06	2	245	5	17436.0982	0.2	-0.12	2
245	3	17436.0978	0.2	0.18	0	245	5	17436.0978	0.2	-0.08	0

Table B.1: *Term energies of the A state of* $^{39}K_2$.

B.2   Transition Frequencies

The term energies given in Table B.1 are derived from measured transitions of the A–X band and level positions of the ground state taken from the analysis by Amiot et al.[67] In order to give the original spectroscopic information, all assigned, newly observed transition frequencies of the A–X band of ^{39}K are listed in Table B.2

line		line		line	
23-0				**25-0**	
R(0)	12632.0164			P(5)	12755.7875
P(1)	12631.8268			P(6)	12755.4998
R(1)	12632.0595			P(7)	12755.1764
P(2)	12631.6806			P(8)	12754.8199
R(2)	12632.0662			R(8)	12756.1268
P(3)	12631.4986			R(9)	12755.8874
R(3)	12632.0385			R(10)	12755.6116
P(4)	12631.2812			R(11)	12755.3010
R(4)	12631.9757			R(12)	12754.9569
P(5)	12631.0284				
R(5)	12631.8783				
R(6)	12631.7455				
R(7)	12631.5783				
R(8)	12631.3760				
R(9)	12631.1382				
84-27		**84-28**		**85-27**	
P(9)	13588.48○	P(9)	13516.57○	P(9)	13628.22○
R(9)	13589.56○	R(9)	13517.65○	R(9)	13629.29○
P(11)	13587.51○	P(11)	13515.61○	P(11)	13627.23○
R(11)	13588.83○	R(11)	13516.935○	R(11)	13628.52○
P(13)	13586.38○				
R(13)	13587.96○				
P(15)	13585.12○				
R(15)	13587.06○				
85-28		**86-27**		**86-28**	
P(9)	13556.32○	P(9)	13667.61○	P(9)	13595.70○
R(9)	13557.38○	R(9)	13668.66○	R(9)	13596.76○
P(11)	13555.34○	P(11)	13666.61○	P(11)	13594.71○
R(11)	13556.63○	R(11)	13667.88○	R(11)	13595.99○
87-27		**87-28**		**88-27**	
P(9)	13706.50○	P(9)	13634.59○	P(9)	13744.91○
R(9)	13707.54○	R(9)	13635.635○	R(9)	13745.95○
P(11)	13705.49○	P(11)	13633.59○	P(11)	13743.89○
R(11)	13706.75○	R(11)	13634.86○	R(11)	13745.14○

Table B.2: *Transition frequencies of A–X band of ^{39}K$_2$.* (continued)

line		line		line	
	88-28		**89-27**		**89-28**
P(9)	13673.00○	P(9)	13782.64○	P(9)	13710.74○
R(9)	13674.04○	R(9)	13783.68○	R(9)	13711.77○
P(11)	13671.99○	P(11)	13781.62○	P(11)	13709.73○
R(11)	13673.25○	R(11)	13782.87○	R(11)	13710.98○
	90-30		**90-28**		**91-30**
P(9)	13606.93○	P(9)	13748.16○	P(9)	13643.78○
R(9)	13607.945○	R(9)	13749.18○	R(9)	13644.79○
P(11)	13605.93○	P(11)	13747.135○	P(11)	13642.78○
R(11)	13607.16○	R(11)	13748.36○	R(11)	13644.00○
	91-28		**92-30**		**92-31**
P(9)	13785.01○	P(9)	13680.12○	P(9)	13610.82○
R(9)	13786.02○	R(9)	13681.12○	R(9)	13611.82○
P(11)	13783.98○	P(11)	13679.10○	P(11)	13609.82○
R(11)	13785.195○	R(11)	13680.31○	R(11)	13611.03○
	93-32		**93-31**		**94-32**
P(9)	13578.5511	P(9)	13646.9528	P(9)	13613.3474
R(9)	13579.6333	R(9)	13648.0347	R(9)	13614.3277
P(11)	13577.6500	P(11)	13646.0363	P(11)	13612.3441
R(11)	13579.0088	R(11)	13647.3948	R(11)	13613.529
	94-31		**95-32**		**95-31**
P(9)	13681.7495	P(9)	13648.0713	P(9)	13716.4736
R(9)	13682.7291	R(9)	13649.0392	R(9)	13717.4399
P(11)	13680.7305	P(11)	13647.0558	P(11)	13715.442
R(11)	13681.9157	R(11)	13648.2267	R(11)	13716.6119
	96-33		**96-32**		**97-33**
P(9)	13614.7431	P(9)	13682.2336	P(9)	13648.3961
R(9)	13615.6984	R(9)	13683.1898	R(9)	13649.3454
P(11)	13613.7309	P(11)	13681.2067	P(11)	13647.3792
R(11)	13614.8886	R(11)	13682.3644	R(11)	13648.5296
	97-32		**98-34**		**98-33**
P(9)	13715.8877	P(9)	13614.6260	P(9)	13681.1922
R(9)	13716.8381	R(9)	13615.5711	R(9)	13682.1370
P(11)	13714.8542	P(11)	13613.619	P(11)	13680.1691
R(11)	13716.0057	R(11)	13614.7595	R(11)	13681.3103

Table B.2: *Transition frequencies of A–X band of ^{39}K$_2$.* (continued)

line		line		line	
	99-34		**99-33**		**100-35**
P(9)	13647.1495	P(9)	13713.7155	P(9)	13613.4115
R(9)	13648.0739	R(9)	13714.6401	R(9)	13614.3237
P(11)	13646.1224	P(11)	13712.6725	P(11)	13612.3893
R(11)	13647.2412	R(11)	13713.7915	R(11)	13613.4939
	100-34		**101-35**		**101-34**
P(9)	13679.0373	P(9)	13644.7292	P(9)	13710.3548
R(9)	13679.9496	R(9)	13645.6313	R(9)	13711.2564
P(11)	13677.9979	P(11)	13643.6964	P(11)	13709.306
R(11)	13679.1031	R(11)	13644.7882	R(11)	13710.3983
	102-36		**102-35**		**103-36**
P(9)	13610.1637	P(9)	13674.8335	P(9)	13640.7241
R(9)	13611.1520	R(9)	13675.8216	R(9)	13641.6042
P(11)	13609.2342	P(11)	13673.8856	P(11)	13639.6856
R(11)	13610.3989	R(11)	13675.0521	R(11)	13640.751
	103-35		**104-35**		**104-36**
P(9)	13705.393	P(9)	13734.9208	P(9)	13670.2505
R(9)	13706.2736	R(9)	13735.7873	R(9)	13671.1176
P(11)	13704.3396	P(11)	13733.8517	P(11)	13669.199
R(11)	13705.4027	R(11)	13734.9004	R(11)	13670.2475
	105-35		**105-36**		**106-35**
P(9)	13763.8345	P(9)	13699.1649	P(9)	13792.2402
R(9)	13764.6881	R(9)	13700.0186	R(9)	13793.0967
P(11)	13762.7522	P(11)	13698.1011	P(11)	13791.1624
R(11)	13763.7866	R(11)	13699.1345	R(11)	13792.2033
	106-36		**107-37**		**107-36**
P(9)	13727.5705	P(9)	13691.2664	P(9)	13754.9639
R(9)	13728.4264	R(9)	13692.1028	P(11)	13753.8802
P(11)	13726.5086	P(11)	13690.2007	R(11)	13754.8899
R(11)	13727.5515	R(11)	13691.2111		
	108-37		**108-36**		**109-37**
P(9)	13718.3691	P(9)	13782.0677	P(9)	13744.8170
R(9)	13719.1879	R(9)	13782.8847	P(11)	13743.7203
P(11)	13717.2872	P(11)	13780.9662	R(11)	13744.6938
R(11)	13718.2767	R(11)	13781.9564		

Table B.2: *Transition frequencies of A–X band of ^{39}K$_2$. (continued)*

line		line		line	
	109-38		**110-37**		**110-38**
P(9)	13682.1094	P(9)	13770.6674	P(9)	13707.9608
R(9)	13682.9151	R(9)	13771.4613	R(9)	13708.7550
P(11)	13681.0317	P(11)	13769.5616	P(11)	13706.8729
R(11)	13682.0046	R(11)	13770.5228	R(11)	13707.8339
	111-37		**111-38**		**112-38**
P(9)	13795.5524	P(9)	13732.8461	P(9)	13757.5506
R(9)	13796.3542	R(9)	13733.6474	R(9)	13758.3179
P(11)	13794.4532	P(11)	13731.7650	R(11)	13757.3632
R(11)	13795.4178	R(11)	13732.7298		
	112-39		**113-38**		**113-39**
P(9)	13695.8529	P(9)	13781.4991	P(9)	13719.8004
R(9)	13696.6192	R(9)	13782.2517	R(9)	13720.5525
P(11)	13694.7545	P(11)	13780.3692	P(11)	13718.6886
R(11)	13695.6820	R(11)	13781.2789	R(11)	13719.5988
	114-38		**114-39**		**115-39**
P(9)	13804.8248	P(9)	13743.1262	P(9)	13766.1700
R(9)	13805.5649	R(9)	13743.8666	R(9)	13766.9907
P(11)	13803.6825	P(11)	13742.0005	P(11)	13765.1249
R(11)	13804.5781	R(11)	13742.8966	R(11)	13766.1541
	115-40		**116-39**		**116-40**
P(9)	13705.4981	P(9)	13787.7303	P(9)	13727.0584
R(9)	13706.3192	R(9)	13788.4449	R(9)	13727.7732
P(11)	13704.4719	P(11)	13786.5808	P(11)	13725.9270
R(11)	13705.5008	R(11)	13787.4449	R(11)	13726.7922
	117-40		**117-39**		**118-40**
P(9)	13748.523	P(9)	13809.1938	P(9)	13769.3592
R(9)	13749.2222	R(9)	13809.8934	R(9)	13770.0458
P(11)	13747.3758	P(11)	13808.0294	P(11)	13768.1983
R(11)	13748.2212	R(11)	13808.8748	R(11)	13769.0291
	119-40		**120-40**		**121-38**
P(9)	13789.6547	P(9)	13809.0387	P(9)	13950.46688
R(9)	13790.3381	R(9)	13809.7032	R(9)	13951.11223
P(11)	13788.4923	P(11)	13807.8577	P(11)	13949.22911
R(11)	13789.3226	R(11)	13808.6600	R(11)	13950.01108

Table B.2: *Transition frequencies of A–X band of ^{39}K$_2$.* (continued)

line		line		line	
	122-38		**123-38**		**124-38**
P(9)	13968.89937	P(9)	13986.77159	P(9)	14003.81121
R(9)	13969.53175	R(9)	13987.39211	R(9)	14004.43268
P(11)	13967.64818	P(11)	13985.50829	P(11)	14002.55028
R(11)	13968.41283	R(11)	13986.26147	R(11)	14003.30030
	129-38		**129-39**		**130-38**
P(9)	14081.95383	P(9)	14020.25603	P(9)	14096.02853
R(9)	14082.49643	R(9)	14020.79543	R(9)	14096.55961
P(11)	14080.61254	P(11)	14018.93275	R(11)	14095.31219
R(11)	14081.26746	R(11)	14019.58689		
	130-39		**131-38**		**131-39**
P(9)	14034.32903	R(9)	14110.11907	P(9)	14047.90454
R(9)	14034.85771	P(11)	14108.23690	R(9)	14048.41965
P(11)	14032.99358			P(11)	14046.55432
R(11)	14033.63161			R(11)	14047.17964
	132-38		**132-39**		**133-38**
P(9)	14122.76158	P(9)	14061.06345	P(9)	14135.21665
P(11)	14121.39461	R(9)	14061.57927	R(11)	14134.42278
R(11)	14122.03045	R(11)	14060.35177		
	133-39		**134-38**		**134-39**
R(9)	14074.01093	P(9)	14147.41021	P(9)	14085.71107
P(11)	14072.14698	R(11)	14146.58817	R(9)	14086.18922
R(11)	14072.74426			P(11)	14084.32434
				R(11)	14084.90564
	135-38		**135-39**		**137-38**
P(9)	14159.14393	P(9)	14097.44360	P(9)	14181.20136
R(9)	14159.60978	R(9)	14097.91145	R(11)	14180.32288
P(11)	14157.72749	P(11)	14096.04612		
R(11)	14158.29268	R(11)	14096.61439		
	137-39		**138-38**		**138-39**
P(9)	14119.50567	P(9)	14191.74513	P(9)	14130.04858
R(9)	14119.95789	R(11)	14190.82156	R(9)	14130.48419
P(11)	14118.09658			P(11)	14128.6188
R(11)	14118.64413			R(11)	14129.14057

Table B.2: *Transition frequencies of A–X band of ^{39}K$_2$.* (continued)

line		line		line	
139-38		**139-39**		**140-38**	
P(9)	14201.84593	P(9)	14140.14812	P(9)	14211.57006
R(9)	14202.26796	R(9)	14140.57048	R(9)	14211.97938
P(11)	14200.38599	R(11)	14139.21633	P(11)	14210.09857
R(11)	14200.89570			R(11)	14210.59666
140-39		**141-38**		**141-39**	
P(9)	14149.87038	P(9)	14220.58018	P(9)	14158.88709
R(9)	14150.28382	R(11)	14219.72621	R(9)	14159.36675
R(11)	14148.91594			P(11)	14157.49936
				R(11)	14158.04810
142-38		**142-39**		**143-38**	
P(9)	14229.84195	P(9)	14168.14206	P(9)	14238.5011
P(11)	14228.3508	R(9)	14168.53428	R(11)	14237.4566
R(11)	14228.8244	P(11)	14166.67145		
		R(11)	14167.1438		
143-39		**144-38**		**144-39**	
P(9)	14176.8024	P(9)	14246.8204	P(9)	14185.1223
R(9)	14177.1819	R(11)	14245.7556	R(9)	14185.4916
P(11)	14175.3172			P(11)	14183.6279
R(11)	14175.7754			R(11)	14184.0743
145-38		**145-39**		**146-38**	
P(9)	14254.8627	P(9)	14193.1638	P(9)	14262.4320
R(11)	14253.8142	R(9)	14193.5384	R(11)	14261.3277
		P(11)	14191.6725		
		R(11)	14192.1343		
146-39		**147-39**		**147-40**	
P(9)	14200.7349	P(9)	14208.1232	P(9)	14147.4520
R(9)	14201.0852	R(9)	14208.4645	R(9)	14147.7922
P(11)	14199.2214	R(11)	14207.0102	R(11)	14146.3580
R(11)	14199.6471				
148-39		**148-40**		**149-39**	
P(9)	14215.2099	P(9)	14154.5375	P(9)	14222.0316
R(11)	14214.0755	R(9)	14154.8691	R(9)	14222.3613
		P(11)	14153.0224	R(11)	14220.8964
		R(11)	14153.4231		

Table B.2: *Transition frequencies of A–X band of* ^{39}K$_2$. (continued)

line		line		line	
	149-40		**150-39**		**150-40**
P(9)	14161.3615	P(9)	14228.4752	P(9)	14167.8032
R(9)	14161.6893	R(11)	14227.3068	R(9)	14168.1191
R(11)	14160.2432			P(11)	14166.2720
				R(11)	14166.6534
	151-39		**151-40**		**152-39**
P(9)	14234.7436	P(9)	14174.0707	P(9)	14240.7400
R(11)	14233.5492	R(9)	14174.3748	R(11)	14239.5279
		P(11)	14172.5284		
		R(11)	14172.8963		
	152-40		**153-39**		**153-40**
P(9)	14180.0687	P(9)	14246.5160	P(9)	14185.8443
R(9)	14180.3638	R(11)	14245.3179	R(9)	14186.1417
P(11)	14178.5184			P(11)	14184.2956
R(11)	14178.8739			R(11)	14184.6641
	154-39		**154-40**		**155-39**
P(9)	14251.9428	P(9)	14191.2713	P(9)	14257.2137
R(11)	14250.6936	R(9)	14191.549	R(11)	14255.9438
		P(11)	14189.7028		
		R(11)	14190.0405		
	155-40		**156-39**		**156-40**
P(9)	14196.5419	P(9)	14262.2522	P(9)	14201.5800
R(9)	14196.8114	R(11)	14260.9669	R(9)	14201.8421
P(11)	14194.9663			P(11)	14199.9949
R(11)	14195.2907			R(11)	14200.3119
	157-39		**157-40**		**158-39**
P(9)	14266.9908	P(9)	14206.3187	P(9)	14271.6312
R(11)	14265.7052	R(9)	14206.581	R(11)	14270.3088
		P(11)	14204.7342		
		R(11)	14205.0519		
	158-40		**159-39**		**159-40**
P(9)	14210.9584	P(9)	14276.0249	P(9)	14215.3534
R(9)	14211.2053	R(11)	14274.6851	R(9)	14215.5908
P(11)	14209.3597			P(11)	14213.7443
R(11)	14209.6555			R(11)	14214.0315

Table B.2: *Transition frequencies of A–X band of* ^{39}*K$_2$.* (continued)

line		line		line	
	160-40		**160-41**		**161-40**
P(9)	14219.3105	P(9)	14159.6848	P(9)	14223.5112
R(9)	14219.6201	R(9)	14159.9946	R(11)	14222.1566
P(11)	14217.7757	P(11)	14158.1680		
R(11)	14218.1124	R(11)	14158.5062		
	161-41		**162-40**		**162-41**
P(9)	14163.8847	P(9)	14227.3207	P(9)	14167.6953
R(9)	14164.1063	R(11)	14225.9515	R(9)	14167.9106
P(11)	14162.2803			P(11)	14166.0824
R(11)	14162.547			R(11)	14166.3438
	163-40		**163-41**		**164-40**
P(9)	14230.8357	P(9)	14171.2076	P(9)	14234.3772
R(11)	14229.5093	R(9)	14171.4554	R(11)	14232.9748
		P(11)	14169.6287		
		R(11)	14169.9029		
	164-41		**165-40**		**165-41**
P(9)	14174.7518	P(9)	14237.6647	P(9)	14178.0376
R(9)	14174.9520	R(11)	14236.2478	R(9)	14178.2326
P(11)	14173.1258			P(11)	14176.4054
R(11)	14173.3681			R(11)	14176.6412
	166-40		**166-41**		**167-40**
P(9)	14240.7566	P(9)	14181.1309	P(9)	14243.7287
R(11)	14239.3279	R(9)	14181.3202	R(11)	14242.2826
		P(11)	14179.4934		
		R(11)	14179.7207		
	167-41		**168-40**		**168-41**
P(9)	14184.1041	P(9)	14246.5861	P(9)	14186.9597
R(9)	14184.2823	R(9)	14246.6283	R(9)	14187.0027
P(11)	14182.4567	R(11)	14244.9728	P(11)	14185.1768
R(11)	14182.6749			R(11)	14185.3663
	169-40		**169-41**		**170-40**
P(9)	14249.1968	P(9)	14189.5701	P(9)	14251.7373
R(11)	14247.7215	R(9)	14189.7385	R(11)	14250.2587
		P(11)	14187.9116		
		R(11)	14188.1141		

Table B.2: *Transition frequencies of A–X band of* $^{39}K_2$. (continued)

line		line		line	
	170-41		**171-40**		**171-41**
P(9)	14192.1099	P(9)	14254.1121	P(9)	14194.4862
R(9)	14192.2752	R(11)	14252.6096	R(9)	14194.6418
P(11)	14190.4483			P(11)	14192.8147
R(11)	14190.6518			R(11)	14193.0033
	172-40		**172-41**		**173-40**
P(9)	14256.3872	P(9)	14196.7609	P(9)	14258.5197
R(11)	14254.8785	R(9)	14196.9134	R(11)	14256.9915
		P(11)	14195.0872		
		R(11)	14195.2711		
	173-41		**174-40**		**174-41**
P(9)	14198.8944	P(9)	14260.5575	P(9)	14200.9325
R(9)	14199.0382	R(11)	14259.0264	R(9)	14201.0734
P(11)	14197.2112			P(11)	14199.2467
R(11)	14197.3851			R(11)	14199.4197
	175-40		**175-41**		**176-40**
P(9)	14262.4626	P(9)	14202.8368	P(9)	14264.2973
R(11)	14260.9109	R(9)	14202.9703	R(11)	14262.6771
		P(11)	14201.1435		
		R(11)	14201.3041		
	176-41		**177-40**		**177-41**
P(9)	14204.6714	P(9)	14265.9822	P(9)	14206.3552
R(9)	14204.7995	R(11)	14264.4068	R(9)	14206.4789
P(11)	14202.9703			P(11)	14204.6512
R(11)	14203.0694			R(11)	14204.7995
	178-40		**178-41**		**179-40**
P(9)	14267.5837	P(9)	14207.9582	P(9)	14269.1157
R(11)	14266.0019	R(9)	14208.0783	R(11)	14267.5189
		P(11)	14206.2509		
		R(11)	14206.3941		
	179-41		**180-40**		**180-41**
P(9)	14209.4892	P(9)	14270.5433	P(9)	14210.9174
R(9)	14209.6022	R(11)	14268.9351	R(9)	14211.0252
P(11)	14207.7753			P(11)	14209.1983
R(11)	14207.9128			R(11)	14209.3294

Table B.2: *Transition frequencies of A–X band of* ^{39}K$_2$. (continued)

line		line		line	
	181-40		**181-41**		**182-40**
P(9)	14271.9214	P(9)	14212.2967	P(9)	14273.1642
R(11)	14270.2623	R(9)	14212.3347	R(11)	14271.5363
		P(11)	14210.5071		
		R(11)	14210.6558		
	182-41		**183-40**		**183-41**
P(9)	14213.5377	P(9)	14274.3542	P(9)	14214.7286
R(9)	14213.6366	R(11)	14272.7194	R(9)	14214.824
P(11)	14211.8103			P(11)	14212.9967
R(11)	14211.9306			R(11)	14213.1124
	184-40		**184-41**		**185-40**
P(9)	14275.5085	P(9)	14215.8834	P(9)	14276.5362
R(9)	14275.5467	R(9)	14215.9205	R(11)	14274.8816
P(11)	14273.7000	P(11)	14214.0934		
R(11)	14273.8244	R(11)	14214.2176		
	185-41		**186-40**		**186-41**
P(3)	14220.1568	R(11)	14275.8613	P(3)	14221.1501
R(3)	14220.1882			R(3)	14221.1814
P(5)	14219.4040			P(5)	14220.3982
R(5)	14219.4548			R(5)	14220.4471
P(9)	14216.9103			P(9)	14217.9019
R(9)	14216.9968			R(9)	14217.9812
P(11)	14215.1698			P(11)	14216.1546
R(11)	14215.2759			R(11)	14216.2551
	187-41		**188-41**		**189-41**
P(3)	14222.0750	P(3)	14222.9688	P(3)	14223.7888
R(3)	14222.1073	R(3)	14222.997	R(3)	14223.8161
P(5)	14221.3234	P(5)	14222.2131	P(5)	14223.0324
R(5)	14221.3737	R(5)	14222.2582	R(5)	14223.0742
P(9)	14218.82022				
R(9)	14218.90264				
P(11)	14217.07564				
R(11)	14217.17541				
	191-41		**192-41**		**193-41**
P(3)	14225.2758	P(3)	14225.9604	P(3)	14226.5890
R(3)	14225.3015	R(3)	14225.9839	R(3)	14226.6110
P(5)	14224.5180	P(5)	14225.2017	P(5)	14225.8276
R(5)	14224.5572	R(5)	14225.2393	R(5)	14225.8620

Table B.2: *Transition frequencies of A–X band of ^{39}K$_2$.* (continued)

line		line		line	
	194-41		**195-41**		**196-41**
P(3)	14227.1776	P(3)	14227.7265	P(3)	14228.2385
R(3)	14227.1984	R(3)	14227.7472	R(3)	14228.2579
P(5)	14226.4155	P(5)	14226.9640	P(5)	14227.4745
R(5)	14226.4483	R(5)	14226.9954	R(5)	14227.5053
	198-41		**199-41**		**200-41**
P(3)	14229.1676	P(3)	14229.5752	P(3)	14229.9646
R(3)	14229.1846	R(3)	14229.5960	R(3)	14229.9805
P(5)	14228.4009	P(5)	14228.8122	P(5)	14229.1957
R(5)	14228.4292	R(5)	14228.8386	R(5)	14229.2210
	201-41		**202-41**		**203-41**
P(3)	14230.3213	P(3)	14230.6532	P(3)	14230.9603
R(3)	14230.3365	R(3)	14230.6672	R(3)	14230.9731
P(5)	14229.5525	P(5)	14229.8831	P(5)	14230.1903
R(5)	14229.5756	R(5)	14229.9048	R(5)	14230.2114
	204-41		**205-41**		**206-41**
P(3)	14231.2448	P(3)	14231.5077	P(3)	14231.7453
R(3)	14231.2578	R(3)	14231.5196	R(3)	14231.7590
P(5)	14230.4738	P(5)	14230.7359	P(5)	14230.9757
R(5)	14230.4927	R(5)	14230.7533	R(5)	14230.9951
	207-41		**208-41**		**209-41**
P(3)	14231.9804	P(3)	14232.185	P(3)	14232.3752
R(3)	14231.992	R(3)	14232.1953	R(3)	14232.3841
P(5)	14231.2092	P(5)	14231.4115	P(5)	14231.6009
R(5)	14231.2448	R(5)	14231.4273	R(5)	14231.6146
	210-41		**211-41**		**212-41**
P(3)	14232.5502	P(3)	14232.7102	P(3)	14232.8573
R(3)	14232.5587	R(3)	14232.7186	R(3)	14232.8646
P(5)	14231.7750	P(5)	14231.9351	P(5)	14232.0819
R(5)	14231.7886	R(5)	14231.9474	R(5)	14232.0935
	213-41		**214-41**		**215-41**
P(3)	14232.9930	P(3)	14233.1164	P(3)	14233.2291
R(3)	14233.0000	R(3)	14233.1233	R(3)	14233.2349
P(5)	14232.2162	P(5)	14232.3387	P(5)	14232.4520
R(5)	14232.2267	R(5)	14232.3491	R(5)	14232.4615

Table B.2: *Transition frequencies of A–X band of* ^{39}K$_2$. (continued)

line		line		line	
	216-41		**218-41**		**219-41**
P(3)	14233.3324	P(3)	14233.5092	P(3)	14233.5874
R(3)	14233.3380	R(3)	14233.5147	R(3)	14233.5921
P(5)	14232.5547	P(5)	14232.7317	P(5)	14232.8085
R(5)	14232.5632	R(5)	14232.7394	R(5)	14232.8158
	220-43		**221-43**		**222-43**
P(3)	14117.5487	P(3)	14117.6128	P(3)	14117.6722
R(3)	14117.5531	R(3)	14117.6164	R(3)	14117.6688
P(5)	14116.7867	P(5)	14116.8505	P(5)	14116.9065
R(5)	14116.7929	R(5)	14116.8563	R(5)	14116.9119
	223-43		**224-43**		**225-43**
P(3)	14117.7245	P(3)	14117.7659	P(3)	14117.8072
R(3)	14117.7209	R(3)	14117.7692	R(3)	14117.8100
P(5)	14116.9574	P(5)	14117.0028	P(5)	14117.0436
R(5)	14116.9625	R(5)	14117.0092	R(5)	14117.0478
	226-42		**226-43**		**227-42**
P(9)	14172.0082	P(3)	14117.8442	P(9)	14172.0399
R(9)	14172.0150	R(3)	14117.8468	R(9)	14172.0461
		P(5)	14117.0799		
		R(5)	14117.0841		
	227-43		**228-42**		**228-43**
P(3)	14117.8767	P(9)	14172.0679	P(3)	14117.9056
R(5)	14117.8791	R(9)	14172.0736	R(3)	14117.9082
P(3)	14117.1132			P(3)	14117.1411
R(5)	14117.1168			R(3)	14117.1445
	229-42		**229-43**		**230-42**
P(9)	14172.0928	P(3)	14117.9313	P(9)	14172.1146
R(9)	14172.0979	R(3)	14117.9335	R(9)	14172.1194
		P(5)	14117.1673		
		R(5)	14117.1703		
	230-43		**231-42**		**231-43**
P(3)	14117.9545	P(9)	14172.1339	P(3)	14117.9740
R(3)	14117.9565	R(9)	14172.1381	R(3)	14117.9756
P(5)	14117.1893			P(5)	14117.2089
R(5)	14117.1921			R(5)	14117.2111

Table B.2: *Transition frequencies of A–X band of ^{39}K$_2$.* (continued)

line			line			line		
	232-42			**232-43**			**233-42**	
P(4)	14175.1578		P(3)	14117.9917		P(3)	14175.5170	
R(4)	14175.1596		R(3)	14117.9929		R(3)	14175.5183	
P(9)	14172.1507		P(5)	14117.2269		P(4)	14175.1578▷	
R(9)	14172.1545		R(5)	14117.2302		R(4)	14175.1596▷	
P(12)	14169.3186		P(7)	14116.1220		P(4)	14175.1730	
R(12)	14168.3235		R(7)	14116.1251		R(4)	14175.1747	
						P(9) s	14172.1652	
						P(9) b	14172.1654	
						R(9) s	14172.1686	
						R(9) b	14172.1688	
						P(12)	14169.3326	
						R(12)	14169.3370	
	233-43			**234-42**			**234-43**	
R(3)	14175.5183▷		P(3) b	14175.5304▷		P(5)	14117.2556	
R(4)	14175.1747▷		R(3)	14175.5316▷		R(5)	14117.2573	
P(5)	14117.2424		P(4)	14175.1863		P(7)	14116.1500	
R(5)	14117.2444		P(4)	14175.1863▷		R(7)	14116.1524	
R(7)	14116.1397		R(4)	14175.1879				
			R(4)	14175.1879▷				
			P(9) s	14172.1778				
			P(9) b	14172.1781				
			R(9) s	14172.1809				
			R(9) b	14172.1811				
			P(12)	14169.3447				
			R(12)	14169.3487				
	235-42			**235-43**			**236-42**	
P(3)	14175.5420▷		P(5)	14117.267		P(3) s	14175.5516▷	
R(3)	14175.5431▷		R(5)	14117.2687		P(3) b	14175.5520▷	
P(4) s	14175.1978		P(7)	14116.1612		R(3) s	14175.5526▷	
P(4) b	14175.1978▷		R(7)	14116.1635		R(3) b	14175.5529▷	
R(4) s	14175.1992					P(4)	14175.2074	
R(4) b	14175.1992▷					P(4)	14175.2074▷	
P(9) s	14172.1888					R(4)	14175.2086	
P(9) b	14172.1891					R(4)	14175.2086▷	
R(9) s	14172.1915					P(9) s	14172.1982	
R(9) b	14172.1918					P(9) b	14172.1986	
P(12)	14169.3552					R(9) s	14172.2007	
R(12)	14169.3586					R(9) b	14172.2010	
						P(12)	14169.3641	
						R(12)	14169.3671	

Table B.2: *Transition frequencies of A–X band of ^{39}K$_2$.* (continued)

line		line		line	
	236-43		**237-42**		**237-43**
P(5)	14117.2768	P(3) s	14175.5601▷	P(5)	14117.2852
R(5)	14117.2784	P(3) b	14175.5605▷	R(5)	14117.2865
P(7)	14116.1710	R(3) s	14175.5609▷	P(7)	14116.1792
R(7)	14116.1730	R(3) b	14175.5613▷	R(7)	14116.1810
		P(4)	14175.2159		
		P(4) s	14175.2157▷		
		P(4) b	14175.2159▷		
		R(4)	14175.2169		
		R(4) s	14175.2167▷		
		R(4) b	14175.2170▷		
		P(9) s	14172.2062		
		P(9) b	14172.2066		
		R(9) s	14172.2082		
		R(9) b	14172.2088		
		P(12)	14169.3743		
		R(12)	14169.3717		
	238-42		**238-43**		**239-42**
P(3) s	14175.5673▷	P(5)	14117.2925	P(3) s	14175.5733▷
P(3) b	14175.5677▷	R(5)	14117.2937	P(3) b	14175.5739▷
R(3) s	14175.5679▷	P(7)	14116.1861	R(3) s	14175.5739▷
R(3) b	14175.5685▷	R(7)	14116.1880	R(3) b	14175.5745▷
P(4) s	14175.2228▷			P(4) s	14175.2288▷
P(4) b	14175.2231▷			P(4) b	14175.2291▷
R(4) s	14175.2238▷			R(4) s	14175.2296▷
R(4) b	14175.2240▷			R(4) b	14175.2299▷
P(9) s	14172.2129			P(9) s	14172.2185
P(9) b	14172.2135			P(9) b	14172.2192
R(9) s	14172.2148			R(9) s	14172.2201
R(9) b	14172.2153			R(9) b	14172.2208
P(12)	14169.3780			P(12)	14169.3832
R(12)	14169.3803			R(12)	14169.3852
	239-43		**240-42**		**240-43**
P(5)	14117.2986	P(3) s	14175.5784▷	P(5)	14117.3037
R(5)	14117.2996	P(3) b	14175.5790▷	R(5)	14117.3046
P(7)	14116.1919	R(3) s	14175.5790▷	P(7)	14116.1972
R(7)	14116.1937	R(3) b	14175.5796▷	R(7)	14116.1983
		P(4) s	14175.2337▷		
		P(4) b	14175.2341▷		
		R(4) s	14175.2344▷		
		R(4) b	14175.2348▷		
		P(9) s	14172.2231		
		P(9) b	14172.2239		

Table B.2: *Transition frequencies of A–X band of* ^{39}K$_2$. (continued)

line		line		line	
		240-42 (continued)		
		R(9) s	14172.2244		
		R(9) b	14172.2253		
		P(12)	14169.3874		
		R(12)	14169.3891		
	241-42		**241-43**		**242-42**
P(3) s	14175.5825▷	P(5)	14117.3104	P(4) s	14175.2411▷
P(3) b	14175.5833▷	R(5)	14117.3112	P(4) b	14175.2415▷
R(3) s	14175.5830▷			R(4) s	14175.2417▷
R(3) b	14175.5837▷			R(4) b	14175.2420▷
P(4) s	14175.2379▷			P(3) s	14175.5859▷
P(4) b	14175.2383▷			P(3) b	14175.5867▷
R(4) s	14175.2385▷			R(3) s	14175.5863▷
R(4) b	14175.2388▷			R(3) b	14175.5870▷
	243-42		**244-42**		**245-42**
P(3) s	14175.5884▷	P(3) s	14175.5904▷	P(4) s	14175.2472▷
P(3) b	14175.5894▷	P(3) b	14175.5914▷	P(4) b	14175.2474▷
R(3) s	14175.5887▷	R(3) s	14175.5908▷	R(4) s	14175.2472▷
R(3) b	14175.5896▷	R(3) b	14175.5917▷	R(4) b	14175.2476▷
P(4) s	14175.2436▷	P(4) s	14175.2456▷		
P(4) b	14175.2440▷	P(4) b	14175.2460▷		
R(4) s	14175.2439▷	R(4) s	14175.2456▷		
R(4) b	14175.2444▷	R(4) b	14175.2463▷		

Table B.2: *Transition frequencies of A–X band of ^{39}K$_2$ in cm^{-1}. All frequencies are measured with an uncertainty of* 0.00035 *cm^{-1} except for those indicated by* ▷ *(0.002 cm^{-1}) or by* ○ *(0.01 cm^{-1}).*

line		line		line	
19-0		**20-0**		**21-0**	
R(0)	12362.5776▷	R(1)	12424.8955▷	R(0)	12488.6296▷
P(1)	12362.3916▷	R(2)	12424.8912▷	P(1)	12488.4437▷
R(1)	12362.6215▷	R(3)	12424.8576▷	R(1)	12488.6731▷
P(2)	12362.2498▷	R(4)	12424.7932▷	P(2)	12488.3010▷
R(2)	12362.6315▷	R(5)	12424.7003▷	R(2)	12488.6828▷
R(3)	12362.6089▷	R(6)	12424.5758▷	P(3)	12488.1255▷
R(4)	12362.5530▷			R(3)	12488.6594▷
R(5)	12362.4656▷			P(4)	12487.9161▷
R(6)	12362.3430▷			R(4)	12488.6030▷
				R(5)	12488.5134▷
				R(6)	12488.3900▷
				R(7)	12488.2351▷
				R(8)	12488.0449▷
				R(9)	12487.8231▷
22-0		**23-0**		**24-0**	
R(1)	12551.6950▷	R(0)	12614.3817▷	R(0)	12677.0173▷
R(2)	12551.7030▷	R(1)	12614.4237▷	P(1)	12676.8304▷
P(3)	12551.1483▷	R(2)	12614.4301▷	R(1)	12677.0590▷
R(3)	12551.6950▷	P(3)	12613.8751▷	P(2)	12676.6875▷
R(4)	12551.6530▷	R(3)	12614.4030▷	R(2)	12677.0681▷
R(5)	12551.5238▷	R(4)	12614.3421▷	P(3)	12676.5120▷
R(6)	12551.3960▷			R(3)	12677.0433▷
				P(4)	12676.3020▷
				R(4)	12676.9861▷
				R(5)	12676.8950▷
				R(6)	12676.7709▷
				R(7)	12676.6129▷
				R(8)	12676.4230▷
				R(9)	12676.2050▷
		26-0			
		R(0)	12799.5748▷		
		P(1)	12799.3897▷		
		R(1)	12799.6147▷		
		R(2)	12799.6199▷		
		P(2)	12799.2462▷		
		P(3)	12799.0672▷		
		R(3)	12799.5894▷		
		P(4)	12798.8534▷		
		R(4)	12799.5241▷		
		R(5)	12799.4249▷		
		R(6)	12799.2900▷		

Table B.3: *Transition frequencies of A–X band of ^{39}K ^{41}K.* (continued)

line		line		line	
		26-0 (continued)			
		R(7)	12799.1212$^\triangleright$		
		R(8)	12798.9174$^\triangleright$		
		R(9)	12798.6775$^\triangleright$		
		R(10)	12798.3214$^\triangleright$		
		R(11)	12797.9120$^\triangleright$		
	220-43		**227-43**		**228-43**
P(9)	14144.6831$^\triangleright$	P(9)	14145.1045$^\triangleright$	P(9)	14145.1429$^\triangleright$
R(9)	14144.6967$^\triangleright$	R(9)	14145.1123$^\triangleright$	R(9)	14145.1501$^\triangleright$
	229-43		**230-43**		**231-43**
P(9)	14145.1773$^\triangleright$	P(9)	14145.2077$^\triangleright$	P(9)	14145.2349$^\triangleright$
R(9)	14145.1837$^\triangleright$	R(9)	14145.2137$^\triangleright$	R(9)	14145.2405$^\triangleright$
	232-43		**233-43**		**234-43**
P(9)	14145.2589$^\triangleright$	P(9)	14145.2810	P(9)	14145.2997
R(9)	14145.2639$^\triangleright$	R(9)	14145.2855	R(9)	14145.3037
	235-43		**236-43**		**237-43**
P(9)	14145.3161	P(9)	14145.3304	P(9)	14145.3428
R(9)	14145.3198	R(9)	14145.3337	R(9)	14145.3457
	238-43		**239-43**		**240-43**
P(9)	14145.3536	P(9)	14145.3628	P(9)	14145.3707
R(9)	14145.3562	R(9)	14145.3652	R(9)	14145.3728

Table B.3: *Transition frequencies of A–X band of* ^{39}K ^{41}K. *All frequencies are measured with an uncertainty of* 0.00035 cm^{-1} *except for those indicated by* $^\triangleright$ *(*0.002 cm^{-1}*).*

Bibliography

[1] A. Trabesinger.
Nobel Prize 2005: Glauber, Hall and Hänsch.
Nature Physics 1 (2005).
DOI: 10.1038/nphys155.

[2] J. J. Hudson, B. E. Sauer, M. R. Tarbutt, and E. A. Hinds.
Measurement of the Electron Electric Dipole Moment Using YbF *Molecules*.
Physical Review Letters 89, 023 003 (2002).
DOI: 10.1103/PhysRevLett.89.023003.

[3] E. Peik, B. Lipphardt, H. Schnatz, T. Schneider, C. Tamm, and S. G. Karshenboim.
Limit on the Present Temporal Variation of the Fine Structure Constant.
Physical Review Letters 93, 170 801 (2004).
DOI: 10.1103/PhysRevLett.93.170801.

[4] E. R. Hudson, J. R. Bochinski, H. J. Lewandowski, B. C. Sawyer, and J. Ye.
Efficient Stark Deceleration of Cold Polar Molecules.
European Physical Journal D 31, 351–358 (2004).
DOI: 10.1140/epjd/e2004-00138-7.

[5] C. Samuelis, E. Tiesinga, T. Laue, M. Elbs, H. Knöckel, and E. Tiemann.
Cold Atomic Collisions Studied by Molecular Spectroscopy.
Physical Review A 63, 012 710 (2001).
DOI: 10.1103/PhysRevA.63.012710.

[6] S. Moal, M. Portier, J. Kim, J. Dugué, U. D. Rapol, M. Leduc, and C. Cohen-Tannoudji.
Accurate Determination of the Scattering Length of Metastable Helium Atoms Using Dark Resonances between Atoms and Exotic Molecules.
Physical Review Letters 96, 023 203 (2006).
DOI: 10.1103/PhysRevLett.96.023203.

[7] T. Bourdel, L. Khaykovich, J. Cubizolles, J. Zhang, F. Chevy, M. Teichmann, L. Tarruell, S. J. Kokkelmans, and C. Salomon.
Experimental Study of the BEC-BCS Crossover Region in Lithium 6.
Physical Review Letters 93, 050 401 (2004).
DOI: 10.1103/PhysRevLett.93.050401.

[8] M. Greiner, C. Regal, and D. Jin.
Probing the Excitation Spectrum of a Fermi Gas in the BCS-BEC Crossover Regime.
Physical Review Letters 94, 070 403 (2005).

DOI: 10.1103/PhysRevLett.94.070403.

[9] T. Weber, J. Herbig, M. Mark, H.-C. Nägerl, and R. Grimm.
Three-Body Recombination at Large Scattering Lengths in an Ultracold Atomic Gas.
Physical Review Letters 91, 123 201 (2003).
DOI: 10.1103/PhysRevLett.91.123201.

[10] P. O. Fedichev, Y. Kagan, G. V. Shlyapnikov, and J. T. M. Walraven.
Influence of Nearly Resonant Light on the Scattering Length in Low-Temperature Atomic Gases.
Physical Review Letters 77, 2913–2916 (1996).
DOI: 10.1103/PhysRevLett.77.2913.

[11] I. Sherstov.
Matter Wave Interferences of Potassium Molecules and the Influence of Collisions with Potassium Atoms in the Ground State.
Ph.D. thesis, Universität Hannover, Germany (2006).

[12] H. L. Bethlem, G. Berden, and G. Meijer.
Decelerating Neutral Dipolar Molecules.
Physical Review Letters 83, 1558–1561 (1999).
DOI: 10.1103/PhysRevLett.83.1558.

[13] S. Jung, E. Tiemann, and C. Lisdat.
Cold atoms and Molecules from Fragmentation of Decelerated SO_2.
Physical Review A 74, 040 701 (2006).
DOI: 10.1103/PhysRevA.74.040701.

[14] W. C. Stwalley and H. Wang.
Photoassociation of Ultracold Atoms: A New Spectroscopic Technique.
Journal of Molecular Spectroscopy 195, 194–228 (1999).
DOI: 10.1006/jmsp.1999.7838.

[15] N. Vanhaecke, C. Lisdat, B. T'Jampens, D. Comparat, A. Crubellier, and P. Pillet.
Accurate Asymptotic Ground State Potential Curves of Cs_2 *from Two-colour Photoassociation.*
European Physical Journal D 28, 351–360 (2004).
DOI: 10.1140/epjd/e2004-00001-y.

[16] E. A. Donley, N. R. Claussen, S. T. Thompson, and C. E. Wieman.
Atom-molecule Coherence in a Bose-Einstein Condensate.
Nature 417, 529–533 (2002).
DOI: 10.1038/417529a.

[17] S. Jochim, M. Bartenstein, A. Altmeyer, G. Hendl, S. Riedl, C. Chin, J. Hecker Denschlag, and R. Grimm.
Bose-Einstein Condensation of Molecules.
Science 302, 2101–2104 (2003).
DOI: 10.1126/science.1093280.

[18] S. B. Nagel, P. G. Mickelson, A. D. Saenz, Y. N. Martinez, Y. C. Chen, T. C. Killian, P. Pellegrini, and R. Côté.

Photoassociative Spectroscopy at Long Range in Ultracold Strontium.
Physical Review Letters 94, 083 004 (2005).
DOI: 10.1103/PhysRevLett.94.083004.

[19] S. Tojo, M. Kitagawa, K. Enomoto, Y. Kato, Y. Takasu, M. Kumakura, and Y. Takahashi.
High-Resolution Photoassociation Spectroscopy of Ultracold Ytterbium Atoms by Using the Intercombination Transition.
Physical Review Letters 96, 153 201 (2006).
DOI: 10.1103/PhysRevLett.96.153201.

[20] J. M. Sage, S. Sainis, T. Bergeman, and D. DeMille.
Optical Production of Ultracold Polar Molecules.
Physical Review Letters 94, 203 001 (2005).
DOI: 10.1103/PhysRevLett.94.203001.

[21] G. Thalhammer, K. Winkler, F. Lang, S. Schmid, R. Grimm, and J. H. Denschlag.
Long-Lived Feshbach Molecules in a Three-Dimensional Optical Lattice.
Physical Review Letters 96, 050 402 (2006).
DOI: 10.1103/PhysRevLett.96.050402.

[22] W. C. Stwalley.
Efficient Conversion of Ultracold Feshbach-resonance-related Polar Molecules into Ultracold Ground State ($X\ ^1\Sigma^+\ v=0,\ J=0$) Molecules.
European Physical Journal D 31, 221–225 (2004).
DOI: 10.1140/epjd/e2004-00147-6.

[23] A. Griesmaier, J. Werner, S. Hensler, J. Stuhler, and T. Pfau.
Bose-Einstein Condensation of Chromium.
Physical Review Letters 94, 160 401 (2005).
DOI: 10.1103/PhysRevLett.94.160401.

[24] C. Lisdat.
Realisation eines Materiewelleninterferometers für Moleküle und neue Möglichkeiten zur Beobachtung von Atom-Molekül-Stößen.
Ph.D. thesis, Universität Hannover, Germany (2001).

[25] C. Samuelis.
Spektroskopie und optische Manipulation kalter Stöße in einem Natrium-Molekülstrahl.
Ph.D. thesis, Universität Hannover, Germany (2003).

[26] M. Elbs.
Experimentelle und theoretische Untersuchung asymptotischer molekularer Zustände am Beispiel Na_2.
Ph.D. thesis, Universität Hannover, Germany (1998).

[27] J. Ohlenbusch.
Eintwicklung eines kostengünstigen, Mikroprozessor gesteuerten Wavemeters (1987).
Diploma Thesis, Universität Hannover, Germany.

[28] S. Gerstenkorn, S. Vergés, and J. Chevillard.

Atlas du spectre de l'absorption de la molécule d'iode [11 000 − 14 000 cm⁻¹] (Paris: Editions du Centre National de la Recherche Scientifique (CNRS)) (1982).
Laboratoire Aimé Cotton, CNRS II, Orsay, France.

[29] H. Knöckel, B. Bodermann, and E. Tiemann.
High precision Description of the Rovibronic Structure of the I_2 *B–X spectrum.*
European Physical Journal D 28, 199–209 (2004).
DOI: 10.1140/epjd/e2003-00313-4.

[30] A. Banerjee and V. Natarajan.
Absolute-frequency Measurements of the D_2 *line and Fine-structure Interval in* ^{39}K.
Physical Review A 70, 052 505 (2004).
DOI: 10.1103/PhysRevA.70.052505.

[31] A. Banerjee, D. Das, and V. Natarajan.
Absolute Frequency Measurements of the D_1 *lines in* ^{39}K, ^{85}Rb, *and* ^{87}Rb *with 0.1 ppb Uncertainty.*
Europhysics Letters 65, 172–178 (2004).
DOI: 10.1209/epl/i2003-10069-3.

[32] W. Scherf, O. Khait, H. Jäger, and L. Windholz.
Remeasurement of the Transition Frequencies, Fine Structure Splitting and Isotope Shift of the Resonance Lines of Lithium, Sodium and Potassium.
Zeitschrift für Physik D 36, 31–33 (1996).
DOI: 10.1007/BF01437417.

[33] J. Ye, H. Schnatz, and L. Hollberg.
Optical Frequency Combs: From Frequency Metrology to Optical Phase Control.
IEEE Journal of Selected Topics in Quantum Electronics 9, 1041–1058 (2003).
DOI: 10.1109/JSTQE.2003.819109.

[34] T. Quinn.
Practical Realization of the Definition of the Metre, Including Recommended Radiations of other Optical Frequency Standards (2001).
Metrologia 40, 103–133 (2003).
And references therein DOI: 10.1088/0026-1394/40/2/316.

[35] D. Das, S. Barthwal, A. Banerjee, and V. Natarajan.
Absolute Frequency Measurements in Yb *with 0.08 ppb uncertainty: Isotope Shifts and Hyperfine Structure in the* 399 nm $^1S_0-^1P_1$ *line.*
Physical Review A 72, 032 506 (2005).
DOI: 10.1103/PhysRevA.72.032506.

[36] V. Gerginov, A. Derevianko, and C. E. Tanner.
Observation of the Nuclear Magnetic Octupole Moment of ^{133}Cs.
Physical Review Letters 91, 072 501 (2003).
DOI: 10.1103/PhysRevLett.91.072501.

[37] V. Gerginov, C. E. Tanner, S. Diddams, A. Bartels, and L. Hollberg.
Optical Frequency Measurements of $6s^2S_{1/2}$ $6p^2P_{3/2}$ *Transition in a* ^{133}Cs *Atomic Beam Using a Femtosecond Laser Frequency Comb.*
Physical Review A 70, 042 505 (2004).

DOI: 10.1103/PhysRevA.70.042505.

[38] J. Ye, S. Swartz, P. Jungner, and J. L. Hall.
      Hyperfine Structure and Absolute Frequency of the ^{87}Rb 5P$_{3/2}$ *state*.
      Optics Letters 21, 1280–1282 (1996).

[39] G. P. Barwood, P. Gill, and W. R. C. Rowley.
      Frequency Measurements on Optically Narrowed Rb-*stabilised Laser Diodes at* 780 nm
          and 795 nm.
      Applied Physics B: Lasers and Optics 53, 142–147 (1991).

[40] A. Banerjee, D. Das, and V. Natarajan.
      Precise Measurements of Atomic Energy Levels: D lines and Fine-structure Interval
          in K.
      Journal of the Optical Society of America B Optical Physics 21, 79–82 (2004).

[41] A. Banerjee, D. Das, and V. Natarajan.
      Precise Frequency Measurements of Atomic Transitions by use of a Rb-*stabilized Res-*
          onator.
      Optics Letters 28, 1579–1581 (2003).

[42] P. Risberg.
      A Revision of the Term Systems for Na I *and* K I *Based on Hollow-cathode Observa-*
          tions.
      Arkiv för Fysik 10, 583 (1956).

[43] P. Buck and I. I. Rabi.
      Hyperfine Structure of ^{39}K *in the* 4P *State*.
      Physical Review 107, 1291–1294 (1957).
      DOI: 10.1103/PhysRev.107.1291.

[44] N. Bendali, H. T. Duong, and J. L. Vialle.
      High-resolution Laser Spectroscopy on the D$_1$ and D$_2$ lines of ^{39,40,41}K *Using RF Mod-*
          ulated laser Light.
      Journal of Physics B Atomic Molecular Physics 14, 4231–4240 (1981).
      DOI: 10.1088/0022-3700/14/22/009.

[45] F. Touchard, P. Guimbal, S. Büttgenbach, R. Klapisch, M. de Saint Simon, J. M.
          Serre, C. Thibault, H. T. Duong, P. Juncar, S. Liberman, J. Pinard, and J. L.
          Vialle.
      Isotope Shifts and Hyperfine Structure of $^{38-47}$K *by Laser Spectroscopy*.
      Physics Letters B 108, 169–171 (1982).
      DOI: 10.1016/0370-2693(82)91167-4.

[46] G. Wilpers, C. Degenhardt, T. Binnewies, A. Chernyshov, F. Riehle, J. Helmcke, and
          U. Sterr.
      Improvement of the Fractional Uncertainty of a Neutral-atom Calcium Optical Fre-
          quency Standard to 2×10^{-14}.
      Applied Physics B: Lasers and Optics 76, 149–156 (2003).
      DOI: 10.1007/s00340-003-1109-7.

[47] C. Lisdat, O. Dulieu, H. Knöckel, and E. Tiemann.

Inversion Analysis of K_2 *Coupled Electronic States with the Fourier Grid Method*.
European Physical Journal D 17, 319–328 (2001).
DOI: 10.1007/s100530170006.

[48] K. Sengstock.
Ramsey-Atominterferometrie an lasermanipulierten, kalten Atomen.
Ph.D. thesis, Universität Bonn, Germany (1993).

[49] B. Edlén.
The Dispersion of Standard Air.
Journal of the Optical Society of America 43, 339 (1953).

[50] H. Wang, P. L. Gould, and W. C. Stwalley.
Long-range Interaction of the $^{39}K\,(4s) + {}^{39}K\,(4p)$ *Asymptote by Photoassociative Spectroscopy. I. The* 0_g^- *Pure Long-range State and the Long-range Potential Constants*.
Journal of Chemical Physics 106, 7899–7912 (1997).
DOI: 10.1063/1.473804.

[51] E. Arimondo, M. Inguscio, and P. Violino.
Experimental Determinations of the Hyperfine Structure in the Alkali Atoms.
Reviews of Modern Physics 49, 31–76 (1977).
DOI: 10.1103/RevModPhys.49.31.

[52] A. Sieradzan, P. Kulatunga, and M. Havey.
Hyperfine-structure measurements in the $4p\,^2P_{3/2}$ *state of* ^{41}K *using polarization quantum-beat spectroscopy*.
Physical Review A 52, 4447–4450 (1995).
DOI: 10.1103/PhysRevA.52.4447.

[53] U. Hefter and K. Bergmann.
Atomic and Molecular Beam Methods, Volume I, 193–253 (G. Scoles (edit.), Oxford University Press, Oxford) (1988).

[54] R. W. Schmieder, A. Lurio, and W. Happer.
Hyperfine Structure and Lifetimes of the $4\,^2P_{3/2}$ *and* $5\,^2P_{3/2}$ *States of* ^{39}K.
Physical Review 173, 76–79 (1968).
DOI: 10.1103/PhysRev.173.76.

[55] J. Ney.
Hyperfeinstrukturuntersuchung der $4p$ *und* $5p\,^2P_{3/2}$*-Terme im K I-Spektrum durch Resonanzstreuung von Licht zur Bestimmung der Kernquadrupolmomente von* ^{39}K *und* K^{41}.
Zeitschrift für Physik A 223, 126–138 (1969).
DOI: 10.1007/BF01392975.

[56] J. Ney, R. Repnow, H. Bucka, and G. Schatz.
Untersuchung des $4p\,^2P_{3/2}$*- und* $5p\,^2P_{3/2}$*-Terms des* K I*-Spektrums durch Resonanzstreuung von Licht zur Bestimmung des Kernquadrupolmoments von* K^{40}.
Zeitschrift für Physik A 213, 192–201 (1968).
DOI: 10.1007/BF01379825.

[57] C. Lisdat, M. Frank, H. Knöckel, M.-L. Almazor, and E. Tiemann.

Realization of a Ramsey-Bordé Matter Wave Interferometer on the K_2 *molecule.*
European Physical Journal D 12, 235–240 (2000).
DOI: 10.1007/s100530070018.

[58] J. L. Roberts, N. R. Claussen, S. L. Cornish, E. A. Donley, E. A. Cornell, and C. E. Wieman.
Controlled Collapse of a Bose-Einstein Condensate.
Physical Review Letters 86, 4211–4214 (2001).
DOI: 10.1103/PhysRevLett.86.4211.

[59] B. DeMarco and D. Jin.
Onset of Fermi Degeneracy in a Trapped Atomic Gas.
Science 285, 1703–1706 (1999).
DOI: 10.1126/science.285.5434.1703.

[60] G. Modugno, G. Roati, F. Riboli, F. Ferlaino, R. J. Brecha, and M. Inguscio.
Collapse of a Degenerate Fermi Gas.
Science 297, 2240–2243 (2002).
DOI: 10.1126/science.1077386.

[61] I. Bloch.
Ultracold Quantum Gases in Optical Lattices.
Nature Physics 1, 23–30 (2005).
DOI: 10.1038/nphys138.

[62] S. Jochim, M. Bartenstein, A. Altmeyer, G. Hendl, C. Chin, J. H. Denschlag, and R. Grimm.
Pure Gas of Optically Trapped Molecules Created from Fermionic Atoms.
Physical Review Letters 91, 240 402 (2003).
DOI: 10.1103/PhysRevLett.91.240402.

[63] S. Dürr, T. Volz, A. Marte, and G. Rempe.
Observation of Molecules Produced from a Bose-Einstein Condensate.
Physical Review Letters 92, 020 406 (2004).
DOI: 10.1103/PhysRevLett.92.020406.

[64] T. Loftus, C. A. Regal, C. Ticknor, J. L. Bohn, and D. S. Jin.
Resonant Control of Elastic Collisions in an Optically Trapped Fermi Gas of Atoms.
Physical Review Letters 88, 173 201 (2002).
DOI: 10.1103/PhysRevLett.88.173201.

[65] J. Werner, A. Griesmaier, S. Hensler, J. Stuhler, T. Pfau, A. Simoni, and E. Tiesinga.
Observation of Feshbach Resonances in an Ultracold Gas of ^{52}Cr.
Physical Review Letters 94, 183 201 (2005).
DOI: 10.1103/PhysRevLett.94.183201.

[66] F. Ferlaino, C. D'Errico, G. Roati, M. Zaccanti, M. Inguscio, G. Modugno, and A. Simoni.
Feshbach spectroscopy of a K-Rb *atomic mixture.*
Physical Review A 73, 040 702 (2006).
DOI: 10.1103/PhysRevA.73.040702.

[67] C. Amiot, J. Vergès, and C. E. Fellows.
The Long-range Potential of the K_2 $X^1\Sigma_g^+$ *Ground Electronic State up to* $15\text{\AA}$.
Journal of Chemical Physics 103, 3350–3356 (1995).
DOI: 10.1063/1.470245.

[68] U. Volz and H. Schmoranzer.
Precision Lifetime Measurements on Alkali Atoms and on Helium by Beam-gas-laser Spectroscopy.
Physica Scripta Volume T 65, 48–56 (1996).

[69] E. Tiemann, H. Knöckel, and H. Richling.
Long Range Interaction at the Asymptote $3s + 3p$ *of* Na_2.
Zeitschrift für Physik D 37, 323–332 (1996).
DOI: 10.1007/s004600050047.

[70] C. Amiot.
private communication.

[71] W. Stwalley.
private communication (2005).

[72] A. J. Ross, P. Crozet, C. Effantin, J. d'Incan, and R. F. Barrow.
Interactions Between the $A(1)$ $^1\Sigma_u^+$ *and* $b(1)$ $^3\Pi_u$ *States of* K_2.
Journal of Physics B Atomic Molecular Physics 20, 6225–6231 (1987).
DOI: 10.1088/0022-3700/20/23/014.

[73] G. Jong, L. Li, T.-J. Whang, W. C. Stwalley, J. A. Coxon, M. Li, and A. M. Lyyra.
CW All-optical Triple-resonance Spectroscopy of K_2: *Deperturbation analysis of the* $A^1\Sigma_u^+$ ($v \leq 12$) *and* $b^3\Pi_u$ ($13 \leq v \leq 24$) *states*.
Journal of Molecular Spectroscopy 155, 115–135 (1992).
DOI: 10.1016/0022-2852(92)90552-Y.

[74] M. R. Manaa, A. J. Ross, F. Martin, P. Crozet, A. M. Lyyra, L. Li, C. Amiot, and T. Bergeman.
Spin-orbit Interactions, New Spectral Data, and Deperturbation of the Coupled $b^3\Pi_u$ *and* $A^1\Sigma_u^+$ *states of* K_2.
Journal of Chemical Physics 117, 11 208–11 215 (2002).
DOI: 10.1063/1.1522716.

[75] O. Allard, C. Samuelis, A. Pashov, H. Knöckel, and E. Tiemann.
Experimental Study of the Ca_2 $^1S + ^1S$ *Asymptote*.
European Physical Journal D 26, 155–164 (2003).
DOI: 10.1140/epjd/e2003-00208-4.

[76] O. Docenko, M. Tamanis, R. Ferber, A. Pashov, H. Knöckel, and E. Tiemann.
Spectroscopic Studies of NaCs for the Ground State Asymptote of $Na + Cs$ *Pairs*.
European Physical Journal D 31, 205–211 (2004).
DOI: 10.1140/epjd/e2004-00156-5.

[77] S. Falke, E. Tiemann, C. Lisdat, H. Schnatz, and G. Grosche.
Transition Frequencies of the D lines of ^{39}K , ^{40}K , *and* ^{41}K *Measured with a Femtosecond Laser Frequency Comb*.

Physical Review A 74, 032 503 (2006).
DOI: 10.1103/PhysRevA.74.032503.

[78] W. Meath.
Retarded Interaction Energies between Like Atoms in Different Energy States.
Journal of Chemical Physics 48, 227–235 (1968).
DOI: 10.1063/1.1667907.

[79] M. Marinescu and A. Dalgarno.
Analytical Interaction Potentials of the Long Range Alkali-metal Dimers.
Zeitschrift für Physik D 36, 239–248 (1996).
DOI: 10.1007/BF01426409.

[80] M. Marinescu and A. Dalgarno.
Dispersion Forces and Long-range Electronic Transition Dipole Moments of Alkali-metal Dimer Excited States.
Physical Review A 52, 311–328 (1995).
DOI: 10.1103/PhysRevA.52.311.

[81] R. S. Mulliken.
The Interaction of Differently Excited Like Atoms at Large Distances.
Physical Review 120, 1674–1684 (1960).
DOI: 10.1103/PhysRev.120.1674.

[82] H. Wang, J. Li, X. T. Wang, C. J. Williams, P. L. Gould, and W. C. Stwalley.
Precise Determination of the Dipole Matrix Element and Radiative Lifetime of the ^{39}K 4p State by Photoassociative Spectroscopy.
Physical Review A 55, 1569–1572 (1997).
DOI: 10.1103/PhysRevA.55.R1569.

[83] U. Volz, M. Majerus, H. Liebel, A. Schmitt, and H. Schmoranzer.
Precision Lifetime Measurements on Na I $3p^2P_{1/2}$ *and* $3p^2P_{3/2}$ *by Beam-Gas-Laser Spectroscopy*.
Physical Review Letters 76, 2862–2865 (1996).
DOI: 10.1103/PhysRevLett.76.2862.

[84] G. Zhao, W. T. Zemke, J. T. Kim, B. Ji, H. Wang, J. T. Bahns, W. C. Stwalley, L. Li, A. M. Lyyra, and C. Amiot.
New Measurements of the $a^3\Sigma_u^+$ state of K_2 *and Improved Analysis of Long-range Dispersion and Exchange Interactions Between Two K Atoms*.
Journal of Chemical Physics 105, 7976–7985 (1996).
DOI: 10.1063/1.472712.

[85] R. Le Roy.
In *Molecular Spectroscopy, Specialist Periodical Report* (eds. R. Barrow, D. Long, and D. Millen), 120 (Chemical Society of London) (1973).

[86] B. Ji, C.-C. Tsai, and W. C. Stwalley.
Proposed Modification of the Criterion for the Region of Validity of the Inverse-power Expansion in Diatomic Long-range Potentials.
Chemical Physics Letters 236, 242–246 (1995).
DOI: 10.1016/0009-2614(95)00216-Q.

[87] E. Hodby, S. T. Thompson, C. A. Regal, M. Greiner, A. C. Wilson, D. S. Jin, E. A. Cornell, and C. E. Wieman.
Production Efficiency of Ultracold Feshbach Molecules in Bosonic and Fermionic Systems.
Physical Review Letters 94, 120 402 (2005).
DOI: 10.1103/PhysRevLett.94.120402.

[88] C. Ospelkaus, S. Ospelkaus, L. Humbert, P. Ernst, K. Sengstock, and K. Bongs.
Ultracold Heteronuclear Molecules in a 3D Optical Lattice.
Physical Review Letters 97, 120 402 (2006).
DOI: 10.1103/PhysRevLett.97.120402.

[89] H. Richling.
Der Na_2 A $^1\Sigma_u^+$ Zustand bei sehr großem Kernabstand: Beobachtung von Hyperfeinstruktur und Zeeman-Effekt und Simulation des Molekülsprektums aus atomaren Konstanten.
Ph.D. thesis, Universität Hannover, Germany (1994).

[90] B. Verhaar, K. Gibble, and S. Chu.
Cold-collision Properties Derived from Frequency Shifts in a Cesium Fountain.
Physial Review A 48, 3429–3432 (1993).
DOI: 10.1103/PhysRevA.48.R3429.

[91] R. J. Le Roy and R. B. Bernstein.
Dissociation Energies of Diatomic Molecules from Vibrational Spacings of Higher Levels: Application to the Halogens.
Chemical Physics Letters 5, 42–44 (1970).
DOI: doi:10.1016/0009-2614(70)80125-7.

[92] A. Pashov, O. Docenko, M. Tamanis, R. Ferber, H. Knöckel, and E. Tiemann.
Potentials for Modeling Cold Collisions Between Na (3S) and Rb (5S) Atoms.
Physical Review A 72, 062 505 (2005).
DOI: 10.1103/PhysRevA.72.062505.

[93] E. J. Salumbides, K. S. E. Eikema, W. Ubachs, H. Hollenstein, U.and Knöckel, and E. Tiemann.
The Hyperfine Structure of $^{129}I_2$ and $^{127}I^{129}I$ in the $B^3\Pi_{0_u^+}$–$X^1\Sigma_u^+$ Band System.
Molecular Physics 104, 2641–2652 (2006).
DOI: 10.1080/00268970600747696.

[94] G. F. Gribakin and V. V. Flambaum.
Calculation of the Scattering Length in Atomic Collisions using the Semiclassical Approximation.
Physical Review A 48, 546–553 (1993).
DOI: 10.1103/PhysRevA.48.546.

[95] A. J. Kerman, J. M. Sage, S. Sainis, T. Bergeman, and D. DeMille.
Production and State-Selective Detection of Ultracold RbCs Molecules.
Physical Review Letters 92, 153 001 (2004).
DOI: 10.1103/PhysRevLett.92.153001.

96 D. Wang, J. Qi, M. F. Stone, O. Nikolayeva, H. Wang, B. Hattaway, S. D. Gensemer,
    P. L. Gould, E. E. Eyler, and W. C. Stwalley.
    Photoassociative Production and Trapping of Ultracold KRb *Molecules*.
    Physical Review Letters 93, 243 005 (2004).
    DOI: 10.1103/PhysRevLett.93.243005.

97 S. D. Kraft, P. Staanum, J. Lange, L. Vogel, R. Wester, and M. Weidemüller.
    Formation of Ultracold LiCs *Molecules*.
    Journal of Physics B Atomic Molecular Physics 39, 993–1000 (2006).
    DOI: 10.1088/0953-4075/39/19/S13.

98 C. Degenhardt, T. Binnewies, G. Wilpers, U. Sterr, F. Riehle, C. Lisdat, and E. Tie-
    mann.
    Photoassociation Spectroscopy of Cold Calcium Atoms.
    Physical Review A 67, 043 408 (2003).
    DOI: 10.1103/PhysRevA.67.043408.

99 M. Theis, G. Thalhammer, K. Winkler, M. Hellwig, G. Ruff, R. Grimm, and J. H.
    Denschlag.
    Tuning the Scattering Length with an Optically Induced Feshbach Resonance.
    Physical Review Letters 93, 123 001 (2004).
    DOI: 10.1103/PhysRevLett.93.123001.

100 T. Laue, E. Tiesinga, C. Samuelis, H. Knöckel, and E. Tiemann.
     Magnetic-field Imaging of Weakly Bound Levels of the Ground-state Na_2 *Dimer*.
     Physical Review A 65, 023 412 (2002).
     DOI: 10.1103/PhysRevA.65.023412.

101 C. Samuelis, S. Falke, T. Laue, P. Pellegrini, O. Dulieu, H. Knöckel, and E. Tiemann.
     Optical Manipulation of Long-range Interactions at the 3s + 3p *Asymptote of* Na_2.
     European Physical Journal D 26, 307–318 (2003).
     DOI: 10.1140/epjd/e2003-00294-2.

102 S. Falke.
     Light Induced Manipulation of Long Range States of Na_2 (2002).
     Diploma Thesis, Universität Hannover, Germany.

103 M. H. Anderson, J. R. Ensher, M. R. Matthews, C. E. Wieman, and E. A. Cornell.
     Observation of Bose-Einstein Condensation in a Dilute Atomic Vapor.
     Science 269, 198–201 (1995).
     DOI: 10.1126/science.269.5221.198.

104 K. B. Davis, M.-O. Mewes, M. R. Andrews, N. J. van Druten, D. S. Durfee, D. M.
     Kurn, and W. Ketterle.
     Bose-Einstein Condensation in a Gas of Sodium Atoms.
     Physical Review Letters 75, 3969–3973 (1995).
     DOI: 10.1103/PhysRevLett.75.3969.

105 C. C. Bradley, C. A. Sackett, J. J. Tollett, and R. G. Hulet.
     *Evidence of Bose-Einstein Condensation in an Atomic Gas with Attractive Interac-
     tions*.
     Physical Review Letters 75, 1687–1690 (1995).

DOI: 10.1103/PhysRevLett.75.1687.

[106] D. G. Fried, T. C. Killian, L. Willmann, D. Landhuis, S. C. Moss, D. Kleppner, and T. J. Greytak.
Bose-Einstein Condensation of Atomic Hydrogen.
Physical Review Letters 81, 3811–3814 (1998).
DOI: 10.1103/PhysRevLett.81.3811.

[107] A. Robert, O. Sirjean, A. Browaeys, J. Poupard, S. Nowak, D. Boiron, C. I. Westbrook, and A. Aspect.
A Bose-Einstein Condensate of Metastable Atoms.
Science 292, 461–464 (2001).
DOI: 10.1126/science.1060622.

[108] F. Pereira Dos Santos, J. Léonard, J. Wang, C. J. Barrelet, F. Perales, E. Rasel, C. S. Unnikrishnan, M. Leduc, and C. Cohen-Tannoudji.
Bose-Einstein Condensation of Metastable Helium.
Physical Review Letters 86, 3459–3462 (2001).
DOI: 10.1103/PhysRevLett.86.3459.

[109] T. Weber, J. Herbig, M. Mark, H.-C. Nägerl, and R. Grimm.
Bose-Einstein Condensation of Cesium.
Science 299, 232–235 (2003).
DOI: 10.1126/science.1079699.

[110] A. Crubellier, O. Dulieu, F. Masnou-Seeuws, M. Elbs, H. Knöckel, and E. Tiemann.
Simple Determination of Na_2 Scattering Lengths Using Observed Bound Levels at the Ground State Asymptote.
European Physical Journal D 6, 211–220 (1999).
DOI: 10.1007/s100500050336.

[111] M. Elbs, H. Knöckel, T. Laue, C. Samuelis, and E. Tiemann.
Observation of the last bound levels near the Na_2 ground-state asymptote.
Physical Review A 59, 3665–3672 (1999).
DOI: 10.1103/PhysRevA.59.3665.

[112] S. Inouye, M. R. Andrews, J. Stenger, H.-J. Miesner, D. M. Stamper-Kurn, and W. Ketterle.
Observation of Feshbach Resonances in a Bose-Einstein Condensate.
Nature 392, 151–154 (1998).
DOI: 10.1038/32354.

[113] S. L. Cornish, N. R. Claussen, J. L. Roberts, E. A. Cornell, and C. E. Wieman.
Stable ^{85}Rb Bose-Einstein Condensates with Widely Tunable Interactions.
Physical Review Letters 85, 1795–1798 (2000).
DOI: 10.1103/PhysRevLett.85.1795.

[114] C. Degenhardt, H. Stoehr, C. Lisdat, G. Wilpers, H. Schnatz, B. Lipphardt, T. Nazarova, P.-E. Pottie, U. Sterr, J. Helmcke, and F. Riehle.
Calcium Optical Frequency Standard with Ultracold Atoms: Approaching 10^{-15} relative uncertainty.
Physical Review A 72, 062 111 (2005).

DOI: 10.1103/PhysRevA.72.062111.

[115] I. Courtillot, A. Quessada, R. P. Kovacich, A. Brusch, D. Kolker, J.-J. Zondy, G. D. Rovera, and P. Lemonde.
Clock Transition for a Future Optical Frequency Standard with Trapped Atoms.
Physical Review A 68, 030 501 (2003).
DOI: 10.1103/PhysRevA.68.030501.

[116] J. C. J. Koelemeij and M. Leduc.
Prospects for Measurement and Control of the Scattering Length of Metastable Helium Using Photoassociation Techniques.
European Physical Journal D 31, 263–271 (2004).
DOI: 10.1140/epjd/e2004-00154-7.

[117] R. Scheunemann, F. S. Cataliotti, T. W. Hänsch, and M. Weitz.
Resolving and Addressing Atoms in Individual Sites of a CO_2-laser Optical Lattice.
Physical Review A 62, 051 801 (2000).
DOI: 10.1103/PhysRevA.62.051801.

[118] H. Pu, L. O. Baksmaty, W. Zhang, N. P. Bigelow, and P. Meystre.
Effective-mass Analysis of Bose-Einstein Condensates in Optical Lattices: Stabilization and Levitation.
Physical Review A 67, 043 605 (2003).
DOI: 10.1103/PhysRevA.67.043605.

[119] J. L. Bohn and P. S. Julienne.
Prospects for Influencing Scattering Lengths with Far-off-resonant Light.
Physical Review A 56, 1486–1491 (1997).
DOI: 10.1103/PhysRevA.56.1486.

[120] V. Kokoouline, J. Vala, and R. Kosloff.
Tuning the Scattering Length on the Ground Triplet State of Cs_2.
Journal of Chemical Physics 114, 3046–3050 (2001).

[121] F. K. Fatemi, K. M. Jones, and P. D. Lett.
Observation of Optically Induced Feshbach Resonances in Collisions of Cold Atoms.
Physical Review Letters 85, 4462–4465 (2000).
DOI: 10.1103/PhysRevLett.85.4462.

[122] G. Thalhammer, M. Theis, K. Winkler, R. Grimm, and J. H. Denschlag.
Inducing an Optical Feshbach Resonance via Stimulated Raman Coupling.
Physical Review A 71, 033 403 (2005).
DOI: 10.1103/PhysRevA.71.033403.

[123] F. H. Mies.
A Multichannel Quantum Defect Analysis of Diatomic Predissociation and Inelastic Atomic scattering.
Journal of Chemical Physics 80, 2514–2525 (1984).
DOI: 10.1063/1.447000.

[124] J. L. Bohn and P. S. Julienne.
Semianalytic Theory of Laser-assisted Resonant Cold Collisions.

Physical Review A 60, 414–425 (1999).
DOI: 10.1103/PhysRevA.60.414.

[125] E. Tiemann.
private communication (2005).

[126] S. Magnier.
Determination des etats electroniques excites des molecules Na_2 *et* K_2. *Application aux collisions entre atomes excites par laser*.
Ph.D. thesis, Universite de Paris-Sud, France (1993).

[127] O. Dulieu.
private communication.

[128] F. James.
MINUIT, Function Minimization and Error Analysis.
CERN Program Library Long Write-up D506.

[129] E. Ahmed, P. Qi, A. Hansson, T. Kirova, A. Lazoudis, A. M. Lyyra, L. Li, J. Qi, and S. Magnier.
Measurement of the Electronic Transition Dipole Moment by Autler-Townes Splitting: Comparing of Three- and Four-level Excitation Schemes for the Na_2 $A\ ^1\Sigma_u^+$–$X\ ^1\Sigma_g^+$ *System*.
Journal of Chemical Physics 084308 (2006).
DOI: 10.1063/1.2164454.

[130] M. L. Citron, H. R. Gray, C. W. Gabel, and C. R. Stroud Jr.
Experimental Study of Power Broadening in a Two-level Atom.
Physical Review A 16, 1507–1512 (1977).
DOI: 10.1103/PhysRevA.16.1507.

[131] O. Allard.
Long-range Interactions in the Calcium Dimer Studied by Molecular Spectroscopy.
Ph.D. thesis, Universität Hannover, Germany and Université Paris-Sud, France (2004).

[132] O. Allard, S. Falke, A. Pashov, O. Dulieu, H. Knöckel, and E. Tiemann.
Study of coupled states for the $(4s^2)^1\,S + (4s4p)^3\,P$ *asymptote of* Ca_2.
European Physical Journal D 35, 483–497 (2005).
DOI: 10.1140/epjd/e2005-00173-x.

[133] V. E. Bondybey and J. H. English.
Laser-induced Fluorescence of the Calcium Dimer in Supersonic Jet: The Red Spectrum of Ca_2.
Chemical Physics Letters 111, 195–200 (1984).

[134] T. Laue, P. Pellegrini, O. Dulieu, C. Samuelis, H. Knöckel, F. Masnou-Seeuws, and E. Tiemann.
Observation of the Long-range Potential Well of the (6) $^1\Sigma_g^+$ *(3s + 5s) State of* Na_2.
European Physical Journal D 26, 173–185 (2003).
DOI: 10.1140/epjd/e2003-00221-7.

[135] A. Nesmeyanov.
Vapor Pressure of Chemical Elements (Elsevier Publishing Company, Amsterdam) (1963).

[136] E. Lax (ed.).
Taschenbuch für Chemiker und Physiker, Band I (Springer-Verlag, Berlin), 3rd edn. (1967).

[137] R. Lide, David (ed.).
CRC Handbook of Chemistry and Physics (CRC Press, Boca Raton), 78th edn. (1997).

[138] C. A. Stan and W. Ketterle.
Multiple Species Atom Source for Laser-cooling Experiments.
Review of Scientific Instruments 76, 3113 (2005).
DOI: 10.1063/1.1935433.

[139] U. Fischer (ed.).
Tabellenhandbuch Metall (Verlag Europa-Lehrmittel), 40th edn. (1997).

[140] B. J. Meyer and E. E. Pietsch.
Mg: Magnesium ; A.
In *Gmelin Handbook of Inorganic and Organometallic Chemistry* (Gmelin-Institut für Anorganische Chemie und Grenzgebiete in der Max-Planck-Gesellschaft zur Förderung der Wissenschaften), 8th edn. (1952).

[141] A. Edmonds.
Angular Momentum in Quantum Mechanics (Princeton University Press, New Jersey), 2nd edn. (1960).

List of Figures

List of Tables

List of Symbols

Chapter 5

Index

μ-metal box, 19

ac-Stark, 39
adiabatic expansion, 19, 45
adiabatic potential curve, 65
adjacent filtering, 72
air conditioning, 118
air cooling, 116
alkaline earth metal, 109
Allan standard deviation, 21
alumina, 112
approximated phase method, 66
argon ion laser, 20
assignment, 53
asymptotic method, 78
atomic beam apparatus, 25
atomic lifetime, 62
Autler-Townes component, 104
Autler-Townes components, 92
avoided crossing, 61

back-reflection, 70
beam, 108
beam apparatus, 45
beam chamber, 17
beat note, 25
BEC, 44
BEC-BCS crossover, 44
black body radiation, 118
Born-Oppenheimer approximation, 12, 43,
     61, 67
Bragg spectroscopy, 82, 87
Brewster angle, 20

calcium, 108, 111
carrier gas, 19
cat's eye, 27
CCD camera, 89

chopper, 89
classical turning point, 83
clock signal, 25
coherence, 106
cold collisions, 11, 85, 86
color glass filter, 18
consistency check, 29
cool down curve, 119
cooling plate, 115
copper, 112
coumarin 6, 88
counter, 25
coupled channel analysis, 49
coupling strength, 41
Cs atomic clock, 25
Cs-clock, 23

dark state, 106
datafield, 50
DCM, 46
density matrix, 31, 41
deperturbation analysis, 49
dichroic beam splitter, 89
differential pump stage, 19
dilute gas, 107
diode laser, 21, 25
dipole coupling strength, 127
dipole moment, 16
dipole trap, 39
dissociation energy, 59
dissociation limit, 47
Doppler shift, 26
Doppler width, 14
Doppler-free spectroscopy, 85
Dunham series, 53, 77
dye laser, 20, 46, 88
dynamical coupling, 67

wavelength meter, 21, 46

Zeemann effect, 33

Curriculum Vitae

Name:	Stephan Falke
Date of Birth:	21.09.1977
Place of Birth:	Bielefeld
Parents:	Christine and Josef Falke
Nationality:	German
Marital Status:	Single

Education:
- 1983-1993
  St.-Johannis Schule in Bremen, Elementary and Secondary School
- 1993-1996
  Schulzentrum Huckelriede in Bremen, High School
  Qualification: Abitur

Studies:
- Oct. 1997 - Oct. 2002
  Physics, University of Hannover
  Qualification: Diplom Physiker
- Apr. 1998 - Nov. 2005
  Mathmatics with a major in Computer Science, University of Hannover
  Qualification: Diplom Mathematiker
- Sep. 2000 - June 2001
  Exchange student (SOCRATES) at the University of Copenhagen, Denmark
- Nov. 2002 - May 2003
  Visit as a scholar of the DAAD at the University of California at Davis, USA
- June 2003 to date
  PhD student and scientific coworker in the group of Prof. Tiemann, Inst. of Quantum Optics, University of Hannover
- June 2004 to date
  Collegiate member of the European Graduate College *Interference and Quantum Applications*

Acknowledgements